

# Energy Dependence of Multiplicity Fluctuations in Heavy Ion Collisions at the CERN SPS

Dissertation  
zur Erlangung des Doktorgrades  
der Naturwissenschaften

vorgelegt beim Fachbereich Physik  
der Johann Wolfgang Goethe - Universität  
in Frankfurt am Main

von  
Benjamin Lungwitz  
aus Frankfurt am Main

Frankfurt, 2008

vom Fachbereich Physik der  
Johann Wolfgang Goethe - Universität als Dissertation angenommen.

Dekan: Prof. Dr. Dirk-Hermann Rischke

Gutachter: Prof. Dr. Marek Gazdzicki, Prof. Dr. Herbert Ströbele

Datum der Disputation:

# Zusammenfassung

In dieser Arbeit wird die Energieabhängigkeit der Multiplizitätsfluktuationen in zentralen Schwerionenkollisionen mit dem NA49-Experiment am CERN SPS- Beschleuniger untersucht.

Die Arbeit beginnt (Kapitel 1: Introduction) mit einer Einleitung in die Grundlagen der stark wechselwirkenden Materie. Im Standardmodell der Teilchenphysik sind die Nukleonen, die Bausteine der Atomkerne, aus Quarks aufgebaut und werden durch die starke Wechselwirkung, vermittelt über ihre Feldquanten, die Gluonen, zusammengehalten. Die Theorie der starken Wechselwirkung wird als Quantenchromodynamik (QCD) bezeichnet, die starke Ladung nennt man Farbladung. In der QCD gibt es drei elementare Ladungen, Quarks können die Ladung Rot, Grün oder Blau tragen, Antiquarks die entsprechenden Antifarben.

Es sind derzeit 6 verschiedene Quarks bekannt, die in 3 Generationen mit aufsteigender Masse eingeordnet werden können. Jede Generation besteht aus einem Quark mit der elektrischen Ladung  $+2/3$  und einem mit der Ladung  $-1/3$ . Zusätzlich zu den 6 Quarks gibt es noch 6 Anti-Quarks. Die Nukleonen, die Bausteine der Atomkerne, bestehen aus den Quarks der 1. Generation. Neben den 3 Quark-Generationen existieren 3 Generationen von Teilchen, die nicht an der starken Wechselwirkung teilnehmen, die Leptonen. Es gibt jeweils ein elektrisch geladenes Lepton und ein neutrales, genannt Neutrino, pro Generation.

Die Austauscheteilchen der Quantenchromodynamik, die Gluonen, tragen je eine Farbe und eine Antifarbe. Da die Gluonen, im Gegensatz z.B. zu den Feldquanten der Elektrodynamik, den Photonen, geladen sind, können sie direkt miteinander wechselwirken. Während das Potential der elektrischen Wechselwirkung zwischen zwei geladenen Teilchen mit der Distanz der beiden Ladungen abnimmt und asymptotisch gegen Null geht, sorgt die Wechselwirkung der Gluonen untereinander dafür, dass das Potential der starken Wechselwirkung zwischen einem Quark und einem Anti-Quark mit zunehmender Entfernung beider ansteigt. Wenn die potentielle Energie in dem so genannten String aus Gluonen, welcher das Quark- Anti-Quark-Paar verbindet, groß genug wird, wird ein weiteres Quark- Anti-Quark- Paar erzeugt und der String bricht. Es ist daher nicht möglich, einen freien farbgeladenen Zustand zu erzeugen. Gebundene, farbneutrale Zustände der starken Wechselwirkung werden als Hadronen bezeichnet. Derzeit sind zwei Arten von Hadronen bekannt. Die Mesonen sind aus einem Quark- Anti-Quark- Paar aufgebaut, die (Anti-) Baryonen aus drei (Anti-) Quarks. Die Nukleonen (Protonen, Neutronen) gehören zu den Baryonen. Es wird derzeit spekuliert, ob ein gebundener Zustand aus vier Quarks und einem Anti-Quark, ein sog. Pentaquark, existiert, die experimentellen Befunde sind jedoch widersprüchlich.

Heiße Kernmaterie bildet ein so genanntes Hadronengas, wo durch die hohe Energiedichte Hadronen laufend gebildet werden und miteinander wechselwirken. Bei sehr hohen Energiedichten (ca.  $1 \text{ GeV}/\text{fm}^3$ ) erwartet man jedoch, dass die Quarks nicht länger in Hadronen gebunden sind sondern sich frei im ganzen Volumen bewegen können. Diesen Materiezustand bezeichnet man als Deconfinement oder Quark-Gluon-Plasma (QGP). Solche Energiedichten können erreicht werden, wenn man Materie auf Temperaturen von ca.  $10^{12} \text{ K}$  (das entspricht

ca. 100.000 mal der Temperatur im Inneren der Sonne) erhitzt. Solche Temperaturen existierten im Universum bis etwa  $1 \mu\text{s}$  nach dem Urknall. Eine andere Möglichkeit, solche Energiedichten zu erreichen, ist stark komprimierte Kernmaterie, wie sie im Kern von Neutronensternen vermutet wird.

Im Phasendiagramm der stark wechselwirkenden Materie erwartet man, dass die Hadronengas-Phase von der QGP-Phase bei höheren Baryondichten durch einen Phasenübergang 1. Ordnung separiert ist. Bei kleineren Baryondichten hingegen ist ein kontinuierlicher Übergang vorhergesagt. Ein kritischer Punkt soll beide Bereiche trennen.

Das Gebiet der relativistischen Schwerionenphysik beschäftigt sich mit der Frage, ob, und wenn ja, bei welchen Energien der Phasenübergang von einem Hadronengas zu einem Quark-Gluon-Plasma auftritt und welche Eigenschaften das QGP besitzt. Im Labor können derartige Energiedichten mit Schwerionenkollisionen erreicht werden. Am SPS-Beschleuniger des europäischen Kernforschungszentrums CERN bei Genf können Blei-Ionen derart beschleunigt werden, dass bei ihren Kollisionen Energiedichten von mehr als  $1 \text{ GeV}/\text{fm}^3$  in einem kleinen Volumen (ca.  $1000 \text{ fm}^3$ ) für eine kurze Zeit (ca.  $10^{-22} \text{ s}$ ) erreicht werden können. Aufgrund des hohen Drucks expandiert dieser Feuerball sehr schnell, das eventuell vorhandene QGP zerfällt und bildet Hadronen, die mit Detektoren gemessen werden können. Anhand verschiedener Observablen dieses hadronischen Endzustandes versucht man, Informationen über die frühe, dichte Phase der Schwerionenkollision zu erhalten.

Verschiedene Signaturen des Quark-Gluon-Plasmas werden diskutiert und weisen darauf hin, dass bei den höchsten am SPS-Beschleuniger erreichbaren Energien tatsächlich ein QGP erzeugt wurde. Weiterhin kann man die vorhandenen experimentellen Daten so interpretieren, dass bei mittleren SPS-Energien erstmalig QGP erzeugt wird (Onset of Deconfinement). Modelle sagen voraus, dass im Bereich des Onsets of Deconfinement verschiedene Observable, wie der Transversalimpuls, die Verhältnisse der Teilchenmultiplizitäten oder die Teilchenmultiplizität selbst, stark von Kollision zu Kollision fluktuieren. Weiterhin werden erhöhte Fluktuationen erwartet, wenn der Feuerball einer Schwerionenkollision in der Nähe des kritischen Punkts hadronisiert.

Der Bestimmung der Multiplizitätsfluktuationen liegt die entsprechende Multiplizitätsverteilung zugrunde. Sie gibt die Wahrscheinlichkeit  $P(n)$  an, dass in einer Kollision  $n$  Teilchen produziert werden. Die in dieser Arbeit verwendete Observable der Multiplizitätsfluktuationen ist die Scaled Variance  $\omega$ , definiert als das Verhältnis der Varianz der Multiplizitätsverteilung und ihres Mittelwerts (Kapitel 2: Multiplicity Fluctuations). Eine grundlegende Eigenschaft von  $\omega$  ist, dass es im Rahmen eines Superpositionsmodells unabhängig von der Anzahl der Quellen der Teilchenproduktion ist. Wenn die Multiplizität der Kollisionen einer Poisson-Verteilung folgt, ist  $\omega = 1$ . Die Scaled Variance kann für positive ( $\omega(h^+)$ ), negative ( $\omega(h^-)$ ) und alle geladenen Hadronen ( $\omega(h^\pm)$ ) bestimmt werden.

Resonanz-Zerfälle erhöhen die Multiplizitätsfluktuationen, wenn alle Tochter-Teilchen einer Resonanz für die Analyse verwendet werden. Wenn die Resonanzen in zwei detektierte Teilchen zerfallen, ist das gemessene  $\omega$  doppelt so groß als das der Resonanzen selbst. In der Praxis zerfallen die meisten Resonanzen in zwei unterschiedlich geladene Tochterteilchen, man erwartet daher höhere Multiplizitätsfluktuationen für  $\omega(h^\pm)$  als für  $\omega(h^+)$  und  $\omega(h^-)$ .

In mehreren Blaskammer-Experimenten wurde die Energieabhängigkeit der Multiplizitätsfluktuationen in inelastischen p+p Kollisionen im vollen Phasenraum studiert. Die Form der Multiplizitätsverteilung in p+p Kollisionen kann in einem großen Energiebereich durch eine universelle Funktion  $\Psi(z)$  beschrieben werden, wenn  $n$  und  $P(n)$  mit der mittleren Multiplizität skaliert werden:  $P(n) = \Psi(n/\langle n \rangle)/\langle n \rangle$ . Diesen Effekt nennt man KNO-Scaling.

Dadurch bedingt ist  $\omega$  in p+p Kollisionen in einem großen Energiebereich eine lineare Funktion der mittleren Multiplizität.

In dieser Arbeit wird nun erstmals die Energieabhängigkeit der Multiplizitätsfluktuationen in zentralen Schwerionenkollisionen untersucht. Dazu werden Daten des NA49- Experiments verwendet, welches am CERN SPS steht (Kapitel 3: The NA49 Experiment). Der SPS- Beschleuniger ist ein Synchrotron mit einem Durchmesser von ca. 7 km, wo Protonen auf eine Energie von bis zu 400 GeV und Bleionen auf bis zu 158 GeV pro Nukleon beschleunigt werden können. Für das Studium von Kollisionen kleinerer Systeme wird der Bleistrahl fragmentiert und die gewünschten Ionen (hier Kohlenstoff oder Silizium) werden mit Hilfe der Magneten in der Beam-Line und ladungsensitiven Detektoren selektiert.

Das NA49- Experiment verfügt über vier großvolumige Time-Projection-Chambers (TPCs), mit denen es möglich ist, Spuren geladener Teilchen in drei Dimensionen zu detektieren. Zwei dieser TPCs, genannt Vertex-TPCs, befinden sich in jeweils einem supraleitenden Magneten. Zwei weitere TPCs, genannt Main-TPCs, befinden sich außerhalb des magnetischen Feldes. Die elektrisch geladenen Strahlteilchen ionisieren die Gasatome in den TPCs. Die dabei freierwerden Elektronen driften aufgrund eines homogenen elektrischen Feldes zur Ausleseebene. Nach Passieren der Kathodendrähte, die das homogene Feld abschließen, werden sie an den Verstärkungsdrähten durch ein inhomogenes Feld stark beschleunigt, so dass sie weitere Elektronen aus dem Gas ausschlagen. Die Anzahl der Elektronen wird so um den Faktor  $10^3 - 10^4$  verstärkt. Die Elektronen fließen rasch über die Drähte ab. Die schwereren Ionen erzeugen eine Spiegelladung auf der dahinter liegenden Pad-Ebene, diese wird von der TPC-Elektronik ausgelesen. Die NA49 Rekonstruktionssoftware wandelt die Elektronik-Signale der einzelnen Pads in Spurpunkte um und verbindet diese zu den Teilchenspuren. Über die Stärke eines Signals kann der Energieverlust der Teilchen im Detektorgas bestimmt werden, über die Krümmung der Teilchenspur im magnetischen Feld ihre Ladung und ihr Impuls.

In Schwerionenkollisionen werden die Multiplizitätsfluktuationen von den Fluktuationen in der Zentralität der Kollisionen dominiert. Ein Schwerpunkt dieser Arbeit ist es, diese Fluktuationen zu eliminieren. Dazu muss die Zentralität der Kollision fixiert werden (Kapitel 4: Analysis). Die Nukleonen der kollidierenden Kerne kann in Partizipanten- und Spektatornukleonen einteilen. Die Partizipantennukleonen wechselwirken stark miteinander, die Spektatornukleonen liegen außerhalb der Kollisionszone und ihr Impuls wird durch die Kollision kaum verändert. Die Spektator-Nukleonen des Projektils werden in dem Veto-Kalorimeter des NA49-Experiments gemessen. Auch wenn über die gemessene Veto-Energie die Projektil-Partizipanten fixiert werden können, zeigen Modellrechnungen, dass die Anzahl der Target-Partizipanten in nicht-zentralen Kollisionen dennoch fluktuiert. Um diese Fluktuationen zu minimieren werden in dieser Analyse die 1% zentralsten Kollisionen selektiert. Um Alterungseffekte des Kalorimeters zu berücksichtigen wird eine zeitabhängige Korrektur der Veto-Energie angewandt. Sowohl diese Korrektur als auch die Bestimmung der Zentralität einer Kollision wurde in die ROOT-basierenden NA49-Datenanalyseklassen implementiert. Durch die endliche Auflösung des Kalorimeters können verbleibende Zentralitätsschwankungen jedoch nicht ausgeschlossen werden. Mit Hilfe eines Fragmentationsmodells wurde die Energieauflösung des Kalorimeters bestimmt und ihr möglicher Einfluss auf die Multiplizitätsfluktuationen untersucht. Für die hier verwendeten zentralen Kollisionen ist er klein und er geht in den systematischen Fehler der experimentellen Daten ein.

Außerdem ist es wichtig, nur die Bereiche des Phasenraums zu selektieren, wo die Teilchenspuren gut definiert sind und effizient rekonstruiert werden können, da Fluktuationen in der Rekonstruktionseffizienz die Multiplizitätsfluktuationen erhöhen können. Studien im Rah-

men dieser Arbeit haben gezeigt, dass Spuren, bei denen ausschließlich Punkte in der ersten Vertex-TPC gemessen wurden, nicht für die Analyse verwendet werden sollten, da in diesem Detektor die Spurdichte hoch ist und es möglich ist, dass einzelne Spuren nicht rekonstruiert werden können. Teilchen, die nur in den Main-TPCs detektiert wurden, werden aufgrund ihrer schlechteren Impuls-Auflösung verworfen, die dadurch bedingt ist, dass ihre Krümmung im Magnetfeld nicht direkt gemessen ist.

Der systematische Fehler der Scaled Variance  $\omega$  wird durch eine Abschwächung der Selektionskriterien für Kollisionen und Teilchenspuren sowie über den Einfluss der Auflösung und Zeitkalibration des Kalorimeters bestimmt. Für C+C und Si+Si-Kollisionen geht weiterhin die Selektion der Strahlteilchen in den Fehler ein.

Bei der Analyse der NA49-Daten der Zentralitätsabhängigkeit der Multiplizitätsfluktuationen wurde entdeckt, dass  $\omega$  größer wird, je peripherer die Kollisionen sind. Dieser Effekt wurde sowohl in Pb+Pb als auch in C+C und Si+Si Kollisionen in der Vorwärtsakzeptanz beobachtet. Dieses Verhalten wird von string-hadronischen Modellen nicht reproduziert. Verschiedene Interpretationen der Daten sind möglich, unter anderem könnten Fluktuationen in der Anzahl der Target-Partizipanten die Multiplizitätsfluktuationen in der Projektil-Hemisphäre verursachen. Als Startpunkt dieser Arbeit wurde die Analyse der Zentralitätsabhängigkeit der Multiplizitätsfluktuationen wiederholt. Die Ergebnisse (Kapitel 5: Centrality Dependence of Multiplicity Fluctuations) stimmen mit den Ergebnissen der ursprünglichen Analyse von M. Rybczynski überein.

Der Schwerpunkt dieser Arbeit ist die Analyse der Energie- und Systemgrößenabhängigkeit der Multiplizitätsfluktuationen. Für eine differenziertere Analyse wurde der gesamte für die Analyse verwendete Phasenraum ( $0 < y(\pi) < y_{beam}$ ) in einen Bereich nahe der Rapidität des Schwerpunkts der Kollision (Midrapidity,  $0 < y(\pi) < 1$ ) und in einen Bereich in Vorwärtsrichtung ( $1 < y(\pi) < y_{beam}$ ) aufgetrennt. Die experimentelle Akzeptanz ändert sich mit der Kollisionsenergie und wird mit einer Simulation des Detektors bestimmt.

In der Vorwärtsakzeptanz für positiv und negativ geladene Hadronen in zentralen Pb+Pb-Kollisionen ist  $\omega < 1$  (Kapitel 6: Multiplicity Fluctuations in Central Collisions: Experimental Results), die Multiplizitätsverteilung ist also schmaler als die entsprechende Poisson-Verteilung. Im Midrapidity-Bereich sind die Fluktuationen größer. Für alle geladenen Hadronen ist  $\omega$  größer als für positive oder negative Hadronen separat. Die Energieabhängigkeit von  $\omega$  in Pb+Pb-Kollisionen zeigt keine signifikante Struktur, die als ein Signal des kritischen Punkts oder des Onsets of Deconfinement interpretiert werden kann.  $\omega$  in C+C und Si+Si-Kollisionen ist größer als in Pb+Pb-Kollisionen bei der gleichen Energie.

Zum Studium der Abhängigkeit von  $\omega$  von der Rapidität  $y$  und des Transversalimpulses  $p_T$  werden die Bins in  $y$  und  $p_T$  so konstruiert, dass die mittlere Multiplizität in jedem Bin gleich ist, da  $\omega$  von dem Anteil des selektierten Phasenraums abhängt.  $\omega$  ist größer für Rapiditäten nahe Midrapidity und für kleine Transversalimpulse.

Die experimentellen Ergebnisse dieser Arbeit wurden auf mehreren Konferenzen gezeigt [83, 84, 122], die finalen Daten sind bei Physical Review C eingereicht [93] und befinden sich derzeit im Review-Prozess.

Ein statistisches Hadron-Gas-Modell [55] macht Vorhersagen für  $\omega$  im vollen Phasenraum (Kapitel 7: Multiplicity Fluctuations in Central Collisions: Models and Discussion). Drei verschiedene statistische Ensembles können dafür verwendet werden. Bei dem großkanonischen Ensemble wird angenommen, dass alle Erhaltungssätze nur im Mittel, jedoch nicht in jeder Kollision einzeln, erfüllt sind. Bei dem kanonischen Ensemble sind die Ladungen, also elektrische Ladung, Baryonenzahl und Seltsamkeit, in jeder Kollision exakt erhalten, Energie

und Impuls jedoch nur im Mittel. Im mikrokanonischen Ensemble sind alle Erhaltungssätze in jeder einzelnen Kollision erfüllt. Für die mittleren Multiplizitäten sind die verschiedenen statistischen Ensemble äquivalent, wenn das betrachtete System groß genug ist. Die experimentellen Daten der Teilchenmultiplizitäten zeigen, dass dies für die meisten Sorten von produzierten Teilchen etwa ab Si+Si-Kollisionen erreicht ist. Die Scaled Variance hingegen unterscheidet sich in den verschiedenen statistischen Ensembles, auch im Grenzfall des unendlichen Volumens des Kollisionssystems. Für alle produzierten Teilchen einer Ladung, bei Vernachlässigung von Quanteneffekten und Resonanzzerfällen, ist  $\omega = 1$  im großkanonischen,  $\omega = 0.5$  im kanonischen und  $\omega = 0.25$  im mikrokanonischen Ensemble. Die Einführung von Erhaltungssätzen reduziert also die Multiplizitätsfluktuationen. In allen Ensembles wird beobachtet, dass ab Energien von ca.  $\sqrt{s_{NN}} \approx 100$  GeV  $\omega$  mit zunehmender Energie konstant bleibt.

Unter der Annahme, dass die produzierten Teilchen im Impulsraum nicht korreliert sind und die Impulsverteilung der Teilchen unabhängig von der Multiplizität sind, steht  $\omega$  in einer begrenzten Akzeptanz mit  $\omega$  im vollen Phasenraum über eine einfache analytische Formel in Beziehung. Insbesondere gilt unter diesen Annahmen, dass  $\omega$  in verschiedenen Impulsintervallen gleich ist, wenn in ihnen die mittlere Multiplizität gleich ist. Für das kanonische und großkanonische Ensemble für positive und negative Hadronen separat werden keine starken Korrelationen im Impulsraum erwartet, daher können die Modellvorhersagen mit den experimentellen Daten in der begrenzten Akzeptanz im Rahmen dieser Arbeit verglichen werden. Für alle geladenen Hadronen sorgen jedoch Resonanzzerfälle dafür, dass diese Annahmen nicht zutreffen. Im mikrokanonischen Ensemble führen die Erhaltungssätze der Energie und des Impulses Korrelationen im Impulsraum ein, daher können die Vorhersagen des Modells für  $\omega$  im vollen Phasenraum nicht mit den experimentellen Daten in der begrenzten Akzeptanz verglichen werden.

Sowohl das großkanonische als auch das kanonische Ensemble sind im Widerspruch zu den Daten.  $\omega$  wird in der Vorwärtsakzeptanz von beiden Ensembles überschätzt. Außerdem steht die beobachtete Abhängigkeit der Scaled Variance von  $y$  und  $p_T$  im Widerspruch zu diesen beiden Ensembles. Das mikrokanonische Ensemble kann zumindest qualitativ die beobachtete Abhängigkeit von  $\omega$  von  $y$  und  $p_T$  als einen Effekt der Energie- und Impulserhaltung erklären.

Eine andere Klasse von Modellen, in denen die Multiplizitätsfluktuationen studiert wurden, sind die string-hadronischen Modelle UrQMD und HSD. Diese Modelle beschreiben gut die experimentellen Daten von  $\omega$  in p+p-Kollisionen im vollen Phasenraum. Im Rahmen dieser Arbeit erstellte Modellrechnungen, publiziert in [98], zeigen für Pb+Pb-Kollisionen eine ähnliche Energieabhängigkeit von  $\omega$  wie für p+p-Kollisionen, nämlich ein Anstieg mit steigender Kollisionsenergie. Dies ist im Gegensatz zu den Rechnungen des Hadron-Gas-Modells, wo bei höheren Energien  $\omega$  konstant ist.

String-hadronische Modelle erlauben auch die Bestimmung von  $\omega$  in der begrenzten experimentellen Akzeptanz, weiterhin kann die experimentelle Methode der Zentralitätsselektion mittels eines Kalorimeters in diesen Modellen implementiert werden. Daher können die Vorhersagen der string-hadronischen Modellen direkt mit den experimentellen Daten verglichen werden. Für alle untersuchten Energien, Kollisionssystemen, Ladungen und Akzeptanzen stimmen die experimentellen Daten und die UrQMD-Modellrechnungen recht gut überein. Auch die Abhängigkeit der Scaled Variance von  $y$  und  $p_T$  wird von UrQMD gut reproduziert.

In UrQMD können zentrale Kollisionen auf zwei Arten selektiert werden. Einerseits kann der Impaktparameter auf Null gesetzt werden ( $b = 0$ ). Alternativ kann man die Kollisionen, wie im Experiment, anhand der Energie im Veto-Kalorimeter selektieren. In Pb+Pb

Kollisionen in der Vorwärtsakzeptanz ist  $\omega$  für beide Zentralitätsselektionen gleich. Bei Midrapidity ist  $\omega$  etwas größer für Kollisionen, die aufgrund ihrer Veto-Energie selektiert sind. Dies kann qualitativ durch die Fluktuationen der Target-Partizipanten erklärt werden, welche sich stärker auf den Midrapidity-Bereich auswirken. In kleinen Systemen (C+C, Si+Si) werden größere Fluktuationen bei zentralen Kollisionen, die durch ihre Veto-Energie selektiert werden, von UrQMD vorhergesagt, was in Übereinstimmung mit den experimentellen Daten ist. Für Kollisionen mit  $b = 0$  sind die erwarteten Fluktuationen jedoch deutlich höher, eine geometrisch zentrale Kollision bedeutet also in kleinen Systemen nicht, dass die Anzahl der Partizipanten fixiert ist.

Fluktuationen in der Energie, die pro Kollision von den kollidierenden Nukleonen an neu produzierte Teilchen übertragen wird (inelastische Energie), sind für einen Teil der Multiplizitätsfluktuationen verantwortlich. Bei Kollisionsenergien, wo in der frühen Phase der Schwerionenkollision eine gemischte Phase aus QGP und Hadronen-Gas existiert, wurde vorhergesagt, dass die Fluktuationen der inelastischen Energie größere Multiplizitätsfluktuationen verursachen als in einer reinen Hadronen-Gas oder QGP-Phase [41]. Eine quantitative Abschätzung dieses Effekts zeigt jedoch, dass die erwartete Erhöhung der Multiplizitätsfluktuationen sehr gering ist, kleiner als die systematischen Fehler des Experiments. Daher können die vorhandenen experimentellen Daten diese Modellvorhersage weder bestätigen noch widerlegen.

Wenn der Feuerball der Schwerionenkollision bei Temperaturen und baryochemischen Potentialen nahe des kritischen Punktes ausfriert, werden erhöhte Fluktuationen, auch in der Multiplizität erwartet [3]. Bei SPS-Energien wird das baryochemische Potential des chemischen Ausfrierens hauptsächlich durch die Kollisionsenergie, die Temperatur jedoch durch die Größe des Kollisionssystems bestimmt. Ein Vergleich der experimentellen Daten der Energieabhängigkeit von  $\omega$  in Pb+Pb Kollisionen und der Systemgrößenabhängigkeit bei 158A GeV mit dem UrQMD-Modell, welches keinen kritischen Punkt enthält, zeigt keinen Hinweis auf eine signifikante Abweichung der Daten. Dabei ist jedoch anzumerken, dass die genaue Größe der durch den kritischen Punkt verursachten zusätzlichen Fluktuationen in der experimentellen Akzeptanz nicht exakt bekannt ist.

Das NA61-Experiment, basierend auf dem NA49-Detektor, plant einen zweidimensionalen Scan in der Kollisionsenergie und der Größe der Kollisionssysteme, um den kritischen Punkt zu finden. Dabei sind Multiplizitätsfluktuationen, neben Fluktuationen des Transversalimpulses, einer der primären Observablen. Vorhersagen des UrQMD und HSD-Modells über die Energie- und Systemgrößenabhängigkeit von  $\omega$  sind in [99] publiziert, die UrQMD-Rechnungen erfolgten im Rahmen dieser Arbeit. Dabei wurden verschiedene Zentralitätsselektionen untersucht. Diese Rechnungen erlauben eine Bestimmung der Fluktuationen, die ohne die Existenz eines kritischen Punktes erwartet werden. Signifikante und nicht-monotonische Abweichungen der experimentellen Daten von diesen Modellrechnungen können Signale des kritischen Punktes sein.



# Contents

<b>Zusammenfassung</b>	<b>8</b>
<b>1 Introduction</b>	<b>13</b>
1.1 Hadrons, Quarks and Gluons . . . . .	13
1.2 Phase Diagram of Strongly Interacting Matter . . . . .	15
1.2.1 The Beginning of the Universe . . . . .	16
1.2.2 Quark Stars . . . . .	17
1.2.3 Heavy Ion Collisions . . . . .	18
1.3 Signals of Quark-Gluon- Plasma at High Energies . . . . .	20
1.3.1 High $p_T$ Suppression and Jet Quenching . . . . .	20
1.3.2 Flow . . . . .	21
1.3.3 $J/\Psi$ Production . . . . .	24
1.4 Signals of the Onset of Deconfinement at SPS Energies . . . . .	27
1.4.1 Pion Multiplicity . . . . .	27
1.4.2 Strangeness . . . . .	28
1.4.3 Transverse Expansion . . . . .	30
1.5 Fluctuations in High Energy Collisions . . . . .	32
1.5.1 Particle Ratio Fluctuations . . . . .	32
1.5.2 Electrical Charge Fluctuations . . . . .	33
1.5.3 Mean Transverse Momentum Fluctuations . . . . .	36
1.5.4 Multiplicity Fluctuations . . . . .	36
<b>2 Multiplicity Fluctuations</b>	<b>39</b>
2.1 Experimental Measures . . . . .	39
2.1.1 Acceptance Dependence . . . . .	39
2.1.2 Participant Fluctuations . . . . .	40
2.2 Theoretical Concepts . . . . .	44
2.2.1 Resonance Decays . . . . .	44
2.2.2 Fluctuations in Relativistic Gases . . . . .	44
2.2.3 String-Hadronic Models . . . . .	45
2.2.4 Onset of Deconfinement and Critical Point . . . . .	45
2.3 Multiplicity Fluctuations in Elementary Collisions . . . . .	45
<b>3 The NA49 Experiment</b>	<b>49</b>
3.1 Nucleus-Nucleus Collisions at the CERN SPS . . . . .	49
3.1.1 History of the SPS . . . . .	49
3.1.2 Working Principle of a Synchrotron . . . . .	49
3.1.3 Fragmentation Beams . . . . .	51

## Contents

3.2	Experimental Setup . . . . .	52
3.2.1	Beam, Target and Trigger . . . . .	54
3.2.2	The Time Projection Chambers . . . . .	54
3.2.3	Time-of-Flight Detectors . . . . .	57
3.2.4	Veto Calorimeter . . . . .	59
3.3	NA49 Software . . . . .	61
3.3.1	Reconstruction of the NA49 Raw Data . . . . .	61
3.3.2	Simulation and Analysis Software . . . . .	64
<b>4</b>	<b>Analysis</b>	<b>65</b>
4.1	Event Selection . . . . .	65
4.2	Selection of Central Collisions . . . . .	65
4.2.1	Event Centrality . . . . .	68
4.2.2	Trigger Centrality . . . . .	69
4.2.3	Resolution of the Veto Calorimeter . . . . .	70
4.2.4	SHIELD Simulation for Calorimeter Resolution . . . . .	72
4.2.5	Time Dependent Veto Calibration . . . . .	76
4.3	Track Selection and Acceptance . . . . .	77
4.3.1	Delta electrons . . . . .	78
4.3.2	Cut on Parametrization of the NA49 Acceptance . . . . .	83
4.4	Errors on Scaled Variance . . . . .	83
4.4.1	Statistical Error . . . . .	83
4.4.2	Systematic Errors . . . . .	86
<b>5</b>	<b>Centrality Dependence of Multiplicity Fluctuations</b>	<b>93</b>
5.1	Published NA49 Results . . . . .	93
5.2	Cross-Check of Results on Centrality Dependence . . . . .	93
5.3	WA98 Results . . . . .	97
5.4	PHENIX Results . . . . .	97
<b>6</b>	<b>Multiplicity Fluctuations in Central Collisions: Experimental Results</b>	<b>101</b>
6.1	Multiplicity Distributions . . . . .	101
6.2	Energy Dependence in Pb+Pb . . . . .	102
6.3	System Size Dependence . . . . .	102
6.4	Rapidity Dependence . . . . .	108
6.5	Transverse Momentum Dependence . . . . .	108
<b>7</b>	<b>Multiplicity Fluctuations in Central Collisions: Models and Discussion</b>	<b>109</b>
7.1	Statistical Hadron-Gas Model . . . . .	109
7.1.1	Scaled Variance in Full Phase-Space . . . . .	111
7.1.2	Comparison to Experimental Data . . . . .	113
7.1.3	Rapidity and Transverse Momentum Dependence . . . . .	115
7.2	String-Hadronic Models . . . . .	117
7.2.1	Energy Dependence of $\omega$ . . . . .	118
7.2.2	System Size Dependence of $\omega$ . . . . .	126
7.2.3	Rapidity and Transverse Momentum Dependence . . . . .	132
7.3	Onset of Deconfinement . . . . .	134

7.4	Critical Point . . . . .	135
7.5	First Order Phase Transition . . . . .	138
<b>8</b>	<b>Additional Observables</b>	<b>139</b>
8.1	Multiplicity Correlations . . . . .	139
8.2	$\Delta\phi$ - $\Delta\eta$ - Correlations . . . . .	140
<b>9</b>	<b>Summary</b>	<b>143</b>
<b>A</b>	<b>Additional Plots and Tables</b>	<b>145</b>
<b>B</b>	<b>Probability Distributions and Moments</b>	<b>157</b>
B.1	The Mean and the Variance . . . . .	157
B.1.1	Binomial distribution . . . . .	158
B.1.2	Poisson distribution . . . . .	159
B.2	Conditional Probabilities . . . . .	160
<b>C</b>	<b>Kinetic Variables</b>	<b>161</b>
C.1	Collision Energy . . . . .	161
C.1.1	Center of Mass Energy . . . . .	161
C.1.2	Fermi-Variable F . . . . .	161
C.2	Kinematic Variables . . . . .	162
C.2.1	Transverse Momentum . . . . .	162
C.2.2	Rapidity . . . . .	162
C.2.3	Pseudo-rapidity . . . . .	163
<b>D</b>	<b>Analysis Programs and T49 Procedures</b>	<b>165</b>
D.1	Software for Centrality Determination . . . . .	165
D.2	Example Program for Centrality Determination . . . . .	167
	<b>Bibliography</b>	<b>169</b>
	<b>Publications and Presentations of the Author</b>	<b>177</b>
	<b>Danksagung</b>	<b>180</b>
	<b>Lebenslauf</b>	<b>181</b>

*Contents*

# 1 Introduction

## 1.1 Hadrons, Quarks and Gluons

The matter which builds the world today, about 13.7 billion years after the big bang, consists of atoms of a size of approximately  $10^{-10}$  m. An atom has an electron hull, which determines its chemical and optical properties, and a nucleus, which carries most of the mass of the atom. A nucleus has a size of the order of  $10^{-14}$  m and is made of protons and neutrons, the nucleons.

The nucleon is believed to be filled by a soup of quarks, anti-quarks and gluons. The quantum numbers of a nucleon correspond to the quantum numbers of three light quarks, called constituent quarks. Within the quantumchromodynamics (QCD), the theory of strong interaction, the quarks and gluons are elementary particles.

Despite of their electrical and weak charge the quarks are carrying the charge of the strong interaction, the so-called color. Three color charges, red, green and blue, and their anti-charges exist. The exchange particles of the strong interaction are the gluons, they carry one charge and one anti-charge. Due to symmetry reasons only 8 different gluons exist.

The theory of strong interactions, the quantumchromodynamics, predicts that only color-neutral (white) objects can exist in the vacuum ("confinement"). This is because the exchange particles of strong interactions, the gluons, carry a strong charge by themselves and are therefore interacting with each other. The color potential for a quark- anti-quark pair has an additional linear term in comparison to the electrical potential:

$$V_{q\bar{q}}(r) = -\frac{4 \cdot \alpha_s}{3 \cdot r} + \kappa \cdot r, \quad (1.1)$$

where  $\alpha_s$  is the coupling constant of the strong interaction and  $k$  the strength of the linear term of the QCD potential. Because of the second term in Eq. 1.1 an infinite amount of energy would be required to separate the quark and the anti-quark. When the quark- anti-quark pair is separated the energy of the "string" connecting both increases. When this energy is large enough the string breaks and a new quark- anti-quark pair is created. The newly created quarks combine with the primordial quarks to color-neutral hadrons.

Two different kinds of color-neutral hadrons exist: The mesons can be seen as a constituent quark- anti-quark state. The lightest and most common meson is the pion with a mass of approximately 140 MeV. Baryons can be seen as states of three constituent quarks carrying the color charges red, blue and green. Similar to the color cycle in optics these add to white. The most common baryons are the protons and neutrons, the building blocks of our nuclei. In addition anti-baryons made of three anti-quarks exist. The constituents of hadrons, the quarks and the gluons, are called "partons".

Three generations of quarks and anti-quarks are known, the quarks in the higher generations have larger masses. Each generation consists of two quarks with a different electrical charge of  $+\frac{2}{3}$  and  $-\frac{1}{3}$ , respectively (Table 1.1). The anti-quarks carry the opposite charge of  $-\frac{2}{3}$  and  $+\frac{1}{3}$ . In addition to the quarks there are three generations of leptons, particles which are not

## 1 Introduction

charge	1st generation		2nd generation		3rd generation	
quarks						
$+\frac{2}{3}$	u	1.5-4.5 MeV	c	1-1.4 GeV	t	175 GeV
$-\frac{1}{3}$	d	5-8.5 MeV	s	80-155 MeV	b	4-4.5 GeV
leptons						
-1	$e$	511 keV	$\mu$	105.7 MeV	$\tau$	1.777 GeV
0	$\nu_e$	< 3 eV	$\nu_\mu$	< 190 keV	$\nu_\tau$	< 18.2 MeV

Table 1.1: The quarks and leptons [1]. Constituent quark masses are given.

participating in the strong interaction. In each generation consists of one lepton carrying an electrical charge ( $e$ ,  $\mu$ ,  $\tau$ ) and one electrically neutral lepton, a neutrino ( $\nu$ ). The hull of an atom is made of the lightest charged lepton species, the electron. Similar to the quarks the leptons can be ordered into three generations with increasing mass.

All elementary particles have a quantum number called spin. The spin may be interpreted as an internal angular momentum of the particle. Particles with an integer spin are called bosons and have different properties to the fermions, particles with fractional spin. All quarks and leptons have a spin of  $1/2$  and are therefore fermions, where the gluons, as well as the photons and the exchange particles of the weak interaction, have a spin of  $1$  and are bosons. The mesons are made of two fermions and are therefore bosons where the baryons, made of three fermions, are fermions by themselves.

The two lightest quarks, the up (u) and the down (d) quark, build the protons (u,u,d) and the neutrons (u,d,d). Note that even so the electrical charges of the quarks are fractional, the charges of hadrons are always integers. When the masses of the three constituent quarks of a proton are added, this would result in a proton mass of  $8 - 17.5$  MeV. In reality the mass of a proton is much larger, namely  $938$  MeV. Therefore only  $\approx 1\%$  of the proton mass is carried by its constituent quarks, the remaining  $99\%$  of the mass is the energy of the quantum-chromodynamical field which manifests itself by virtual quark- anti-quark pairs and gluons inside the proton. The mechanism of the hadronic bound states is fundamentally different to the atomic and nuclear bound states where the binding energy is negative and the bound state has a smaller energy than its constituents. Such a "confined" bound-state can only exist because the colored objects are not allowed to exist freely.

Even though free quarks can not be observed in the detectors it is predicted that in nuclear matter at sufficiently high energy density the quarks and gluons are no longer confined into hadrons but can move freely in the whole high density volume. This effect is called "deconfinement" and the deconfined quark matter is called "quark-gluon-plasma" (QGP). These high energy densities can either be reached by high temperatures (like directly after the big bang,  $T \approx 150$  MeV  $\approx 1.5 \cdot 10^{12}$  K, about 100,000 times the temperature in the core of the sun) or high baryon densities (possibly in the core of neutron stars).

The energy densities needed to create QGP are extremely high ( $\approx 1$  GeV/fm<sup>3</sup>). One cubic centimeter of QGP would have the energy of  $10^{29}$  Joule and the mass of  $10^{13}$  kg. Until now, only three different scenarios which can reach these energy densities are known: the early universe shortly after the big bang, the interior of a neutron star and ultra-relativistic heavy ion collisions.

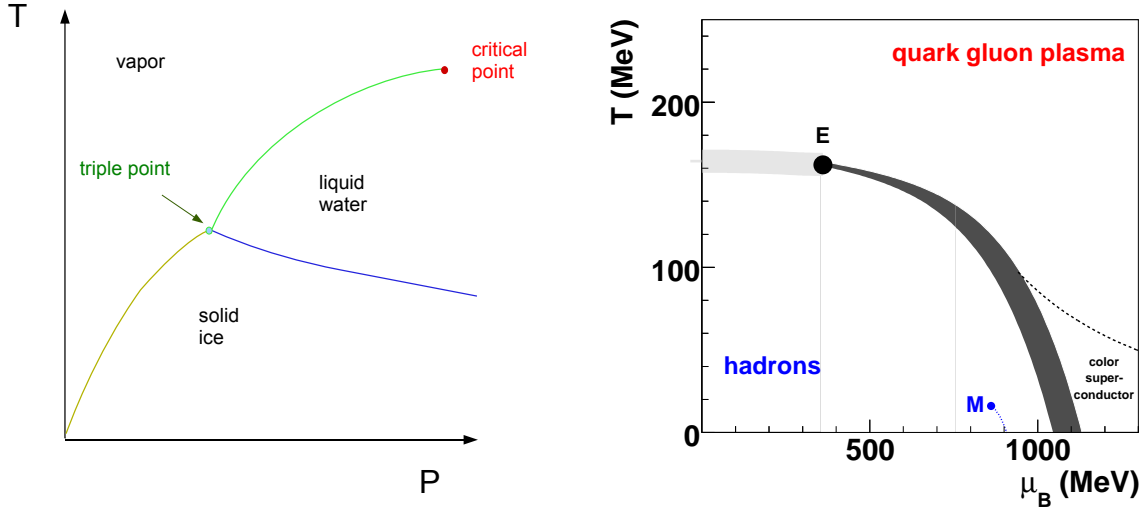


Figure 1.1: Left: Phase diagram of water as a function of the temperature  $T$  and the pressure  $P$ . Right: Phase diagram of strongly interacting matter as a function of the temperature  $T$  and the baryo-chemical potential  $\mu_B$ .

## 1.2 Phase Diagram of Strongly Interacting Matter

The phase diagram of water is shown in Fig. 1.1, left. At normal pressures ( $P \approx 1$  bar) the liquid and the vapor phases are separated by a first order phase transition line. The first order phase transition line in the  $T$ - $P$ -plane ends in a critical point. For higher pressures no phase transition but a smooth cross-over lies in between the liquid and the vapor phase. In the vicinity of the critical point several phenomena like the critical opalescence can be observed.

It is predicted that the phase diagram of strongly interacting matter has qualitatively similar features [2, 3, 4, 5]. This hypothetical phase diagram is shown in Fig. 1.1, right. The temperature  $T$  is a measure of the kinetic energy of the particles, the baryo-chemical potential  $\mu_B$  is related to the baryon density. For low temperatures and densities the system is in a hadronic phase. For sufficiently large temperatures and/or baryon densities the system is expected to be in a deconfined phase with quarks and gluons as the relevant degrees of freedom. It is currently under discussion in the heavy ion physics community how the hadron and quark-gluon phase are separated. Lattice QCD calculations at vanishing baryo-chemical potential predict a smooth cross-over instead of a phase transition between hadron gas and quark-gluon-plasma in this region of the phase diagram at temperatures of about 160 – 190 MeV. For higher chemical potentials a first order phase transition between the two phases is suggested by the QCD inspired models. If this is the case the first order phase transition line is expected to end in a critical end-point when going to smaller baryo-chemical potentials. The exact location of the critical end-point in the phase diagram is unknown, different lattice QCD calculations give different results [6]. One of them suggests that it might be as well possible that no critical point exists at all, then a crossover would be between the two phases for all baryo-chemical potentials [7].

In the following different scenarios are discussed where energy densities sufficient for the creation of quark-gluon-plasma may be realized in nature.

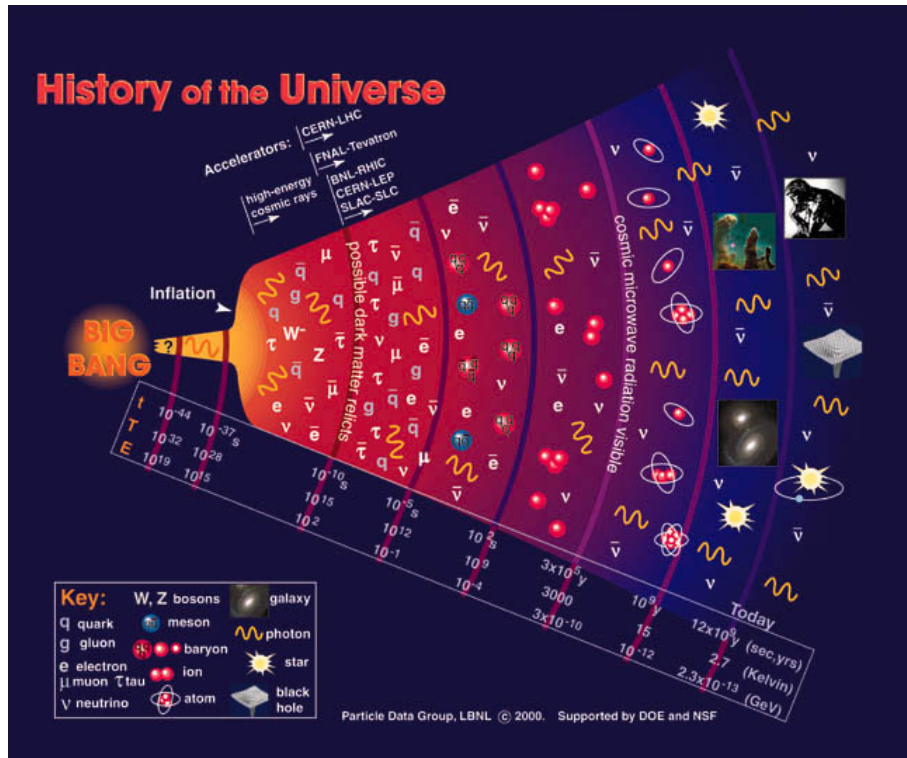


Figure 1.2: Sketch of the evolution of the universe.

### 1.2.1 The Beginning of the Universe

The big bang theory says that the universe developed from an extremely dense and hot state. In the Planck epoch the universe was so small ( $10^{-35}$  m) and its energy density was so high ( $\rho \approx 10^{94}$  g/cm<sup>3</sup>,  $T \approx 10^{32}$  K) that the known laws of physics can not be applied. Grand unification theories (GUT) predict that the four known forces of nature, the gravitational, the electromagnetic, the strong and the weak force, were unified at these times. The universe started to expand and after the Planck epoch the gravitational force separated. At the age of  $10^{-36}$  s the temperature of the universe was cooled down to  $10^{27}$  K and the strong force separated from the electroweak force. GUT predict that the latent heat related to this phase transition lead to an inflationary expansion of the universe by a factor  $10^{30} - 10^{50}$ . The universe, which was much smaller than a proton before, expanded to a size of about 10 cm.

Starting from  $10^{-33}$  s after the big bang the quarks were formed (Fig. 1.2). These quarks were not confined into hadrons because of the high energy density. They are expected to be in a QGP phase. One micro-second after the big bang the temperature dropped below  $10^{13}$  K and the transition between QGP and a gas of hadrons took place. The net baryon number of the universe was close to zero and consequently the transition point was located at  $\mu_B \approx 0$  (Fig. 1.1, right).

This, hadron-gas dominated, universe lasted until 100 micro-seconds after the big bang. When the temperature dropped below  $10^{12}$  K most of the hadrons decayed or were annihilated, only a small number of protons and neutrons survived because of a small asymmetry of matter and antimatter.



## 1.2 Phase Diagram of Strongly Interacting Matter

The temperature at this time was still high enough for the creation and annihilation of electron-positron pairs. One second after the big bang the temperature dropped below  $10^{10}$  K, too low for electron-positron pair production. A small number of electrons survived because of the matter-antimatter asymmetry.

Ten seconds after the big bang the temperature of the universe was smaller than the binding energy of light nuclei, the nucleosynthesis of deuterons and helium started and continued until 5 minutes after the big bang. The amount of protons, deuterons and helium observed in the universe of today gives us information about the epoch of nucleosynthesis.

400,000 years after the big bang the temperature of the universe dropped below 3000 K and the electrons and nuclei formed atoms. The universe started being transparent for electromagnetic radiation and the cosmic microwave background, which is observable today, was emitted in that time [8].

The big bang theory is supported by many observations of the universe of today. Unfortunately important information about the early stages of the universe, for instance the quark-gluon-plasma epoch, is not accessible.

### 1.2.2 Quark Stars

Neutron stars are extremely dense objects. In a radius of 10 – 20 km a mass of 1.35 – 2.1 solar masses [9] is concentrated. Neutron stars consist of a crust of ordinary atomic nuclei. Proceeding inward, the amount of neutrons in the nuclei increases. Such nuclei are only stable because of the large pressure in the neutron star. For the composition of the inner part of the neutron star, different scenarios are under discussion [10].

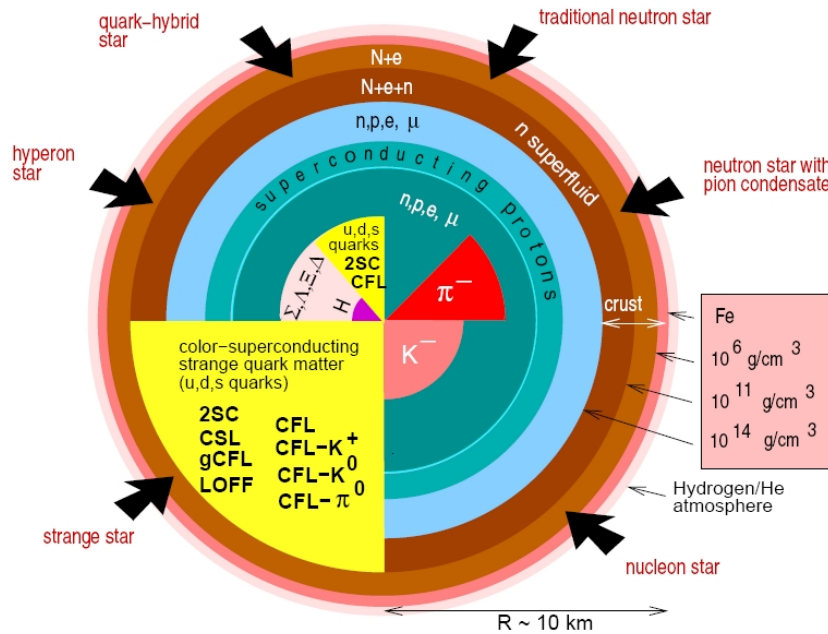


Figure 1.3: Composition of a neutron star [10].

In most scenarios the neutron star consists of free moving neutrons, nuclei and electrons when further approaching to the center. The higher the pressure is, the larger the number of

## 1 Introduction

neutrons and the smaller the number of (neutron rich) nuclei. In the inner part, the density of a neutron star reaches the density of atomic nuclei,  $10^{12}$  kg/cm<sup>3</sup> ( $\approx 0.1$  GeV/fm<sup>3</sup>), or even more. A neutron star is stabilized by the Fermi pressure of the neutrons, which acts against the gravitational force. The Fermi-pressure occurs because two neutrons can not be in the same quantum state due to the Pauli-principle.

The matter in the core of a neutron star might consist of hadrons. A composition of light baryons, namely protons and neutrons, is as well under discussion as a composition of heavier baryons ( $\Delta$ ,  $\Lambda$ , etc.) or mesons (pions or kaons).

It is also speculated that the interior of the dense stars consist of quark matter. Such a star with core of deconfined matter can reach much higher densities and is called "quark star". The matter in the core of a quark star would be located in the lower right part of the phase diagram (Fig. 1.1) at a small temperature and a high baryo-chemical potential. The quark matter may be in a state of color superconductivity where the quarks become correlated in Cooper pairs. The observation of neutron stars with unusual high masses and small radii might be interpreted as a sign of deconfined matter inside them.

### 1.2.3 Heavy Ion Collisions

The only presently known way to study quark matter and the possible phase transition to hadron-gas in the laboratory are heavy ion collisions. Nuclei of heavy elements (like lead or gold) are accelerated to ultra-relativistic velocities. They collide and form a state of a high temperature and baryon-density. In these collisions energy densities exceeding 1 GeV/fm<sup>3</sup> are created in a small volume ( $\approx 1000$  fm<sup>3</sup>) and for a short time ( $\approx 10^{-22}$  s). Only two laboratories in the world have the capabilities to accelerate heavy ions to the energies needed: the CERN near Geneva, Switzerland with its SPS and LHC accelerators and the BNL in Brookhaven, USA with the AGS and RHIC accelerators. In the future also the GSI FAIR facility in Darmstadt, Germany and the NICA facility in the JINR, Dubna, Russia, can reach these energies.

The nucleons inside the nuclei which are interacting strongly, either with a nucleon of the collision partner or a newly produced particle, are called participants. These nucleons lose a major part of their energy (stopping). The nucleons not interacting strongly in the collision, the so-called spectators, are moving forward with essentially unchanged momentum. The number of spectator nucleons can be measured by a calorimeter and thus the centrality of a collision can be determined.

Different pictures exist to describe the evolution of a heavy ion collision. In the Landau-picture [11], the participant nucleons are fully stopped and form a system with high energy and baryon density in the center of mass of the collision. This so called "fireball" starts to expand hydro-dynamically. Because of the Lorentz-contraction of the colliding nuclei the pressure gradient is higher in longitudinal direction and consequently the expansion in this direction is faster.

An alternative approach is the Bjorken picture [12], where the participant nucleons are not totally stopped but continue to travel forward, losing only a part of their kinetic energy. The baryon and energy density in the center of the collision are smaller than the corresponding values in the Landau picture.

In both scenarios it is possible to have an energy density in the center of the collision which is large enough for the creation of a quark-gluon-plasma when the kinetic energy of the colliding nuclei is sufficient.

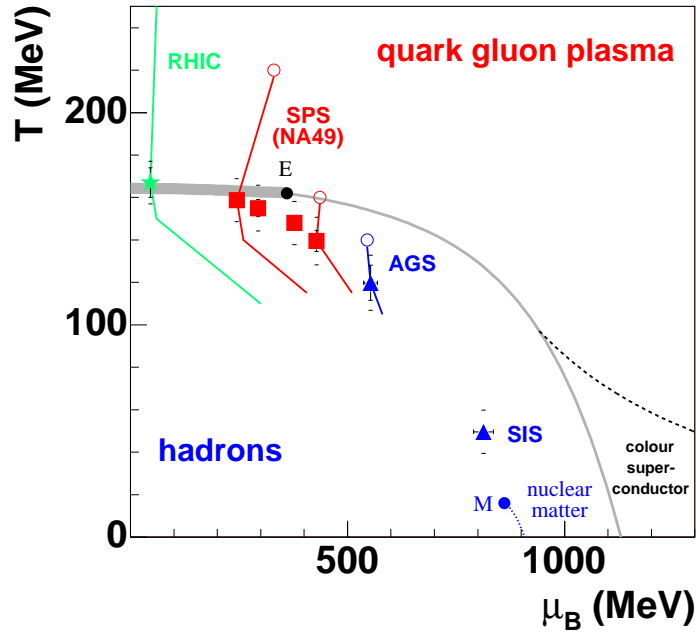


Figure 1.4: Phase diagram of strongly interacting matter as a function of the temperature  $T$  and the baryo-chemical potential  $\mu_B$  including the points of the chemical freeze-out of Pb+Pb (Au+Au) collisions at SIS, AGS, SPS and RHIC energies [13]. The colored lines indicate hypothetical trajectories of the matter evolution in the  $T$ ,  $\mu_B$  plane before and after the chemical freeze-out.

After the initial non-equilibrium phase the system starts to thermalize forming, depending on the energy density, either a hadron gas or a quark-gluon-plasma. The system is rapidly expanding, therefore the energy density drops quickly and if a QGP was created in the collision it will hadronize. The hadrons in a hadron-gas are interacting both elastically and inelastically, creating and destroying different hadron species. Starting from the moment when the energy density reaches a value too low for inelastic interactions to occur, the so called "chemical freeze-out", the yields of the different hadrons are changed only by decays.

Statistical models [14, 13, 15] have been successful in describing the yields of many different hadrons using only several parameters. They include the volume, the temperature and the baryo-chemical potential of the freezing-out matter (section 7.1). The points of the chemical freeze-out of heavy ion collisions in a wide collision energy range in the temperature- baryo-chemical potential plane are shown in figure 1.4. The freeze-out temperature increases with increasing energy of the collision until saturating at values of about  $T = 170$  MeV at top SPS and RHIC energies. The baryo-chemical potential decreases with increasing collision energies as expected due to the increasing number of produced hadrons per baryon with energy.

After the chemical freeze-out the hadrons still interact elastically. At the thermal freeze-out the distance between the hadrons becomes so large that they stop to interact. The shape of the momentum distributions of the hadrons is fixed at this time. The temperature of the thermal freeze-out can be determined by fitting the momentum spectra of the hadrons with a hydrodynamical model, for example the Blast-Wave model [16]. Clearly the thermal

## 1 Introduction

freeze-out temperature is lower than the chemical freeze-out temperature.

The hadrons after freeze-out are registered in the experiment. Most of the information on the early stage of the collision is lost, but several signatures of the possible quark-gluon plasma in the early stage are predicted to survive.

### 1.3 Signals of Quark-Gluon- Plasma at High Energies

Lattice QCD calculations expect that at energy densities exceeding values of about  $1 \text{ GeV}/\text{fm}^3$  the matter is in a deconfined phase. The energy density in the early stage of Pb+Pb collisions at  $158A \text{ GeV}$  was estimated by the NA49 collaboration to be about  $3 \text{ GeV}/\text{fm}^3$  [17] in the Bjorken picture, many times the value for the onset of deconfinement estimated by lattice QCD. In the Landau picture the estimated energy density is even higher, namely  $12 \text{ GeV}/\text{fm}^3$ . Therefore it is expected that the matter in the early stage at top SPS and RHIC energies is in the deconfined phase. In this section several observables which are expected to be signals of quark-gluon-plasma are discussed.

#### 1.3.1 High $p_T$ Suppression and Jet Quenching

Particles with a high momentum in the direction transverse to the beam axis ( $p_T$ ) are believed to be created by jet fragmentation. A jet is produced when quarks or gluons collide in the early stage of the collision with large relative momenta. The color charged partons move outside the interacting zone. The strong interaction forms a string between the kicked out parton and the remaining partons. When the energy of the string gets too large the string beaks and quark- anti-quark pairs are created, which hadronize together with the scattered quark and the hadron from which it was kicked off. Depending on the energy of the initial parton a number of hadrons with high transverse momentum is produced, the so called "jet". The two initially colliding partons form two jets in the opposite direction due to momentum conservation. In matter with a large parton density a high energy parton can quickly loose its energy in collisions with the quarks and gluons. Therefore the suppression of jets and the appearance of mono-jets are predicted to be signals for a large energy density and therefore an indication of deconfinement.

The high  $p_T$  suppression can be quantified by the nuclear modification factor:

$$R_{AB} = \frac{dn/dp_T(A) \cdot N_{coll}(B)}{dn/dp_T(B) \cdot N_{coll}(A)}, \quad (1.2)$$

where  $N_{coll}(X)$  is the number of binary nucleon-nucleon collisions in the system  $X$ . Commonly the system A is the heavy ion collision and the system B a proton-proton interaction.

At RHIC a significant reduction of the nuclear modification factor for high transverse momentum particles is observed [18] (Fig. 1.5) in heavy ion collisions, different to the observations in nucleon-nucleus collisions. This may be interpreted as a signature for very high partonic densities at the early stage of nucleus-nucleus collisions and as a hint of deconfined matter.

A more differential observable are the correlations between high  $p_T$  hadrons. A measured particle with the highest transverse momentum in one collision is defined as the "trigger particle". For all other particles with high transverse momentum created in the collision the difference in the azimuthal angle between the so-called "associated" particle and the trigger particle,  $\Delta\Phi$ , is calculated. In a proton-proton and proton-nucleus interaction a peak around

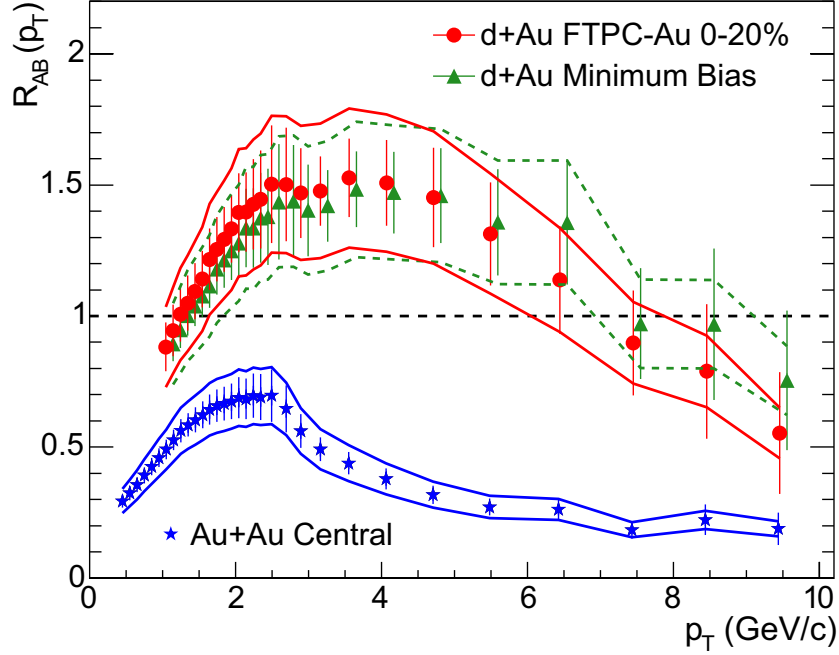


Figure 1.5: Transverse momentum dependence of the nuclear modification factor  $R_{AB}$  relative to p+p interactions for central Au+Au, central d+Au and minimum bias d+Au collisions at  $\sqrt{s_{NN}} = 200$  GeV [18].

$\Delta\Phi = 0$  and a peak around  $\Delta\Phi = \pi$  is observed. The "near side" peak at  $\Delta\Phi = 0$  is caused by particles in the same jet as the trigger particle. The "away side" peak at  $\Delta\Phi = \pi$  is created by the jet of the other initially colliding parton. In a system with a very high parton density the away side peak is expected to be suppressed. When the initial parton-parton interaction occurs at the edge of the fireball, one scattered parton can escape quite unbiased and form the near side peak, whereas the other one has to travel through the fireball and loses its energy. The RHIC data indeed show a suppression of the away side peak [18] (Fig. 1.6).

### 1.3.2 Flow

The fireball expands rapidly after the collision. The collective velocity of matter (fluid) elements which is caused by the expansion is called flow. In general, the flow velocity depends on the direction, in particular the longitudinal and the transverse flows are studied.

For non-central collisions the transverse flow depends on the azimuthal angle with respect to the reaction plane. This flow is called anisotropic flow. The reaction plane (the x-z-plane in Fig. 1.7) is defined by the momentum vector of the projectile nucleus and the vector of the impact parameter. The latter is defined as the vector between the center of the target and the projectile nucleus. Its azimuthal angle is called  $\phi_R$ . In order to study the anisotropic flow, the particle distribution as a function of the difference in the azimuthal angle of the produced particles to the reaction plane  $\Delta\phi = \phi - \phi_R$  is plotted. This distribution can be

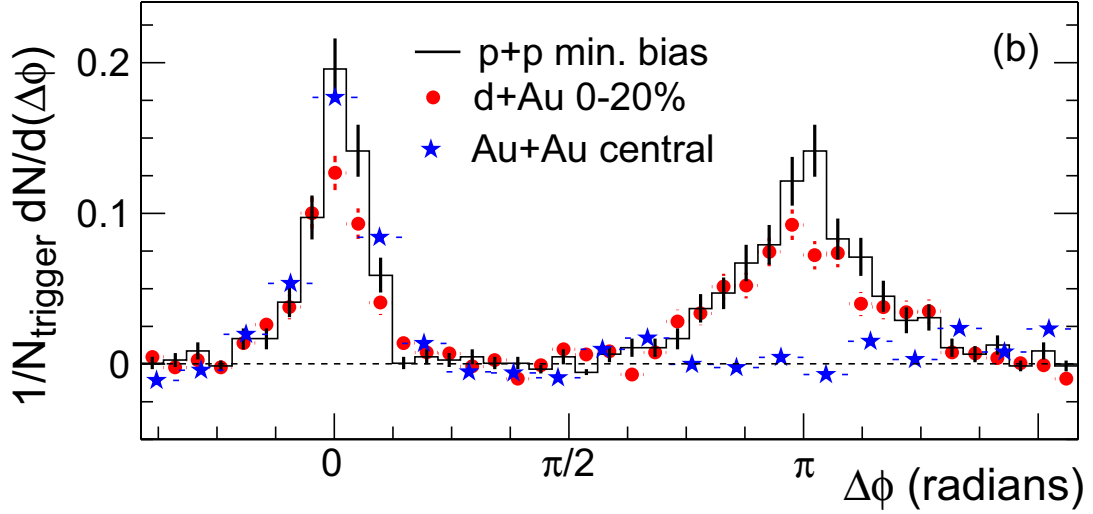


Figure 1.6: Two particle azimuthal distributions in p+p, d+Au and Au+Au collisions at  $\sqrt{s_{NN}} = 200$  GeV [18]. Trigger particles:  $4 < p_T(trig) < 6$  GeV/c, associated particles:  $2 < p_T < p_T(trig)$ .

expanded into its Fourier components:

$$\frac{dN}{d\Delta\phi} = \frac{1}{2\pi} \sum_{i=0}^{\infty} 2v_i \cos(i\Delta\phi), \quad (1.3)$$

where  $v_i$  are the  $i$ -th Fourier coefficients. The Fourier coefficient  $v_1$  is called directed flow. Integrated over the full phase space the directed flow is zero due to the projectile-target symmetry. The symmetry yields  $v_1(y) = -v_1(-y)$ . Therefore  $v_1$  is usually studied as a function of rapidity  $y$ . For protons the directed flow for central and mid-central collisions is positive in the forward hemisphere [19]. This effect can be explained by the "bounce-off" of the projectile participants at the edge of the interaction region [20]. For pions the directed flow in the projectile hemisphere is negative, probably because of shadowing effects of the projectile spectators. It is predicted [21] that the directed flow of protons collapses at mid-rapidity at the onset of deconfinement.

The coefficient  $v_2$  is called the elliptic flow. In high energy collisions ( $E_{lab} > 4A$  GeV) a high pressure is created in the interaction zone (see figure 1.7). For a non-central collision this zone has an ellipsoid shape with its main axis orthogonal to the reaction plane. Therefore the pressure gradient is larger in the direction of the reaction plane what favors the emission of particles in this direction. The strong emission of particles in the reaction plane yields a positive  $v_2$ . For lower energies the velocity of the projectile and target spectators is lower than the expansion velocity of the fireball. The spectator nucleons prevent particles from being emitted in the reaction plane, therefore they are preferably emitted orthogonal to it ("squeeze-out"). This yields a negative  $v_2$ . For very low energies ( $E_{lab} < 100A$  MeV) only a small amount of pressure is built up in the collision. The interaction zone of a non-central collision is rapidly rotating and has a large lifetime. When the fireball decays particles are emitted preferably in the reaction plane due to the centrifugal forces,  $v_2$  is therefore positive.

### 1.3 Signals of Quark-Gluon- Plasma at High Energies

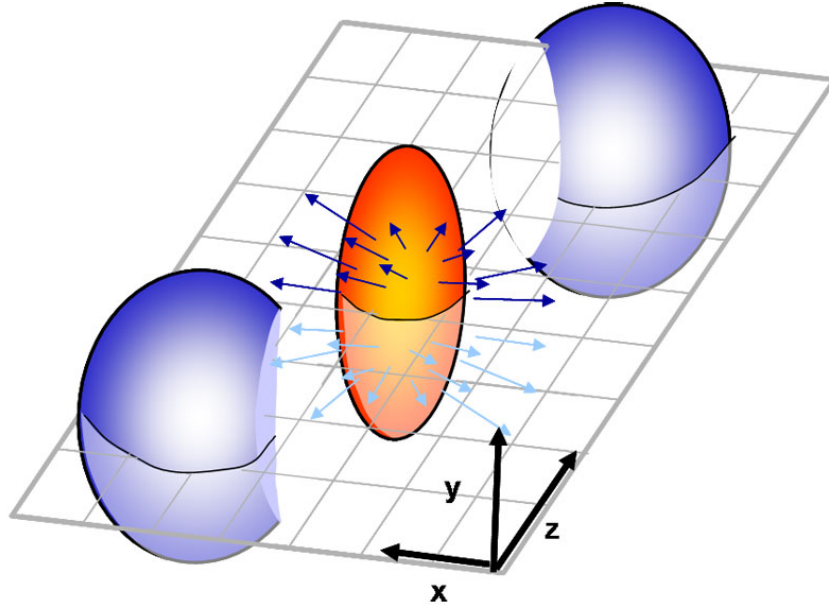


Figure 1.7: A sketch of a non-central heavy ion interaction [22]. The fireball is orange, the spectator nucleons are blue. Due to the ellipsoid shape of the fireball particle emission in the reaction plane is enhanced at high collision energies.

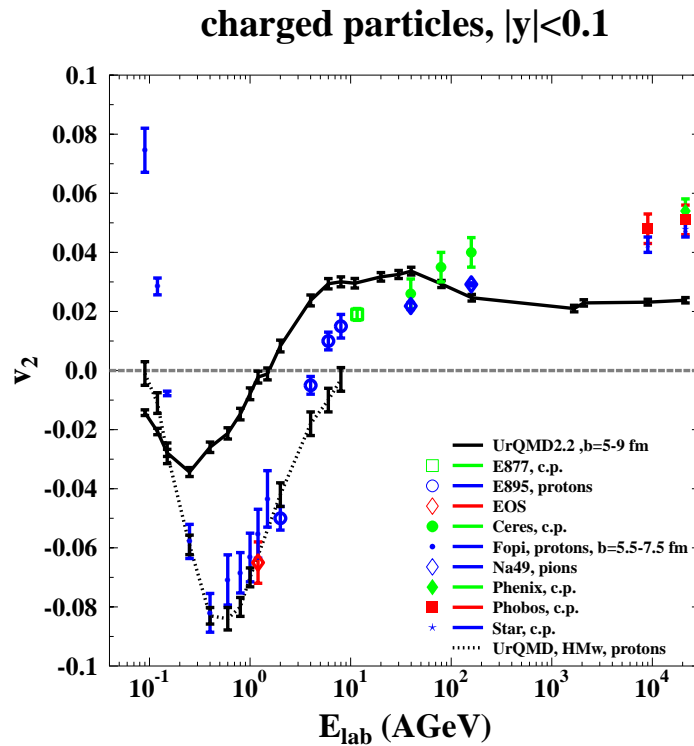


Figure 1.8: Energy dependence of the elliptic flow  $v_2$  in heavy ion collisions [23]. The points indicate experimental data, the lines UrQMD model calculations.

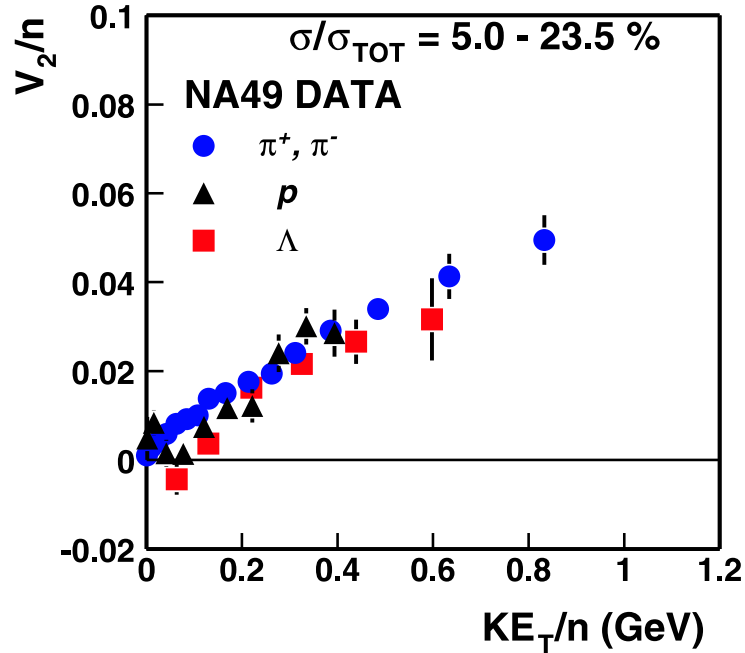


Figure 1.9: Elliptic flow per constituent quark as a function of transverse kinetic energy per constituent quark for different particle species in mid-central Pb+Pb collisions at 158A GeV, measured by the NA49 experiment [24].

The dependence of elliptic flow on the particle species is predicted to give information about the state of matter in the early stage of the collision. If a quark-gluon-plasma is created in the early stage of a collision, the quarks will flow. When the quarks combine to hadrons in a constituent quark picture ("coalescence"), the baryons carry the flow and the momentum of three quarks, the mesons, however, carry the flow and the momentum of two quarks. When the elliptic flow per constituent quark as a function of transverse kinetic energy per constituent quark is plotted for different particle species, they should all lie on a single line, if the picture described above is correct. Experimental data of the NA49 [24] and STAR [25] collaborations confirm this prediction (Figs. 1.9 and 1.10) and give an evidence for a quark phase in the early stage of the collisions at top SPS and RHIC energies.

### 1.3.3 $J/\Psi$ Production

The  $J/\Psi$  meson is a bound state of a charm and an anti-charm quark. Due to its high rest mass of 3.1 GeV it is predicted to be created in hard parton-parton interactions in the first stage of heavy ion collisions. In this picture the number of produced  $J/\Psi$  mesons would scale with the number of initial binary parton collisions. If QGP is created in the collision, the color force between the charm and the anti-charm quark is weakened by the presence of the color charged quarks and gluons. This effect called "Debye-screening" is also observed in electromagnetic plasmas. In [26] it is predicted that the production of  $J/\Psi$  mesons in heavy ion collisions is suppressed when QGP is created. Recent QCD calculations [27] suggest a more complicated picture. A large amount of  $J/\Psi$  mesons is predicted to originate from



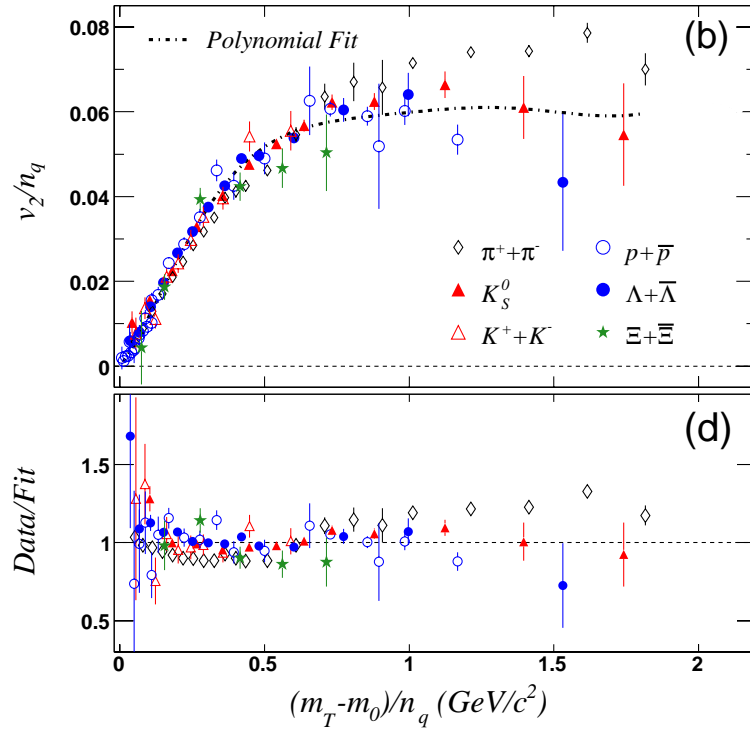


Figure 1.10: Top: Elliptic flow per constituent quark as a function of transverse kinetic energy per constituent quark for different particle species in minimum bias Au+Au collisions at  $\sqrt{s_{NN}} = 62.4$  GeV, measured by the STAR experiment [25]. Bottom: Difference of the measured point to a polynomial fit to all data points except pions.

## 1 Introduction

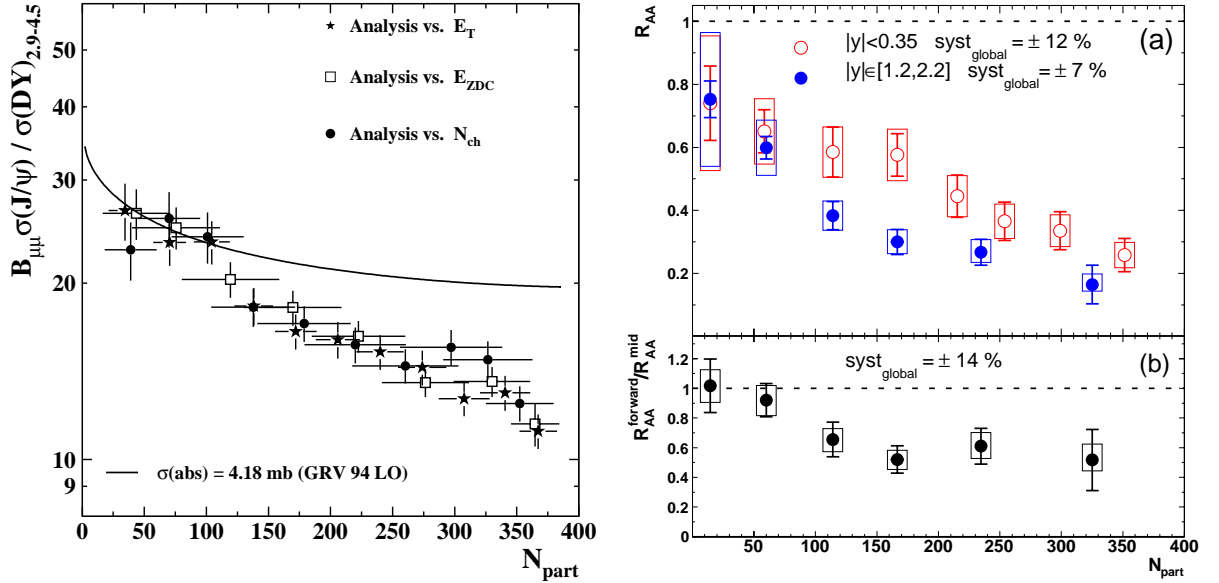


Figure 1.11: Left: Cross-section of  $J/\Psi$  production relative to Drell-Yan cross-sections (which are proportional to the number of initial binary parton collisions) as a function of the number of participants for Pb+Pb collisions at 158A GeV as measured by the NA50 experiment [28]. Right: Nuclear modification factor  $R_{AA}$  for  $J/\Psi$  production as a function of the number of participants for Au+Au collisions at  $\sqrt{s_{NN}} = 200$  GeV as measured by the PHENIX experiment [29].

decays of heavier charmonium resonances like  $\chi_C$  and  $\Psi'$ . The  $J/\Psi$  is only dissolved in QGP in sufficiently high temperatures ( $T \approx 2 T_C$ ). The heavier charmonium resonances are less stable and melt earlier ( $T \approx T_C$ ).

In the experiment,  $J/\Psi$ s can be detected by their leptonic decay channels. The reconstruction of the  $J/\Psi$  from the (more frequent) hadronic decay channels is not possible because of the re-scattering of hadrons in the fireball and the large hadronic background. The leptons are not interacting strongly and can therefore escape from the fireball unbiased. In the NA38/50/60 [28] experiments the  $\mu^+\mu^-$  decay channel is used, the PHENIX [29] experiment uses both the muonic and the  $e^+e^-$  channel.

Results of the NA50 and the PHENIX collaborations (Fig. 1.11) show a suppression of  $J/\Psi$  production per number of binary collision in central Pb+Pb (Au+Au) collisions in comparison to p+p interactions. The suppression is larger than expected for normal nuclear absorption and therefore might be interpreted as a signal for QGP. When going to more peripheral collisions (smaller number of participants), the suppression gets smaller.

However, different approaches exist describing the  $J/\Psi$  production in a statistical hadronization model [30]. In this picture the  $J/\Psi$ s are not produced in initial parton-parton interactions but together with the bulk of particles during the freeze-out of the fireball.

In [31] it is suggested that all charm quarks are created in hard parton-parton interactions in the first stage of heavy ion collisions. They do not form charm hadrons immediately but are dissolved in the QGP. The charmonium production then takes place at the phase boundary to the hadron gas with statistical weights.

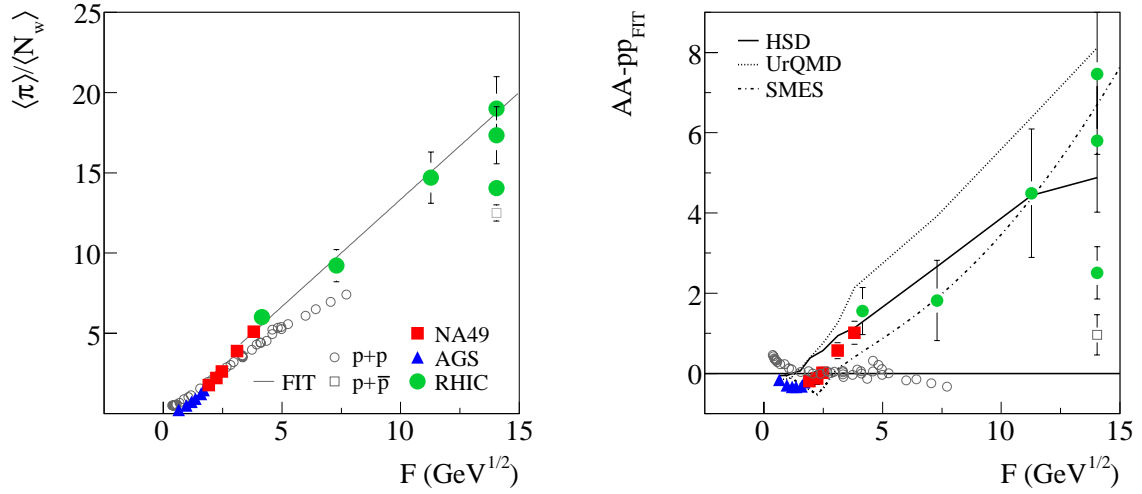


Figure 1.12: Left: Energy dependence of the mean pion multiplicity per wounded nucleon measured in central Pb+Pb and Au+Au collisions (full symbols), compared to the corresponding results from p + p( $\bar{p}$ ) reactions (open circles). Right: Energy dependence of the difference between the measured mean pion multiplicity per wounded nucleon and a parametrization of the p + p data. The meaning of the full and open symbols is the same as in the left-hand plot [33].

## 1.4 Signals of the Onset of Deconfinement at SPS Energies

As seen above there are several indications that deconfined matter is created in the early stage of a heavy ion collision at RHIC and top SPS energies. As it is supposed that the QGP phase is not reached in collisions at low energies, the onset of deconfinement, i.e. the lowest collision energy where QGP is created in the early stage of a collision, may be located at SPS energies. Indeed, several observables discussed below show anomalies in their energy dependence at low SPS energies which might be related to the onset of deconfinement [32].

### 1.4.1 Pion Multiplicity

The energy dependence of the pion production per number of wounded nucleon ( $\langle \pi \rangle / \langle N_W \rangle$ ) is shown in Fig. 1.12 both for nucleon-nucleon and heavy ion collisions as a function of the Fermi-variable  $F$  (see appendix C.1.2). For nucleus-nucleon-collisions (p+p( $\bar{p}$ )) the pion multiplicity is approximately proportional to the energy variable  $F$ . For heavy ion collisions the pion multiplicity per wounded nucleon is smaller than for nucleon-nucleon interactions at low energies but larger at high energies. The difference of the pion multiplicity per wounded nucleon in A+A and p+p has a constant negative value at low energies and increase approximately linearly with  $F$  starting at low SPS energies, the same energy where the maximum in the relative strangeness is observed (see below).

In the statistical model of the early stage [32] this behaviour is interpreted as follows: The entropy per wounded nucleon is proportional to the collision energy  $F$  and the number of degrees of freedom  $g^{1/4}$ . As most of the produced particles are pions the pion multiplicity is proportional to the entropy. No phase transition is expected in p+p interactions, therefore

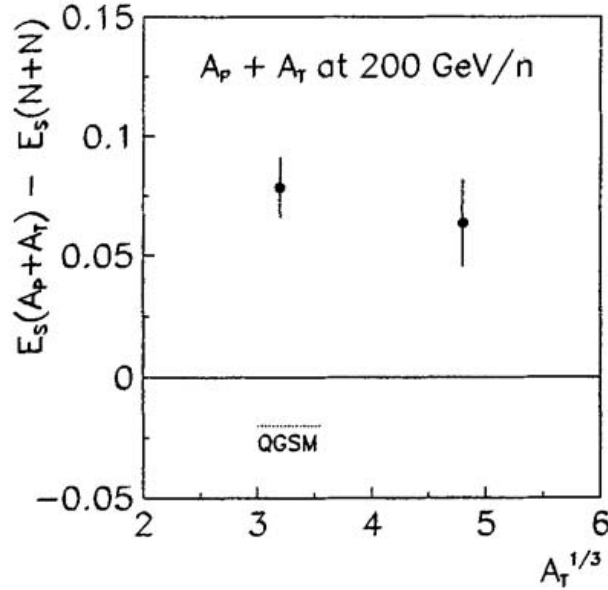


Figure 1.13: Difference of the relative strangeness  $E_s$  in S+S (left point) and S+Ag collisions (right point) to p+p collisions as measured by the NA35 experiment [35].

the pion multiplicity is a linear function of  $F$ . For heavy ion collisions a part of the entropy is transferred from the pions to the baryons, therefore the pion multiplicity per wounded nucleon is smaller than for p+p at low energies. In the QGP phase the number of degrees of freedom is larger than in the hadron-gas phase. Starting at the onset of deconfinement it is predicted that the pion multiplicity in A+A should increase stronger with energy as for p+p leading to a change from a suppression to an enhancement of pion production per wounded nucleons in heavy ion collisions. This prediction is in agreement with the experimental data (Fig. 1.12).

### 1.4.2 Strangeness

It was predicted in [34] that the strangeness production is enhanced in quark-gluon plasma. In a hadronic scenario the channel of strangeness production requiring the smallest amount of energy is  $N + N^- \rightarrow \Lambda + K^+ + N$ . The energy of 670 MeV is needed for this reaction. In a quark-gluon plasma strange quarks are needed to be produced. The production of a  $s\bar{s}$  pair “costs” only 190 MeV [1]. Therefore strangeness production is expected to be enhanced in QGP. The used measure of the relative strangeness is  $E_s$  defined as

$$E_s = \frac{\langle \Lambda \rangle + \langle K \rangle + \langle \bar{K} \rangle}{\langle \pi \rangle}, \quad (1.4)$$

where  $\langle X \rangle$  is the mean multiplicity per event of the particle species  $X$ . Measurements of the NA35 collaboration [35] at CERN SPS showed indeed a larger amount of relative strangeness in S+S and S+Ag collisions in comparison to p+p interactions (Fig. 1.13).

Further measurements put the interpretation of strangeness enhancement as a signal of deconfinement into question. This is because the enhancement is observed at all energies, even for energies expected to be too small for the creation of a QGP. In statistical hadron-gas

#### 1.4 Signals of the Onset of Deconfinement at SPS Energies

models the strangeness enhancement in A+A relative to p+p is partly related to the canonical suppression of strangeness production in p+p collisions. In small systems the number of strangeness carriers is  $\lesssim 1$ , lower than the value ( $\approx 5$ ) where the mean strangeness multiplicity obtained by the different statistical ensembles is similar. Therefore the micro-canonical ensemble, which gives a lower mean strangeness yield has to be used for a reasonable description of small systems.

Some hadron-gas models [13, 15] assume that the strange quarks are not equilibrated yet. In a heavy ion collision the strange particles are closer to their equilibrium value than in p+p interactions and therefore their production is further enhanced.

In the statistical model of the early stage (SMES) [32] it is predicted that the energy dependence of the ratio of strangeness to entropy should have a non-monotonous behaviour at the onset of deconfinement. In this model, a statistical production of strange particles in the early stage is assumed. The strangeness to entropy ratio depends mainly on the mass of the strangeness carriers and the ratio of strange to non-strange degrees of freedom. In the hadron phase the number of non-strange degrees of freedom can be calculated as follows. There are 4 different quark- anti-quark- combinations of the light quarks up and down that can form a light meson. Each quark can have two different spin directions, therefore the number of non-strange degrees of freedom is expected to be  $g_{ns}^H = 16$ . The strange degrees of freedom, consisting mainly of kaons and lambdas, are fitted to the AGS data in this model:  $g_s^H = 14$ . In the quark-gluon plasma phase the non-strange degrees of freedom are the up and down quarks. They can be particle or anti-particle with two different quark flavors, two different spin directions and three different color charges. Therefore the number of non-strange degrees of freedom of the quarks is  $g_f = 24$ . The energy of the gluons at temperatures close to the expected phase transition is too small to form strange particles when they interact with each other. Therefore the gluonic degrees of freedom are counted as non-strange. The gluons have a spin of one, but the spin vector can not be orthogonal to the momentum vector of the gluon because it is massless. It can carry eight different color charges, therefore the gluons have  $g_b = 16$  degrees of freedom. For the calculation of the total number of degrees of freedom the fermionic degrees have to be scaled with  $7/8$  because of the properties of the fermionic distribution function (Eq. 1.5). The total number of non-strange degrees of freedom in the QGP phase is  $g_{ns}^Q = g_b + 7/8 \cdot g_f = 37$ . The strange degrees of freedom are the strange quarks:  $g_s^Q = 12$ . The ratio of strange to non-strange degrees of freedom is therefore larger in the hadron-gas phase than in the QGP. On the other hand the mass of the strangeness carriers is much higher in the hadron phase. In a statistical model in the grand-canonical ensemble the distribution function of one particle species is

$$\frac{dn_i}{d\vec{p}d\vec{x}} = \frac{g_i}{(2\pi)^3} \frac{1}{\exp(E/T) \pm 1}, \quad (1.5)$$

with the  $-1$  in the denominator is for bosons and the  $+1$  is for fermions. The particle production is proportional to the number of degrees of freedom  $g_i$ . As the energy  $E$  contains the rest mass of the particle, the production of particles with higher masses is suppressed. In the statistical model of the early stage it is predicted that the ratio of strange to non-strange particles, which is similar to the strangeness to entropy ratio, should have the following energy dependence: At energies where no QGP is formed, the strangeness to entropy ratio should rapidly increase with energy. At low energies the strangeness production is strongly suppressed because of the high mass of the strangeness carriers ( $m_K \approx 500$  MeV). With increasing energy the temperature of the system increases and therefore the suppression of

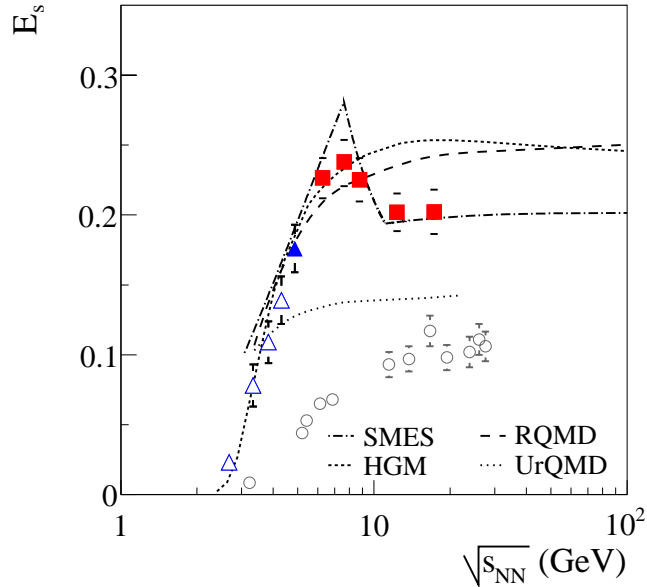


Figure 1.14: Relative strangeness yield  $E_s$  as a function of energy for Pb+Pb (colored solid points) in comparison to p+p data (open points) and model predictions [33].

heavy particles is reduced. If no QGP phase would exist, the strangeness to entropy ratio would increase further until reaching its saturation value. In the QGP phase the mass of the strangeness carriers is much lower than in the hadron phase, therefore the saturation value is practically already reached at the onset of deconfinement. On the other hand the ratio of the strange to non-strange degrees of freedom is much smaller in the QGP phase as in the hadron phase, therefore the strangeness to entropy ratio in the QGP phase is predicted to be smaller than in the hadron phase at energies just above the onset of deconfinement.

In the NA49 experiment such a non-monotonous behaviour of the relative strangeness was observed [36] for central Pb+Pb collisions (Fig. 1.14). String hadronic models (UrQMD, RQMD) fail to reproduce this behaviour but the data is in agreement with the prediction of the statistical model of the early stage (SMES). For p+p collisions no indication of a non-monotonic behaviour of the relative strangeness is observed.

### 1.4.3 Transverse Expansion

In Fig. 1.15 the inverse slope parameter  $T$  of kaons, obtained by an exponential fit of the transverse mass spectra, is shown. The inverse slope parameter is a measure of the transverse expansion of the system and it is supposed to have two contributions: one due to the temperature of the fireball and one due to its collective expansion. A similar measure is the mean transverse mass (Fig. 1.16).

The inverse slope parameter of kaons, as well as the mean transverse mass of pions, kaons and (anti-) protons, increases approximately linearly with collision energy at AGS energies. At SPS energies it is constant with energy, at RHIC energies it increases again. This non-monotonic behavior is not observed in p+p interactions [37].

This behaviour is similar to the behaviour of the temperature of water when it is heated.

1.4 Signals of the Onset of Deconfinement at SPS Energies

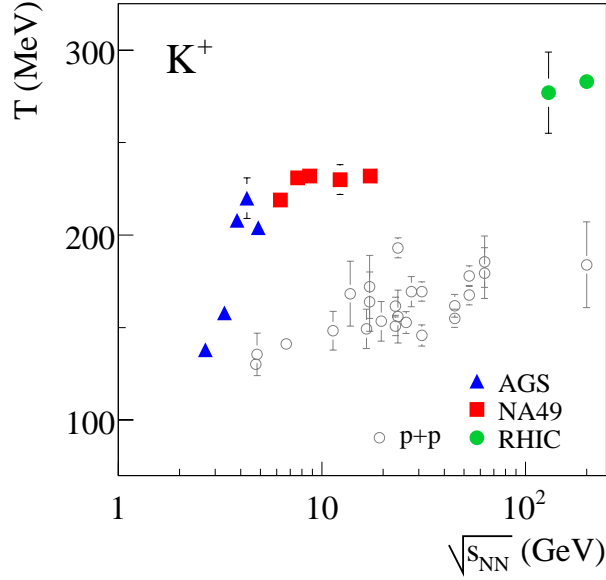


Figure 1.15: Energy dependence of the inverse slope parameter of positively charged kaons in heavy ion collisions [33] in comparison to p+p interactions [37].

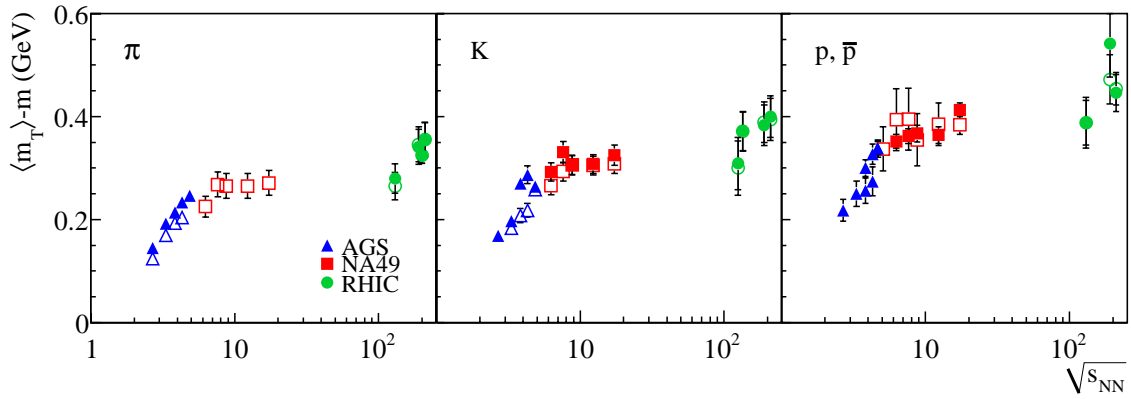


Figure 1.16: Energy dependence of the mean transverse mass of pions (left), kaons and (anti) protons (right) in central Pb+Pb (Au+Au) collisions [33]. Positively charged particles are indicated by the full, negatively charged by the open symbols.

## 1 Introduction

In the liquid phase the temperature of the water increases linearly with the amount of energy added. When the temperature reaches a value of about  $100^{\circ}\text{C}$ , additional energy to the system does not increase its temperature but the amount of water which is in the gas phase. Only when the system is completely in the gas phase its temperature increases again. The energy needed for a phase transition is called "latent heat".

In [32] it is suggested that the step in the kaon slope and the mean transverse masses at SPS energies is related to the latent heat of the phase transition between hadron-gas and QGP.

### 1.5 Fluctuations in High Energy Collisions

Increased fluctuations of various observables are expected at the onset of deconfinement, near the critical point or when the system passes the first order phase transition line during expansion.

In a very simplified picture, due to fluctuations the system can either be in a quark-gluon plasma phase or not when the mean temperature of the fireball is close to the transition temperature. Even if the collision energy is fixed, the temperature in that picture fluctuates and can therefore be in some collisions sufficient for the creation of QGP and in some not. As observables like total particle multiplicity and relative strangeness yield are predicted to be sensitive to the QGP creation in the early stage of the collision, two classes of events with different total multiplicity and strangeness might be observable. One of the original motivations of the NA49 experiment was to look for this effect [38], but no indication of different classes of events was observed.

Further studies [32] showed that the collision energy determines the energy density of the collision, not the temperature. For a first order phase transition it is expected that a mixed phase of hadrons and QGP is formed at the temperature of the phase transition. For a large range of energy densities the temperature stays constant while more matter is transformed to QGP ("latent heat"). Therefore, at a fixed collision energy, one does not expect two different classes of events, but the events should only differ in the amount of QGP created at the early stage of the collision.

It is therefore not sufficient to look just for two different classes of events, a more sophisticated analysis of fluctuations is needed. The commonly used fluctuation observables are the event-by-event fluctuations of particle ratios, the electrical charge, the mean transverse momentum and the particle multiplicity.

#### 1.5.1 Particle Ratio Fluctuations

In [39, 40] preliminary results of the NA49 and the STAR collaboration on the event-by-event fluctuations of the kaon to pion and the proton to pion ratio are presented. Particles are identified by their energy loss ( $dE/dx$ ) in the gas of the time projection chambers of the experiments. The energy loss of charged particles in the gas depends on their velocities. As the momentum can be measured by their deflection in a magnetic field, the mass and therefore the identity of a particle can be determined. Unfortunately the resolution of the energy loss measurement is not sufficient for a particle identification on the track-by-track basis. Instead, for each track a probability to be proton, pion or kaon can be calculated. This allows a determination of mean particle yields. For the determination of the "dynamical" particle ratio fluctuations the width of the event-by-event particle ratio distribution is taken and the width



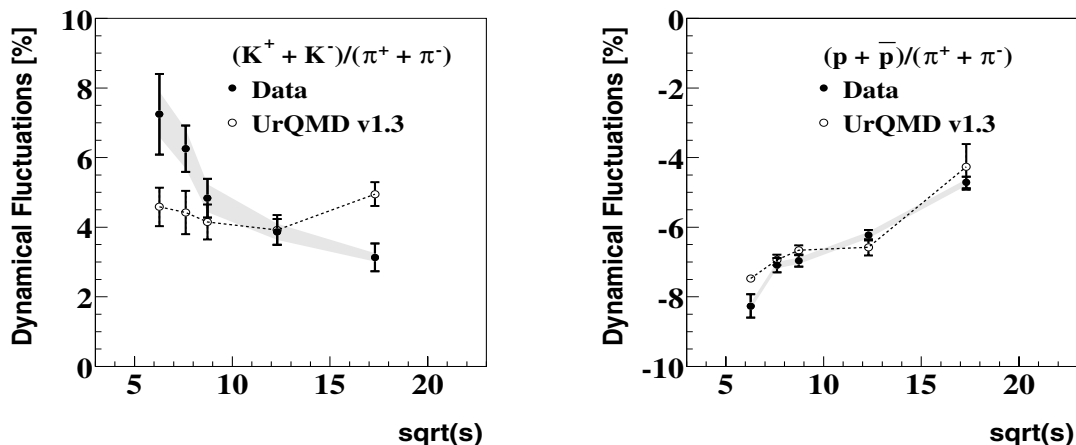


Figure 1.17: Dynamical fluctuations of the kaon to pion (left) and the (anti-) proton to pion (right) ratio obtained by the NA49 experiment [39] in comparison to the results of the UrQMD model.

of a corresponding distribution for mixed events is subtracted. Mixed events are artificially constructed events where tracks from different real events are randomly combined in order to take effects like the limited  $dE/dx$  resolution and statistical fluctuations into account.

In Fig. 1.17 it can be seen that the dynamical fluctuations in the (anti-) proton to pion are negative, that means that the production of protons and pions is positively correlated. This correlation is attributed to the decay of baryonic resonances like  $\Delta$ s into an (anti-) proton-pion pair and a string-hadronic model (UrQMD) reproduces this effect.

The dynamical fluctuations of the kaon to pion ratio are positive (Figs. 1.17,1.18). Thus the K and  $\pi$  production is anti-correlated. The dynamical fluctuations increase with decreasing collision energy. The UrQMD model predicts a similar order of magnitude of these fluctuations but does not reproduce their energy dependence. The excess of relative strangeness fluctuations is located at similar energies as the maximum of the mean relative strangeness, which can be interpreted as a sign for the onset of deconfinement [32]. Therefore it was suggested [41] to interpret the large relative strangeness fluctuations at low SPS energies as an indication for the onset of deconfinement. However, the relative strangeness fluctuations are the only fluctuations observable where an excess of fluctuations at low SPS energies was observed, both transverse momentum and multiplicity fluctuations do not show an excess at these energies. Furthermore the experimental data on  $K/\pi$ -fluctuations are still preliminary.

## 1.5.2 Electrical Charge Fluctuations

The event-by-event fluctuations of the electric charge in a limited region of the phase space was studied by the NA49 collaboration [42]. It was predicted [43, 44] that these fluctuations are suppressed in the QGP phase because the amount of electrical charge carried by a quark ( $\pm 1/3e, \pm 2/3e$ ) is smaller than the one carried by a hadron ( $\pm 1e$ ). Hence, the electrical charge in a QGP is expected to be more uniformly distributed in the phase-space than in the hadron-phase. Consequently the charge fluctuations are expected to be smaller.

For charge fluctuations different measures exist. In [42] the  $\Phi_q$  measure is used, it is defined

## 1 Introduction

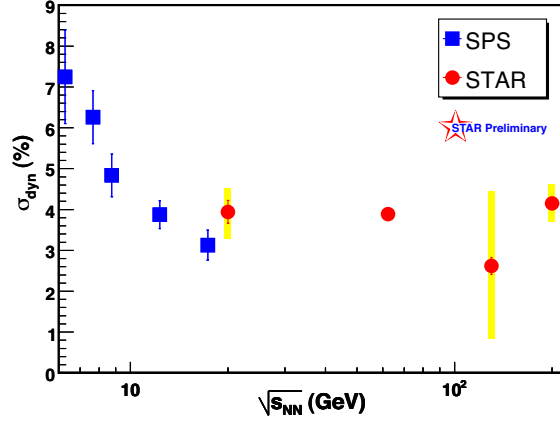


Figure 1.18: Energy dependence of the dynamical fluctuations of the kaon to pion ratio obtained by the NA49 and STAR [40] experiment.

as:

$$\Phi_q = \sqrt{\frac{\langle Z^2 \rangle}{\langle N \rangle}} - \sqrt{z^2} \quad (1.6)$$

with  $z = q - \bar{q}$  defined for a single particle and  $Z = \sum z$  defined for one event. The bar denotes averaging over the inclusive single particle distribution, the brackets  $\langle \dots \rangle$  averaging over all events.

Global charge conservation introduces a correlation between positively and negatively charged particles. When only global charge conservation (GCC) is present, the value of  $\Phi_q$  is given by

$$\Phi_{q,GCC} = \sqrt{1-p} - 1, \quad (1.7)$$

where  $p$  is the ratio of all charged particles in the observed phase space to the total number of charged particles in the full phase space. In order to remove the sensitivity to GCC, the measure

$$\Delta\Phi_q = \Phi_q - \Phi_{q,GCC} \quad (1.8)$$

is used.  $\Delta\Phi_q$  will be negative if an additional correlation between positively and negatively charged particles besides global charge conservation is present. It will be positive for an anti-correlation. For a hadron-gas correlated only by global charge conservation  $\Delta\Phi_q$  is zero. For an ideal gas of quarks and gluons values of  $\Delta\Phi_q$  around  $-0.5$  are expected because the quark charges are correlated in hadrons.

In figure 1.19 the charge fluctuations are shown as a function of the size of the phase space used for the analysis. The data points are in clear contradiction to the predictions of an ideal gas of quarks and gluons but are consistent to the predictions for an ideal pion gas. These results do not exclude the existence of a QGP phase at the early stage of the collision as the signal of the suppression of charge fluctuations in QGP may be lost during freeze-out. A model with a QGP phase in the early stage incorporating intermediate resonances as  $\rho$  during freeze-out [45] is also in agreement with the experimental data (Fig. 1.19).

The energy dependence of charge fluctuations is shown in Fig. 1.20. A weak decrease of  $\Delta\Phi_q$  with collision energy is observed.

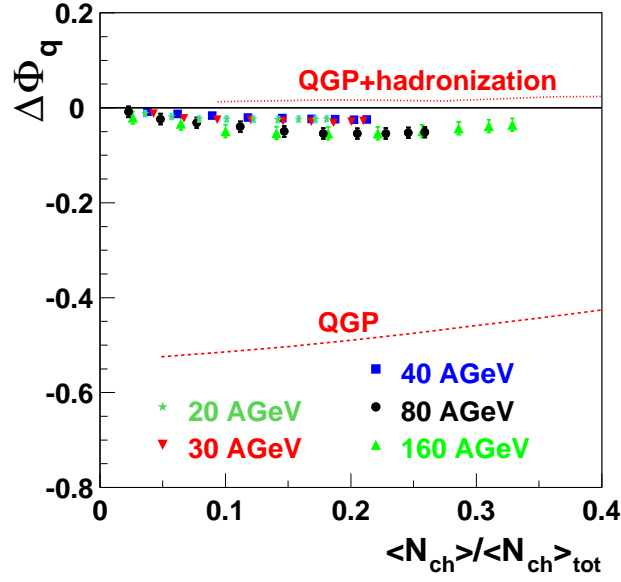


Figure 1.19: The dependence of  $\Delta\Phi_q$  on the fraction of accepted particles in central Pb+Pb collisions at 20A-158A GeV [42].

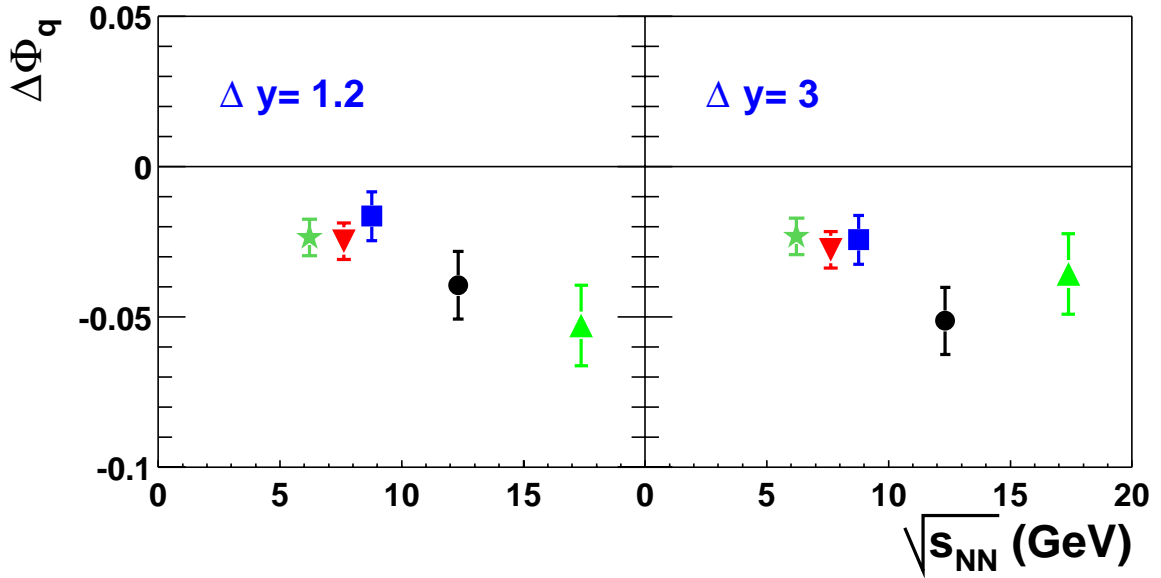


Figure 1.20: Energy dependence of  $\Delta\Phi_q$  for two different rapidity intervals as measured in central Pb+Pb collisions at 20A-158A GeV [42].

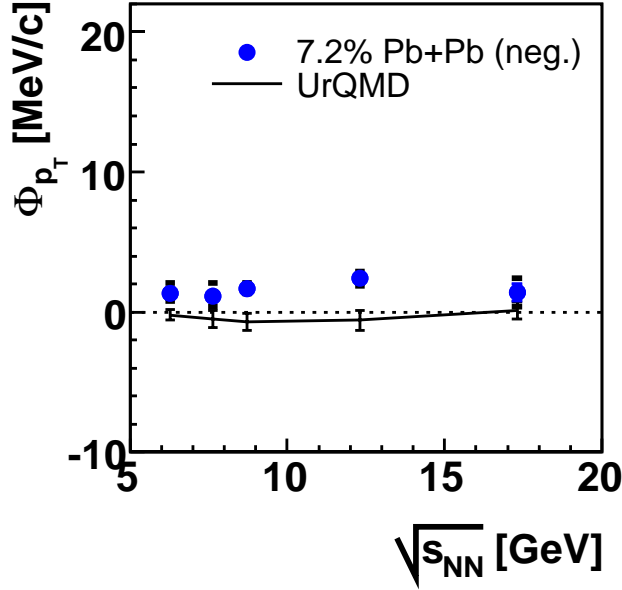


Figure 1.21: Energy dependence of transverse momentum fluctuations for negatively charged particles measured by the NA49 experiment (blue points) and obtained by a UrQMD simulation (black line) [47].

### 1.5.3 Mean Transverse Momentum Fluctuations

The fluctuations of the mean transverse momentum are studied by the NA49 collaboration [46, 47]. The simplest method of measuring  $p_T$ -fluctuations would be to look at the distribution of mean  $p_T$ . It could be compared to the mean  $p_T$  distribution obtained by mixed events. The disadvantage of this method is that the result depends on centrality fluctuations, therefore a comparison of different centralities and different systems is difficult. A more appropriate measure of transverse momentum fluctuations is  $\Phi_{p_T}$  defined in a similar way as for the electrical charge fluctuations:

$$\Phi_{p_T} = \sqrt{\frac{\langle Z_{p_T}^2 \rangle}{\langle N \rangle}} - \sqrt{\langle z_{p_T}^2 \rangle} \quad (1.9)$$

where  $z_{p_T} = p_T - \bar{p}_T$  defined for a single particle and  $Z_{p_T} = \sum_i z_{p_T}$  defined for one event. When no inter-particle correlations are present and the single particle distribution is independent of multiplicity,  $\Phi_{p_T} = 0$ .

The transverse momentum fluctuations show no significant dependence on collision energy (Fig. 1.21). The UrQMD model predicts also a flat energy dependence but slightly underpredicts the amount of fluctuations. At RHIC energies an increase of  $p_T$ -fluctuations is observed which is attributed to the appearance of mini-jets [48].

### 1.5.4 Multiplicity Fluctuations

The energy, system size, rapidity and transverse momentum dependence of event-by-event fluctuations in the particle multiplicity in central collisions are studied in this thesis.

It is predicted [49] that the onset of deconfinement should lead to a non-monotonous behaviour in the energy dependence of multiplicity fluctuations, the so-called "shark fin". Furthermore an increase of multiplicity fluctuations near the critical point of strongly interacting matter is expected [50].

Despite these additional sources of fluctuations the energy dependence of fluctuations predicted by different models is very different. String-hadronic models like UrQMD and HSD predict an increase of scaled variance in the full phase space with increasing collision energy, similar to the behavior observed in p+p interactions.

Statistical hadron-gas models predict a much weaker energy dependence of multiplicity fluctuations. In these models the widths of the multiplicity distributions are dependent on the conservation laws the system obeys. They are different in different statistical ensembles. Even though the mean multiplicity is the same in the infinite volume limit for different statistical ensembles, this is not true for higher moments like fluctuations [51].

The used measure of multiplicity fluctuations, the scaled variance, together with some general properties and theoretical concepts of multiplicity fluctuations, are presented in chapter 2. The NA49 experiment which delivers the experimental data for this work is described in chapter 3. The procedure for the data analysis as well as the used event and track selection criteria and the errors of the measurements are shown in chapter 4. The centrality dependence of multiplicity fluctuations is discussed in chapter 5. The main focus of this work is on the multiplicity fluctuations in very central collisions. The experimental results are presented in chapter 6. Model predictions on the energy, rapidity and transverse momentum dependence of the scaled variance are shown in chapter 7. In chapter 8 additional observables which are related to multiplicity fluctuations are briefly discussed. A summary (chapter 9) and an appendix close this thesis.

## *1 Introduction*

# 2 Multiplicity Fluctuations

## 2.1 Experimental Measures

In this work the multiplicity distribution  $P(n)$  and its scaled variance  $\omega$  are used to characterize the multiplicity fluctuations.

Let  $P(n)$  denotes the probability to observe a particle multiplicity  $n$  in a high energy nuclear collision. By definition  $P(n)$  is normalized to unity  $\sum_n P(n) = 1$ .

The scaled variance  $\omega$  is defined as

$$\omega = \frac{Var(n)}{\langle n \rangle} = \frac{\langle n^2 \rangle - \langle n \rangle^2}{\langle n \rangle}, \quad (2.1)$$

where  $Var(n) = \sum_n (n - \langle n \rangle)^2 P(n)$  and  $\langle n \rangle = \sum_n n \cdot P(n)$  are the variance and the mean of the multiplicity distribution, respectively.

In the following the scaled variance of positively, negatively and all charged hadrons are denoted as  $\omega(h^+)$ ,  $\omega(h^-)$  and  $\omega(h^\pm)$ .

In many models the scaled variance is independent of the number of particle production sources. First, in grand-canonical statistical models neglecting quantum effects and resonance decays the multiplicity distribution is a Poisson one, namely

$$P(n) = \frac{\langle n \rangle^n}{n!} \cdot e^{-\langle n \rangle}. \quad (2.2)$$

The variance of a Poisson distribution is equal to its mean, and thus the scaled variance is  $\omega = 1$ , independently of mean multiplicity (appendix B.1.2). Second, in the Wounded Nucleon Model [52], the scaled variance in  $A + A$  collisions is the same as in nucleon-nucleon collisions provided that the number of wounded nucleons is fixed.

### 2.1.1 Acceptance Dependence

The experimental acceptance of heavy ion experiments is restricted to a limited region of the phase space. This is mostly because of technical constraints due to high track densities and cost limitations. As the scaled variance might have a non-trivial dependence on the phase-space acceptance, the scaled variance in full phase space can not be determined in a model-independent way for heavy ion collisions with the present experiments.

However, providing that the particles are produced independently in momentum space and that the form of the momentum distribution is independent of multiplicity, the scaled variance in a limited acceptance is related to the scaled variance in full phase-space ("4 $\pi$ ") by an analytic formula.

Under these assumptions, having an experimental acceptance registering the fraction  $p$  of the total number of tracks  $N_{4\pi}$  is equivalent to roll a die for each particle in the full phase

## 2 Multiplicity Fluctuations

space and to accept it with a probability of  $p$ . Therefore the probability to measure a number of particles  $N$  in a fixed acceptance  $p$  is a binomial distribution

$$P(N|N_{4\pi}) = P_{N_{4\pi}}(N) = \frac{N_{4\pi}!}{N!(N_{4\pi} - N)!} p^N (1 - p)^{N_{4\pi} - N}. \quad (2.3)$$

For a varying number of particles in the full phase space according to  $P(N_{4\pi})$ , the probability to measure a number of particles  $N$  in the limited acceptance is (using Eq. B.21 in the appendix)

$$P(N) = \sum_{N_{4\pi}} P(N|N_{4\pi}) P(N_{4\pi}). \quad (2.4)$$

The mean number of particles in acceptance is (using Eqs. B.13, B.22)

$$\langle N \rangle = p \langle N_{4\pi} \rangle \quad (2.5)$$

The variance of the number of particles in acceptance  $N$  is given by (using Eqs. B.23, B.13, B.6, B.14):

$$\begin{aligned} \text{Var}(N) &= \langle \text{Var}(N|N_{4\pi}) \rangle + \text{Var}(\langle N|N_{4\pi} \rangle) \\ &= \langle \text{Var}(N|N_{4\pi}) \rangle + \text{Var}(pN_{4\pi}) \\ &= \langle N_{4\pi} \rangle p(1 - p) + p^2 \text{Var}(N_{4\pi}) \end{aligned} \quad (2.6)$$

Finally scaled variance in the limited acceptance  $\omega_{acc}$  is therefore related to the scaled variance in the full phase space  $\omega_{4\pi}$ :

$$\omega_{acc} = p(\omega_{4\pi} - 1) + 1 \quad (2.7)$$

The acceptance dependence given by Eq. 2.7 is not valid when effects like resonance decays, quantum statistics and energy- momentum conservation introduce correlations in momentum space. In this work Eq. 2.7 is only used as a baseline for the study of acceptance effects and for a comparison with models where the effects mentioned above are not included or expected to be small.

For the study of the dependence of scaled variance on rapidity and transverse momentum, the "trivial" dependence on the fraction of accepted tracks has to be ruled out. Therefore in the following the bins in rapidity and transverse momentum are constructed in such a way that the mean particle multiplicity in each bin is the same. If there would be no correlations in momentum space and no dependence of the momentum spectra on multiplicity, the scaled variance in bins constructed in such a way would not depend on rapidity or transverse momentum.

### 2.1.2 Participant Fluctuations

If the scaled variance for all inelastic Pb+Pb collisions would be determined, this value would be dominated by fluctuations in the number of participant nucleons. In order to remove this "trivial" source of fluctuations the centrality of the collision has to be fixed.

Fluctuations in the number of participants lead to an increase of multiplicity fluctuations. In a superposition model the total multiplicity  $N$  is the sum of the number of particles produced by different independent particle production sources:

$$N = \sum_i N_{i,so}. \quad (2.8)$$



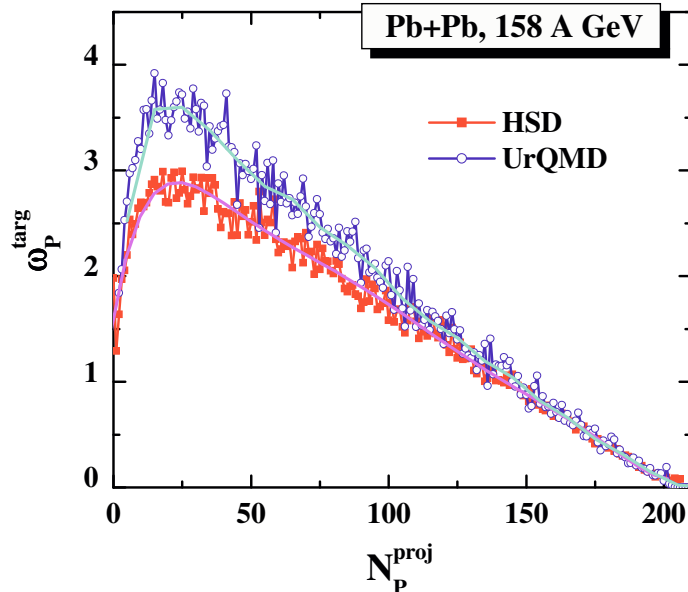


Figure 2.1: Fluctuations in the number of target participants for a fixed number of projectile participants in the UrQMD and HSD [53] models.

In these models the scaled variance has two contributions. The first is due to the fluctuations of the number of particles emitted by a single source  $\omega_{so}$ , the second is due to the fluctuations in the number of sources  $\omega_k$ :

$$\omega = \omega_{so} + \langle N_{so} \rangle \cdot \omega_k, \quad (2.9)$$

where  $\langle N_{so} \rangle$  is the mean multiplicity of hadrons from a single source. The participant nucleons of a collision are considered to be proportional to the sources of particle production.

In order to minimize the fluctuations of the number of sources, the centrality variation in the ensemble of events should be as small as possible. In the NA49 experiment this is achieved by measuring and fixing the number of projectile spectator nucleons with a zero degree calorimeter (chapter 3). This procedure strongly reduces the fluctuations in the number of projectile participants, but small fluctuations due to the finite width of the centrality bins and the finite resolution of the zero degree calorimeter still might remain.

Furthermore the fixation of the number of projectile participant  $N_P^{Proj}$  does not fix the number of target participants  $N_P^{Targ}$ . Even though their mean number is the same in collisions of equal nuclei except for very central or very peripheral collisions, this is not true on an event-by-event basis. The scaled variance of target participant fluctuations for a fixed number of projectile participants

$$\omega(N_P^{Targ}) = Var(N_P^{Targ}) / \langle N_P^{Targ} \rangle \quad (2.10)$$

was calculated in [53] within the string-hadronic models UrQMD and HSD (Fig. 2.1). Both models show a huge amount of target participant fluctuations for collisions with an intermediate number of projectile participants. For very central collisions, where the number of projectile participants is similar to the total number of nucleons in the projectile, the fluctuations in the number of target participants are small.

It is *a priori* not known how the fluctuations in the number of projectile- and target participants contribute to the multiplicity fluctuations in different regions of the phase-space.

## 2 Multiplicity Fluctuations

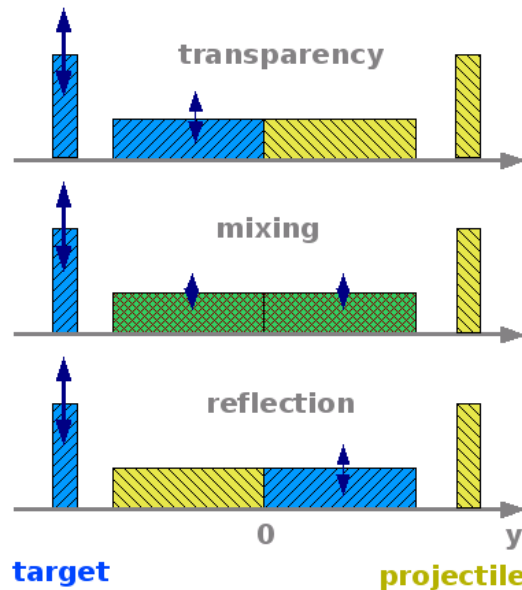


Figure 2.2: A sketch of the different reaction scenarios, how the fluctuations in the number of target participants contribute to the fluctuations in particle multiplicity [54].

In [54] three different extreme scenarios are discussed.

The "transparency" scenario is inspired by the Bjorken reaction picture (section 1.2.3). In this picture the incoming projectile and target nucleons lose only a part of their kinetic energy, which is then used for particle production, and continue to move into their original direction. In the transparency scenario the projectile participants are responsible for the particle production in the projectile hemisphere (the hemisphere where the longitudinal momentum of particles in the center of mass frame has the same sign as the incoming projectiles) and vice versa. Therefore fluctuations in the number of target participants lead only to additional fluctuations in the target hemisphere and not in the projectile hemisphere.

The "mixing" scenario is inspired by the Landau-picture where the incoming nucleons are fully stopped and form a fireball from which particles are emitted. In the mixing scenario, the fluctuations in the number of target participants lead to an equally distributed increase of multiplicity fluctuations in both hemispheres.

In the (unrealistic) "reflection" scenario the fluctuations in the target participants lead to an increase of multiplicity fluctuations in the projectile hemisphere only.

String-hadronic models like UrQMD and HSD show a behaviour similar to the "transparency" scenario. In these models fluctuations in the number of target participants cause an increase of multiplicity fluctuations mostly in the target hemisphere. In the projectile hemisphere, more than one unit of rapidity away from mid-rapidity, no increase of scaled variance is observed (Fig. 2.3). When the target participants are fixed and the projectile participants are allowed to fluctuate, the scaled variance in the projectile hemisphere shows additional fluctuations.

In principle it might be possible to correct for participant fluctuations in the framework of a superposition model. But in the limited phase space used for the analysis of multiplicity fluctuations this correction strongly depends on which of the scenarios described above is used. Therefore it is preferable to minimize the projectile and target participant fluctuations

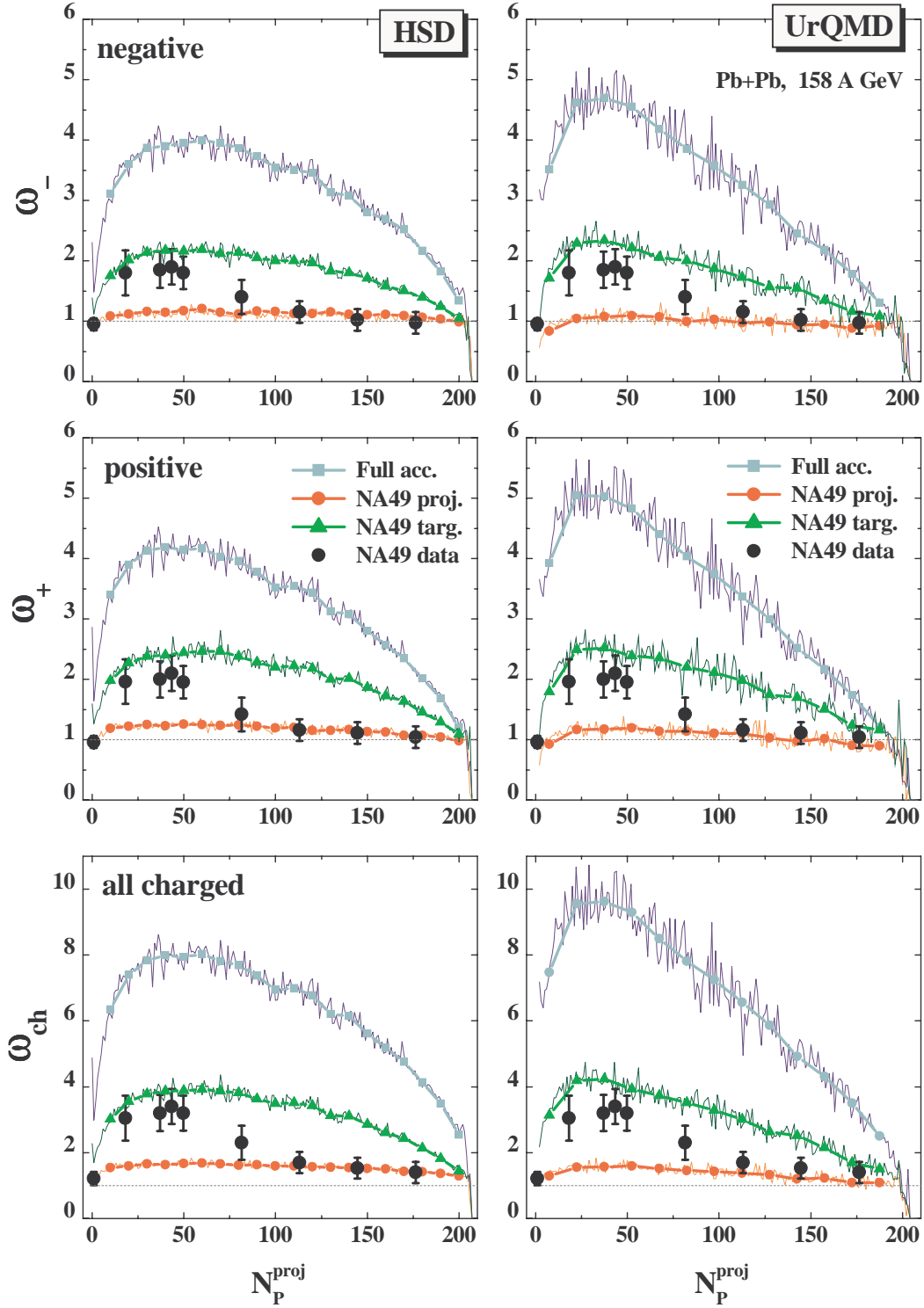


Figure 2.3: UrQMD and HSD simulations of the centrality dependence of scaled variance for Pb+Pb collisions at 158A GeV [53]. The calculations are performed for negatively (top), positively and all charged hadrons (bottom) in full acceptance and in a forward acceptance labeled as NA49 proj ( $1.1 < y < 2.6$ , limited  $p_T$  and  $\phi$ ) corresponding to the acceptance of the NA49 points shown for comparison. In addition the fluctuations in the same acceptance (labeled as NA49 targ) are shown for a fixed number of target participants and fluctuating projectile participants.

## 2 Multiplicity Fluctuations

experimentally that no correction is needed. For further analysis the 1% most central collisions, according to the number of projectile participants (section 4.2), are selected. For these very central collisions, the fluctuation in the number of target participants is expected to be smallest and its scaled variance  $\omega_P^{Targ}$  is expected to be about 0.1.

## 2.2 Theoretical Concepts

In this section several theoretical concepts concerning multiplicity fluctuations are shortly introduced. For a more detailed discussion the reader is referred to chapter 7.

### 2.2.1 Resonance Decays

The fluctuations are expected to be enhanced if more than one daughter track of a decay of a resonance is used for the fluctuation analysis. This effect can be understood in the following way: a gas of resonances is assumed to have a scaled variance of  $\omega(R)$ . If all resonances decay into two particles, which are all used for fluctuation analysis, each resonance  $R$  is counted as two particles  $N$ . The scaled variance is therefore

$$\omega(N) = \frac{\langle N^2 \rangle - \langle N \rangle^2}{\langle N \rangle} = \frac{\langle (2R)^2 \rangle - \langle 2R \rangle^2}{\langle 2R \rangle} = \frac{4 \langle R^2 \rangle - 4 \langle R \rangle^2}{2 \langle R \rangle} = 2\omega(R), \quad (2.11)$$

two times the scaled variance of the initial resonances. If only one of the daughter tracks of a resonance is used for the fluctuation analysis, the resulting scaled variance is the same as for the resonances itself. This is for example the case if only hadrons of one charge are used but the resonances decay into two oppositely charged particles.

If no other correlations in momentum space are present the acceptance dependence Eq. 2.7 is valid for primordial particles and resonances where only one daughter track is used for the fluctuation analysis.

### 2.2.2 Fluctuations in Relativistic Gases

In statistical hadron-gas models the widths of the multiplicity distributions depend on the conservation laws which the system obeys. Even though for different statistical ensembles the mean multiplicity is the same for sufficiently large volumes, this is not necessarily so for higher moments of the multiplicity distribution like multiplicity fluctuations [51]. Fluctuations are largest in the grand-canonical ensemble, where all conservation laws are fulfilled only on average and not on an event-by-event basis. The multiplicity fluctuations are much smaller in the canonical ensemble, where the total charges are exactly conserved. The smallest fluctuations are obtained within the micro-canonical ensemble, for which the total charges as well as the total energy and momentum are conserved. For high collision energies the scaled variance obtained by hadron-gas model calculations saturates at values of  $\omega(h^-) \approx 1$  for the grand-canonical and  $\omega(h^-) < 1$  for the canonical and micro-canonical ensemble [55] (section 7.1).

It should be underlined that in non-relativistic gases the situation is very different, namely the particle number is conserved in the micro-canonical and canonical ensembles and consequently the multiplicities in these ensembles do not fluctuate.

### 2.2.3 String-Hadronic Models

String-hadronic models, like the UrQMD transport approach [56, 57], are based on the propagation of constituent quarks and di-quarks accompanied by mesonic and baryonic degrees of freedom. They simulate multiple interactions of in-going and newly produced particles, the excitation and fragmentation of colour strings and the formation and decay of hadronic resonances. A phase transition is not incorporated explicitly into these models.

The string-hadronic model UrQMD can reproduce the energy dependence of scaled variance of the multiplicity distribution in p+p collisions in a wide energy range (section 7.2). Furthermore it is possible to take both the experimental acceptance and the experimental method of centrality selection into account for calculations in this model. Therefore it can provide a reference in  $\omega$  for the search for the critical point or signals of the onset of deconfinement.

In the string-hadronic models  $\omega$  in Pb+Pb collisions increases with collision energy, similar to  $\omega$  in p+p interactions. The different energy dependence of  $\omega$  in hadron-gas and string-hadronic models might allow to distinguish between them with the experimental data.

### 2.2.4 Onset of Deconfinement and Critical Point

It is predicted that both the onset of deconfinement [49] and a freeze-out of the matter near the critical point [50] should lead to an increase of multiplicity fluctuations at a specific collision energy (sections 7.3 and 7.4).

## 2.3 Multiplicity Fluctuations in Elementary Collisions

Multiplicity fluctuations were extensively studied for p+p and p +  $\bar{p}$  interactions by bubble- and streamer-chamber experiments in a wide energy range. These experiments cover the full phase space for all charged particles and record all inelastic collisions.

It has been found that the multiplicity distributions in a wide energy range can be parametrized by using a single scaling function (Fig. 2.4):

$$P(n) = \frac{1}{\langle n \rangle} \Psi \left( \frac{n}{\langle n \rangle} \right), \quad (2.12)$$

where  $\Psi(z)$  is independent of the collision energy (Fig. 2.5). This property of elementary interactions is called Koba-Nielsen-Olesen- (KNO-) scaling [59, 60]. The KNO-scaling implies that all moments of a multiplicity distribution scale like

$$\langle n^q \rangle \approx c_q \langle n \rangle^q \quad (2.13)$$

with a constant  $c_q$ . The scaled variance is therefore

$$\omega = \frac{\langle n^2 \rangle - \langle n \rangle^2}{\langle n \rangle} = \frac{c_2 \langle n \rangle^2 - \langle n \rangle^2}{\langle n \rangle} = (c_2 - 1) \langle n \rangle, \quad (2.14)$$

a linear function of the mean multiplicity  $\langle n \rangle$ .

For the function  $\Psi(z)$  a log-normal distribution can be used [61]

$$\Psi(z) = \frac{1}{\sqrt{2\pi}\sigma} \frac{1}{z+c} \exp \left[ -\frac{[\ln(z+c) - \mu]^2}{2\sigma^2} \right], \quad (2.15)$$

## 2 Multiplicity Fluctuations

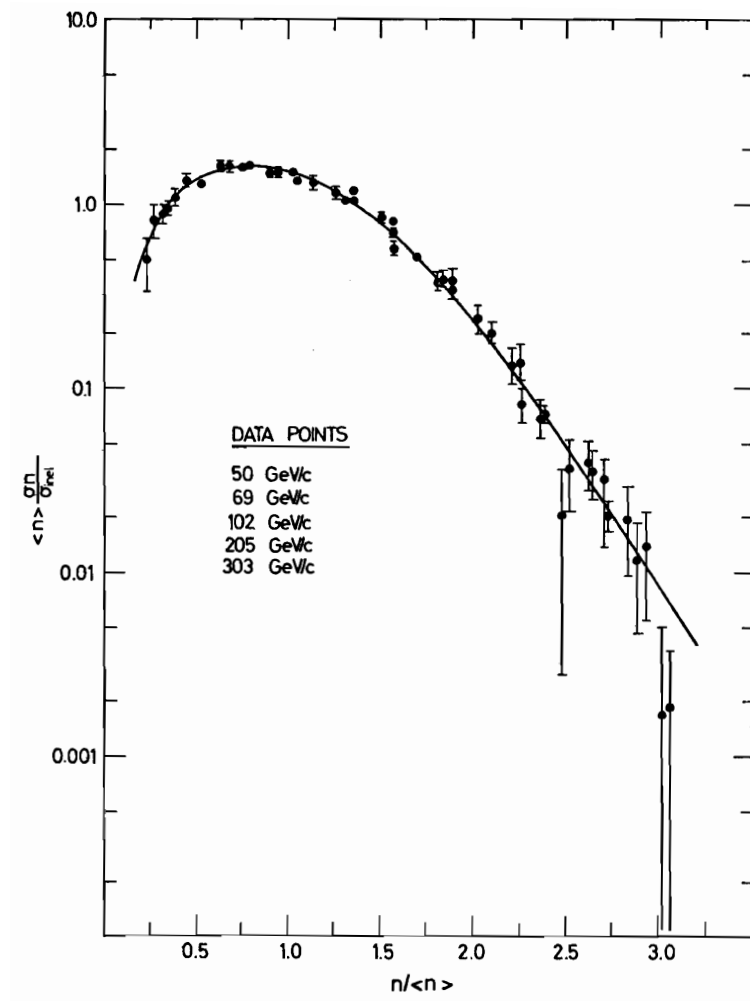


Figure 2.4: Scaled multiplicity distribution  $\langle n \rangle P(n)$  as a function of  $n / \langle n \rangle$  for bubble-chamber data on p+p collisions with  $p_{lab} \geq 50$  GeV [58].

### 2.3 Multiplicity Fluctuations in Elementary Collisions

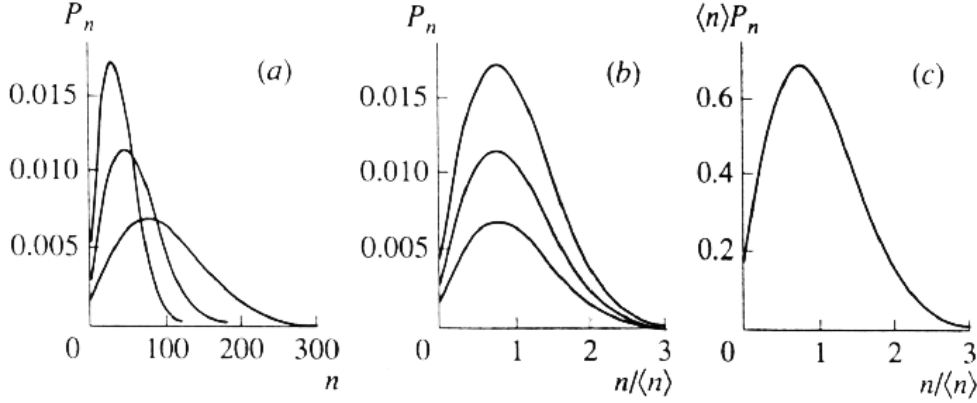


Figure 2.5: Illustration of the concept of similarity of continuous functions (KNO-scaling). Normalized functions (a) are similar if upon a linear contraction of each of them along the horizontal direction in proportion to some of its horizontal dimensions, for example  $\langle n \rangle$  (b), and a linear extension along the vertical direction in the same proportion (c) they coincide at each point [59].

where  $\sigma$ ,  $c$  and  $\mu$  are free parameters.

The KNO-scaling fails at low multiplicities because it does not take into account that only integer values of the multiplicity  $n$  are allowed. The slightly modified KNO-G-scaling [62] is also valid for small collision energies:

$$P(n) = \int_{nz_0}^{(n+1)z_0} \frac{1}{\langle n \rangle} \Psi \left( \frac{n}{\langle n \rangle} \right) d \frac{n}{\langle n \rangle}. \quad (2.16)$$

In the limit  $\langle n \rangle \rightarrow \infty$  the KNO-G-scaling is equivalent to the KNO-scaling.

In the experiment a linear dependence of the scaled variance of all charged particles in full phase space on the mean multiplicity is found (Fig. 2.6, right), in agreement to the KNO-scaling.

The energy dependence of the mean multiplicity of charged hadrons in elementary collisions can be parametrized by [63] (Fig. 2.6, left):

$$\langle N_{ch} \rangle \approx -4.2 + 4.69 \left( \frac{s}{\text{GeV}^2} \right)^{0.155}. \quad (2.17)$$

Its energy dependence can be parametrized by [63]:

$$\omega(h^\pm) \approx 0.35 \left( \frac{(\langle N_{ch} \rangle - 1)^2}{\langle N_{ch} \rangle} \right) \quad (2.18)$$

and shows an approximate linear behavior of scaled variance on mean multiplicity.

## 2 Multiplicity Fluctuations

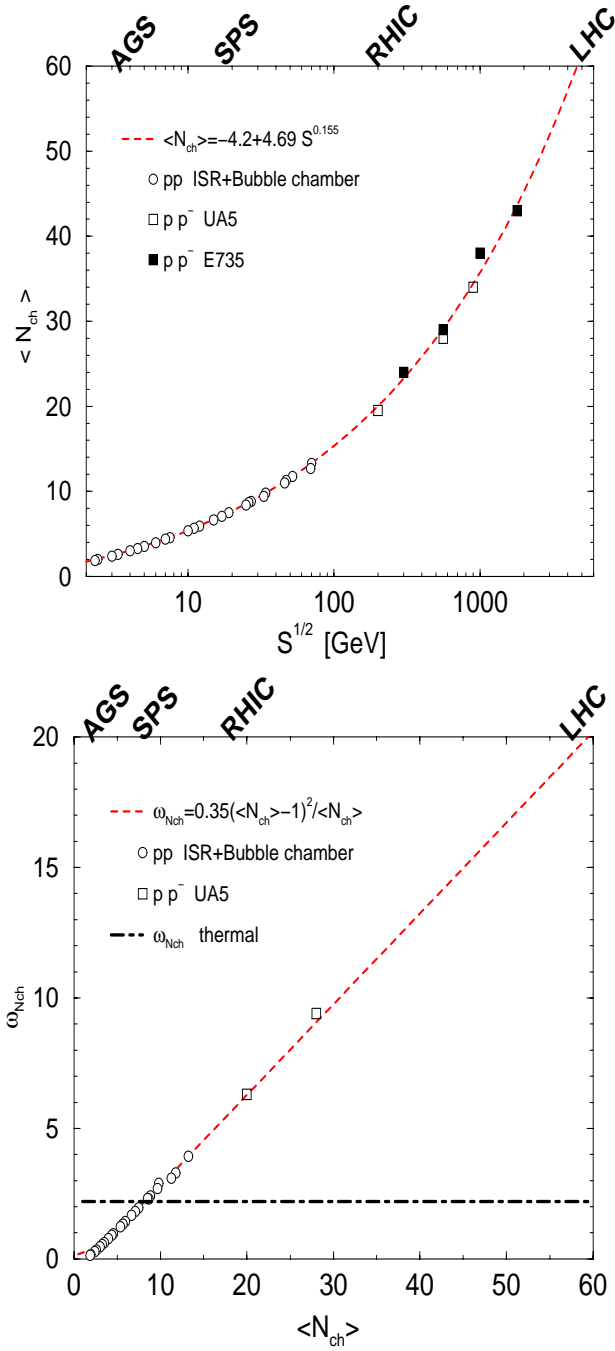


Figure 2.6: Top: Energy dependence of mean charged hadron multiplicity in p+p (p+p̄) interactions [63]. Bottom: Dependence of scaled variance of charged hadrons on the mean charged particle multiplicity for p+p (p+p̄) interactions [63].



## 3 The NA49 Experiment

The NA49 experiment [64] was designed to detect the hadronic final state of both high energy elementary (p+p) and heavy ion collisions. It is located at the H2 beam-line of the CERN SPS accelerator.

### 3.1 Nucleus-Nucleus Collisions at the CERN SPS

#### 3.1.1 History of the SPS

The construction of the Super-Proton-Synchrotron (SPS) with a circumference of 7 km was approved in 1971, it was finished in 1976 and delivered the first proton beams.

Later on, the SPS was modified to accelerate both protons and anti-protons simultaneously in opposite directions in the same ring. This collider mode of the SPS was called Sp $\bar{p}$ S and in that mode much higher collision energies could be reached. In a fixed target experiment a large amount of the incident beam energy is used for the movement of the center of mass of the collision and it can not be used for particle production (appendix C). In a collider, in contrast, no energy is wasted for the movement of the center of mass of the collision, therefore higher collision energies in the center of mass frame can be reached. The Sp $\bar{p}$ S program was a major success, the carriers of the weak interaction, the W and Z bosons, were discovered.

The heavy ion program at CERN SPS started in 1986 with beams of oxygen ( $^{16}\text{O}$ ) and sulfur ( $^{32}\text{S}$ ) to a maximum energy of 200A GeV. Along others, the predecessor experiment of NA49, NA35 [35], was used for investigating these collisions.

Since 1994 it is possible to accelerate lead (Pb) ions up to an energy of 158A GeV at the SPS, NA49 is one of the experiments taking data with such beams. In 2003 indium beams were delivered.

#### 3.1.2 Working Principle of a Synchrotron

In a synchrotron the particles are kept on a circular path by strong magnetic fields. Magnetic quadrupole lenses are focusing the particle beam for the compensation of the electrostatic repulsion and thermal motion of the charged beam particles. The beam is accelerated by high-frequency electromagnetic fields. The particle beam is not continuous but bunched. The bunches are timed in such a way that each time the particles pass the high-frequency accelerator elements the momentum of the particles increases. Therefore the magnetic field of the bending magnets has to be raised, too, in order to keep the particles on their circular path. The largest possible beam energy for hadron accelerators is determined by the possibility to keep the particles on the circular path. The larger the accelerator circle and the stronger the bending magnets the larger is the maximum beam energy.

Every time a particle is bent it loses energy due to synchrotron radiation. For hadrons this energy loss is negligible, but it is significant for light particles like electrons. For electrons the maximum energy which can be reached in a synchrotron is determined by the power of the

### 3 The NA49 Experiment

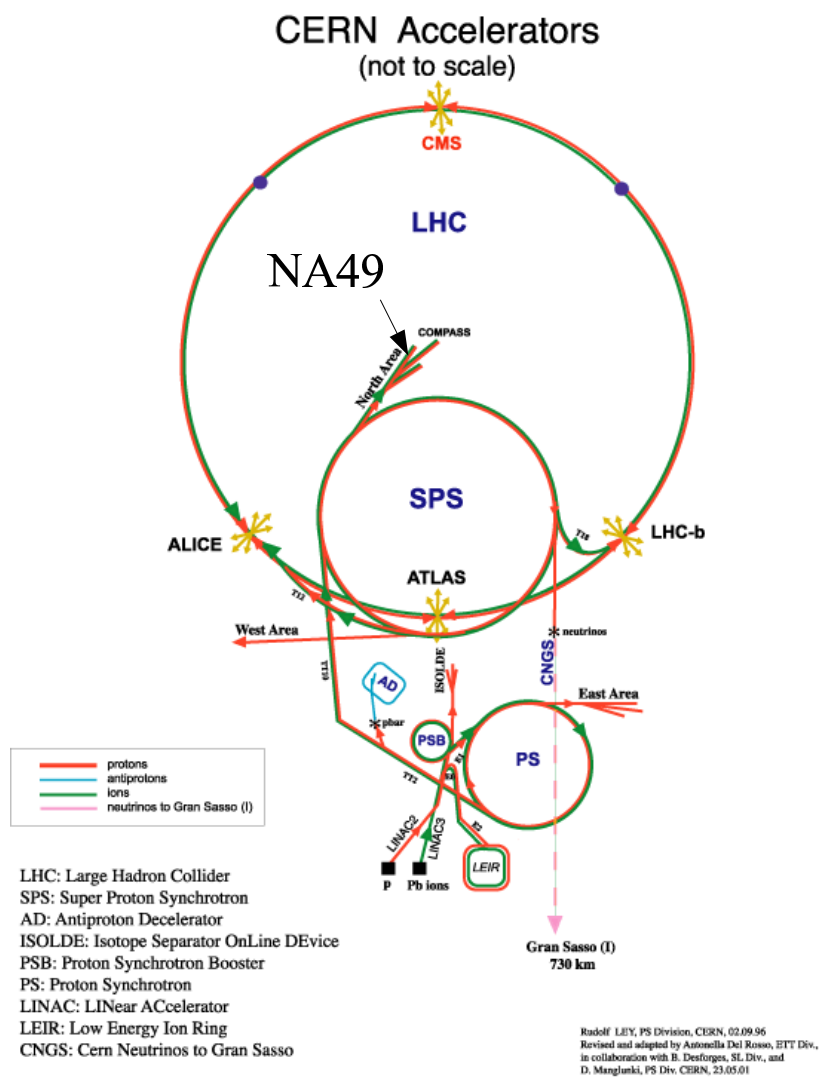


Figure 3.1: Overview of the accelerators at CERN.

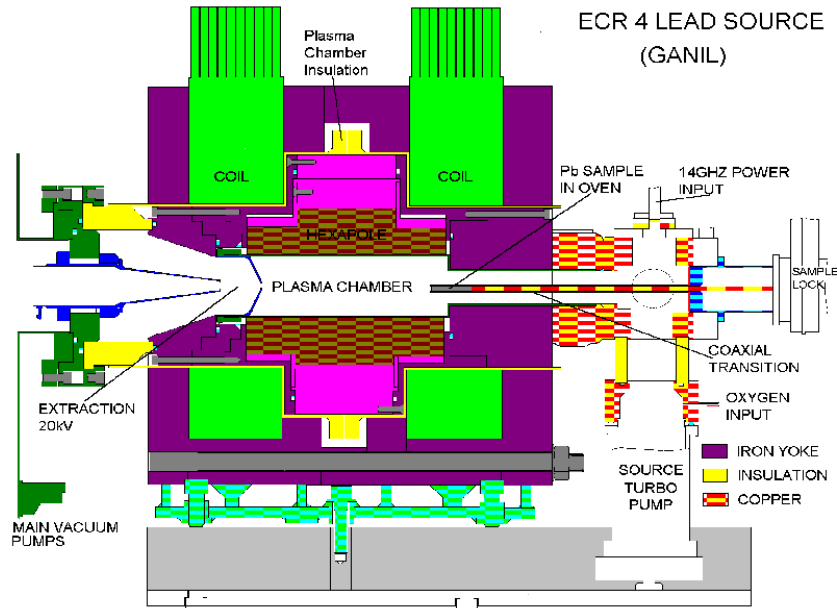


Figure 3.2: Sketch of the Pb ion source at CERN [65].

acceleration units to compensate synchrotron radiation. As synchrotron radiation is smaller for larger circles the Large Electron-Positron Collider (LEP) at CERN had a circumference of 27 km and could reach center of mass energies of up to 209 GeV. The LEP is decommissioned, in its tunnel the Large Hadron Collider (LHC) is under construction and will be commissioned soon.

A synchrotron is not only limited in its maximum beam energy but also in its minimum energy. For example the bending magnets can not provide a homogeneous magnetic field for a too low field strength. Therefore a chain of accelerators is used (Fig. 3.1).

27 times charged Pb ions are produced in an Electron Cyclotron Resonance (ECR) source by electrostatic extraction of the ions out of a Pb plasma (Fig. 3.2). They are pre-accelerated in a linear accelerator (LINAC 3). As the ion source does not ionize lead completely, the ions pass several stripper foils where they lose in different steps all their electrons. After the linear accelerator they enter the Proton Synchrotron Booster (PSB), the first synchrotron in the CERN acceleration chain. After that they are accelerated in the Proton Synchrotron (PS) before they enter the Super Proton Synchrotron (SPS), which delivers the beam to the NA49 experiment. When the LHC goes into operation it will be filled with the ions accelerated by the SPS.

### 3.1.3 Fragmentation Beams

Beams of lighter ions than Pb have not been delivered directly to NA49. For the production of C and Si ions the lead beam is shot on a 10 mm thick carbon converter located directly after the extraction point of the beam from the SPS. When hitting the converter some of the Pb ions break up and different fragments are created. The bending magnets in the beam line are adjusted in such a way that only fragments with  $Z/A = 1/2$  can reach the NA49 experiment. The distribution of these fragments is shown in Fig. 3.3.

### 3 The NA49 Experiment

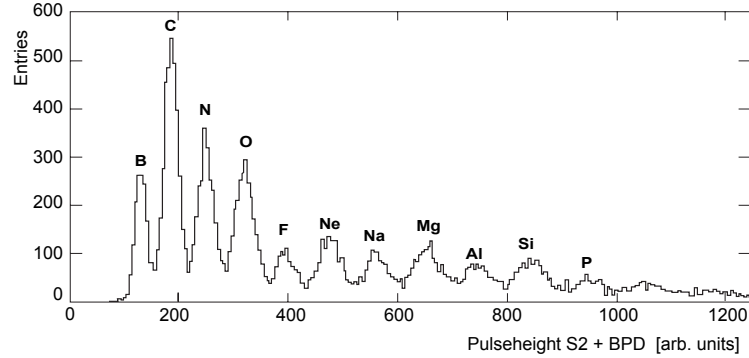


Figure 3.3: Charge distribution of fragments with  $Z/A = 1/2$  for 158A GeV as measured by the S2 and the beam position detectors.

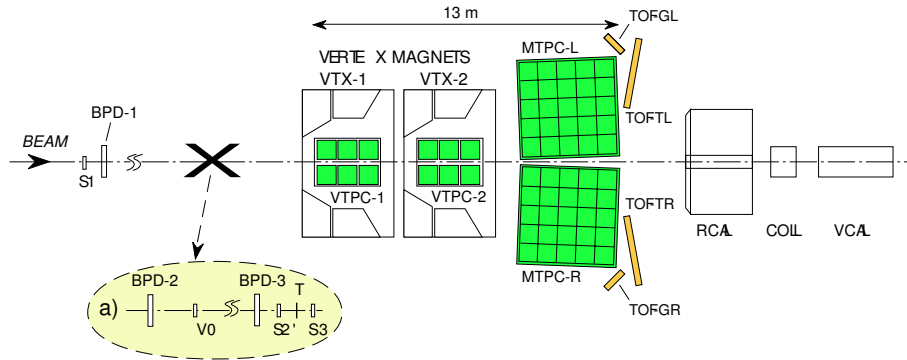


Figure 3.4: Setup of the NA49 experiment [64] for Pb+Pb collisions, see text for more details.

The charge of the fragments can be measured by the energy they deposit in the three beam position detectors, which are multi-wire proportional chambers, and in a helium Cerenkov detector (S2). For NA49 both an on-line trigger is used to select the beam charge and the information on beam charge is stored for an off-line event selection (section 4.1).

## 3.2 Experimental Setup

The NA49 detector [64] (Fig. 3.4) is a large acceptance fixed target hadron spectrometer. Its main devices are four large volume time projection chambers (TPCs). These gaseous detectors allow a reconstruction of the path of charged particles in three dimensions (see section 3.2.2). Furthermore the measurement of the energy loss  $dE/dx$  in the detector gas allows particle identification in a large momentum range. For higher momenta ( $p > 4$  GeV) particle identification is possible in the TPCs alone, for lower momenta in combination with the time of flight (TOF) measurement system (see below).

Two of the TPCs, called vertex TPCs (VTPC1 and 2), are located in two superconducting

dipole magnets (VTX-1 and 2). Each vertex TPC consists of two parts located around the beam with a dead area for the beam in between. The two other TPCs (MTPC-L and MTPC-R) are installed behind the magnets on the left and the right side of the beam line allowing precise particle tracking in the high density region of heavy ion collisions.

The magnetic field deflects charged particles and allow therefore both the measurement of the charge and of the momentum of the particle. In a homogeneous magnetic field the momentum of a particle can be determined by the following equation:

$$p[\text{GeV}/c] \approx 0.3 \cdot q[e] \cdot r[\text{m}] \cdot \frac{1}{\cos \lambda}, \quad (3.1)$$

where  $r$  is the curvature of the particle track and  $\lambda$  the angle between the track and the plane orthogonal to the magnetic field.

The two superconducting magnets of the NA49 experiment have a combined maximum bending power of 9 Tm with a current of 5000 A. For the highest SPS energy for Pb ions, 158A GeV, the magnetic field of the VTX-1 magnet is set to 1.5 T and the one of VTX-2 to 1.1 T, which gives a combined bending power of 7.8 Tm. For lower energies the magnetic field is scaled down in proportion to the beam energy.

As an exact knowledge of the magnetic field is essential for the track reconstruction and momentum determination, the magnetic field of NA49 was measured with Hall-probes. In addition it was calculated using the known current and iron configuration with a software called TOSCA. The long-term stability of the magnetic field is controlled with Hall-probes installed in the experiment.

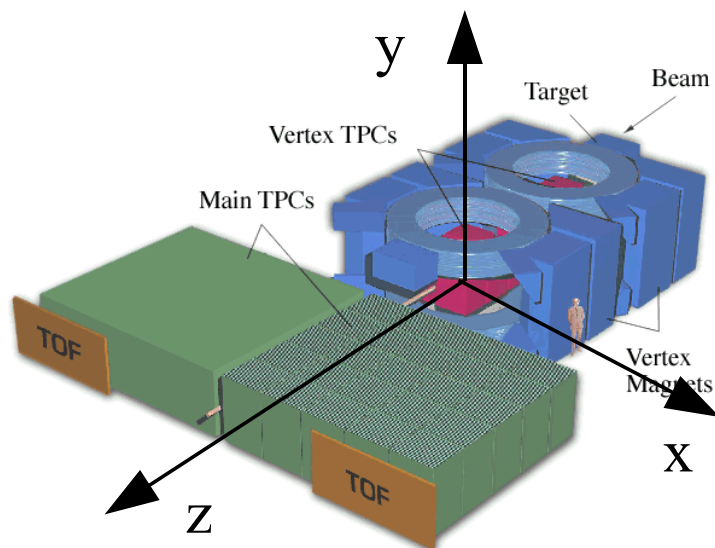


Figure 3.5: The coordinate system of NA49.

The centrality of a collision can be determined by the measurement of the energy of the projectile spectators in the veto calorimeter (section 3.2.4).

In the following the standard coordinate system of the NA49 experiment (Fig. 3.5) is used. The zero-point of the experiment is located in the middle of VTPC2. The z-axis goes into

### 3 The NA49 Experiment

the beam direction, the y-axis goes to the top of the experiment and the x-axis in direction to the Jura mountains in order to form a right-hand coordinate system.

#### 3.2.1 Beam, Target and Trigger

The target is located 80 cm in front of the first vertex TPC. Both solid target foils (C, Si, Pb) and liquid hydrogen can be used. For heavy ion beams the 200  $\mu\text{m}$  thick quartz- Cerenkov-counter S1 and the helium-gas Cerenkov counter S2' are used to indicate beam particles approaching the target. Behind the target the S3 counter detects beam particles which have not interacted. The veto counter V0 has a hole in the middle where the beam should pass and is used to reject particles which are not in the nominal position of the beam.

Three beam-position-detectors (BPDs), multi-wire proportional chambers filled with Ar/CH<sub>4</sub>, are located in the beam line. They have an active area of  $3 \cdot 3 \text{ cm}^2$  and the point where the beam hits the target foil can be calculated with an accuracy of 40  $\mu\text{m}$  by an extrapolation to the target plane. In addition the strength of the signal in the BPDs allow a determination of the charge of the beam particle for the separation of different beam species in a fragmentation beam.

Different trigger settings can be applied for the selection of collisions using the beam counter and veto calorimeter information. When an event fulfils the trigger conditions the read-out of the various detectors start. The data of the TPCs, the beam counters and the veto calorimeter is read out by a CAMAC bus system, the TOF walls by a FASTBUS system. The event builder combines these informations and the data is written onto tapes of a capacity of 100 GB by a SONY DIR-1000M tape drive with a speed of up to 16 MB/s. Each central Pb+Pb event at 158A GeV has a size of approximately 8 MB.

#### 3.2.2 The Time Projection Chambers

Time projection chambers (TPCs) allow a precise tracking of charged particles in three dimensions in a large volume. In addition their small material budget reduce the probability of secondary interactions. A TPC consists of a large gas volume where charged particles ionize the gas atoms along their path. The freed electrons are drifting towards the read-out plane. Using the position on that plane and the time the electrons needed for the drift the position of the track point can be reconstructed in three dimensions.

The gas volume is located in a field cage where a homogeneous electric field is created. Due to this field the electrons are accelerated towards the read-out chambers of the TPC. They quickly reach a constant drift velocity due to collisions with the gas atoms. This velocity is dependent on the drift voltage and the gas mixture, but also on the gas temperature. Therefore these parameters are kept as stable as possible in the NA49 experiment. The atmospheric pressure, which also influences the drift velocity, and the drift velocity itself are measured during data taking in order to allow to correct for any changes. In addition to the drift in the direction of the read-out chambers the collisions with the gas atoms also cause a diffusion of the electrons both in and orthogonal to the drift direction.

The read-out chambers consist of three wire planes and a pad plane. The first wire plane the electrons have to pass is the gating grid. When the TPC is read out it is put on the same potential as the drift field and the electrons can pass it. After the read out the wires are put on an alternating voltage. This prevents electrons to drift into the read-out chambers when the detector is not read out. In addition it prevents positive ions created in the gas

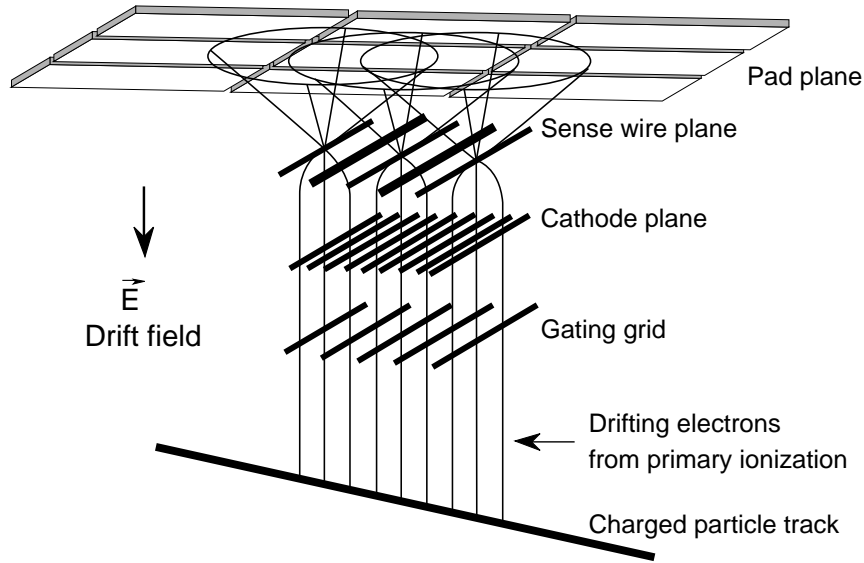


Figure 3.6: Read-out plane of the NA49 TPCs [64].

amplification region from drifting back into the TPC volume and disturbing the electric field. The cathode grid separates the drift volume (with a homogeneous electric field) from the amplification volume of the TPC. A large fraction of the ions created in the gas amplification region are collected by the cathode wires and are therefore not going into the drift volume and disturbing the electric field.

The sense wire plane consists of field wires with a diameter of  $125\ \mu\text{m}$ , which are on ground potential, and amplification wires with a diameter of  $20\ \mu\text{m}$ , which are on a positive potential. Due to their small size the electrical field near the amplification wires is very high. Electrons are accelerated by this field and ionise additional gas atoms. As the mean free path of the electrons near the amplification wires is larger than the way they need to gain enough energy to ionise an atom, an avalanche is created and the number of electrons is increased by a factor of  $10^3 - 10^4$ . However the wire voltage is chosen in such a way that the gas amplification is linear. In addition to electron-ion pairs also photons are produced. If their energy is large enough to ionise atoms they can create additional avalanches and unwanted spark discharges. Therefore a quencher gas with a high absorption cross-section for photons, like  $\text{CO}_2$ , is added to the detector gas. Due to their small mass the electrons are quickly reaching the wires and flowing away. The heavier ions remain in their position for a longer time and create a positive space charge near the wires. This positive space charge induces a negative mirror charge in the pads of the pad-plane. This mirror charge is read out by the TPC electronics. Due to the diffusion of the electrons during the drift and the spread of the mirror charges one track point causes a charge in several pads. By determining the center of gravity of the charge distribution the position of the track point can be determined with a precision much better than the size of the pad. The integrated charge on these pads is proportional to the initial energy loss of the charged particle in the detector gas according to the Bethe-Bloch formula.

The pad sizes and the geometry are optimized for a good momentum resolution and a good track separation in the high density region at  $158A\ \text{GeV}$ . The gas mixture (Table 3.1) is different for the vertex TPCs and the main TPCs. The vertex TPCs are located in a magnetic

### 3 The NA49 Experiment

	VTPC-1	VTPC-2	MTPC
Width	2m	2m	3.9m
Length	2.5m	2.5m	3.9m
Height	0.98m	0.98m	1.8m
Gas	90% Ne, 10% CO <sub>2</sub>	90% Ne, 10% CO <sub>2</sub>	90% Ar, 5% CO <sub>2</sub> , 5% CH <sub>4</sub>
Sectors	6	6	25
Pad rows per sector	24	24	18
pads per row	192	192	192/128
Pads	27648	27648	63360
Pad length	16/28 mm	28 mm	40 mm
Pad Width	3.5 mm	3.5 mm	3.6/5.5 mm
Angle to beam	12 – 55	3 – 20	0/15

Table 3.1: Sizes and characteristics of the NA49 TPCs [64].

field and have to deal with high track densities whereas the main TPCs are optimised for a precise determination of the energy loss  $dE/dx$ .

The read-out of the 182,016 pads in total is done in several steps. The front-end cards reading out 32 pads each. They consist of two pre-amplifiers and pulse shapers, analog memories and analog-digital (ADC) converters. The maximum drift time of 50  $\mu s$  is usually divided into 512 (or 256) time bins. The ADCs are running with a frequency of 10 MHz and each read-out channel and time bin consists of 8 Bit of information. In total the 5688 front-end cards produce about 100 MB of raw data for each event.

The data of 24 front-end cards is transferred to one of the 237 control-and-transfer (CT-) boards, where the data is transferred via optical link to the receiver boards. Each receiver board gets its input from four CT- boards. There the background signals of the channels (Pedestals) are subtracted. The information on the pads which are after background subtraction below a certain level is discarded (threshold-cut). This reduces the amount of raw data in a central Pb+Pb event at 158A GeV to about 8 MB. The data is then transferred via a CAMAC bus system to the event builder.

#### **$dE/dx$ Measurement**

The charge and the momentum of the particles are determined by the reconstruction chain (section 3.3.1) with high precision, but in order to identify a particle, additional information is needed. The measurement of the mean energy loss of charged particles in the detector gas in addition allows to distinguish between different particle species. The energy loss of a charged particle in the gas is described with the Bethe-Bloch formula [66] and is proportional to the number of electron-ion pairs created in the gas:

$$\left\langle \frac{dE}{dx} \right\rangle = -\frac{4\pi N_e e^4 z^2}{mc^2 \beta^2} \left[ \ln \frac{2mc^2 \beta^2}{I(1-\beta^2)} - \beta^2 \right], \quad (3.2)$$

where  $N_e$  is the electron density,  $I$  the ionization potential of the gas and  $z$  is the electric charge (in elementary units) of the particle. For a single charged particle the energy loss is only dependent on the velocity of the particle.



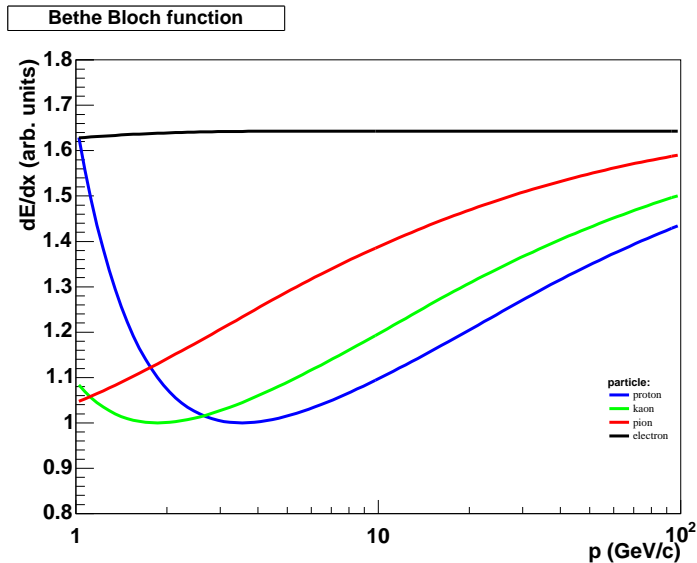


Figure 3.7: Energy loss of several particle species in the detector gas as a function of particle momenta according to the Bethe- Bloch- formula.

The cluster finder gives the information about the integrated charge in each cluster. This value is corrected for detector effects, like different amplifications of different electronic channels and the drift length of the electrons in the TPC.

The distribution of the cluster charges for tracks with a fixed mean energy loss is shown in Fig. 3.8. The distribution is not symmetric but has a tail towards higher energy losses. For the calculation of the mean energy loss of a track it turned out that the arithmetic mean of the cluster charges would be strongly influenced by this tail and would not be stable. Therefore the truncated mean is used where the 35% highest measured cluster charges are discarded. Because of different gas mixtures the averaging is done separately for each TPC (local  $dE/dx$ ). In addition a global  $dE/dx$  is calculated using the local  $dE/dx$  values.

The resolution of the energy loss measurement is not good enough for a track-by-track particle identification, but the  $dE/dx$  distributions can be unfolded in order to extract mean multiplicities of identified particles (Fig. 3.9).

### 3.2.3 Time-of-Flight Detectors

In addition to the TPCs several time of flight detectors are installed for the identification of low momentum particles. These are two pixel-scintillator walls (TOF-L/R) with a time resolution of 60 ps and two grid-scintillator walls (TOF-GL/GR) with a time resolution of 85 ps. These time of flight walls are used for the measurement of the time a particle needs for travelling from the interaction point to the TOF detectors. As the momentum of the particle is known by its curvature in the magnetic field it is possible to determine its mass. Unfortunately even though the time resolution of the NA49 TOF system is very good, it is not possible to separate high momentum particles because they are travelling essentially with the speed of light, weakly depending on their mass. In combination with the energy loss measurement in the TPCs a good separation of the different particle species is possible for low momenta. The acceptance of the TOF detectors is mainly located at mid-rapidity and is

### 3 The NA49 Experiment

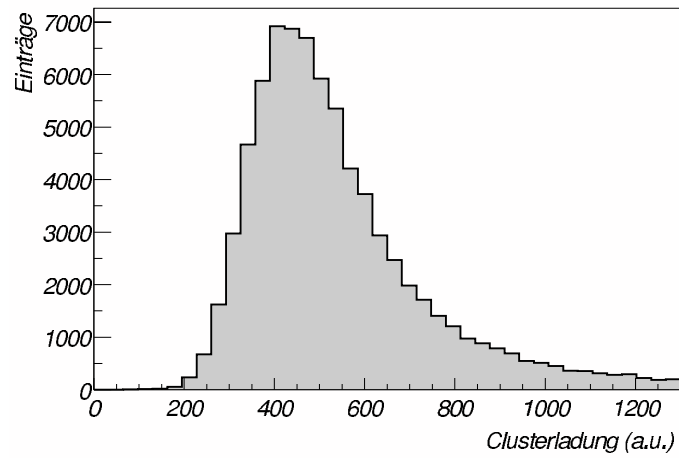


Figure 3.8: Cluster-charge distribution for pions with a momentum between 9 and 10 GeV/c [67].

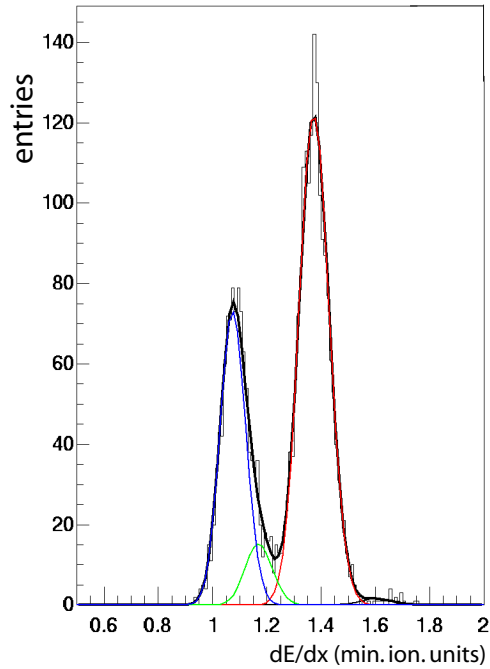


Figure 3.9: Example of a MTPC  $dE/dx$  distribution in one momentum and transverse momentum bin [68]. The particle yields are extracted by a fit of modified Gaussians to the data (red: pions, green: kaons, blue: protons).

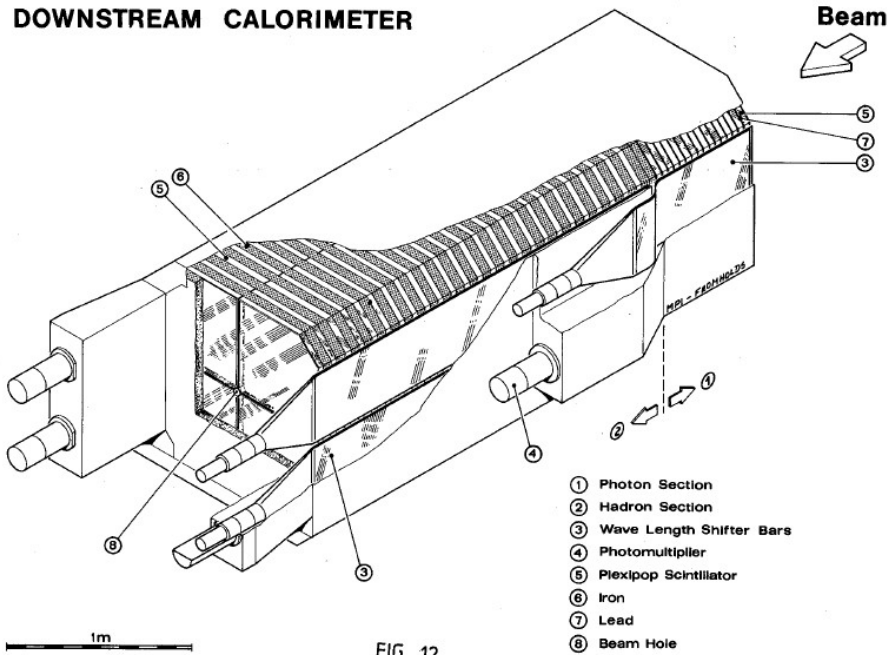


FIG. 12

Figure 3.10: Sketch of the veto calorimeter [69].

complementary to the region where particle identification is possible using only  $dE/dx$  in the TPCs.

### 3.2.4 Veto Calorimeter

The centrality of a collision is determined by measuring the forward going energy of projectile spectators in the veto calorimeter (VCAL, Fig. 3.10) located 26 m behind the target. The downstream veto calorimeter [69] of NA49, originally designed for NA5, allows a determination of the energy in the projectile spectator region [70]. It consists of an electromagnetic section of a lead/scintillator sandwich of 16 radiation lengths which is followed by a hadron section of an iron/scintillator sandwich of 7.5 interaction lengths. Each section is divided into four segments. The light produced by the scintillators of each segment is transported by light-conductors located at the left and the right side of the calorimeter to a photo-multiplier. Due to this design the response of the calorimeter is strongly dependent on the position the particle passes the scintillators, the light created in the center of the calorimeter has to go a longer way through the scintillator material and is weakened due to absorption or misses the photo-multipliers. This influences the resolution of the calorimeter, see section 4.2.3.

A collimator in front of the calorimeter is located 25 m downstream from the target and is adjusted for each energy in such a way that all projectile spectator protons, neutrons and fragments can reach the veto calorimeter, but the amount of produced particles hitting the calorimeter is as small as possible. For 158A GeV the hole in the collimator is with respect to the beam axis  $\pm 5$  cm in vertical (y-) direction and  $-5$  cm and  $+38$  cm in horizontal (x-) direction taking into account the deflection of charged particles by the magnetic field (Fig. 3.11, Table 3.2). For lower energies the particle spread due to Fermi-motion is larger because of the smaller particle momenta in z-direction. Therefore the hole of the collimator

### 3 The NA49 Experiment

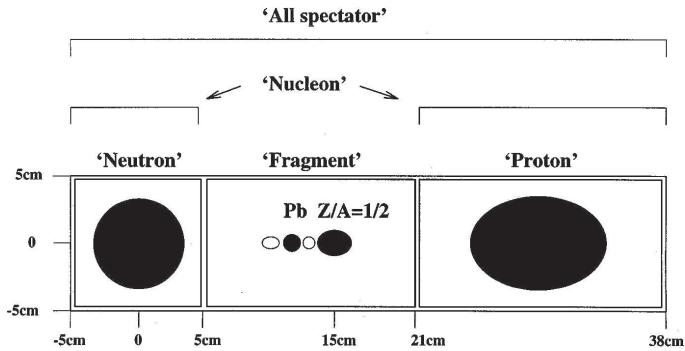


Figure 3.11: An illustration of the horizontal deflection for 158A GeV of charged particles at the front face of the iron collimator. The broadened distribution of each species is due to the Fermi motion of nucleons or fragments; additionally, the oval shapes are due to the deflection of charged particles in the magnetic field. The sizes of the distributions correspond to one standard deviation. The open circles in the fragment acceptance represent particles of  $Z/A$  other than one half [70].

energy	collimator		ring calorimeter
	x (cm)	y (cm)	x (cm)
20			10
30			10
40	-13	+47	$\pm 12$
80	-13	+47	$\pm 12$
158	-5	+38	$\pm 5$

Table 3.2: Settings of the collimator and the ring calorimeter defining acceptance of the veto calorimeter for different energies with respect to the position of neutrons with zero transverse momentum.

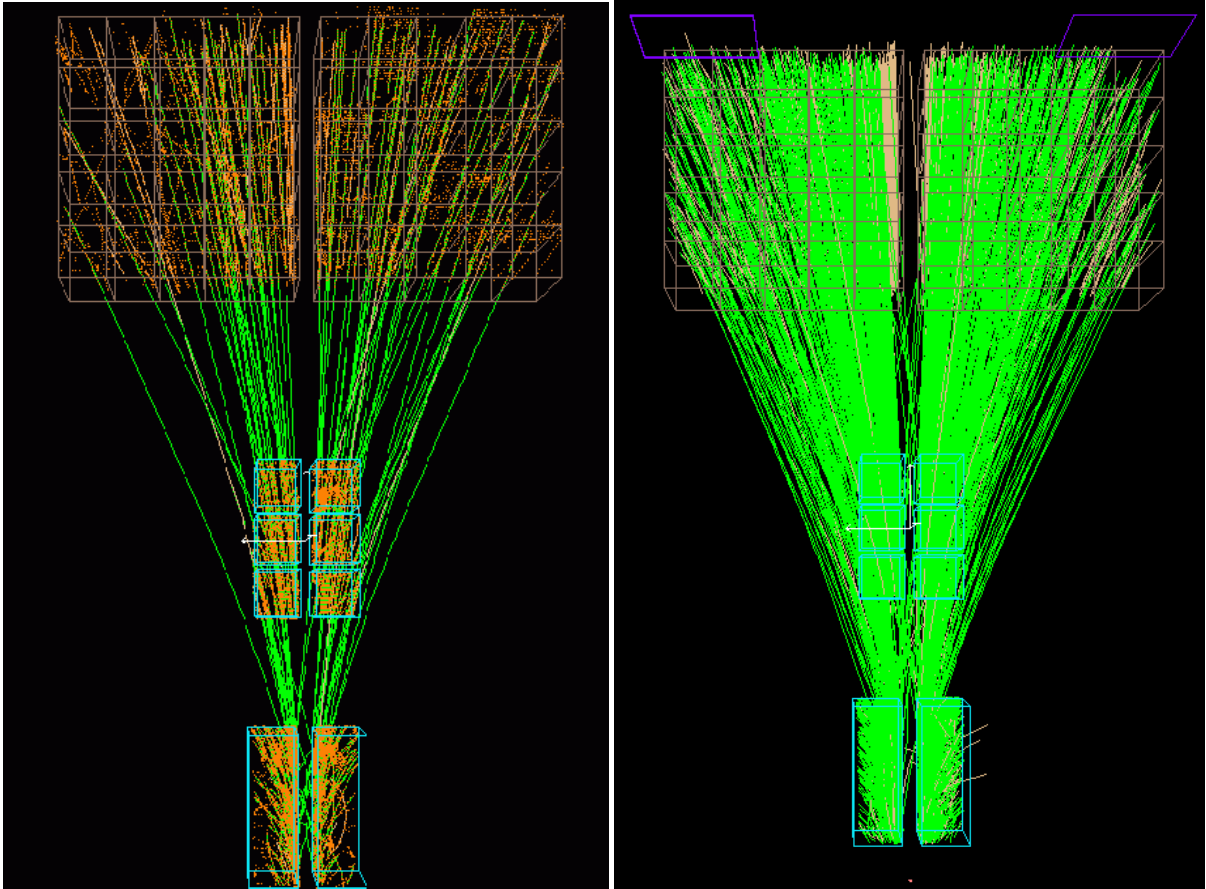


Figure 3.12: Visualisation of an NA49 event for Si+Si (left) and Pb+Pb collisions at 158A GeV.

is larger for 40A and 80A GeV. For 20A and 30A the collimator is removed and the ring calorimeter positioned 18 m downstream from the target is used as a collimator. For 40A-158A GeV the ring calorimeter is also positioned in the beam line but it has only a small influence on the acceptance of the veto calorimeter because of the presence of the collimator.

The settings of the hole in the collimator and the position of the ring calorimeter for the different energies are given in Table 3.2. The zero point is the point where neutrons with no transverse momentum would pass the collimator. The collimator is not symmetric around the zero point because the nuclear fragments and spectator protons carry positive charge and are deflected by the magnetic field around the vertex TPCs in positive x direction. The last column in the table is the position of the center of the ring calorimeter. Its hole has a radius of 28 cm.

### 3.3 NA49 Software

#### 3.3.1 Reconstruction of the NA49 Raw Data

The raw detector signals are written onto the SONY tapes. In order to extract physical information the raw data has to be reconstructed. The reconstruction was done offline, one

### 3 The NA49 Experiment

central Pb+Pb event at 158A GeV took about 6-8 minutes on a Pentium II machine with 233 MHz.

#### Reconstruction Chain

The reconstruction chain of NA49 [68] (Fig. 3.13) is based on DSPACK [72] an object-oriented client-server data-management system. Three different versions of the reconstruction chain, for p+p, p+A (also used for C+C, Si+Si) and Pb+Pb collisions, exist. In the p+p chain the procedure of the determination of the main vertex is different because the liquid hydrogen target for p+p interactions is much thicker than the solid target foils used for p+A and A+A collisions. The Pb+Pb chain is optimized for high track densities in the TPCs, furthermore a phenomenological residual correction for the TPC information is applied for this version of the reconstruction chain.

The reconstruction of the raw data starts with the cluster finder. The corresponding client in the reconstruction chain is called `dipt`. In each pad row of the TPCs this client looks for connected areas where the ADC value of the TPC signal is above the threshold value. For each of these "clusters" the position of the center and the total charge (related to the energy loss  $dE/dx$  of the particle in the detector gas) is determined. The position of the cluster center is stored both in  $x,y,z$  and in pad, pad-row, time-bin coordinates. In a high density area problems can occur when the charge distributions of two particle tracks overlap. Such an overlapping charge distribution is only treated as two clusters if the distance between both maximums is at least three pads or time-bins.

The space points of the cluster finder are corrected for various detector effects like inhomogeneities of the electric and magnetic field,  $E \times B$ - effects and different signal propagation delays (`edisto`, `vt_ncalc`). In the Pb+Pb reconstruction chain a phenomenological residual correction (`tpc_resorb`) is applied.

The track reconstruction starts in the main TPCs (`mtrack`) where the track density is low and the tracks are straight because they are not bent by a magnetic field. Under the assumption that they originate from the main vertex a preliminary momentum is assigned to each track. Track reconstruction in the vertex TPCs is more difficult because the tracks are curved due to the magnetic field and the track density is higher. In order to reconstruct the tracks in the vertex TPCs the following strategy is applied.

- The track parts reconstructed in the main TPCs are extrapolated back to VTPC2, where clusters are searched which would match to the MTPC track (`mpat`). By this procedure a large number of clusters in VTPC2 is assigned to tracks already found in the MTPCs, therefore it is easier to reconstruct the remaining tracks in VTPC2 (`patrec`) which are not assigned to a track in the MTPCs.
- Each reconstructed track in VTPC2 is extrapolated to the MTPC to look for clusters which match to the track (`mpat`).
- All tracks found in VTPC2 and in the MTPCs are extrapolated to VTPC1, where the track density is highest, and clusters matching to the tracks are searched (`mpat`). In the clusters of VTPC1, which are not matched to VTPC2 and MTPC tracks, additional tracks are reconstructed (`patrec`). These are extrapolated to VTPC2 and the MTPCs and matching clusters are searched (`mpat`).



Figure 3.13: NA49 reconstruction chain for Pb+Pb collisions [71].

### 3 The NA49 Experiment

- Afterwards in the MTPCs the reconstruction chain looks for tracks which do not originate from the main vertex.

The local track pieces in the TPCs are combined to global tracks and the momentum of the particles is determined by their curvature in the magnetic field (`r3d`). The position of the main vertex is determined by an extrapolation of the tracks to the target plane (`vtx`). The momenta of the reconstructed tracks are determined again using the fitted position of the main vertex.

For each track the number of potential points in the TPCs, the number of points the track can have according to its geometry, is determined (`ppoints`). During track reconstruction the merging of local tracks in a single TPC to global tracks was not successful for all particle tracks. These split tracks are now combined to global tracks using the information on particle momentum and potential points now available (`reform` for p+p, p+A- chain, `domerge` for Pb+Pb- chain).

Particles with a short life-time like  $\Lambda$ s,  $\Xi$ s and  $\Omega$ s are detected by their decays. The tracks of their decay products do not originate from the main vertex but from the secondary vertex of the particle decay. The  $V^0$  and the  $\Xi$  finder (`v0find`, `v0fit`, `xi_find`) looks for such secondary vertexes.

At the end of the reconstruction the time of flight information (`tofl_client`, `tofr_client`, `tofg_client`) and the dE/dx information is calculated for each track.

#### 3.3.2 Simulation and Analysis Software

The NA49 simulation software can be used for the determination of experimental acceptance, reconstruction efficiencies and other corrections for experimental data. The input of the simulation can either be a model like Venus or UrQMD or a simple particle generator creating tracks according to an input distribution. The simulated particles are tracked through the NA49 experiment by a software package called GEANT [73], incorporating the geometry and magnetic field of NA49 as well as particle decays and interactions with the detector material. The potential points a track can have inside the TPCs according to its geometry are calculated within GEANT.

The GEANT tracks can be translated to detector signals (`mtsim`) and can be used as an input for the NA49 reconstruction chain, either alone or overlaid with a measured collision event ("embedding"). The reconstructed tracks are connected to the corresponding simulated GEANT tracks by the matching procedure.

In this work the simulation chain is used for the determination of the experimental acceptance of the TPCs.

The analysis of this work was done mainly in ROOT [74, 75], an object oriented data analysis framework based on C++.



## 4 Analysis

In this chapter the method for the analysis of the multiplicity fluctuations of central collisions is described in detail and the statistical and systematic errors are discussed.

### 4.1 Event Selection

In order to get a clean sample of events excluding for instance collisions outside the target or event pileup the following event selection criteria are applied to data.

The fit of the interaction point, based on the reconstructed TPC tracks, has to be successful. This might be not the case if two collisions occur in a time too short to distinguish both (event pileup) or in the case of other experimental problems.

The position of the fitted interaction point (fitted vertex) has to be close to the position obtained by extrapolation of the beam particle measured by the beam position detectors to the target foil (BPD vertex) (Fig. 4.1). For the determination of the cut values for the vertex cuts in x, y and z- direction the histograms containing the differences of the BPD- and the fitted vertexes are fitted with Gaussians ( $N(x) = C \cdot \exp\left(-\frac{(x-\langle x \rangle)^2}{2 \cdot \sigma^2}\right)$ ). In every coordinate the event cuts are defined to be  $\pm 4\sigma$  of the Gauss fit around its mean  $\langle x \rangle$ . The cut values for different data-sets are shown in Table 4.1.

The reconstruction of the interaction point was optimized for precision by selecting long and well measured tracks in an iterative procedure. At least 10% of the total tracks have to be used for the reconstruction of the interaction point in order to accept an event.

Beam lead ions which do not interact strongly in the target might produce delta electrons both in the target foil and the detector gas. These electrons increase the occupancy of the TPCs and might therefore reduce the reconstruction efficiency. In order to avoid this effect for Pb+Pb collisions only those events are selected for the analysis in which there are no beam ions passing through the detector within the read-out time of the event (section 4.3.1).

For C+C and Si+Si interactions no direct beam of light ions was available. For the NA49 experiment the carbon and silicon beam is produced by a fragmentation of the primary lead beam on a carbon converter foil (section 3.1.3). For that reason the beam does not only contain C and Si ions but also other ions with the same charge to mass ratio but a different atomic number. The distribution of the beam charge measured by the NA49 beam position detectors is shown in Fig. 4.2. A strict cut on the beam charge is applied for the analysis of multiplicity fluctuations to ensure that only C+C and Si+Si collisions are selected (Table 4.2).

The influence of the different event selection criteria on the scaled variance is discussed along the systematic errors (section 4.4.2).

### 4.2 Selection of Central Collisions

In a simple participant/spectator model the nucleons of the projectile and the target nuclei which interact inelastically in the collision are called the participants. The remaining nucleons

## 4 Analysis

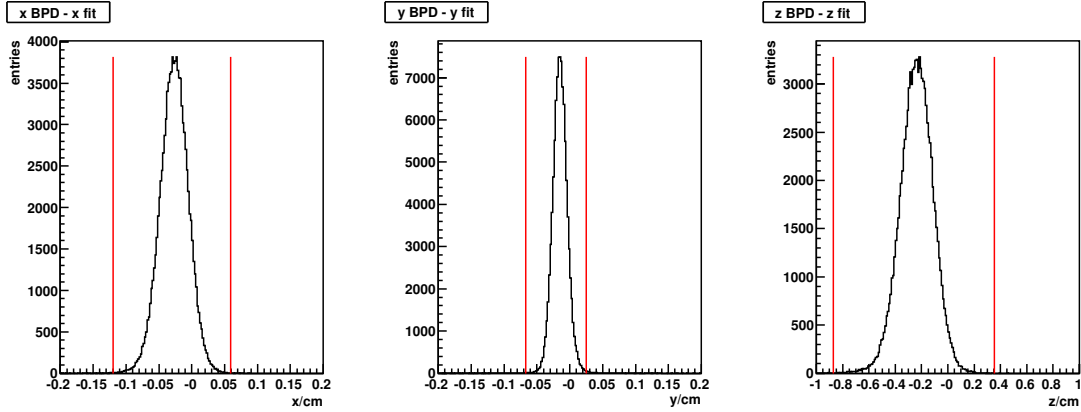


Figure 4.1: x- y- and z- coordinate of the difference of the vertex position determined by the beam position detectors to the one determined by the vertex fit of the produced particles for 80A GeV. The event cuts used for further analysis are indicated by vertical lines.

Dataset	Tag	BPD x- fit x		BPD y- fit y		BPD z- fit z		
		min	max	min	max	min	max	
20A GeV Pb+Pb	03A	-0.1503	0.1233	-0.08998	0.08042	-0.811	0.325	
20A GeV Pb+Pb s.c.	05B	-0.0512	0.1735	-0.0502	0.0861	-0.7399	0.6353	
30A GeV Pb+Pb	02J	-0.086	0.1063	-0.0659	0.0582	-0.605	0.555	
30A GeV Pb+Pb s.c.	05A	-0.0855	0.1103	-0.0493	0.0848	-0.9113	0.3903	
40A GeV Pb+Pb	00C	-0.0758	0.0943	-0.0762	0.0353	-0.5745	0.5289	
40A GeV Pb+Pb	00W	-0.12	0.12	-0.081	0.035	-0.845	0.795	
40A GeV Pb+Pb m.b.	02C	-0.1503	0.1233	-0.08998	0.08042	-0.8453	0.7947	
40A GeV Pb+Pb m.b.	01D	-0.1173	0.1542	-0.1103	0.0711	-0.8491	0.8207	
80A GeV Pb+Pb	01E	-0.1196	0.0588	-0.0667	0.0253	-0.872	0.352	
158A GeV Pb+Pb	00B	-0.1264	0.0344	-0.0685	0.0534	-0.7344	0.5852	
158A GeV Pb+Pb	00O	-0.063	0.092	-0.048	0.067	-0.845	0.795	
158A GeV Pb+Pb m.b.	00M-a	*				-1.742	1.546	
158A GeV Pb+Pb m.b.	00M-b	*				-1.742	1.546	
158A GeV Pb+Pb m.b.	00N-a	*				-1.067	0.877	
158A GeV Pb+Pb m.b.	00N-b	*				-1.067	0.877	
158A GeV Pb+Pb m.b.	01J	-0.117	0.0866	-0.0344	0.0521	-1.8090	-0.2058	
	2nd run period (beginning with run 4078)						-1.0019	0.5543
158A GeV Pb+Pb 256tb	01I	-0.1179	0.0603	-0.0827	-0.0184	-1.122	0.3443	
40A GeV C+C	01F	-0.742*	0.538	-0.309	0.2266	-3.67	2.482	
40A GeV Si+Si	01G	-0.3698*	0.1726	-0.2255	0.2721	-1.508	1.3	
158A GeV C+C	00V-10mm	-0.4046	0.2472	-0.2168	0.0884	-2.409	2.627	
158A GeV C+C	00V-3mm	-0.409	0.259	-2.303	0.076	-1.555	2.684	
158A GeV Si+Si	00X	-0.27505	0.1369	-0.1684	0.0428	-0.9657	1.9177	

\*: No cuts on Vertex x and y position used for determination of centrality for these data sets.

Table 4.1: Event cuts in the difference of the BPD- and the fitted vertex coordinates.

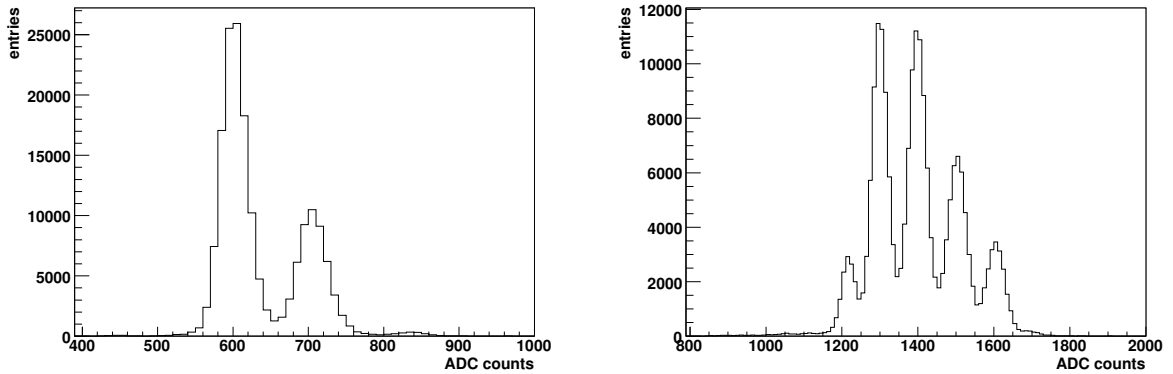


Figure 4.2: Beam charge distribution in ADC counts (100 ADC counts  $\approx$  1 Z) for C+C (left) and Si+Si (right) collisions at 158A GeV.

	C		Si	
	min	max	min	max
standard cuts	570	630	1380	1420
loose cuts	500	650	1350	1450

Table 4.2: Beam-charge cut in ADC counts used for the analysis of C+C and Si+Si collisions at 158A GeV and looser cut used for the study of the influence of beam charge on scaled variance.

are called spectators and they are preserving essentially their initial momenta. In order to minimize fluctuations due to varying collision centrality the number of participants has to be fixed. In the NA49 experiment only the number of projectile spectators, and therefore the number of projectile participants, can be measured. The number of target spectators is unknown.

The projectile spectators consist of free protons and neutrons as well as nuclear clusters of different sizes. In addition to the momentum of the beam, the spectators also have a momentum due to their Fermi-motion in the nucleus. Therefore the spectators do not hit the calorimeter at a fixed point. The distribution of the hit position is broader for the free nucleons than for the nuclear fragments, in the latter the Fermi-momenta of the constituent nucleons compensate each other partially. The charged spectators are deflected by the magnetic field of the NA49 experiment, this is why the protons, neutrons and fragments hit the calorimeter at different positions in x- direction. The collimator positioned in front of the veto calorimeter is adjusted for each collision energy in such a way that the majority of all projectile spectators hit the calorimeter but the amount of produced particles hitting the calorimeter is minimized (section 3.2.4).

The acceptance of the veto calorimeter is a non-trivial function on particle momentum. It is shown for neutral and positive particles at 158A GeV in Fig. 4.3. It was calculated using a map of the NA49 magnetic field (`T49TrkStep`), taking the configuration of the veto collimator, the position of the ring calorimeter and the magnet irons into account as absorbers. Acceptance tables in  $p$ ,  $p_T$  and  $\phi$  can be obtained at [76].

Due to the geometry of the collimator and the magnetic field, a small amount of positive

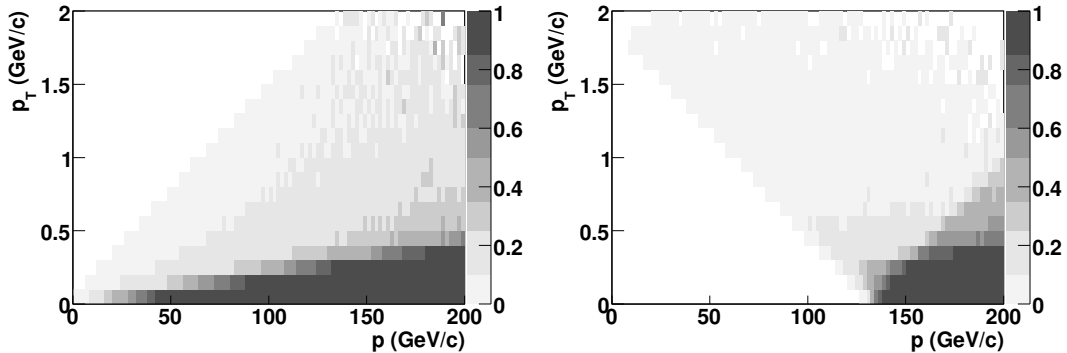


Figure 4.3: Acceptance probability of the Veto calorimeter for neutral (left) and positively charged (right) main vertex particles at 158A GeV as a function of total momentum  $p$  and transverse momentum  $p_T$ .

and neutral non-spectator particles can hit the veto calorimeter. For positive particles, the acceptance of the TPCs and the veto calorimeter overlap partly, a small auto-correlation can not be excluded. The acceptance of the veto calorimeter for negative particles is very small because they are bent by the magnetic field into the opposite direction than the positive ones and the collimator is adjusted to detect positive and neutral projectile spectators.

#### 4.2.1 Event Centrality

Assuming that the energy deposited in the veto calorimeter is the energy of the projectile spectators, the number of projectile participants could in principle be calculated as:

$$N_{Proj}^P = A - (E_{Veto}/E_N), \quad (4.1)$$

where  $E_N$  is the (beam) energy per nucleon and  $E_{Veto}$  is the (calibrated) energy deposited in the veto calorimeter. In this work a different measure of centrality of a collision is used for several reasons. There is a significant systematic uncertainty of  $N_{Proj}^P$  calculated according to Eq. 4.1. This is firstly due to the absolute calibration of the veto calorimeter which turned out to be somewhat model-dependent. Secondly it is due to the fact that not only spectator nucleons are measured in the calorimeter, especially for central collisions a significant amount of produced particles hit the calorimeter. Furthermore a number of nucleons are scattered elastically in the collision and can either hit or miss the calorimeter. It is not obvious if these nucleons should be called participants or spectators.

For these reasons a different measure of centrality which is both independent of the (absolute) calibration of the veto calorimeter and of the origin of the particles hitting the calorimeter is used. The projectile centrality  $C_{Proj}$  of an event with a veto energy  $E_{Veto}$  is defined as the percentage of all inelastic events which are as central or more central as the given event according to the energy deposited in the veto calorimeter. The smaller  $C_{Proj}$ , the more central is the event. In addition to the points mentioned above this measure of centrality has the advantage that the centrality of colliding nuclei of different sizes can be compared directly, for example the 1% most central collisions can be selected both for C+C and Pb+Pb interactions.

The projectile centrality is calculated as:

$$C_{Proj} = \frac{\sigma_{E_{Veto}}}{\sigma_{inel}} = \frac{\int_0^{E_{Veto}} dN/dE'_{Veto} dE'_{Veto}}{\int_0^\infty dN/dE'_{Veto} dE'_{Veto}} = C_{trig} \cdot \frac{\int_0^{E_{Veto}} dN/dE'_{Veto,trig} dE'_{Veto}}{\int_0^\infty dN/dE'_{Veto,trig} dE'_{Veto}}, \quad (4.2)$$

where  $dN/dE'_{Veto}$  is the unbiased veto energy distribution and  $dN/dE'_{Veto,trig}$  is the one for a given trigger (Fig. 4.4, right).

As the on-line event trigger of an experiment accepts not all inelastic collisions, only a part of the veto spectrum is registered. Therefore the trigger centrality of the data set, defined as the fraction of all inelastic events which are accepted by the trigger (section 4.2.2), has to be taken into account.

Note that  $C_{Proj}$  is biased for veto energies where the on-line trigger accepts only a part of the events, which is the case for collisions with a centrality close to the trigger centrality.

### 4.2.2 Trigger Centrality

The centrality of a data-set is defined as the ratio of the trigger cross-section to the total inelastic cross-section of a collision:

$$C_{trig} = \frac{\sigma_{trig}}{\sigma_{inel}}. \quad (4.3)$$

The trigger cross-section can be calculated using the following equation:

$$\sigma_{trig} = R_{trig} \cdot \left( \frac{M}{\rho \cdot d \cdot N_A} \right), \quad (4.4)$$

where  $M$  is the molar mass of the target nuclei,  $d$  the thickness of the target,  $\rho$  its density and  $N_A = 6.0221 \cdot 10^{23} \text{ mol}^{-1}$  the Avogadro constant.

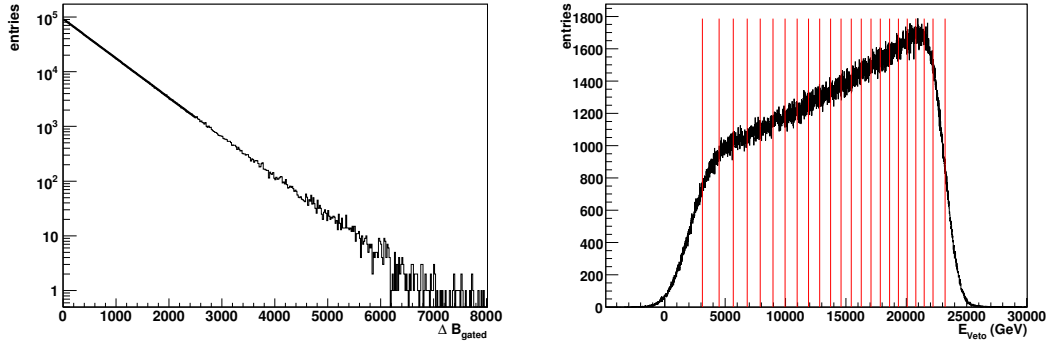


Figure 4.4:  $\Delta B_{gated}$ - distribution for accepted events (left) and veto energy distribution for 158A GeV Pb+Pb collisions (01I). The red lines indicate the borders for the 1% centrality bins.

The trigger rate  $R_{trig}$  is the ratio of "good" triggered events over the number of beam particles on the target.

For every event the number of the corresponding beam particle is stored in the mini-DSTs. Unfortunately this number is sometimes set to zero so it is not possible to use the ratio of

## 4 Analysis

the number of events over the number of beam particles stored in the mini-DSTs directly. For the method used here to calculate the trigger cross-section a histogram with the number of beam particles between two events ( $\Delta B_{gated}$ ) which fulfill the event cuts (Fig. 4.4, left) and a histogram of  $\Delta B_{gated}$  for background events is filled. For the minimum bias data a significant amount of events are background, even if they fulfill all the event cuts. Under the assumption that the z-position of the reconstructed main vertex of the collision of the background is uniformly distributed, the background can be determined by calculating the trigger probability  $p_{\text{target out}}$  in a z-vertex interval away from the target of the same size as the interval around the target. Then the trigger rate of “good” events is:

$$R_{trig} = p_{\text{target in}} - p_{\text{target out}}. \quad (4.5)$$

The probability  $P(\Delta B_{gated})$  to have a specific number of beam particles  $\Delta B_{gated}$  between two events (“good” or background) can be calculated by:

$$\begin{aligned} P(\Delta B_{gated}) &= P(2 \text{ accepted events}) \\ &\quad \cdot P((\Delta B_{gated} - 2) \text{ not accepted events}) \\ &= p^2 \cdot (1 - p)^{\Delta B_{gated} - 2} \\ &= p^2 \cdot \exp((\Delta B_{gated} - 2) \ln(1 - p)) \\ &= p^2 \cdot (1 - p)^{-2} \cdot e^{\Delta B_{gated} \ln(1 - p)} \\ &= A \cdot e^{D \cdot \Delta B_{gated}}. \end{aligned} \quad (4.6)$$

The parameter  $D = \ln(1 - p)$  is obtained by an exponential fit to the  $\Delta B_{gated}$ - distribution. The trigger probability to accept one event is  $p = 1 - e^D$ . Event cuts on the difference of the fitted x and y-vertex position of the main vertex to the position obtained by the beam position detectors (BPD), a cut on the vertex IFlag signalling events where the main vertex reconstruction was successful and a cut on the number of tracks used for the fit of the main vertex over the ones not used for this fit are applied both for the  $\Delta B_{gated}$ - distribution in the target z- vertex range and out of it (section 4.1).

The inelastic cross-section for C+C, Si+Si and Pb+Pb collisions is obtained by geometrical considerations [77].

The results for the trigger centrality obtained by this method for all NA49 heavy ion data sets are shown in Table 4.3.

### 4.2.3 Resolution of the Veto Calorimeter

The resolution of the veto calorimeter has a direct influence on multiplicity fluctuations because it limits the possibility of fixing the number of projectile participants and therefore the centrality of the collisions.

Two effects dominate the resolution of the veto calorimeter: the energy resolution at a fixed impact point and the non-uniformity. The energy resolution can be measured by the width of the signal of the beam in the calorimeter. It is parametrized as [70]:

$$\frac{\Delta E_{Veto}}{E_{Veto}} \approx \frac{2}{\sqrt{E_{Veto}}}. \quad (4.7)$$

This parametrization can not be used directly for the resolution of the calorimeter in heavy ion collisions. The spectator nucleons and fragments hit the calorimeter at different positions in each event, therefore the non-uniformity of the calorimeter has to be taken into account.

## 4.2 Selection of Central Collisions

Dataset	Tag	target thickness [g/cm <sup>2</sup> ]	$\sigma_{inel}[b]$	$C_{trig}[\%]$
20A GeV Pb+Pb	03A	0.224	7.15	7.22841
20A GeV Pb+Pb s.c.	05B	0.907	7.15	32.7136
30A GeV Pb+Pb	02J	0.224	7.15	7.91303
30A GeV Pb+Pb s.c.	05A	0.907	7.15	32.8661
40A GeV Pb+Pb	00C	0.224	7.15	7.36146
40A GeV Pb+Pb	00W	0.224	7.15	7.3491
40A GeV Pb+Pb m.b.	02C	0.224	7.15	60.8948
40A GeV Pb+Pb m.b.	01D	0.224	7.15	61.1158
80A GeV Pb+Pb	01E	0.224	7.15	7.53304
158A GeV Pb+Pb	00B	0.224	7.15	11.0058
158A GeV Pb+Pb	00O	0.224	7.15	11.5912
158A GeV Pb+Pb m.b.	00M-a	0.224	7.15	74.5977
158A GeV Pb+Pb m.b.	00M-b	0.224	7.15	51.3159
158A GeV Pb+Pb m.b.	00N-a	0.224	7.15	77.5382
158A GeV Pb+Pb m.b.	00N-b	0.224	7.15	54.1115
158A GeV Pb+Pb m.b.	01J	0.224	7.15	59.9861
158A GeV Pb+Pb 256tb	01I	0.336	7.15	22.3736
40A GeV C+C	01F	1.84	0.839	51.0489
40A GeV Si+Si	01G	1.169	1.768	19.0039
158A GeV C+C	00V-10mm	1.84	0.856	13.5594
158A GeV C+C	00V-3mm	0.561	0.856	13.8862
158A GeV Si+Si	00X	1.169	1.768	11.586

Table 4.3: Target thickness, inelastic cross-section and trigger centrality for different datasets.

## 4 Analysis

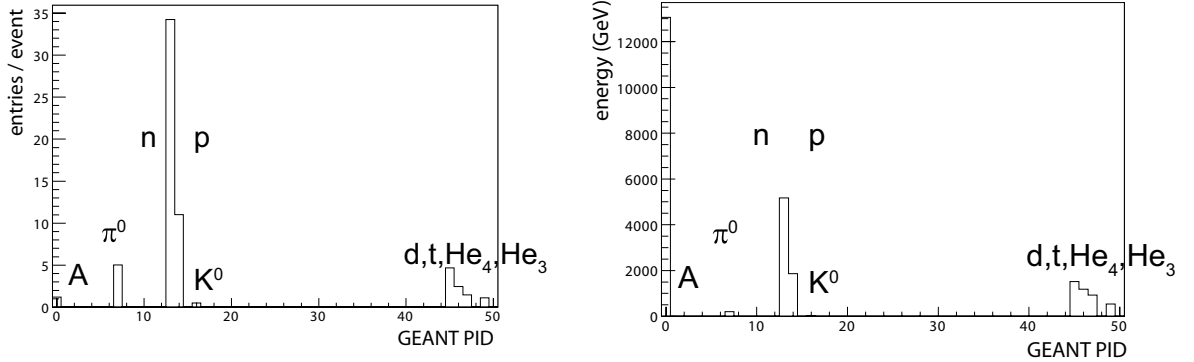


Figure 4.5: Distribution of the number (left) and the energy (right) of different particle species in the veto calorimeter versus their GEANT PID as simulated for minimum bias Pb+Pb collisions at 158A GeV using the SHIELD model [80].

In [78, 79] the veto resolution for heavy ion collisions was estimated using the signals of the different sectors of the calorimeter. It is assumed that the veto energy is the same in the upper half (sectors 1 and 2) and the lower half (sectors 3 and 4) of the calorimeter:

$$E_{Veto} = 2(E_3 + E_4). \quad (4.8)$$

When the sum of the energy in the sectors 3 and 4 is fixed, no strong correlation between the energy in the sectors 1 and 2 is measured. Therefore the resolution of one individual sector of the calorimeter can be estimated by following equation:

$$\sigma_{ind} = \frac{1}{\sqrt{2}}\sigma(E_1 - E_2), \quad (4.9)$$

where  $\sigma(E_1 - E_2)$  is the dispersion of the distribution of the signal difference in sector 1 and 2. The total resolution of the sum of the signals of all sectors is estimated to be

$$\sigma(E_{Veto}) = \sqrt{2}\sigma(E_1 - E_2). \quad (4.10)$$

A parametrization of the resolution obtained by this procedure is [78]:

$$\frac{\sigma(E_{Veto})}{E_{Veto}} \approx \frac{2.85}{\sqrt{E_{Veto}}} + \frac{16}{E_{Veto}}. \quad (4.11)$$

### 4.2.4 SHIELD Simulation for Calorimeter Resolution

In order to check the parametrization of the resolution of the veto calorimeter (Eq. 4.11), a different approach to determine the resolution of the veto calorimeter is followed in this work. The distribution of the projectile spectators is simulated by SHIELD [80]. This model delivers both spectator nucleons and nuclei, in contrast to most string hadronic models, where only free spectator nucleons are included.

For minimum bias collisions most spectators are protons and neutrons (Fig. 4.5) but most of the spectator energy is carried by heavy nuclear fragments ( $A > 2$ ). The contribution of produced particles to the veto energy is small for minimum bias collisions, but is expected



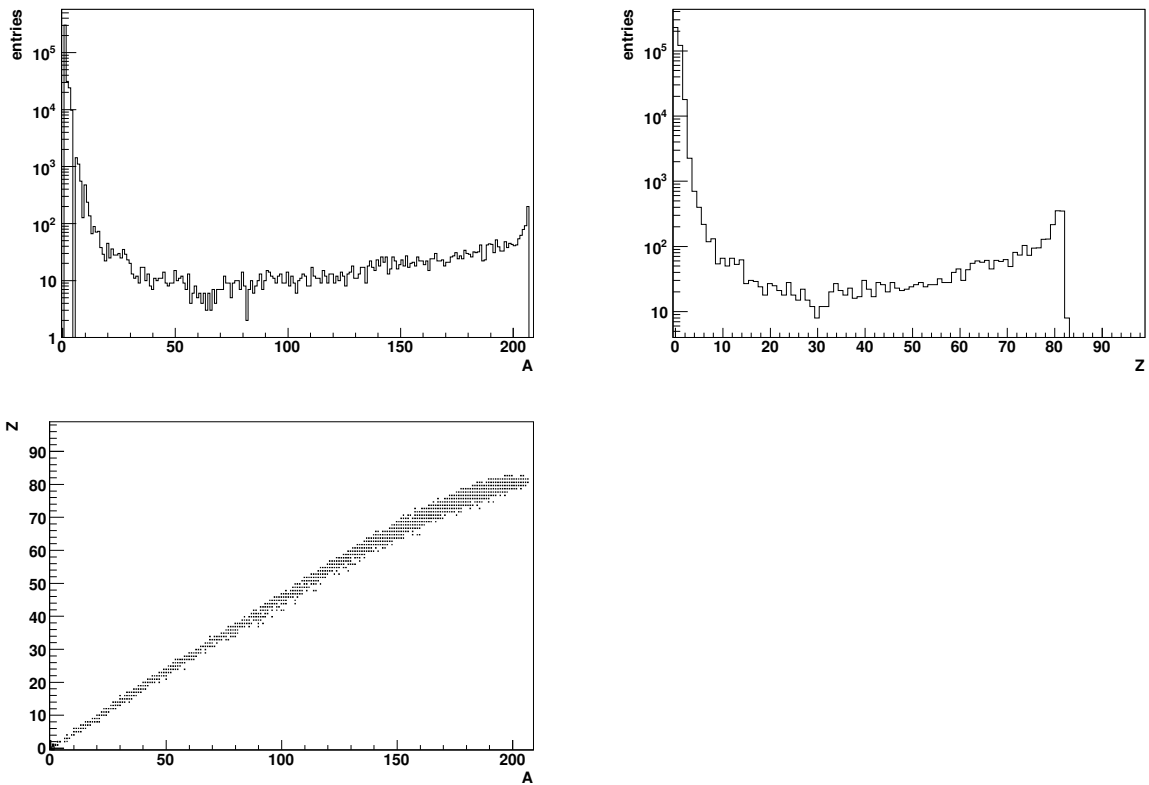


Figure 4.6: Distribution of the atomic number (top left) and the electric charge (top right) of spectator fragments as simulated for minimum bias Pb+Pb collisions at  $158A$  GeV using the SHIELD model. Bottom: correlation of atomic number and charge of spectator fragments.

## 4 Analysis

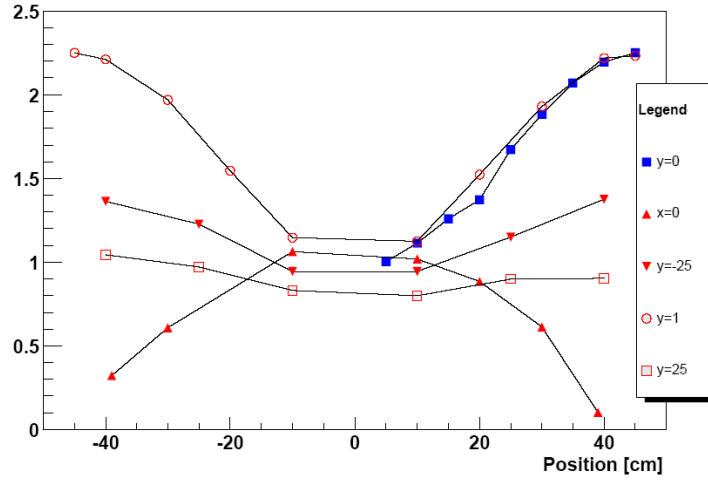


Figure 4.7: Response of the veto calorimeter [81] as a function of the  $x$ - coordinate of the hit position for different  $y$ - coordinates. Solid triangles, spike up indicate veto response as a function of the  $y$ - coordinate for  $x = 0$ .

to be significant for very central collisions. The distribution of the atomic number and the electric charge of the spectator fragments is shown in Fig. 4.6. In the SHIELD model spectator fragments up to Pb are produced. The plot on the correlation of atomic number and charge of spectator fragments shows that no fragments with a  $Z/A$  ratio far away from the one of stable nuclei are produced.

A detailed simulation of the NA49 experiment including the magnetic field (T49TrackStep), the magnet iron, the collimator and the ring calorimeter allow to determine which particle hits the veto calorimeter. Furthermore the point where it hits the calorimeter can be determined.

The non-uniformity of the response of the veto calorimeter was measured and is shown in Fig. 4.7. Unfortunately, no complete measurement of the veto response in two dimensions is available. Thus it is assumed that the dependence on the  $x$ - and the  $y$ -position is independent. For the estimate of the calorimeter resolution both the dependence on the  $x$ - hit position at  $y = 0$  and on the  $y$ - hit position at  $x = 0$  was parametrized with polynomial functions  $X(x)$  and  $Y(y)$ . The veto response for each particle hitting the calorimeter is calculated in the following way:

$$E_{Veto,resp} = X(x)X(y)G(E_{Veto}), \quad (4.12)$$

where  $G(E_{Veto})$  is the energy of the particle smeared by the energy resolution of the calorimeter according to equation 4.10.

The simulated veto energy distribution obtained by the SHIELD model and the corresponding distribution of the veto response is shown in Fig. 4.8. The veto response as a function of the simulated veto energy as is shown in Fig. 4.9, left. It is fitted by a polynomial function and the difference of the veto response to the fitted mean veto response is shown in Fig. 4.9, right. The veto calorimeter resolution is then calculated in different veto energy bins by the spread of the points. The resulting resolution of the calorimeter for 20A and 158A GeV is shown in Fig. 4.10 and confirms parametrization Eq. 4.11 as an upper limit. Therefore it is reasonable to use Eq. 4.11 to estimate the systematic error of  $\omega$  related to the resolution of the veto calorimeter.

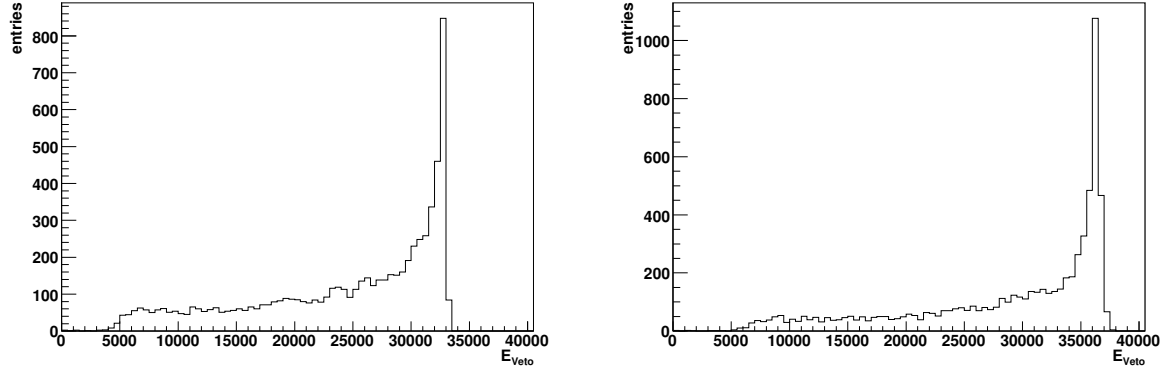


Figure 4.8: Simulated Veto energy distribution for 158A GeV ( $E_{Veto}$ , left) and the distribution obtained including energy resolution and non-uniformity of the veto calorimeter ( $E_{Veto,resp}$ , right).

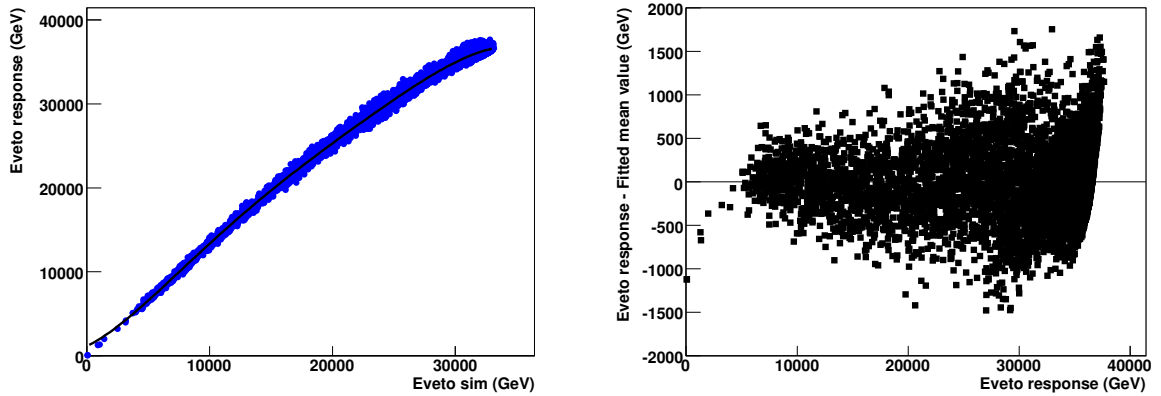


Figure 4.9: Left: Veto response versus simulated Veto energy for 158A GeV. Each point represents one simulated event. The line indicates a polynomial fit to the data. Right: Difference of Veto response to fitted mean veto response versus Veto response.

## 4 Analysis

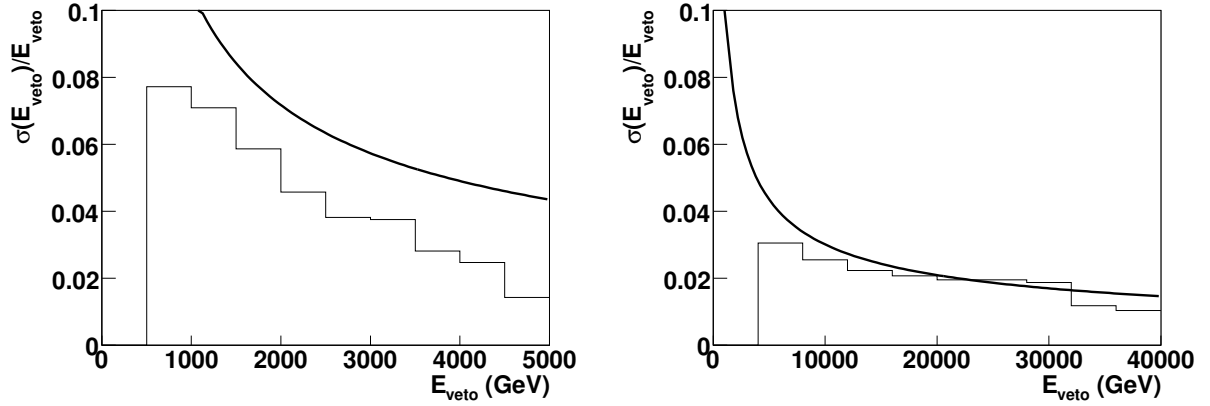


Figure 4.10: Resolution of the veto calorimeter estimated by a SHIELD simulation (histogram) in comparison to the parametrization 4.11 (solid line) for 20A (left) and 158A GeV (right).

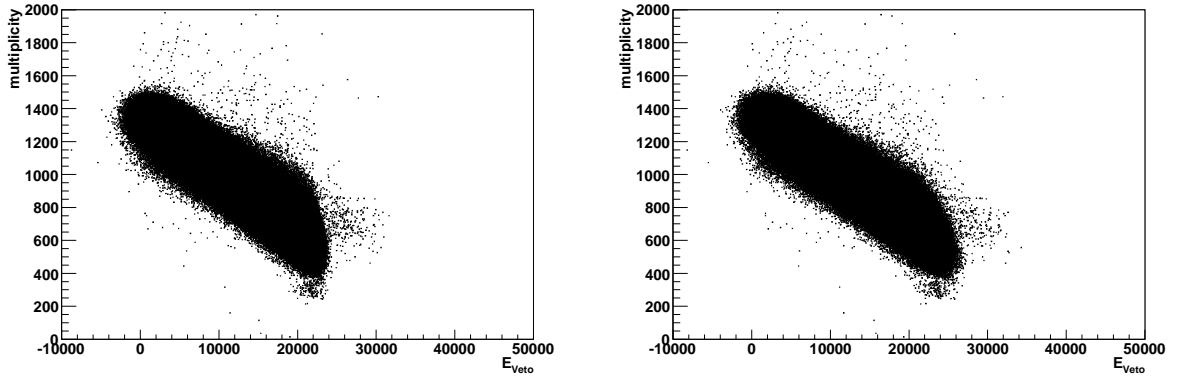


Figure 4.11: Multiplicity versus uncalibrated (left) and calibrated (right) veto energy for 158A GeV Pb+Pb collisions (01I-data-set). The correlation coefficients are  $-0.939$  (uncalibrated) and  $-0.943$  (calibrated).

### 4.2.5 Time Dependent Veto Calibration

Events with a larger veto energy are more peripheral and have on average a smaller multiplicity (Fig. 4.11), hence both observables are strongly anti-correlated. The veto calorimeter response can, in principle, change with time due to various effects like aging and different electronics settings. This may weaken the anti-correlation.

Therefore a time dependent calibration of the veto energy [82] was applied. For this calibration it is assumed that the correlation between the calibrated veto energy and the particle multiplicity is constant for different runs of data taking. In order to achieve this a linear correction is applied to the veto energy:

$$E_{Veto}^{TDcal}(run) = \left( E_{Veto}^{uncal} - \frac{b_{ref} - b_{run}}{a_{run}} \right) \frac{a_{run}}{a_{ref}}, \quad (4.13)$$

where  $a_{run}, b_{run}$  are the correction constants for the corresponding run and  $a_{ref}, b_{ref}$  the

constants of a reference run. For the centrality selection used in this work it is not necessary to calibrate the veto energy on an absolute scale, therefore in the following always the first run of a data set is chosen as a reference run.

The multiplicity versus the uncalibrated and calibrated veto energy is shown in Fig. 4.11. By eye no difference is visible, but the correlation coefficients indicate a stronger anti-correlation between multiplicity and veto energy after calibration. The influence of the time dependent veto calibration on scaled variance is discussed in section 4.4.2.

#### Summary

For the analysis of the energy, system size, rapidity and transverse momentum dependence of multiplicity fluctuations the 1% most central collisions, selected according to the procedure described in section 4.2.1, are taken. The veto energy used for the determination of the centrality is calibrated for time dependence effects. No correction on scaled variance for the finite resolution of the calorimeter is applied, the influence of this effect is estimated to be small and considered as a part of the systematic error.

### 4.3 Track Selection and Acceptance

Since detector effects like track reconstruction efficiency might have a significant influence on multiplicity fluctuations, it is important to select a sample of well defined tracks for the analysis. The following track selection criteria are used and are discussed in this section:

- Number of potential points (the number of points a track can have according to its geometry) in the TPCs:  $> 30$ .
- The ratio of the number of reconstructed points to the number of potential points:  $> 0.5$ .
- Sum of the number of reconstructed points in VTPC-1 and 2:  $> 5$ .
- Sum of the number of reconstructed points in VTPC-2 and MTPC:  $> 5$ .
- The track is extrapolated to the plane of the target foil. This point must be closer than 4 cm in x- and 2 cm in y-direction to the interaction point of the collision.
- In order to exclude electrons from the analysis, a cut on the energy loss ( $dE/dx$ ) in the detector gas was applied. All tracks with an energy loss more than 0.2 minimum ionising units higher than the pion  $dE/dx$  (in the region of the relativistic rise of the Bethe-Bloch formula) are rejected.
- The rapidity interval  $0 < y(\pi) < y_{beam}$  is chosen.

In order to have only well-defined tracks with a good momentum resolution each track is required to have a sufficient number of potential points in the TPCs. Split tracks are tracks where its local tracks in different TPCs were not put together, therefore they might be double-counted. In order to avoid this it is required that more than 50% of the potential points of a track have to be found by the reconstruction chain.

## 4 Analysis

Reconstruction inefficiencies mostly occur for tracks which only have points in the first vertex TPC (VTPC-1). In addition to the high occupancy of the VTPC-1 caused by the high track density, delta electrons caused by beam particles not interacting strongly in the target but passing the detector may additionally blind the detector. The influence of delta electrons is studied in section 4.3.1. Tracks which have reconstructed points only in a main TPC have a bad momentum resolution because their curvature in the magnetic field is not measured directly in a vertex TPC. For these reasons tracks having only points in VTPC-1 or only in the MTPCs are not used for this analysis.

Each track is extrapolated to the plane of the target foil and the distance of that point to the main interaction point is calculated. For a main vertex track this distance is small, depending on momentum resolution. Secondary tracks usually do not point to the main vertex. Therefore a cut applied for this analysis to reduce the contribution of secondary particles in the track sample.

As the fluctuations of produced hadrons should be studied a cut on the energy loss ( $dE/dx$ ) in the detector gas is applied in order to exclude electrons from the analysis. The NA49 acceptance corresponds to the momentum regime of the relativistic rise in the Bethe-Bloch formula for electrons and pions. In order to reduce the electron contribution the energy loss of a pion with the same momentum as the track is calculated. If the energy loss of the track is more than 0.2 minimum ionising units higher than the pion  $dE/dx$  the track is rejected.

For this analysis no particle identification is used, therefore the mass of the particles is not known. In the following it is assumed for the calculation of rapidity that all particles have pion mass. The rapidity is given in the center of mass frame and is denoted as  $y(\pi)$ .

The distributions of the registered tracks after applying the track selection criteria are shown in Fig. 4.12 as a function of rapidity  $y(\pi)$  and transverse momentum  $p_T$ . Acceptance tables in  $y(\pi)$ ,  $p_T$  and  $\phi$  can be obtained from [76]. Only tracks in the rapidity interval starting at midrapidity and ending at beam rapidity are used.

In order to study the multiplicity fluctuations differentially, the rapidity interval  $0 < y(\pi) < y_{beam}$  is divided into two parts, the “midrapidity” ( $0 < y(\pi) < 1$ ) and the “forward” ( $1 < y(\pi) < y_{beam}$ ) region (Fig. 4.13). The fractions of negatively charged pion multiplicity falling into the different rapidity intervals obtained by a simulation are given in Table 4.4 and Fig. 4.14. In both regions a similar number of particles is detected by NA49. In the forward acceptance the particles are mostly passing through both the vertex- and the main- TPCs and are therefore efficiently reconstructed for all collision energies. The midrapidity region suffers from reconstruction inefficiencies at 158A GeV (section 4.4.2). According to the UrQMD model the fluctuations in the number of target participants contribute mostly to the particle number fluctuations in the target hemisphere and the midrapidity region. Their influence on  $\omega$  in the forward region ( $y(\pi) > 1$ ) is expected to be small (section 4.2).

Note that the acceptance used for this analysis is larger than the one used for the preliminary data shown in [83, 84].

### 4.3.1 Delta electrons

In order to avoid secondary interactions, thin target foils are used in the experiment. The probability for an incoming Pb ion to have an inelastic collision with a Pb nuclei in the target foil is only about 1%. Hence the amount of beam particles passing the detector is much larger than the collision rate (Fig. 4.15). These not strongly interacting beam particles can kick off electrons from the hulls of the atoms the beam ion hits, the so-called delta electrons.

### 4.3 Track Selection and Acceptance

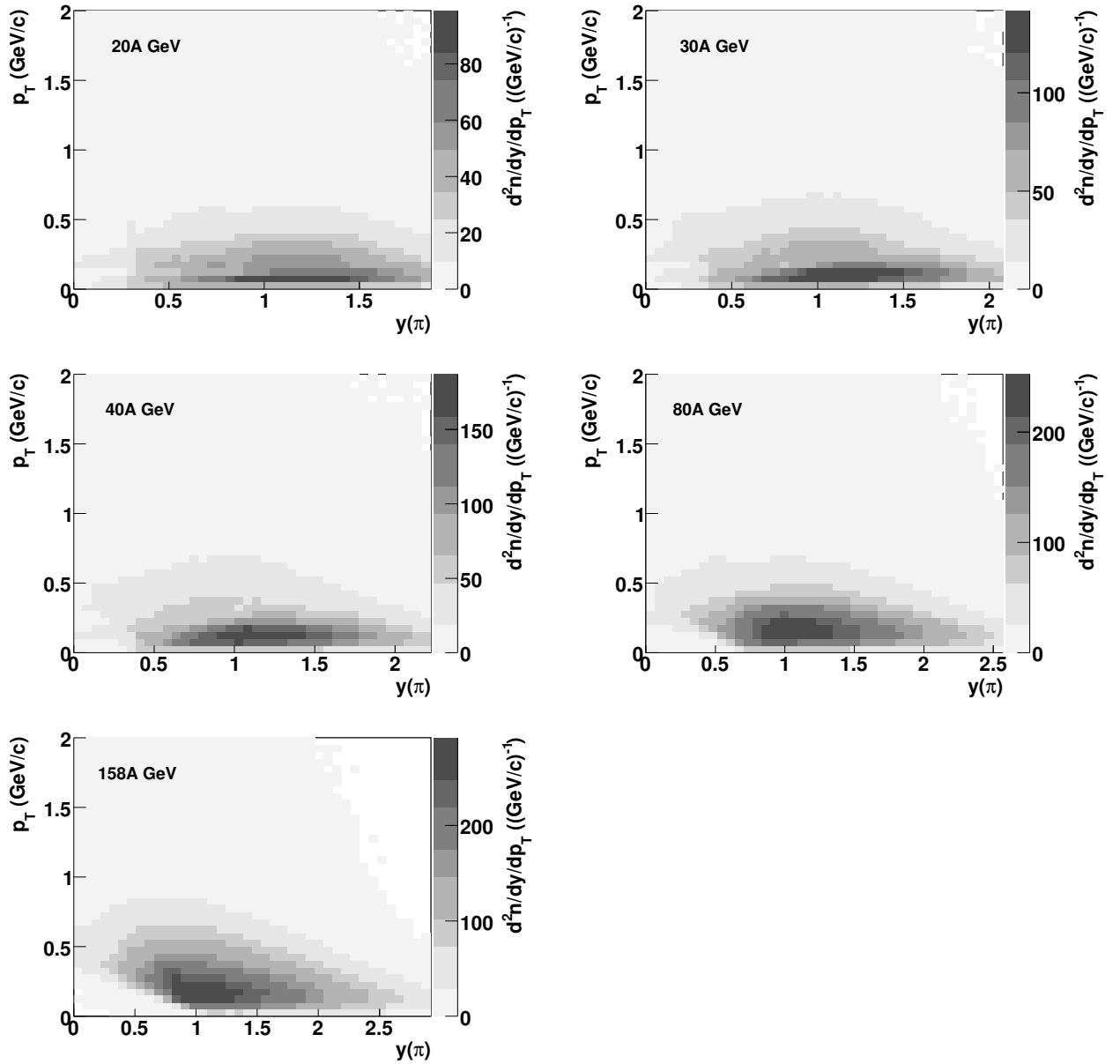


Figure 4.12: Distribution of detected negatively charged particles which fulfill the track selection criteria as a function of  $y(\pi)$ ,  $p_T$  for 20A (top left), 30A, 40A, 80A and 158A GeV (bottom).

## 4 Analysis

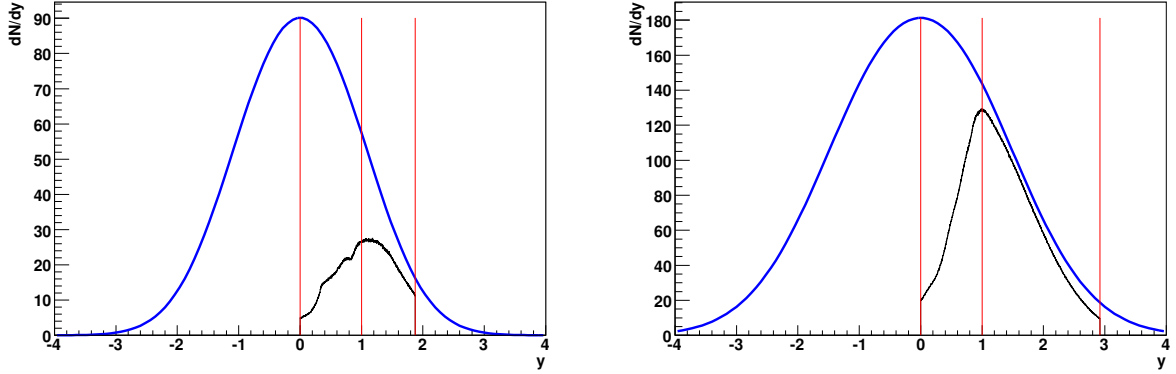


Figure 4.13: Blue line: Double-Gauss parametrization of the inclusive rapidity distribution of negative pions and kaons in Pb+Pb collisions at 20A (left) [33] and 158A GeV (right) [85]. The black line is the measured rapidity distribution with the track selection criteria described in section 4.3. The vertical red lines indicate the borders of the rapidity intervals used for this analysis.

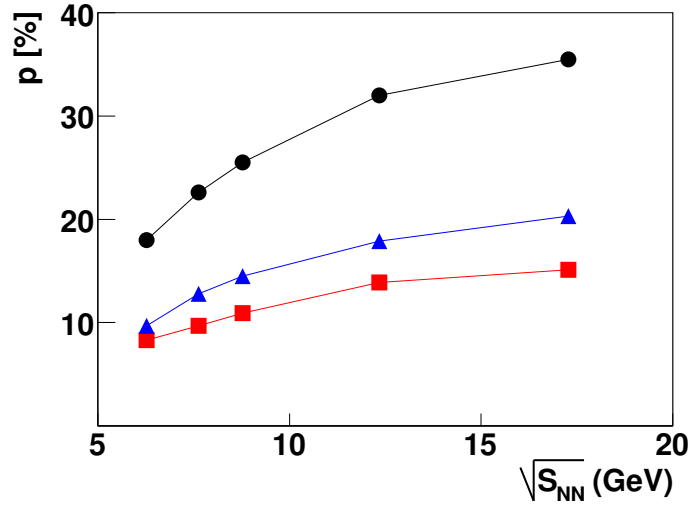


Figure 4.14: Fraction of total mean multiplicity in acceptance. Black circles:  $0 < y(\pi) < y_{beam}$ , red boxes:  $0 < y(\pi) < 1$ , blue triangles:  $1 < y(\pi) < y_{beam}$ .

energy	$0 < y(\pi) < y_{beam}$	$0 < y(\pi) < 1$	$1 < y(\pi) < y_{beam}$	acc. par.	$\sigma(y, \pi^-)$
20	18%	8.3%	9.7%	4 %	1.01
30	22.6%	9.7%	12.8%	6.5 %	1.08
40	25.5%	10.9%	14.5%	8 %	1.1
80	32%	13.9%	17.9%	14 %	1.23
158	35.5%	15.1%	20.3%	16.5 %	1.38

Table 4.4: Acceptance probability for negatively charged main vertex particles in different rapidity intervals in percent. In acc. par. the acceptance in the forward region using a cut on the acceptance parametrization (section 4.3.2) is given. In addition, the width of the pion rapidity distribution is shown.



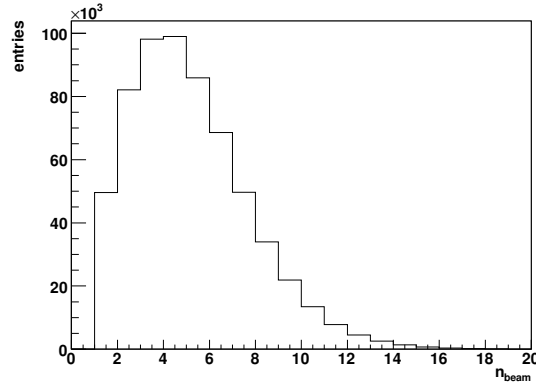


Figure 4.15: Number of beam particles travelling through the detector during TPC readout for Pb+Pb collisions at 158A GeV.

This may happen both in the target foil and in the heavy detector gas (Ne/CO<sub>2</sub>/CH<sub>4</sub>) of the vertex TPCs. These electrons have rather low momentum (in the order of a few MeV in transverse, in the order of 100 MeV in longitudinal direction) and have a spiral trajectory in the magnetic field. Between the main TPCs the beam particles are travelling through a helium bag where the probability to create delta electrons is much smaller. If the delta electrons are created during the read-out of the TPCs, when the trigger registered a collision event, they can influence the measurement.

Even though the delta electrons spiralling in the TPCs are not reconstructed as fake tracks because of their different topology, they deposit an additional charge in the TPCs and therefore increase their occupancy. In high density regions, especially in the VTPC-1 in Pb+Pb collisions at higher energies, these additional tracks can push the TPC occupancy over the limit where an efficient track reconstruction is possible. Especially tracks with only points in the VTPC-1 are expected to be influenced by this effect, tracks which pass in addition other TPCs are reconstructed in the VTPC-1 by an extrapolation of their track pieces in the other TPCs. Consequently they are expected to be less sensitive to high occupancy effects.

As described above  $\omega$  for very central Pb+Pb collisions at 158A GeV in the midrapidity region ( $0 < y(\pi) < 1$ ), where a large number of tracks have only points in VTPC-1, is expected to be biased by delta electrons most. Indeed in this region an increase of  $\omega$  when going from mid-central to central collisions (open red circles in Fig. 4.16, top) is observed whereas in the forward region ( $1 < y(\pi) < y_{beam}$ ), where no tracks have only points in VTPC-1,  $\omega$  monotonically decreases. The occupancy effects related to delta electrons seem to increase the multiplicity fluctuations.

In order to remove the bias in  $\omega$  due to delta electrons, an event sample can be selected where no not strongly interacting beam particles are passing the detector during read-out (n-beam-cut). For these events no significant amount of delta electrons is expected to be produced. Indeed  $\omega$  for central Pb+Pb collisions at midrapidity is much smaller when this event cut is applied (green triangles in Fig. 4.16).

As VTPC-1-only tracks are expected to be biased most by delta electrons and by reconstruction inefficiencies related to high track densities, a track cut can be applied in order to remove these tracks. In addition the tracks with only points in the MTPCs are removed, because of their bad momentum resolution. When applying these track cuts a much smaller

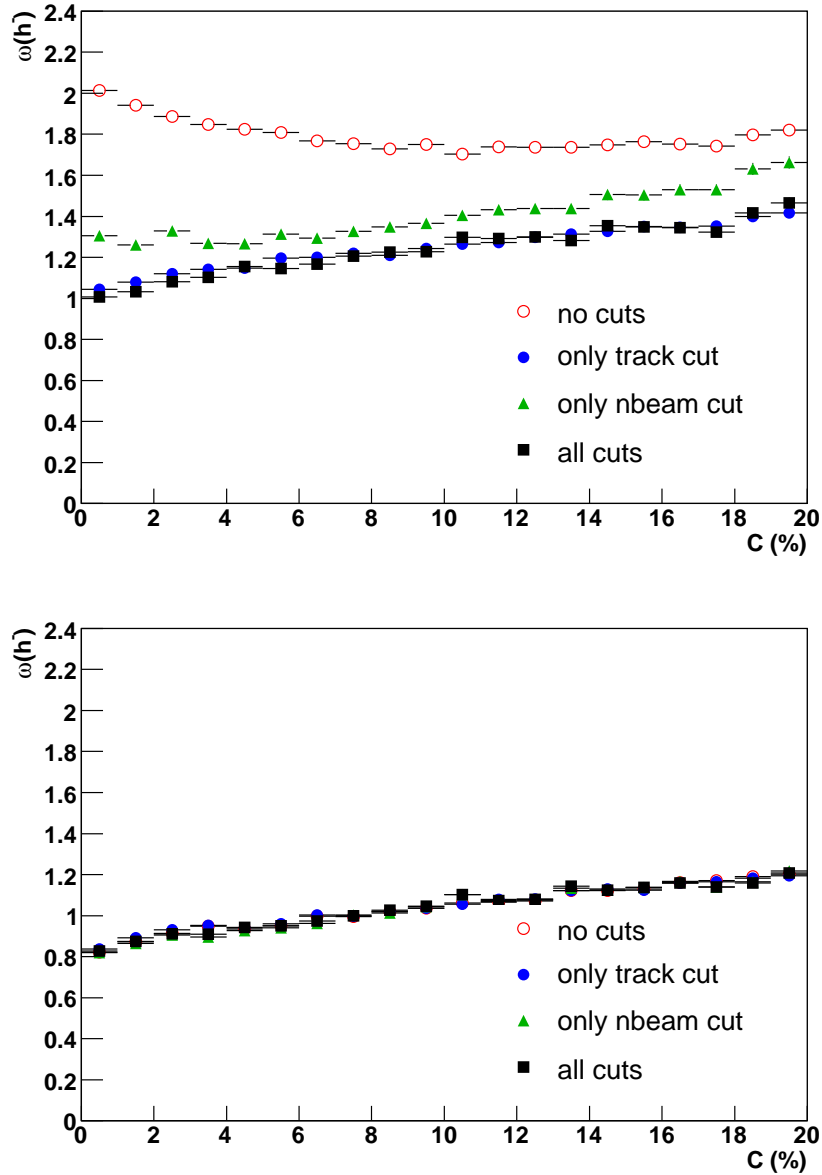


Figure 4.16: Centrality dependence of multiplicity fluctuations of negatively charged particles in Pb+Pb collisions at 158A GeV (01I) in the rapidity intervals  $0 < y(\pi) < 1$  (top) and  $1 < y(\pi) < y_{beam}$  (bottom). The blue solid circles indicate the results when rejecting VTPC-1 and MTPC-only tracks, the green triangles when rejecting events with more than one beam particle passing detector during read-out (n-beam-cut). For the black boxes both cuts are applied, for the open red circles none of these.

$\omega$  is obtained in central Pb+Pb collisions at midrapidity, no significant change is observed at forward rapidity (blue solid circles in Fig. 4.16). Excluding VTPC-1- and MTPC-only-tracks gives an even smaller scaled variance than applying the n-beam-cut and results in a monotonic decrease of  $\omega$  when going to more central collisions in the midrapidity region, similar to the decrease observed at forward rapidity. This suggests remaining reconstruction inefficiencies for VTPC-1-only-tracks at very central Pb+Pb collisions even when no delta electrons are present.

For the final data both the n-beam-cut and the track cut excluding VTPC-1- and MTPC-only-tracks are applied.

### 4.3.2 Cut on Parametrization of the NA49 Acceptance

For the published NA49 data on the centrality and system size dependence of multiplicity fluctuations [78], as well as for the preliminary data on the energy dependence of multiplicity fluctuations [83, 84], an additional cut based on an acceptance parametrization was used. The advantage of this procedure is that the acceptance parametrization can be easily implemented into model calculations. The acceptance parametrization [42] delivers a cut on the maximum transverse momentum, depending on the rapidity and azimuthal angle of the track.

$$p_T^{max}(y, \phi) = \frac{1}{A(y) + \left(\frac{D(y+\phi)}{C(y)}\right)^6} + B(y). \quad (4.14)$$

The corresponding parameters A, B, C, D as a function of rapidity for different collision energies are shown in Table 4.5.

For the preliminary data on the energy dependence of multiplicity fluctuations the rapidity interval  $1 < y(\pi) < y_{beam}$  was used for 20A- 80A GeV, for 158A GeV the same interval as for the data on the centrality dependence of multiplicity fluctuations,  $1.08 < y(\pi) < 2.57$ , was selected.

The acceptance for the track selection described above is shown in Table 4.4. The cut based on an acceptance parametrization strongly reduces the fraction of the tracks which are accepted for the analysis, especially for lower energies. As a smaller acceptance reduces the sensitivity of multiplicity fluctuations for the physics we are interested in, the cut on the acceptance parametrization is not used for the final data on the energy dependence of multiplicity fluctuations presented in this work.

## 4.4 Errors on Scaled Variance

### 4.4.1 Statistical Error

The mean value of a random variable with a known probability  $P_k(n)$  to have the value  $n$  is defined as

$$\langle n \rangle = \sum_n n P_k(n). \quad (4.15)$$

The variance of  $P_k(n)$  is defined as

$$Var(n) = \sum_n (n - \langle n \rangle)^2 P_k(n) = \langle n^2 \rangle - \langle n \rangle^2. \quad (4.16)$$

4 Analysis

$y$	20AGeV				30AGeV				40AGeV				80AGeV				158AGeV			
	A	B	C	D	A	B	C	D	A	B	C	D	A	B	C	D	A	B	C	D
-0.5									0	0	23	4	0	0	35	-10	0	-1	63	-8
-0.3					0	0	25	-7	0	0	30	7	0	0.07	40	-10	0	0	57	-10
-0.1	0	-1	32	-7	0	0	31	-8	0	0	38	10	0	0.07	46	-10	0	0.09	63	-13
0.1	0	0	34	-8	0	0	40	-8	0	0	43	8	0	0.05	52	-12	0	0.08	67	-4
0.3	0	0	41	-8	0	0	44	-8	0	0	46	7	0	0	58	-7	0	0.08	65	-3
0.5	0	-0.05	47	-8	0	0	46	-7	0	0	40	0	0	-1	29	-2	0	0.05	27	0
0.7	0	-0.1	50	-7	0	0	42	0	0	0	22	0	0	0.05	26	0	0	0	35	0
0.9	0	-0.3	53	-3	0	0	35	-10	0	0	34	6	0	0.08	35	0	0	0.1	41	0
1.1	0	-0.2	38	-10	0	0	39	-13	0	0	46	15	0.3	0.1	67	-27	0.34	0.43	109	0
1.3	0	-0.1	42	-12	0	0	44	-14	0	0	52	15	0.3	0.3	75	-15	0.36	0.43	100	0
1.5	0	0	43	-8	0	0	55	-21	0	0.1	58	20	0.3	0.27	85	0	0.55	0.4	100	0
1.7	0	0	51	-18	0	0.08	62	-2	0	0.08	72	0	0.3	0.18	75	0	0.6	0.4	88	0
1.9	0	0	63	-4	0	0.08	67	0	0	0.08	68	0	0.45	0.15	70	0	0.61	0.35	73	0
2.1	0	0	62	0	0	0.05	61	0	0	0.09	60	0	0.5	0.12	50	0	0.73	0.34	55	0
2.3	0	0	57	0	0.6	0.05	57	0	0.5	0.08	50	0	0.75	0.08	50	0	1.7	0.28	60	0
2.5	0.7	0	54	0	0.6	0	46	0	0.6	0.05	40	0	2.2	0.08	50	0	2.8	0.25	60	0
2.7	0.7	0	41	0	1	0	33	0	1.5	0.05	35	0	3.2	0.08	45	0	5	0.2	57	0
2.9	1.5	0	30	0	2.7	0	32	0					4.5	0.08	45	0	7	0.15	60	0
3.1													5.5	0	45	0	7	0.1	70	0

Table 4.5: Values of the parameters A, B, C and D of the acceptance limits, Eq. 4.14, for different energies and rapidities [42]. The dimensions of the parameters are such that the use of the angle in degrees and the rapidity in the center-of mass system results in the  $p_T$  limit in GeV/c.

In a real measurement  $P_k(n)$  is not known because only a finite sample  $x_1, \dots, x_N$  of the underlying probability distribution is known. The unbiased estimate of the mean value is identical to the one for the known probability distribution

$$\langle n \rangle = \frac{1}{N} \sum_i x_i = \sum_n nP(n). \quad (4.17)$$

where  $N$  is the number events of the measured probability distribution  $P(n) = A(n)/N$ , with  $A(n)$  being the number of measurements of the value  $n$  in the sample. For the population variance two different estimates are possible. If the mean value of the distribution is known the population variance can be defined similar to the variance of the probability distribution:

$$s_n^2 = \frac{1}{N} \sum_i (x_i - \langle x \rangle)^2 = \sum_n (n - \langle n \rangle)^2 P(n). \quad (4.18)$$

If the mean value is not known a different estimator for the variance should be used:

$$s^2 = \frac{1}{N-1} \sum_i (x_i - \langle x \rangle)^2 = \frac{N}{N-1} \sum_n (n - \langle n \rangle)^2 P(n). \quad (4.19)$$

For a large number of measurements both estimates of the population variance yield similar results. In the following the first definition of the population variance  $s_n^2$  is used and it is called for simplicity “variance”  $Var(n)$ .

Both the mean and the variance have a statistical error due to the fact that only the probability distribution  $P(n)$  for a finite sample and not the underlying probability distribution  $P_k(n)$  is measured.

The statistical error of the mean value is

$$\delta(\langle n \rangle) = \sqrt{Var(n)/N}. \quad (4.20)$$

The statistical error of the variance of a measured probability distribution is [1]:

$$\delta(Var(n)) = \left[ \frac{1}{N} \left( I_4 - \frac{N-3}{N-1} I_2^2 \right) \right]^{1/2} \underset{N \gg 1}{\approx} \frac{Var(n)}{\sqrt{N}} \sqrt{\frac{I_4}{I_2^2} - 1}, \quad (4.21)$$

where  $I_j = \sum_n P(n)(n - \langle n \rangle)^j$  is the  $j$ -th moment of the probability distribution.

If the variance and the mean value of the multiplicity distribution would be statistically independent, the statistical error of the scaled variance of the multiplicity distribution would be

$$\delta(\omega) = \omega \sqrt{\frac{\delta^2(Var(n))}{Var^2(n)} + \frac{\delta^2(\langle n \rangle)}{\langle n \rangle^2}}. \quad (4.22)$$

If the mean and the variance are determined from the same sample they are correlated. Therefore the error of the scaled variance is [78]:

$$\delta(\omega) = \omega \sqrt{\frac{\delta^2(Var(n))}{Var^2(n)} + \frac{\delta^2(\langle n \rangle)}{\langle n \rangle^2} - \frac{2Cov(\langle n \rangle, Var(n))}{\langle n \rangle Var(n)}}, \quad (4.23)$$

where the covariance is  $Cov(\langle n \rangle, Var(n)) = I_3/N$ . The covariance term is positive for a Poisson distribution because of its tail towards higher multiplicities. For the measured

## 4 Analysis

	$\Delta\omega^+$ (%)	$\Delta\omega^-$ (%)	$\Delta\omega^\pm$ (%)
event selection	1.5	1	1.5
calorimeter resolution	1	0.5	1.5
calorimeter calibration	0.5	1	1
track selection	1.5	1	3
assumed total error	2	2	3
0.5% vs. 1% most central	3	2	5

Table 4.6: Change of  $\omega$  in Pb+Pb collisions for positively, negatively and all charged hadrons when applying a correction or neglecting a cut.

	$\Delta\omega^+$ (%)	$\Delta\omega^-$ (%)	$\Delta\omega^\pm$ (%)
event selection	2	1	3
calorimeter resolution	1	1	2
calorimeter calibration	4	2	6
track selection	3	1	5
beam charge selection	4	2	5
assumed total error	4	4	6

Table 4.7: Change of  $\omega$  in C+C and Si+Si collisions for positively, negatively and all charged hadrons when applying a correction or neglecting a cut.

multiplicity distributions it was found to be also positive, which is related to the finding that the ratio of the multiplicity distribution to a Poisson distribution is approximately symmetric around its mean value (chapter 6).

As a Gaussian error distribution is assumed above, these calculations are not applicable for low mean multiplicities. Therefore, equation 4.23 might give an imaginary value for the statistical error for the scaled variance of the multiplicity distribution in collisions of small systems (p+p) or when only small fractions of the phase space are considered. In the further analysis the covariance term is neglected and the error estimate according to Eq. 4.22, which is the upper limit of the statistical error for a positive covariance term, is used.

### 4.4.2 Systematic Errors

The influence of several effects on the scaled variances of the multiplicity distributions have been studied and are presented in Table 4.6 and Figs. 4.17-4.19 for Pb+Pb collisions and in Table 4.7 and Figs. 4.20-4.22 for C+C and Si+Si collisions.

The event selection criteria, described in section 4.1, may change the scaled variance compared to the value obtained when not applying these cuts.

The finite resolution of the calorimeter should increase the measured multiplicity fluctuations because of fluctuations in the centrality of the collision. In a superposition model the effect of the calorimeter resolution is estimated [78] to be:

$$\delta = \frac{\langle N \rangle \cdot Var(E_{Veto})}{(E_{beam} \cdot N_P^{Proj})^2}, \quad (4.24)$$

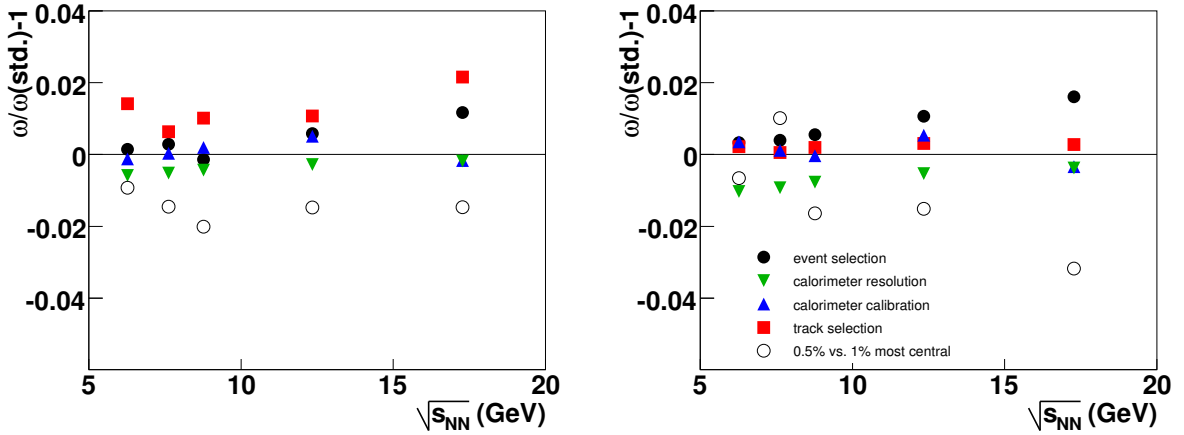


Figure 4.17: Systematic errors and difference between the 0.5% and the 1% most central collisions of the scaled variance  $\omega$  of the multiplicity distribution for positively charged hadrons at midrapidity ( $0 < y(\pi) < 1$ , left) and forward acceptance ( $1 < y(\pi) < y_{beam}$ , right) in Pb+Pb collisions as a function of collision energy.

assuming that only spectators are registered in the veto calorimeter. The parametrization Eq. 4.11, which serves as an upper limit of the resolution of the calorimeter, was used to determine the potential influence of the resolution on the scaled variance. For very central collisions selected for this analysis the measured scaled variance is found to be only slightly ( $< 2\%$ ) increased by the finite calorimeter resolution. In addition, a possible correction depends on some assumptions, therefore it is not applied for this data and the size of the correction is included into the systematic error. In order to take possible aging effects of the calorimeter (section 4.2) into account, a time dependent calibration is applied to the measured veto energy. The effect of this calibration is small for Pb+Pb collisions ( $< 1\%$ ), but larger for C+C and Si+Si collisions (Table 4.7). Track selection criteria are applied to remove electrons and tracks not originating from the main interaction point. The change in scaled variance is small ( $< 3\%$ ) for positively and negatively charged hadrons, but slightly larger ( $< 5\%$ ) for all charged hadrons, probably because of resonance decays.

For C+C and Si+Si collisions no direct beam of C or Si was available but the beam ions were obtained by a fragmentation of a Pb beam (section 3.1.3). Due to the magnet configuration in the beam line all fragments with  $Z/A = 1/2$  reach the target. The C or Si ions are selected using the signal strength of the ions in the beam position detectors and in a Cerenkov detector, both an on-line cut on the signal strength during data taking and a (stricter) off-line cut during analysis was applied to select only C or Si ions. Due to the finite resolution of the beam-charge determination it is not excluded that a very small number of selected beam particles are not C or Si. In order to study the possible systematic error related to this effect the scaled variance was determined with a looser beam-charge cut and compared to the results for the stricter cut. The systematic errors of the scaled variance for C+C and Si+Si interactions are shown in Figs. 4.20-4.22. Beside the error related to the beam-charge cut the same possible error sources as for Pb+Pb are studied.

The total systematic error is estimated as the maximum of the effects of the cuts and corrections described above. In Pb+Pb collisions it is 2% for positively and negatively charged

#### 4 Analysis

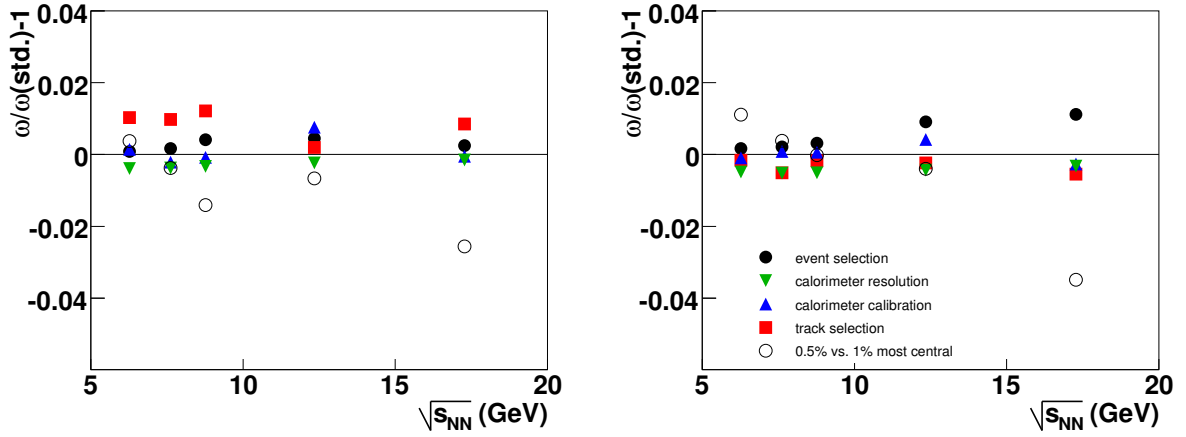


Figure 4.18: Systematic errors and difference between the 0.5% and the 1% most central collisions of the scaled variance  $\omega$  of the multiplicity distribution for negatively charged hadrons at midrapidity ( $0 < y(\pi) < 1$ , left) and forward acceptance ( $1 < y(\pi) < y_{beam}$ , right) in Pb+Pb collisions as a function of collision energy.

hadrons and 3% for all charged hadrons. For C+C and Si+Si interactions it is estimated to be 4% for  $\omega(h^+)$  and  $\omega(h^-)$  and 6% for  $\omega(h^\pm)$ .

In order to estimate the effect of centrality selection, the 0.5% most central collisions are selected. The scaled variance in Pb+Pb collisions for this more restrictive selection is up to 5% different from the scaled variance obtained for the 1% most central collisions. For C+C and Si+Si interactions the available statistics is not sufficient for such a study. As the centrality selection is a well-defined procedure and can be repeated in model calculations, the difference of the 0.5% and 1% most central collisions is not considered as a part of the systematic error.

For Pb+Pb collisions in the midrapidity region at top SPS energy (158A GeV) the track density in the detector is the highest and it cannot be excluded that a significant number of tracks can not be reconstructed, especially in events with high multiplicity. Indeed the ratio of the measured multiplicity distribution of negatively charged particles to a Poisson one shows an asymmetry which might be related to these detector effects (Fig. 4.23, bottom). This asymmetry is much weaker for lower energies (Fig. 4.23, top for 80A GeV) where the track density is smaller. In order to quantify this effect it is assumed that the unbiased multiplicity distribution is symmetric with respect to a Poisson distribution with the same mean multiplicity. The scaled variance of the multiplicity distribution was determined after a symmetrization of the ratio to the Poisson distribution around the mean multiplicity by reflecting the values below the mean with respect to the mean value. This procedure was applied for positively, negatively and all charged particles in the full experimental and the midrapidity acceptance separately. The  $\omega$  obtained by the symmetrization is up to 5% higher than the one for the measured multiplicity distribution. This value is taken as an estimate of the upper limit of the systematic error of  $\omega$  related to detector inefficiencies for the midrapidity and full experimental acceptance region for Pb+Pb collisions at 158A GeV. It is added to the systematic error of the other sources yielding a total systematic error of 7% for  $\omega(h^+)$  and  $\omega(h^-)$  and 8% for  $\omega(h^\pm)$ .



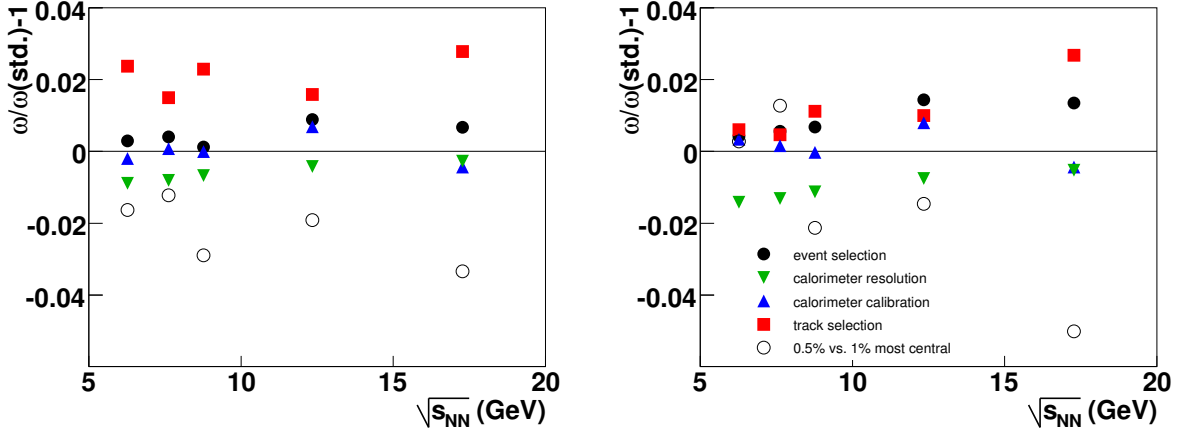


Figure 4.19: Systematic errors and difference between the 0.5% and the 1% most central collisions of the scaled variance  $\omega$  of the multiplicity distribution for all charged hadrons at midrapidity ( $0 < y(\pi) < 1$ , left) and forward acceptance ( $1 < y(\pi) < y_{beam}$ , right) in Pb+Pb collisions as a function of collision energy.

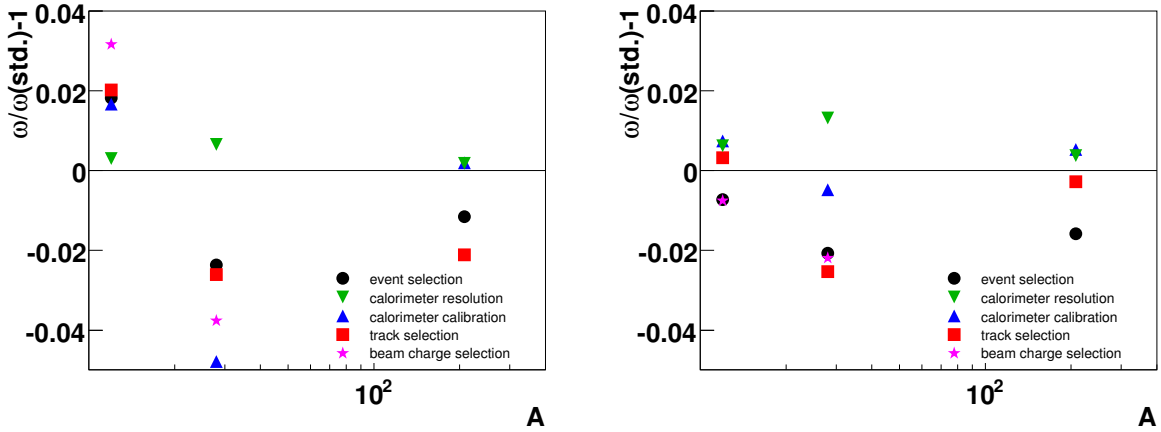


Figure 4.20: Systematic errors of the scaled variance  $\omega$  of the multiplicity distribution for positively charged hadrons at midrapidity ( $0 < y(\pi) < 1$ , left) and forward acceptance ( $1 < y(\pi) < y_{beam}$ , right) at 158A GeV as a function of the size of the colliding system.

4 Analysis

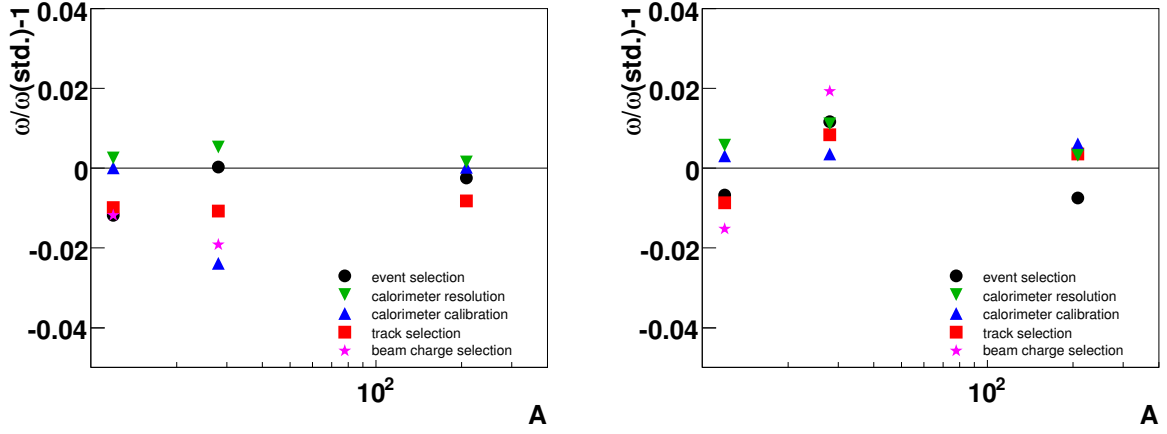


Figure 4.21: Systematic errors of the scaled variance  $\omega$  of the multiplicity distribution for negatively charged hadrons at midrapidity ( $0 < y(\pi) < 1$ , left) and forward acceptance ( $1 < y(\pi) < y_{beam}$ , right) at 158A GeV as a function of the size of the colliding system.

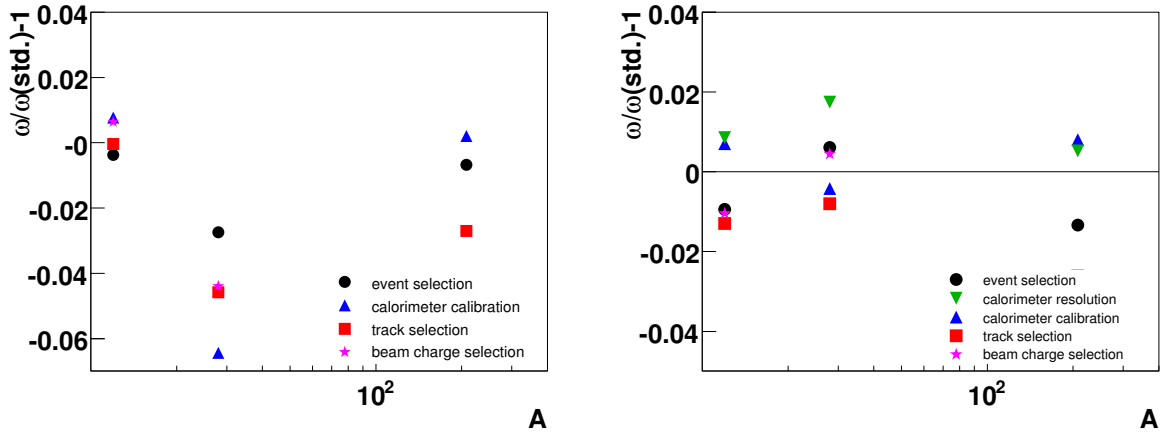


Figure 4.22: Systematic errors of the scaled variance  $\omega$  of the multiplicity distribution for all charged hadrons at midrapidity ( $0 < y(\pi) < 1$ , left) and forward acceptance ( $1 < y(\pi) < y_{beam}$ , right) at 158A GeV as a function of the size of the colliding system.

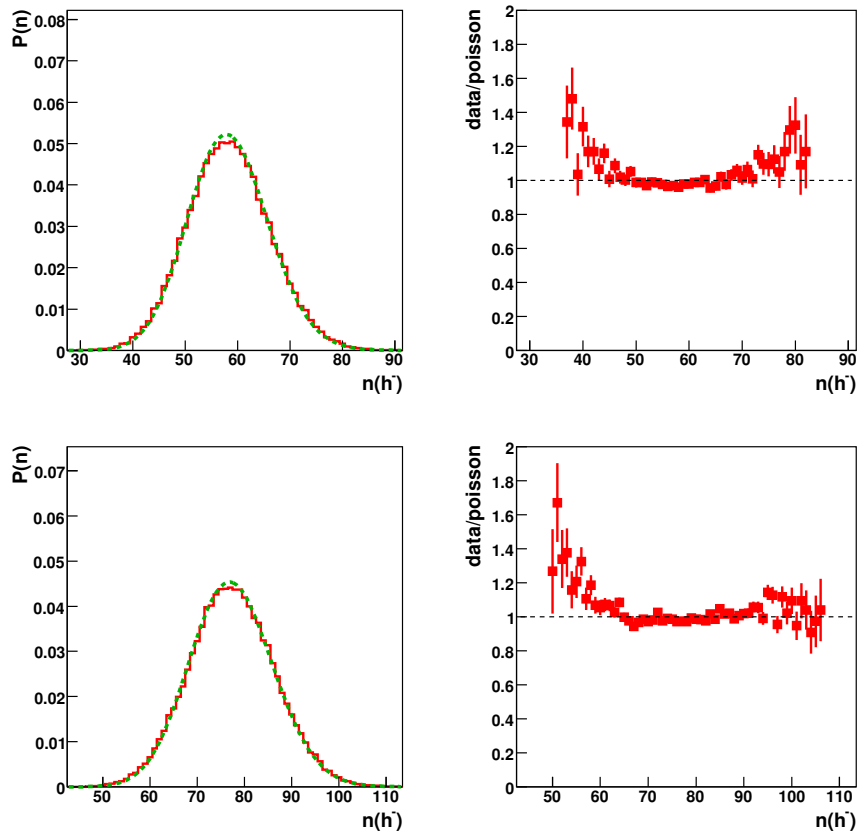


Figure 4.23: Left: multiplicity distributions of negatively charged hadrons in midrapidity acceptance in the 1% most central Pb+Pb collisions at 80A (top) and 158A GeV (bottom). In order to get more statistics the requirement of no other beam ions passing the detector during read-out was not applied. The dashed lines indicate Poisson distributions with the same mean multiplicity as in data. Right: the ratio of the measured multiplicity distribution to the corresponding Poisson one.

## 4 Analysis

# 5 Centrality Dependence of Multiplicity Fluctuations

## 5.1 Published NA49 Results

The centrality dependence of the scaled variance for positively, negatively and all charged hadrons for Pb+Pb collisions at 158A GeV is shown in Fig. 5.1 [78, 84]. The scaled variance increases with decreasing centrality of the collision. For very peripheral collisions there is a hint that it decreases again, but the systematic errors are large in this region.

This analysis was done for particles in the forward hemisphere in the acceptance described in section 4.3.2. As the finite resolution of the veto calorimeter and the finite widths of the veto bins might increase artificially the multiplicity fluctuations, a correction for these effects is applied. In a superposition model (section 2.1.2) the increase of the scaled variance in the forward hemisphere created by the fluctuations in the number of projectile participants can be estimated by Eq. 4.24. The correction is larger for more peripheral collisions, for very central collisions it can be neglected. Note that this correction formula assumes a transparency scenario where the fluctuations in the forward hemisphere are only influenced by the fluctuations in the number of projectile participants.

The data is compared to predictions of various string hadronic models (UrQMD, HSD, HIJING, Venus) for  $Pb + Pb$  collisions; they all predict, in contradiction to data, a flat centrality dependence.

Scaled variance behaves similar in  $p + p$ ,  $C + C$ ,  $Si + Si$  and  $Pb + Pb$  collisions if plotted against centrality defined as  $N_P^{proj}/A$ , where  $A$  is the number of nucleons in nuclei (Fig. 5.2). This is a hint that not the size of the collision system is the correct scaling parameter for the observed increase of  $\omega$  but the fraction of the colliding nucleons in the projectile nuclei. In [54] it is suggested that target participants contribute to particle production in the projectile hemisphere and their fluctuations therefore result in an increase of multiplicity fluctuations. The data as shown in Fig. 5.3 is in approximate agreement with a model which includes this effect (mixing model). Inter-particle correlations [86] and percolation models [87] provide alternative explanations of the results.

## 5.2 Cross-Check of Results on Centrality Dependence

As a starting point of this thesis and as a preparation for the publication of the experimental data on the centrality and system size dependence of multiplicity fluctuations [78], the results obtained by M. Rybczynski [79] were checked. For both analyses the same track selection criteria and acceptance cuts (section 4.3.2) are used, but a different method of centrality determination. While in this thesis the centrality of a collision is determined (section 4.2) and is translated into the number of projectile participants by a HSD simulation, in [79] the number of projectile participants is determined directly by the energy deposited into the veto calorimeter.

5 Centrality Dependence of Multiplicity Fluctuations

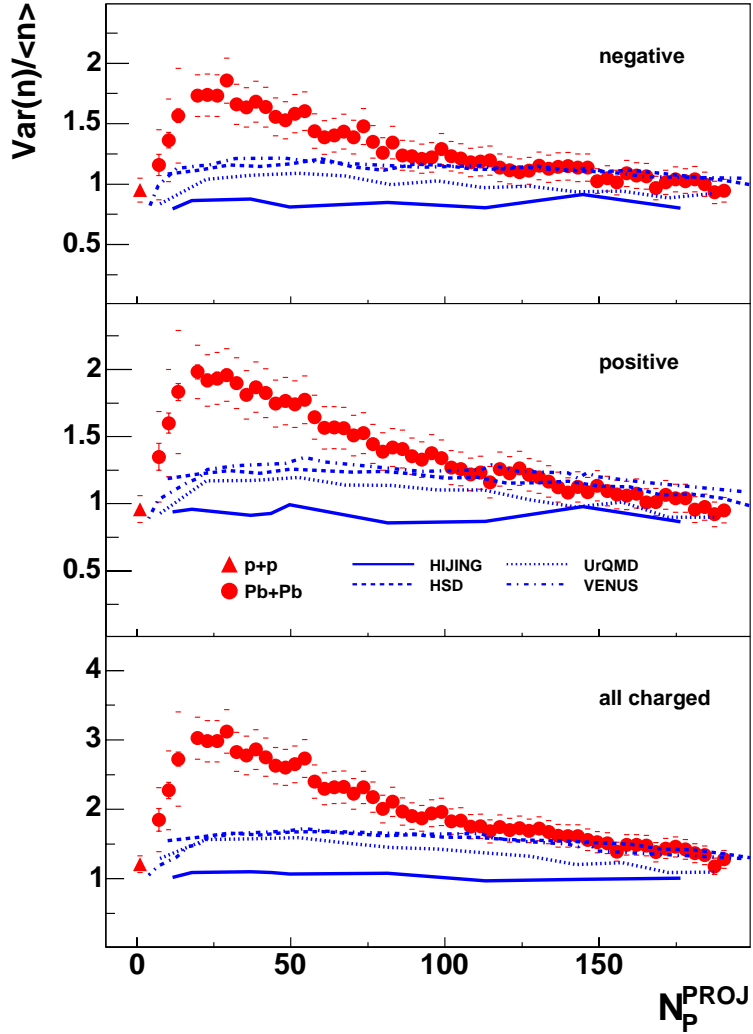


Figure 5.1: The scaled variance of the multiplicity distribution for negatively (upper panel), positively (middle panel) and all (bottom panel) charged particles as a function of the number of projectile participants [78] compared with model simulations in the NA49 acceptance (HSD and UrQMD predictions were taken from [53]). The horizontal bars show the systematic uncertainties, the statistical errors are smaller than the symbols.

## 5.2 Cross-Check of Results on Centrality Dependence

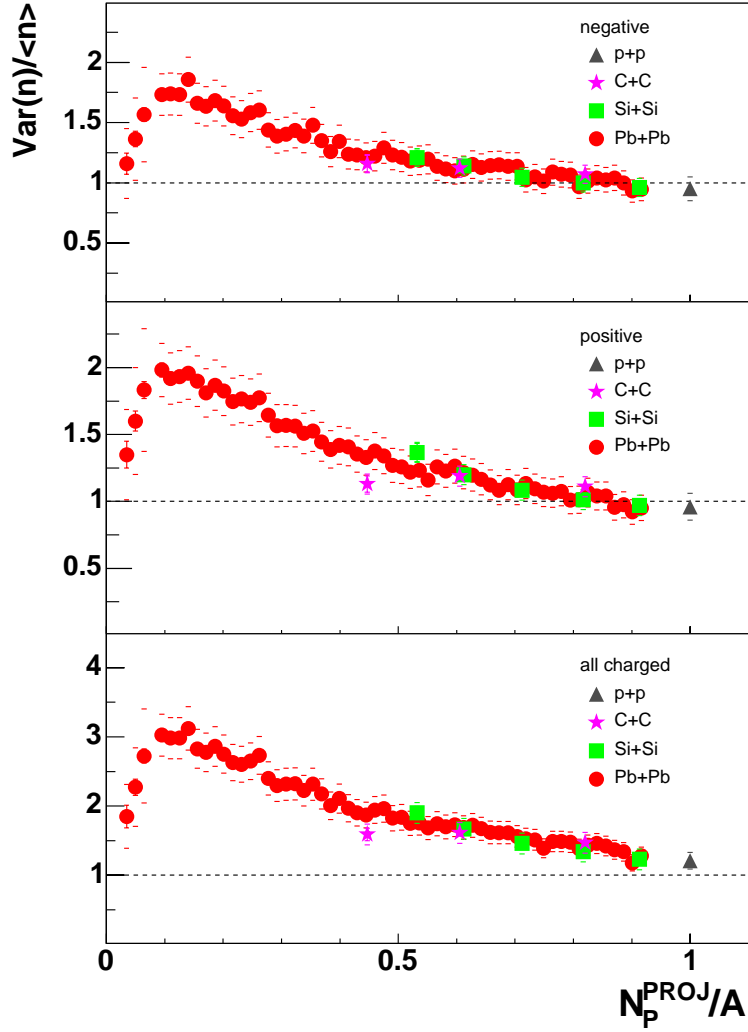


Figure 5.2: The scaled variance of the multiplicity distribution of negatively (upper panel), positively (middle panel) and all (bottom panel) charged particles produced in p+p, semi-central C+C, semi-central Si+Si and Pb+Pb collisions as a function of the fraction of nucleons which participate in the collision [78]. The horizontal bars show the systematic uncertainties, the statistical errors are, except the most peripheral C+C and Si+Si points, smaller than the symbols.

## 5 Centrality Dependence of Multiplicity Fluctuations

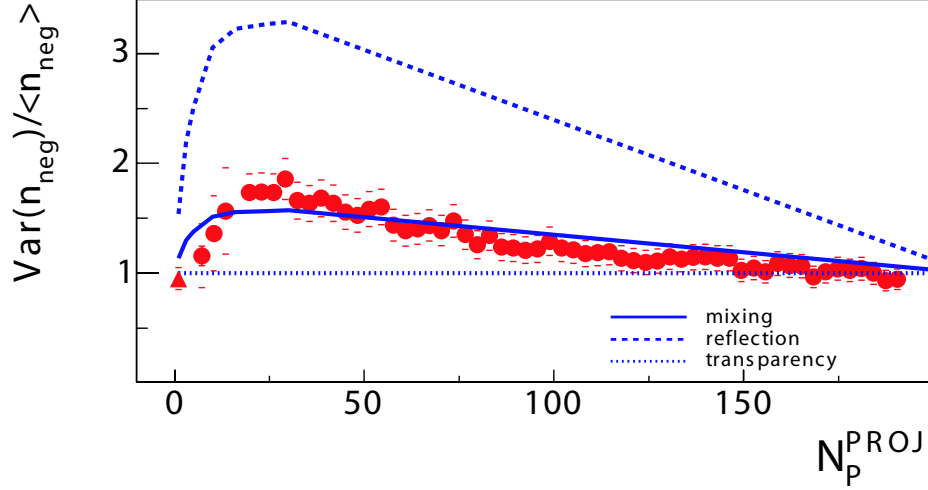


Figure 5.3: Scaled variance of  $h^-$  in comparison to model calculations for transparency, mixing and reflection of matter in the early stage [54].

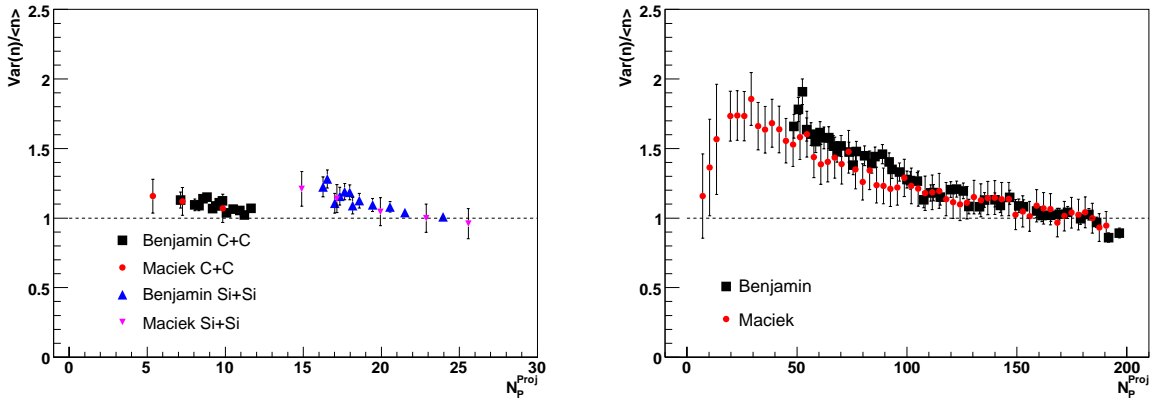


Figure 5.4: Comparison of the centrality dependence of the scaled variance obtained by M. Rybczynski [79] and B. Lungwitz for C+C, Si+Si (left) and Pb+Pb (right) collisions.



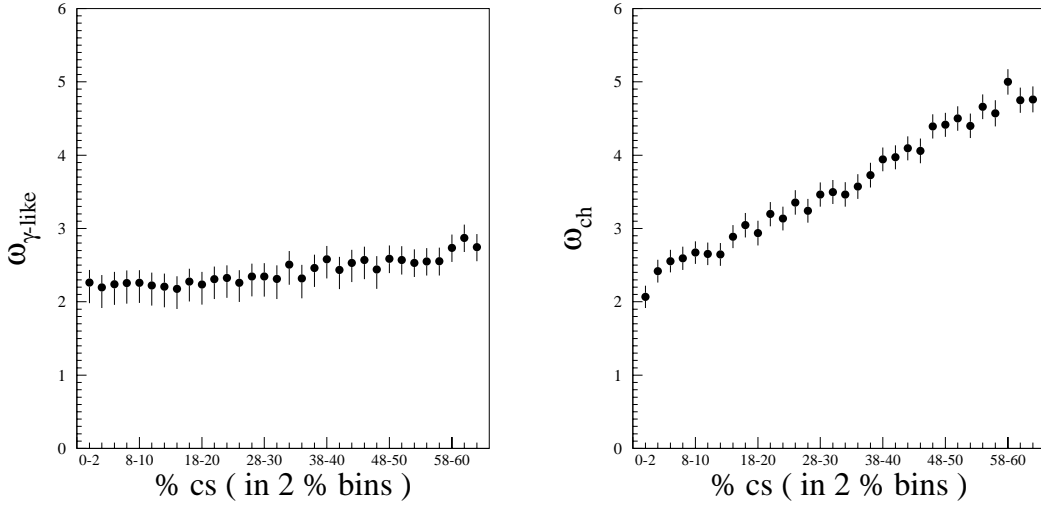


Figure 5.5: Scaled variance of photons (left) and all charged particles (right) as a function of collision centrality measured by the WA98 experiment [88].

As shown in Fig. 5.4 the scaled variances obtained in both analyses are in agreement.

### 5.3 WA98 Results

The WA98 experiment at the CERN SPS was designed to detect both photons and charged particles in heavy ion collisions.

The charged particle multiplicity was measured by the circular Silicon Pad Multiplicity Detector (SPMD) covering the pseudo-rapidity region in the laboratory frame of  $2.35 \leq \eta \leq 3.75$ . For massless particles the pseudo-rapidity is equal to the rapidity (appendix C.2.3), for pions in the energy range studied by the SPS experiments the equality of both is an approximation. The center of mass rapidity of the top SPS energy is 2.92, therefore the pseudo-rapidity interval of the charged particle acceptance is located around midrapidity. The photon multiplicity was measured using the pre-shower photon multiplicity detector (PMD) covering the pseudo-rapidity range of  $2.9 \leq \eta \leq 4.2$  located in the forward hemisphere. For measuring centrality the transverse energy measured by the MIRAC calorimeter covering the range  $3.5 \leq \eta \leq 5.5$  was used.

The scaled variance measured by the WA98 experiment is shown in Fig. 5.5. A strong increase of scaled variance for decreasing centrality of the collision is observed for the charged particles measured at midrapidity, for photons measured at forward rapidity the increase is much weaker. This behaviour is qualitatively similar to the one observed by NA49, a quantitative comparison is not possible in a model independent way because of the different acceptance and centrality selection.

### 5.4 PHENIX Results

The PHENIX experiment [89] at the RHIC in Brookhaven, USA, measured the centrality dependence of multiplicity fluctuations of Au+Au collisions at  $\sqrt{s_{NN}} = 62.4$  and 200 GeV

## 5 Centrality Dependence of Multiplicity Fluctuations

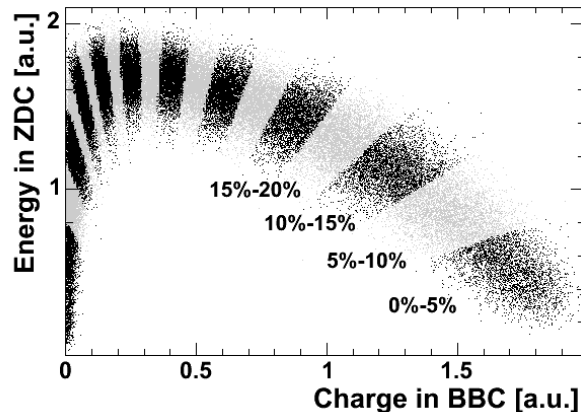


Figure 5.6: Distribution of the ZDC versus the BBC signal for centrality determination in the PHENIX experiment [91].

and of Cu+Cu collisions at  $\sqrt{s_{NN}} = 62$  GeV [90]. For the analysis particles in the central detector arms, covering the pseudo-rapidity interval  $|\eta| < 0.35$  around midrapidity and  $180^\circ$  in azimuthal angle, are used.

For the determination of centrality both the multiplicity of produced particles in the Beam-Beam-Counters (BBCs) and the energy of the spectator neutrons measured in the Zero-Degree-Calorimeters (ZDCs) are used. The BBCs cover the full azimuthal angle in the pseudo-rapidity interval  $3.0 < |\eta| < 3.9$ . The ZDCs cover  $|\eta| > 6$  and measure the energy of neutron spectators with an accuracy of 20%. Events are considered as more central when the multiplicity in the BBCs is larger and the energy in the ZDCs is smaller. For the determination of centrality the response of the sum of both BBCs versus the response of the sum of both ZDCs is used (Fig. 5.6).

It has to be mentioned that this method of centrality determination is not independent on the multiplicity of produced particles. Global fluctuations in multiplicity can not be observed correctly with this method of centrality selection because events with a higher multiplicity in the BBCs are considered to be more central, even though the number of participants might be the same.

The ZDCs measure the energy of neutron spectators. For central collisions most of the spectators are protons and neutrons, therefore the number of spectator neutrons is expected to be a reasonable measure of centrality. For peripheral collisions most of the spectators are nuclear clusters (Figs. 4.5 and 4.6) which are not detected by the ZDCs.

In the present analysis of the PHENIX data the total number of participants is used. Especially for peripheral interactions collisions with the same number of total participants can look very different. They can either be symmetric or one nuclei can have a much larger number of participants than the other one (a similar effect is discussed in section 2.1.2 and Fig. 2.1). According to this asymmetry effect, the shape of the rapidity distributions can differ event-by-event, and therefore also the amount of particles detected by the PHENIX central arm in the (small) rapidity interval around midrapidity.

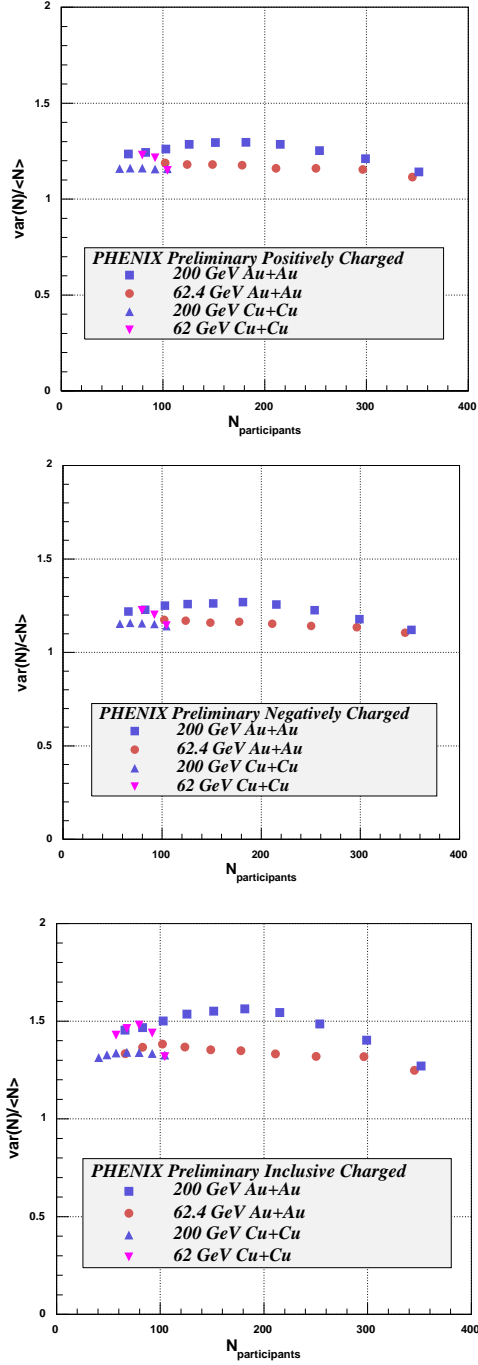


Figure 5.7: Scaled variance of positively, negatively and all charged hadrons as a function of the number of participants for Au+Au collisions at  $\sqrt{s_{NN}} = 62.4$  and 200 GeV and for Cu+Cu collisions at  $\sqrt{s_{NN}} = 62$  GeV [90].

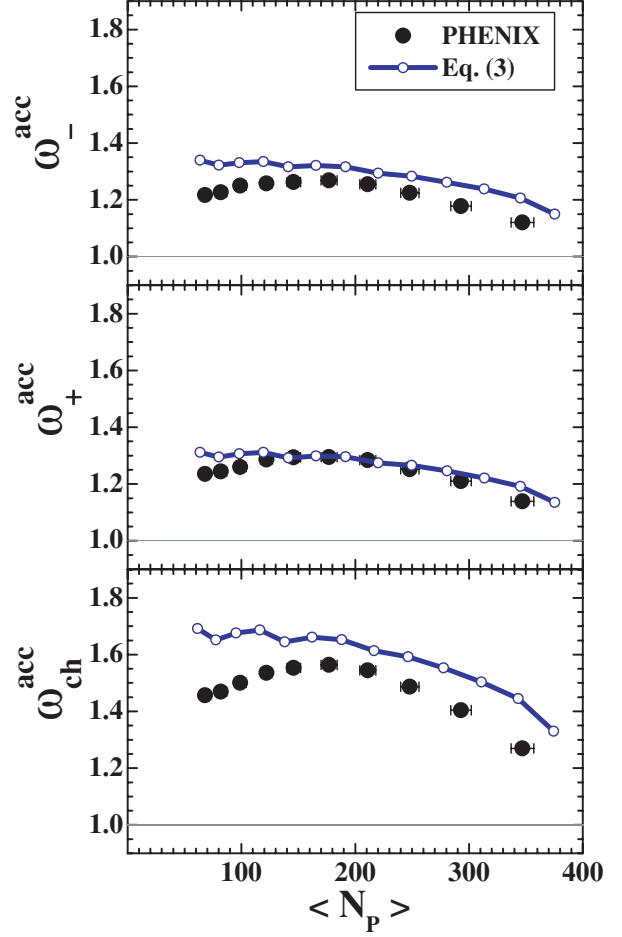


Figure 5.8: PHENIX results for scaled variance of positively, negatively and all charged hadrons as a function of the number of participants for Au+Au collisions at  $\sqrt{s_{NN}} = 200$  GeV in comparison to HSD model calculations [92]. In contrast to the data the centrality in the model is determined by a simulation of the BBCs only.

## 5 Centrality Dependence of Multiplicity Fluctuations

The results for the centrality dependence of scaled variance measured by the PHENIX collaboration are shown in Fig. 5.7. An increase of fluctuations when going from central to mid-central collisions, and a decrease when going to peripheral collisions, is observed for both energies and both collision systems. The observed effect is similar to the one observed by the NA49 collaboration even though both the acceptance and the centrality selection procedure are different.

It is suggested that the observed centrality dependence of scaled variance is related to the asymmetry of the collision (see above). An HSD simulation [92] taking this effect into account roughly reproduces the PHENIX data (Fig. 5.8). It has to be mentioned that in the HSD simulation the centrality of the events is determined using the BBC multiplicity only, the ZDCs are not implemented yet.

# 6 Multiplicity Fluctuations in Central Collisions: Experimental Results

Results on the multiplicity fluctuations for negatively, positively and all charged hadrons are presented for Pb+Pb collisions at 20A, 40A, 80A and 158A GeV (published in [93]) as well as for C+C and Si+Si collisions at 158A GeV (still preliminary). For minimizing the fluctuations in the number of participants, the 1% most central collisions according to the energy of projectile spectators measured in the veto calorimeter are selected (section 2.1.2). In order to take aging effects of the calorimeter into account, a time dependent calibration is applied (section 4.2.5). To exclude reconstruction inefficiencies caused by delta electrons, for Pb+Pb collisions only events without beam particles passing the detector during TPC readout are taken (section 4.3.1). The total rapidity interval  $0 < y(\pi) < y_{beam}$  used for this analysis is divided into two subintervals,  $0 < y(\pi) < 1$  ("midrapidity") and  $1 < y(\pi) < y_{beam}$  ("forward rapidity", section 4.3).

In this chapter the statistical errors are indicated by vertical lines, the systematic errors by horizontal bars. For the determination of the errors see section 4.4.

## 6.1 Multiplicity Distributions

The multiplicity distributions for the different collision systems, energies, charges and rapidity intervals as well as the ratios of the measured multiplicity distributions to a Poisson one with the same mean multiplicity are shown in Figs. A.1-A.18. For Pb+Pb collisions all multiplicity distributions have a bell-like shape, no significant tails or events with a very high or very low multiplicity are observed. The ratios of measured multiplicity distributions to corresponding Poisson distributions are mostly symmetric around their mean values.

The measured multiplicity distributions are significantly narrower than the Poisson ones in the forward acceptance for positively and negatively charged hadrons in Pb+Pb collisions

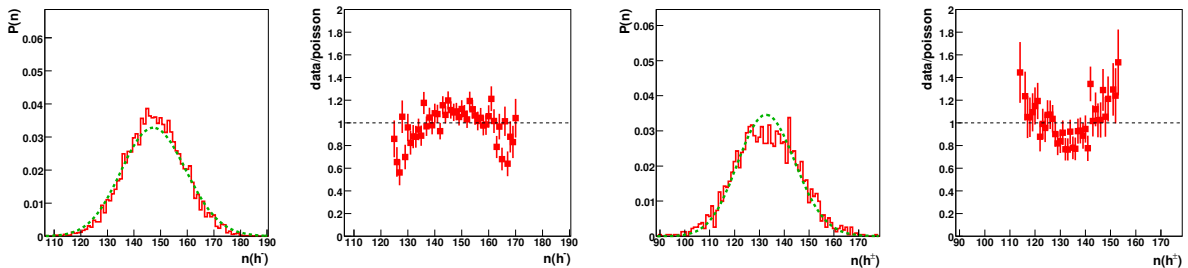


Figure 6.1: Example multiplicity distributions and ratios to the corresponding Poisson distributions for central ( $C < 1\%$ ) Pb+Pb collisions. Left:  $\omega(h^-)$  in  $1 < y(\pi) < y_{beam}$  at 158A GeV. Right:  $\omega(h^\pm)$  in  $0 < y(\pi) < 1$  at 80A GeV.

## 6 Multiplicity Fluctuations in Central Collisions: Experimental Results

at all energies. In the midrapidity acceptance the measured distributions are wider than the Poisson ones. The distributions for all charged hadrons are broader than the ones for positively and negatively charged particles separately. In C+C and Si+Si collisions the multiplicity distributions are broader than for the corresponding Pb+Pb collisions.

Examples of one multiplicity distribution smaller and one broader than a Poisson distribution are shown in Fig. 6.1. For the ratio to the Poisson distributions only points with statistical errors smaller than 20% are plotted.

### 6.2 Energy Dependence in Pb+Pb

The energy dependence of the scaled variance of the multiplicity distributions for positively, negatively and all charged particles for three different acceptances is shown in Figs. 6.2-6.4.

For positively and negatively charged hadrons the scaled variances are similar and smaller than 1 in the forward acceptance at all energies. At midrapidity they are larger than 1. For all charged particles the scaled variances are larger than the ones for a single charge.

No significant structure or non-monotonous behaviour at a specific energy is observed.

As the experimental acceptance and the selected region of the phase-space is different for different energies, the energy dependence of  $\omega$  might be dominated by acceptance effects. Therefore as a guideline the experimental data is compared to the predictions of the UrQMD model. For a study of trigger effects on multiplicity fluctuations and to exclude a possible correlation of particles in the TPCs and in the veto calorimeter the UrQMD results are shown both for zero impact parameter collisions and the 1% most central collisions selected in a similar way as for the experimental data. A detailed discussion of the UrQMD model is given in section 7.2.

Signatures of the critical point are expected to occur mostly at low transverse momenta [50]. The energy dependences of multiplicity fluctuations for particles with  $p_T < 0.3$  and  $p_T < 0.5$  GeV are shown in Fig. 6.12. No non-monotonous behaviour is observed.

### 6.3 System Size Dependence

The scaled variances for the 1% most central C+C, Si+Si and Pb+Pb collisions at 158A GeV are shown in Figs. 6.5-6.7.

The scaled variance is larger for smaller systems. It is suggested that the increase of fluctuations in C+C and Si+Si collisions is related to larger relative fluctuations in the number of participants, see section 7.2.

For 158A GeV C+C and Si+Si the available statistics is just sufficient for the determination of  $\omega$  with still acceptable statistical errors. For 40A GeV C+C and Si+Si the statistics is too low for a study of multiplicity fluctuations in a very clean event sample for the 1% most central collisions [68]. The 40A GeV C+C data-set has a much larger trigger centrality than the 158A GeV C+C data-set therefore the available statistics for the 1% most central collisions is about three times smaller. The 40A GeV Si+Si data-set has about three times less events than the 158A GeV Si+Si data-set. In addition the beam charge information seems to be corrupt. Due to these reasons the system size dependence of multiplicity fluctuations is only studied at 158A GeV.

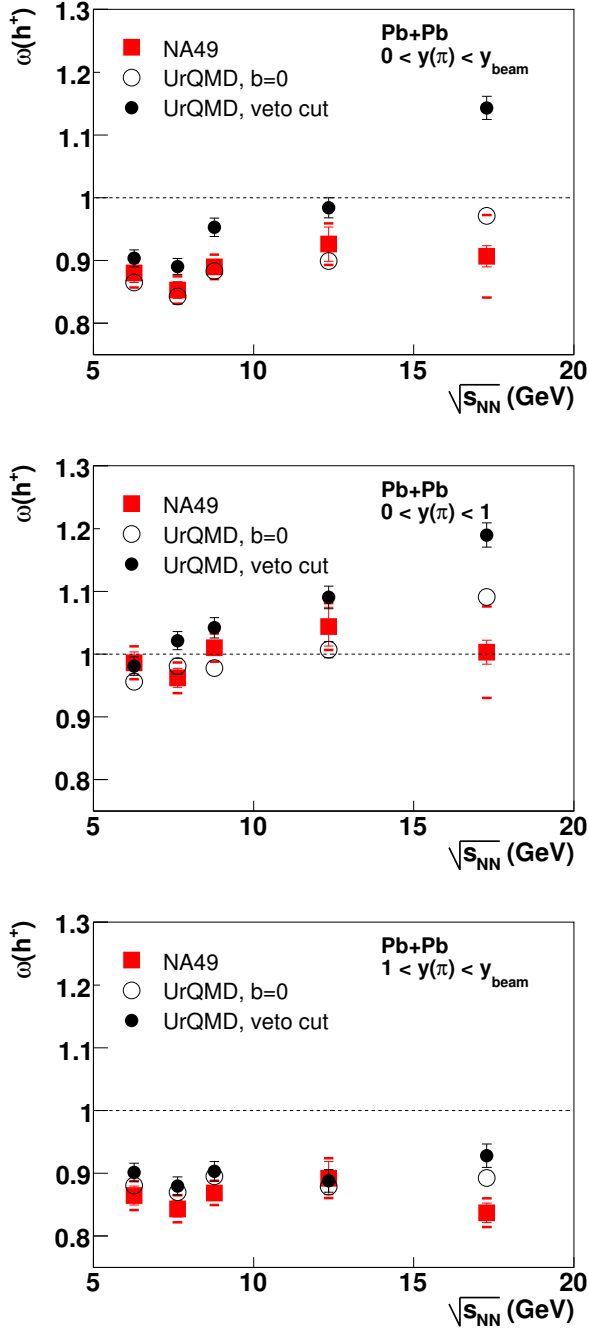


Figure 6.2: Scaled variance of the multiplicity distribution of positively charged hadrons produced in central Pb+Pb collisions as a function of collision energy for NA49 data and the UrQMD model. Top: full experimental acceptance, middle: midrapidity, bottom: forward rapidity.

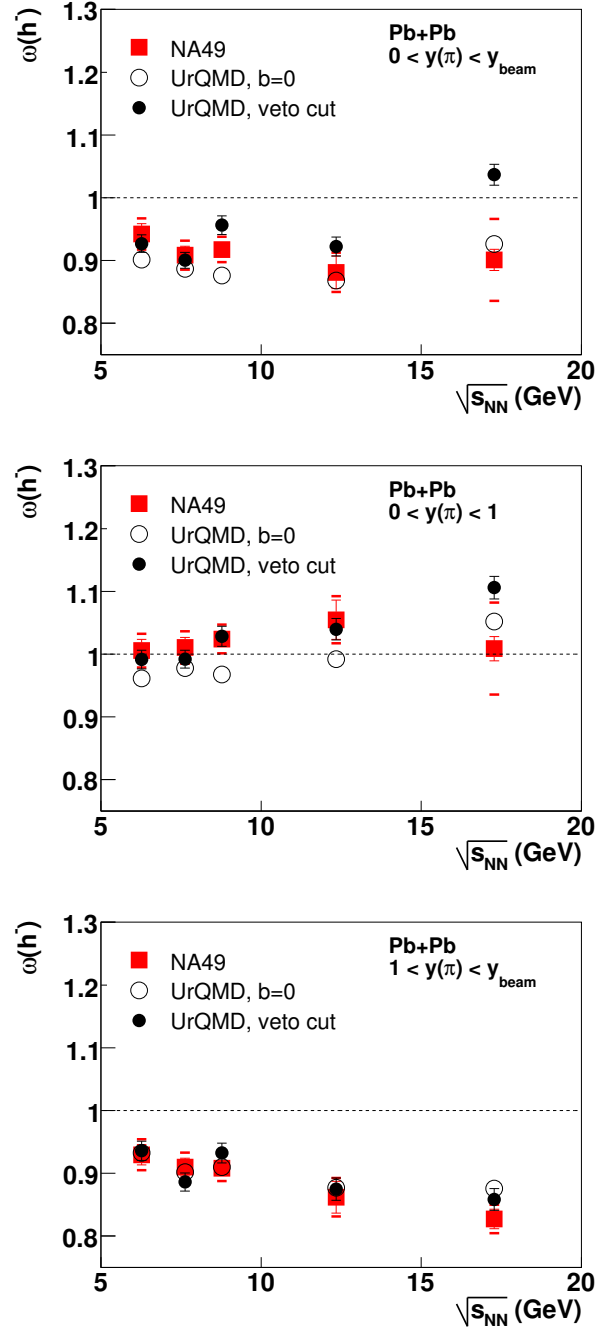


Figure 6.3: Scaled variance of the multiplicity distribution of negatively charged hadrons produced in central Pb+Pb collisions as a function of collision energy for NA49 data and the UrQMD model. Top: full experimental acceptance, middle: midrapidity, bottom: forward rapidity.

6 Multiplicity Fluctuations in Central Collisions: Experimental Results

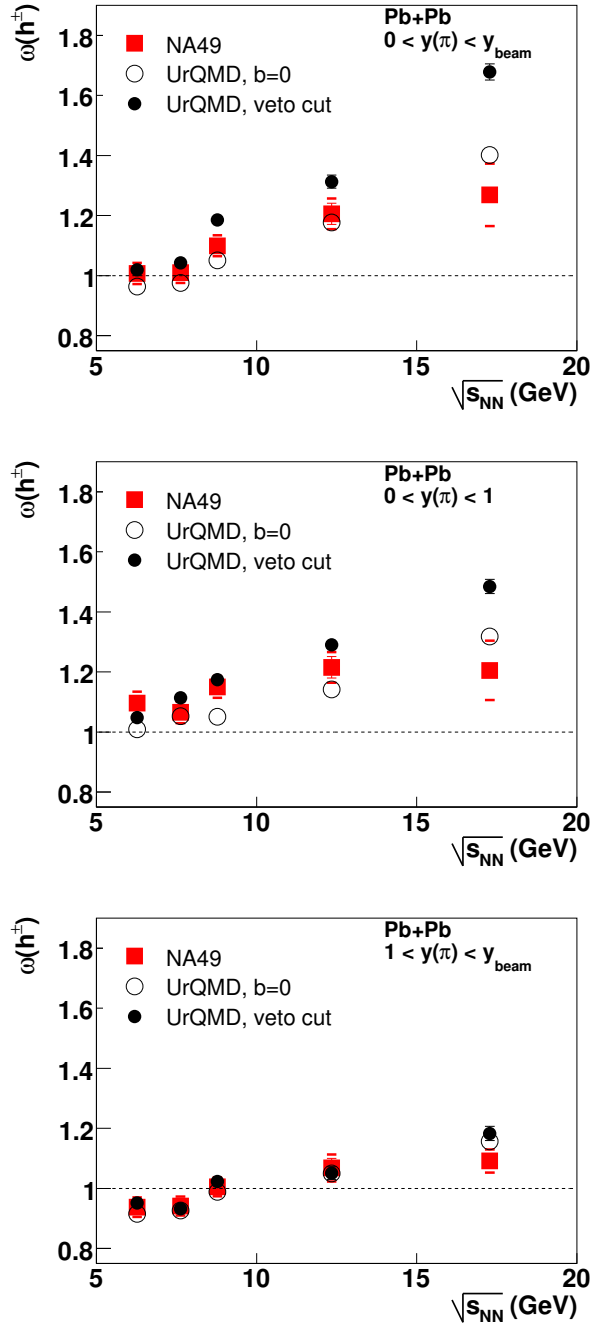


Figure 6.4: Scaled variance of the multiplicity distribution of all charged hadrons produced in central Pb+Pb collisions as a function of collision energy for NA49 data and the UrQMD model. Top: full experimental acceptance, middle: midrapidity, bottom: forward rapidity.

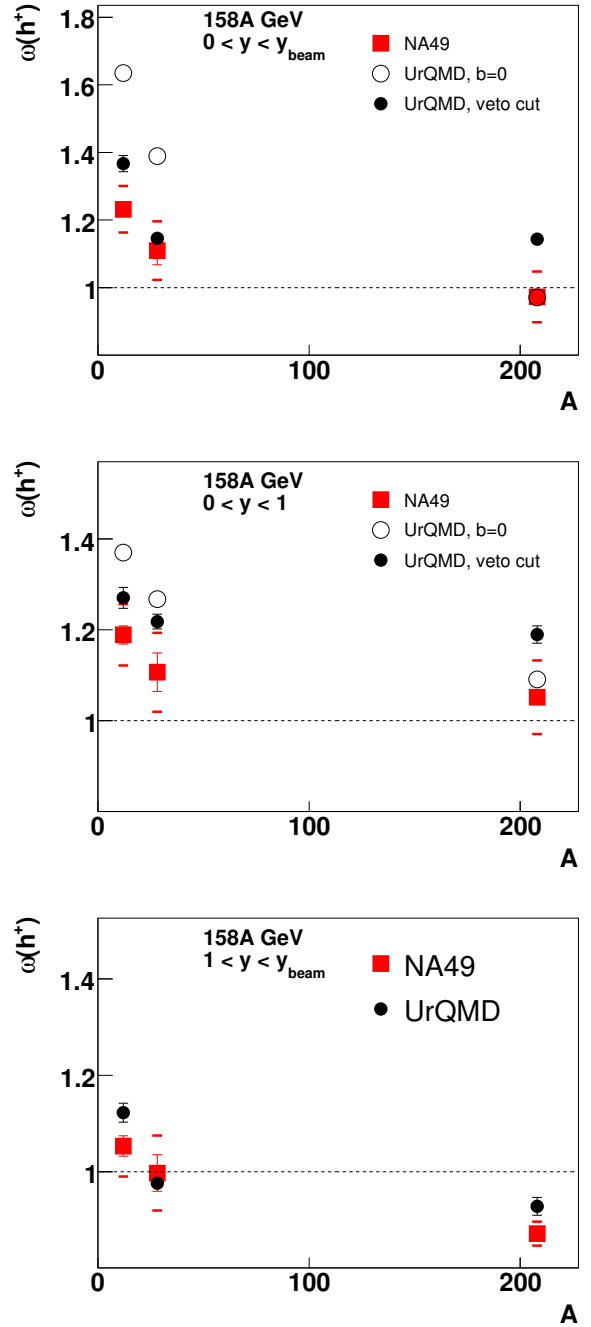


Figure 6.5: Scaled variance of the multiplicity distribution of positively charged hadrons produced in central Pb+Pb collisions as a function collision system size at 158A GeV for NA49 data and the UrQMD model. Top: full experimental acceptance, middle: midrapidity, bottom: forward rapidity.



### 6.3 System Size Dependence

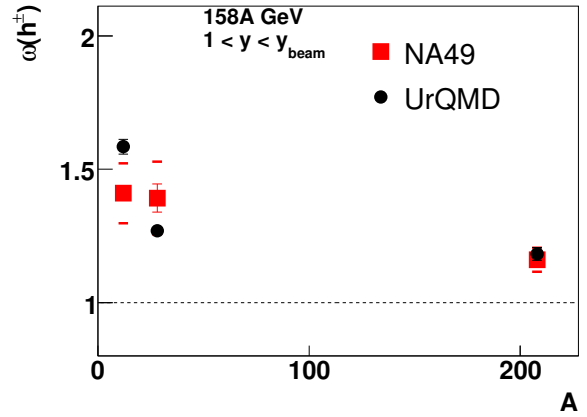
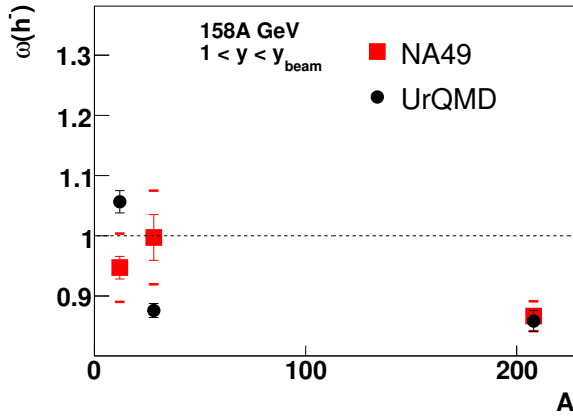
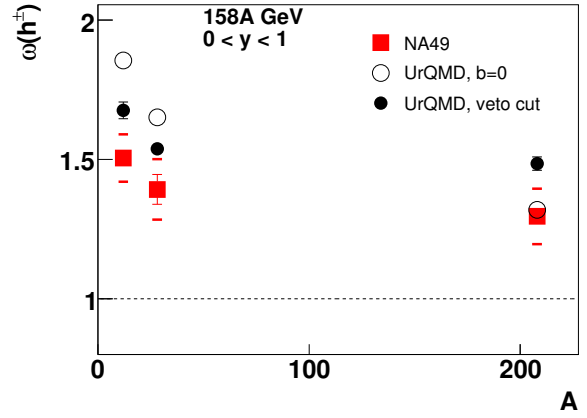
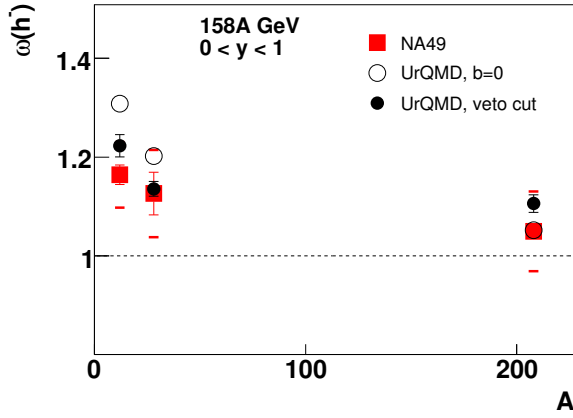
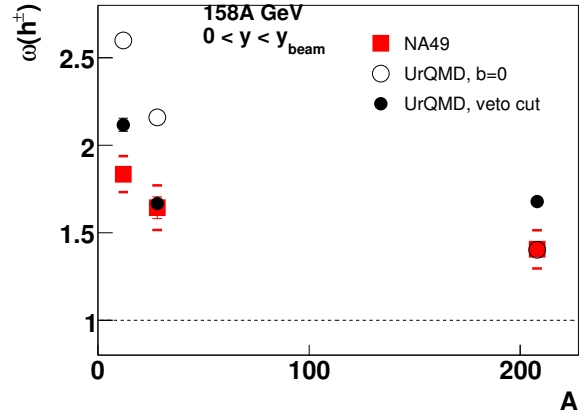
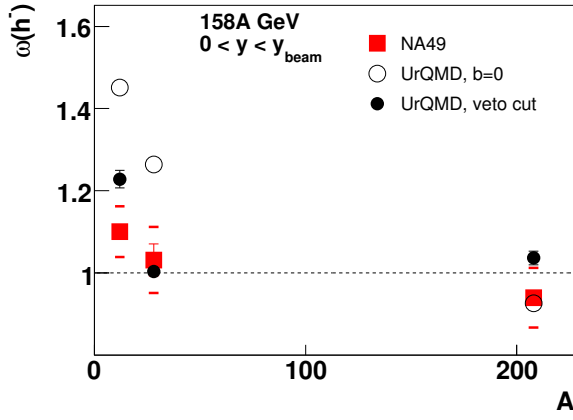


Figure 6.6: Scaled variance of the multiplicity distribution of negatively charged hadrons produced in central Pb+Pb collisions as a function collision system size at 158A GeV for NA49 data and the UrQMD model. Top: full experimental acceptance, middle: midrapidity, bottom: forward rapidity.

Figure 6.7: Scaled variance of the multiplicity distribution of all charged hadrons produced in central Pb+Pb collisions as a function collision system size at 158A GeV for NA49 data and the UrQMD model. Top: full experimental acceptance, middle: midrapidity, bottom: forward rapidity.

## 6 Multiplicity Fluctuations in Central Collisions: Experimental Results

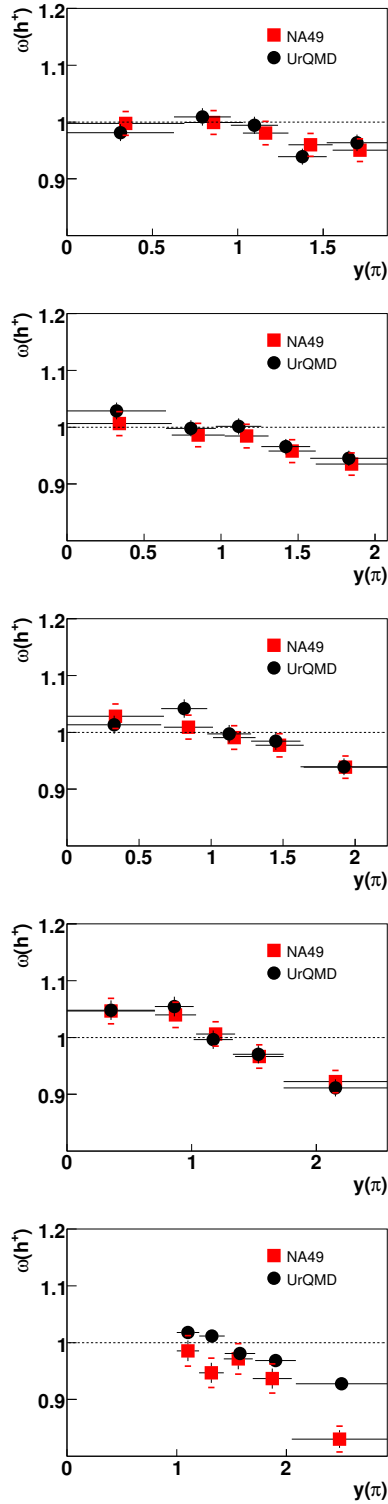


Figure 6.8: Rapidity dependence of the scaled variance of the multiplicity distribution of positively charged hadrons in central Pb+Pb collisions for NA49 data and the UrQMD model at 20A (top), 30A, 40A, 80A and 158A GeV (bottom).

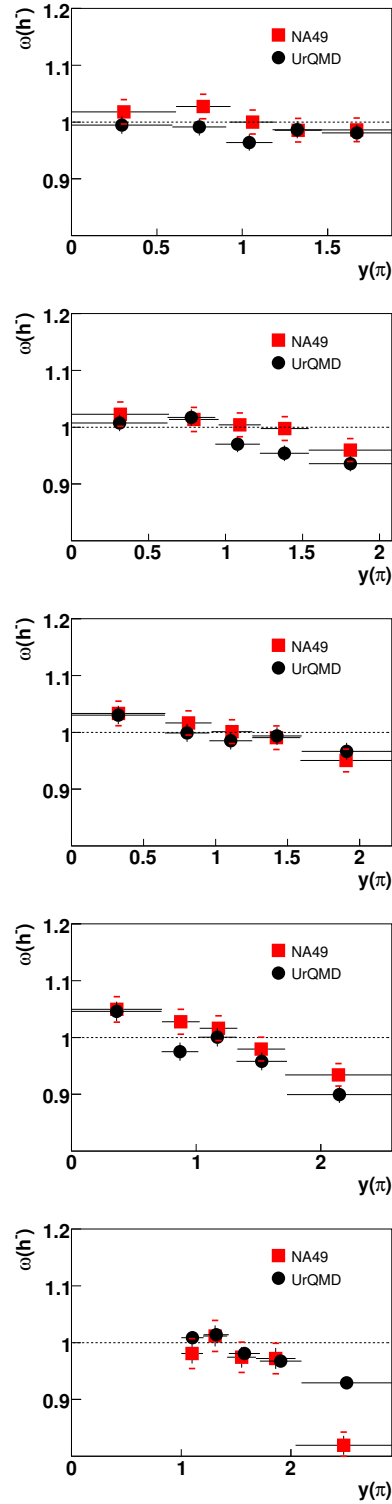


Figure 6.9: Rapidity dependence of the scaled variance of the multiplicity distribution of negatively charged hadrons in central Pb+Pb collisions for NA49 data and the UrQMD model at 20A (top), 30A, 40A, 80A and 158A GeV (bottom).

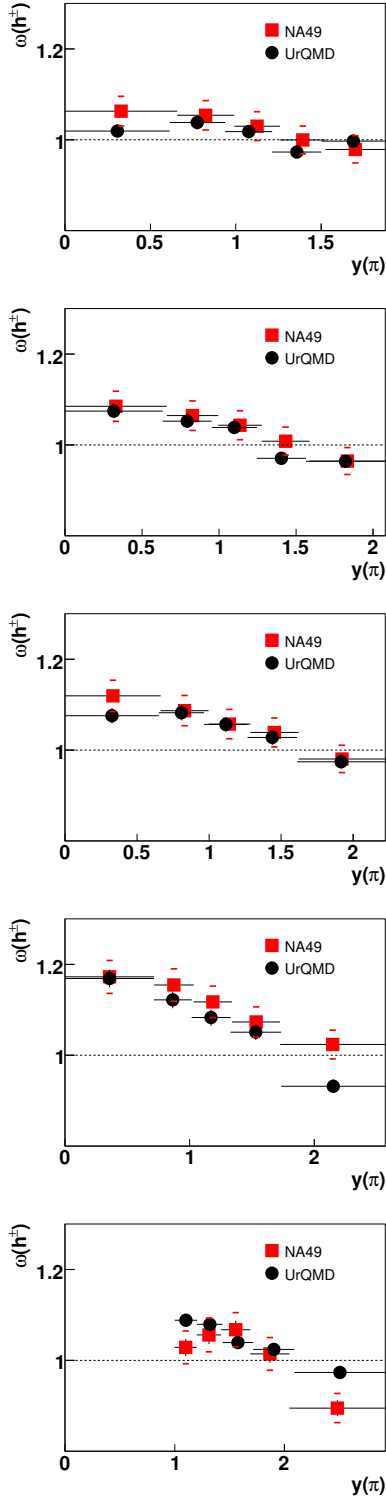


Figure 6.10: Rapidity dependence of the scaled variance of the multiplicity distribution of all charged hadrons in central Pb+Pb collisions for NA49 data and the UrQMD model at 20A (top), 30A, 40A, 80A and 158A GeV (bottom).

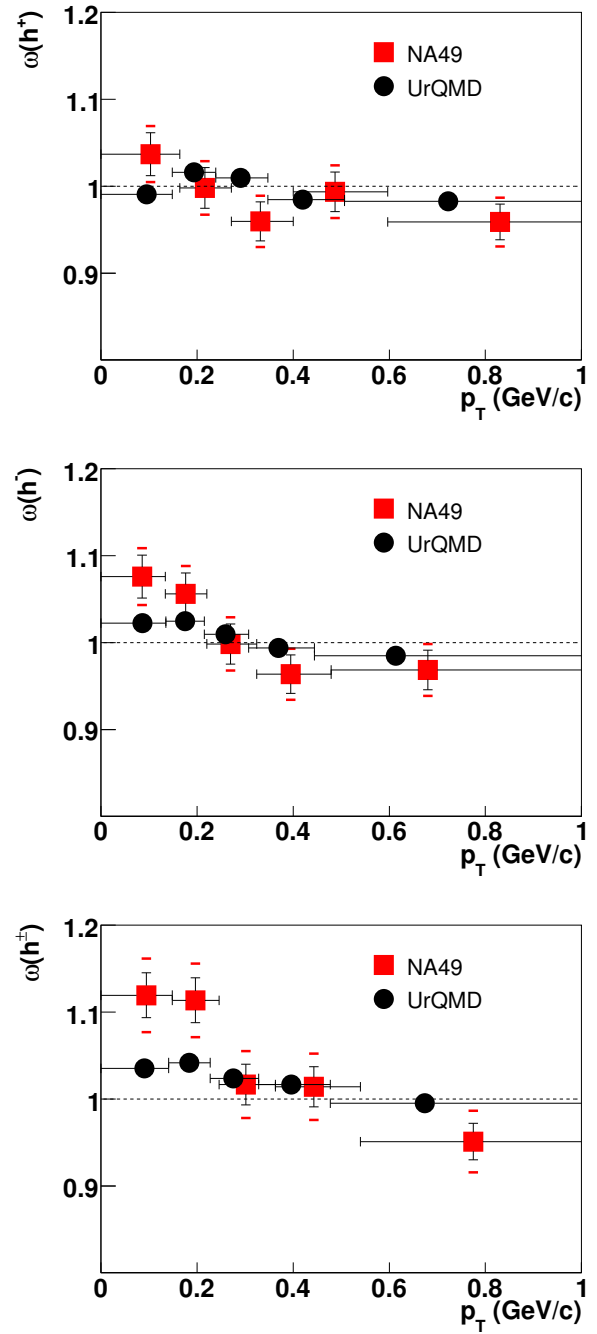


Figure 6.11: Transverse momentum dependence of the scaled variance of the multiplicity distribution of positive (top), negative and all charged (bottom) hadrons for NA49 data and the UrQMD model in the rapidity interval  $1.25 < y(\pi) < 1.75$  in central Pb+Pb collisions at 158A GeV.

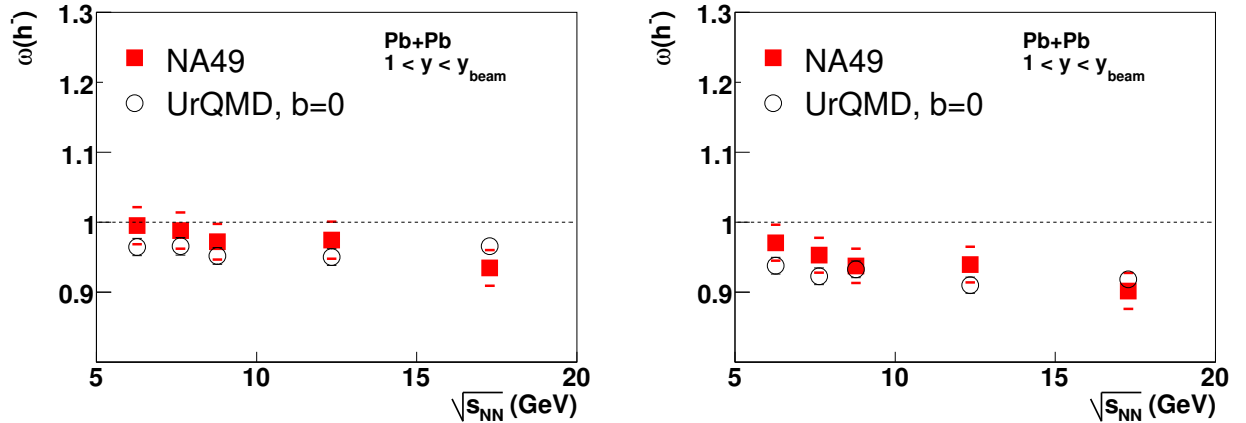


Figure 6.12: Scaled variance of the multiplicity distribution of negatively charged hadrons with low transverse momentum at forward rapidities produced in central Pb+Pb collisions as a function of collision energy. Left:  $p_T < 0.3$  GeV/c, right:  $p_T < 0.5$  GeV/c.

## 6.4 Rapidity Dependence

The rapidity dependence of the scaled variance of the multiplicity distributions for central Pb+Pb collisions at 20A, 30A, 40A, 80A and 158A GeV is shown in Figs. 6.8-6.10. For 158A GeV only the rapidity interval  $1 < y(\pi) < y_{beam}$  is used, because the midrapidity region suffers from reconstruction inefficiencies (section 4.4.2). In order to remove the "trivial" dependence of the scaled variance on the fraction of accepted tracks (Eq. 2.7) the rapidity bins  $y_c - \Delta y < y < y_c + \Delta y$  are constructed in such a way that the mean multiplicity in the acceptance for each bin is the same.

If there would be no correlations in momentum space and the momentum distributions would be independent on multiplicity, the scaled variances in Figs. 6.8-6.10 would be independent of rapidity. This is not the case, the experimental data show an increase of the scaled variance towards midrapidity for all charges and energies.

## 6.5 Transverse Momentum Dependence

The transverse momentum ( $p_T$ ) dependence of the scaled variances at the top SPS energy is shown in Fig. 6.11. Only a small rapidity interval in the forward acceptance ( $1.25 < y(\pi) < 1.75$ ) is used for this study. A larger rapidity interval might cause a bias because the acceptance in rapidity is different for different transverse momenta and it can not be excluded that the  $p_T$  dependence includes artifacts of the rapidity dependence. As for the study of the rapidity dependence of  $\omega$  the transverse momentum bins are constructed in such a way that the mean multiplicity in the acceptance for each bin is the same. The horizontal bars in Fig. 6.11 indicate the transverse momentum bins and the horizontal position of the symbols the mean  $p_T$  for each bin.

The scaled variance increases with decreasing transverse momentum. Only the top SPS energy is shown because at lower energies the azimuthal acceptance of the NA49 detector is much smaller.

# 7 Multiplicity Fluctuations in Central Collisions: Models and Discussion

In this section predictions of several models for the energy, system size, rapidity and transverse momentum dependence of scaled variance in very central collisions are discussed.

In section 7.1 a statistical hadron-gas model is introduced, predictions for  $\omega$  in full phase space are shown and they are compared to the experimental data.

Results of the string-hadronic models UrQMD and HSD concerning multiplicity fluctuations are presented in section 7.2. In the sub-sections the energy dependence, the system size dependence and the rapidity and transverse momentum dependence of  $\omega$  are shown in the full acceptance, in a limited region of the phase-space and in comparison to the experimental data.

Furthermore theoretical considerations concerning the influence of the onset of deconfinement (section 7.3), the critical point (section 7.4) and a first order phase transition (section 7.5) are discussed.

## 7.1 Statistical Hadron-Gas Model

Statistical hadron-gas models are very successful in describing mean hadron multiplicities, both in elementary (e+e, p+p) and heavy ion collisions (Fig. 7.1). Different formulations of statistical hadron-gas models exist. These models can assume chemical equilibrium for all particle species [14] or an under-saturation of strangeness production [13]. In [15] it is assumed that both the strange and the non-strange quarks are not in chemical equilibrium.

For heavy ion collisions the agreement of experimental data on mean multiplicities with statistical model calculations can be understood in a dynamical picture where a fireball is formed where hadrons are created and annihilated. If these processes are fast enough equilibrium can be reached and the particle ratios can be described by statistical models. The agreement of the measured particle yields with the statistical models is however surprising for elementary collisions, where the number of produced particles is so small that they can not interact with each other sufficiently in order to achieve an equilibrium. It is suggested that the hadrons are created already in an equilibrium state [95].

Three different statistical ensembles can be used, the grand-canonical, the canonical and the micro-canonical ensemble, which differ in the way the conservation laws are taken into account. In the grand-canonical ensemble all conservation laws are fulfilled only in the average, not on an event-by-event basis. In the canonical ensemble all charges are conserved in each event. In the micro-canonical ensemble in addition the energy and the momentum of the particles are conserved in each event. For small systems the conservation laws play an important role for mean multiplicities, therefore the micro-canonical ensemble has to be used for elementary interactions. For the mean multiplicities in heavy ion collisions the conservation laws are not important, all ensembles give the same results. Consequently, the grand-canonical ensemble is commonly used as it is easier to calculate.

## 7 Multiplicity Fluctuations in Central Collisions: Models and Discussion

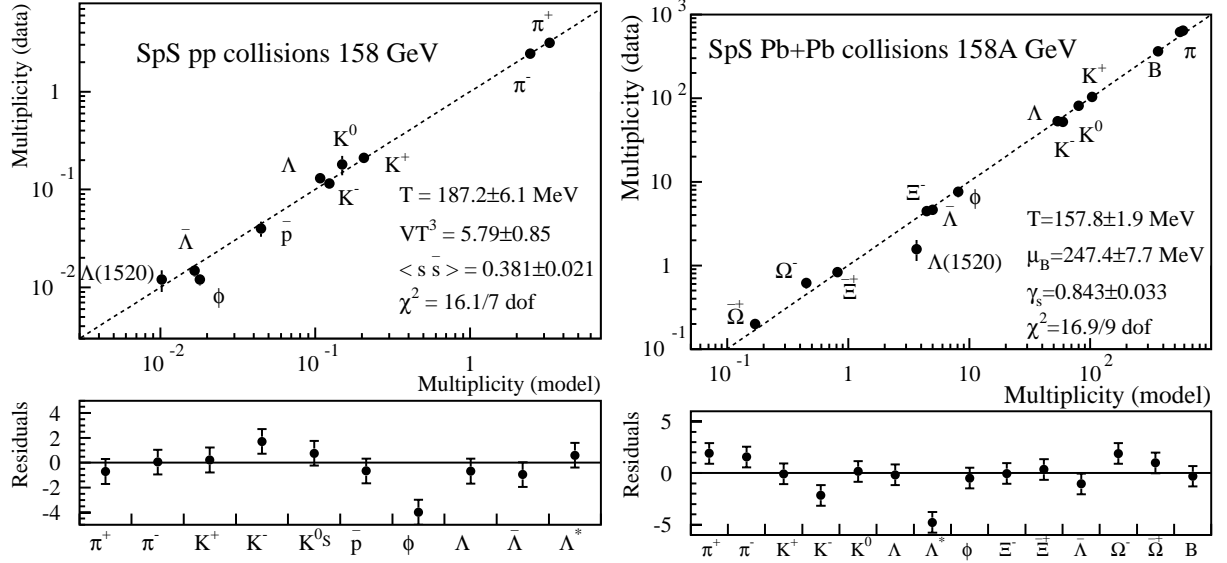


Figure 7.1: Statistical hadron-gas model fits [94] to particle multiplicities in p+p (left) and Pb+Pb (right) collisions at 158A GeV.

In the infinite volume limit all three ensembles give the same results for mean multiplicities. Recent model calculations [51] showed that this equivalence of the statistical ensembles is not true for higher moments, hence fluctuations. The scaled variance of each ensemble quickly converges for larger volumes, but the limiting values are different for each ensemble. Variables like the scaled variance, which are volume independent in the large volume limit, but different in different statistical ensembles, are called “semi-intensive”, in analogy to the intensive variables which are independent of volume but identical in all ensembles.

In a non-relativistic gas the particle number is conserved in the canonical and micro-canonical ensemble and consequently the scaled variance is zero. In a relativistic gas particle and antiparticle pairs can be produced and annihilated, therefore the conserved quantities in these ensembles are the charges and not the particle numbers.

In the grand-canonical formulation the mean multiplicity of a particle species  $j$  can be calculated by

$$\langle N_j \rangle = \sum_p \langle n_{p,j} \rangle = \frac{g_j V}{V \rightarrow \infty} \frac{g_j V}{2\pi^2} \int_0^\infty p^2 dp \langle n_{p,j} \rangle, \quad (7.1)$$

where  $V$  is the volume of the system and  $g_j$  the degeneracy factor of the particle species  $j$ . In the thermodynamic limit,  $V \rightarrow \infty$ , the sum can be replaced by an integral over the momentum states  $p$ .  $\langle n_{p,j} \rangle$  is the mean occupation number of a single quantum state with the momentum vector  $p$ :

$$\langle n_{p,j} \rangle = [\exp[(\epsilon_{p,j} - \mu_j)/T] - \alpha_j]^{-1}, \quad (7.2)$$

where  $T$  is the temperature of the system and  $\epsilon_{p,j}$  the single particle energy ( $\epsilon_{p,j} = \sqrt{p^2 + m_j^2}$ ). The quantum statistics parameter  $\alpha_j$  is +1 for bosons and -1 for fermions,  $\alpha_j = 0$  would give the Boltzmann approximation. The chemical potential  $\mu_j$  consists of the potentials for the electric charge, the baryon number and the strangeness for the particle species. These

chemical potentials ensure the conservation of charges on the average in the grand-canonical ensemble, but the charges are not conserved individually in each event.

The variance of hadron multiplicity is calculated in this model using the correlators

$$Var(N) = \langle (\Delta N)^2 \rangle = \sum_{i,j,q_i < 0, q_j < 0} \langle \Delta N_i \Delta N_j \rangle, \quad (7.3)$$

where  $\Delta N_i = N_i - \langle N_i \rangle$ . In the grand-canonical ensemble no correlations between different momentum states and particle species exist, beside of Bose and Fermi statistics and resonance decays. Neglecting these effects, the scaled variance in the grand-canonical ensemble would be one for all energies and charges.

Bose statistics increases multiplicity fluctuations because it is more likely to produce a second particle in the same quantum state when one particle is produced. Fermi statistics decrease fluctuations because it forbids the production of a particle in the same quantum state as an existing one. In the grand-canonical and canonical ensemble resonance decay enhances fluctuations if the resonances decay into at least two daughter particles which are used for the fluctuation analysis (section 2.2.1).

### 7.1.1 Scaled Variance in Full Phase-Space

In the following the predictions for the energy dependence of scaled variance in A+A collisions of a statistical hadron-gas model [55] in the full phase space are presented. The scaled variances of the grand-canonical, canonical and micro-canonical ensemble are shown in Fig. 7.3. The colored lines indicate the scaled variances after resonance decays, the thin black lines before the resonance decays.

In the canonical ensemble the baryon number, the strangeness and the electrical charge are conserved in each event, in contrast to the grand-canonical ensemble, where they are conserved only on average. These constrains on particle production strongly reduce the multiplicity fluctuations. Where the grand-canonical ensemble predicts a scaled variance of about one, the canonical ensemble predicts values of 0.5 for positively and negatively charged hadrons before resonance decays. For all charged hadrons values of about one are predicted, because for each positive a negative particle have to be produced to ensure electric charge conservation. In this ensemble different particle species are expected to have different fluctuations. For example  $\rho^0$ , which has zero electric charge, zero baryon number and zero strangeness, is expected to behave similar as in the grand-canonical ensemble.

Resonance decays mix the contributions of different particle species. For positively and negatively charged hadrons the suppressed scaled variance of the primordial particles is mixed with the scaled variance of neutral resonances, which decay into a pair of oppositely charged particles. Therefore the fluctuations of positively and negatively charged hadrons are strongly enhanced due to resonance decays in the canonical ensemble. For all charged hadrons the enhancement of fluctuations due to resonance decays has the same origin as for the grand-canonical ensemble: resonances decaying into two oppositely charged particles, both of them are used for the fluctuation analysis.

The canonical ensemble is a more realistic description of the physics in a heavy ion collision than the grand-canonical ensemble, because in nature charge conservation has to be fulfilled in each event.

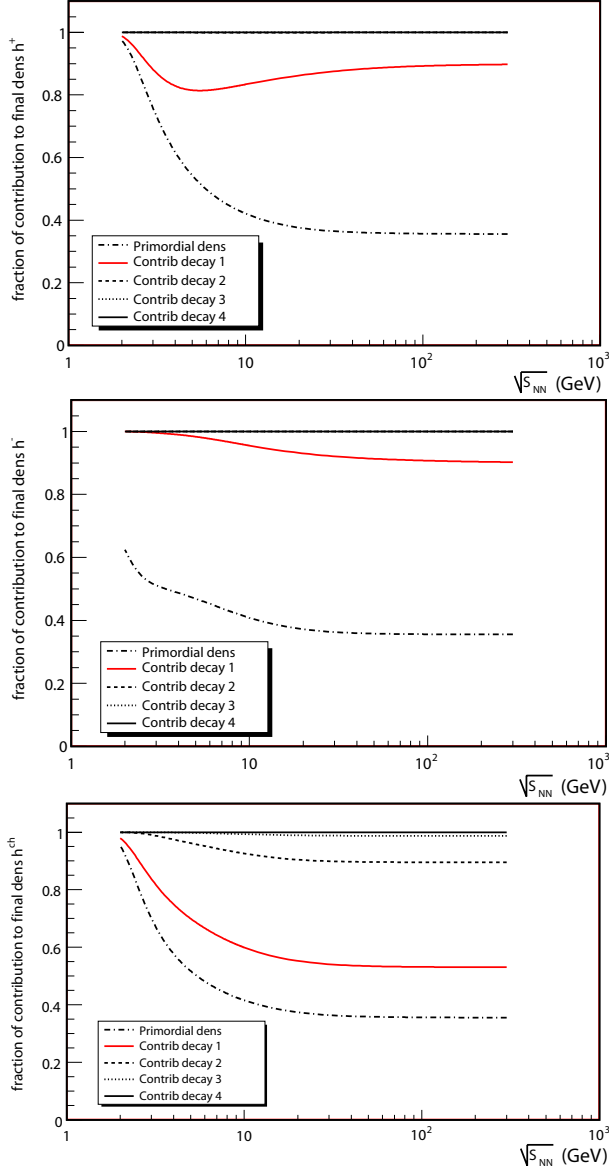


Figure 7.2: Fraction of positively, negatively and all charged final state particles which are originating from a resonance decay into a different numbers of particles with the corresponding charge [55].

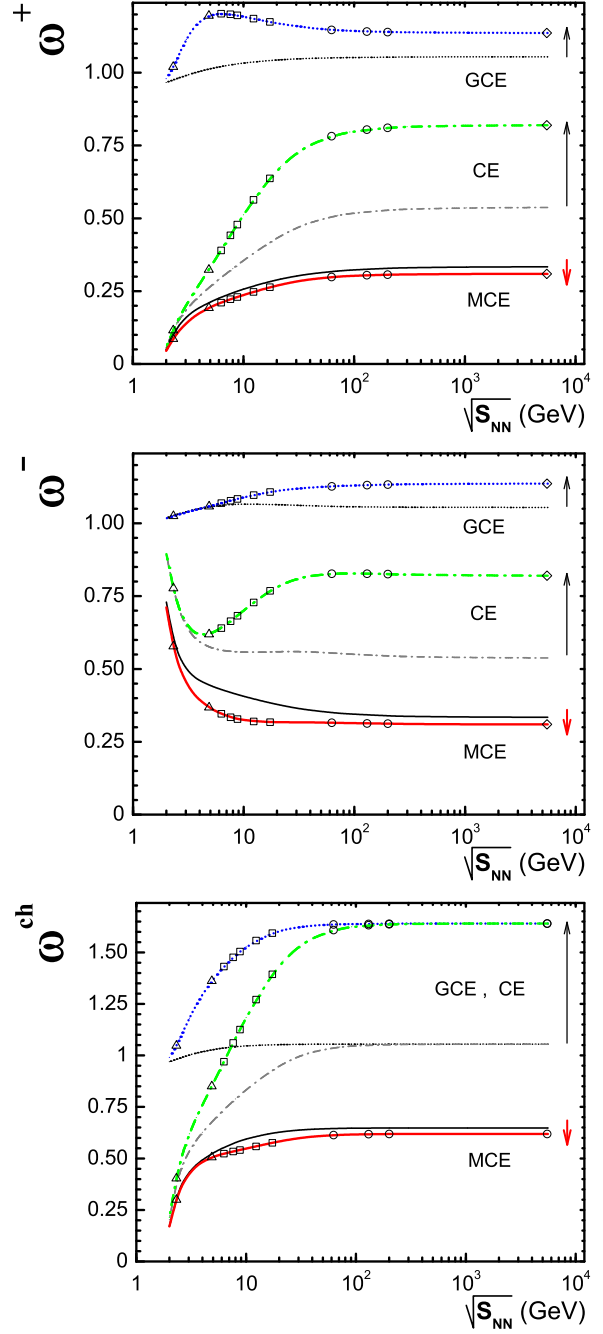


Figure 7.3: Predictions of the hadron-gas model [55] for the scaled variance of positively, negatively and all charged hadrons for A+A collisions in the full phase space.



In the micro-canonical ensemble, in addition to the charges, the energy and the momentum are conserved in each collision. This ensemble is therefore the most realistic one of the statistical ensembles. The conservation of momenta turned out to be not relevant for the scaled variance in the full phase space and is therefore neglected in [55].

The scaled variance in the micro-canonical ensemble is much lower than in the canonical ensemble. The additional constrain of energy conservation reduces the possibility of the system to fluctuate. For a single charge the scaled variance has values of about 0.25, for all charged hadrons of about 0.5. Resonance decays do not increase fluctuations of the scaled variance in this ensemble, because neutral particles are also influenced by the energy conservation. In contrast, the scaled variance even decreases slightly after resonance decay, because a larger fraction of the total fireball is used for the fluctuation analysis.

It should be mentioned that it is assumed in the micro-canonical ensemble that the energy, which is used for newly produced particles, is the same in each collision. If this energy fluctuates, the multiplicity fluctuations are expected to be enhanced. UrQMD simulations however showed that these fluctuations in the inelastic energy of a collision are very small (sections 7.2, 7.3).

### 7.1.2 Comparison to Experimental Data

The calculations for  $\omega$  presented above are performed for the full phase space. In order to compare the model calculations to the experimental data the scaled variance has to be extrapolated to the limited experimental acceptance. Assuming that the particles are produced independent in momentum space and that the form of the momentum distribution is independent of multiplicity,  $\omega$  in the experimental acceptance can be calculated using Eq. 2.7 (section 2.1.1).

As quantum statistic and resonance decays have a small influence on scaled variance for positively and negatively charged hadrons and effects like energy and momentum conservation are not included in the grand-canonical and canonical ensemble, the scaled variance in a limited acceptance can be approximated in these ensembles with Eq. 2.7. Most resonances, like  $\rho^0$ , decay into two oppositely charged particles and therefore enhance only the fluctuations of all charged hadrons. Only a few number of resonances, like  $\Delta^{++}$ , decay into two positively charged daughters and enhance the fluctuations of positively charged hadrons, the yield of resonances decaying into two negatively charged daughters is even smaller.

The majority ( $\approx 90\%$ ) of the positively and negatively charged particles are either primordial particles or are originating from a resonance decay in only one daughter track of the corresponding charge (Fig. 7.2) [55]. Therefore they do not increase fluctuations in the grand-canonical ensemble significantly and the acceptance scaling Eq. 2.7 is expected to be valid in terms of resonance decays. For the scaled variance of all charged hadrons this is not the case because a large fraction of particles originate from a decay of a resonance with two or more charged daughters.

The energy and momentum conservation of the micro-canonical ensemble introduces a strong correlation in momentum space, therefore the acceptance dependence Eq. 2.7 is not valid for this ensemble.

The predictions of the hadron-gas model [55] in its grand-canonical and canonical formulation for the scaled variance of positively and negatively charged hadrons, extrapolated to the experimental acceptance, are shown in Fig. 7.4 and compared to the experimental data. For the mid-rapidity region the influence of participant fluctuations is estimated using the

7 Multiplicity Fluctuations in Central Collisions: Models and Discussion

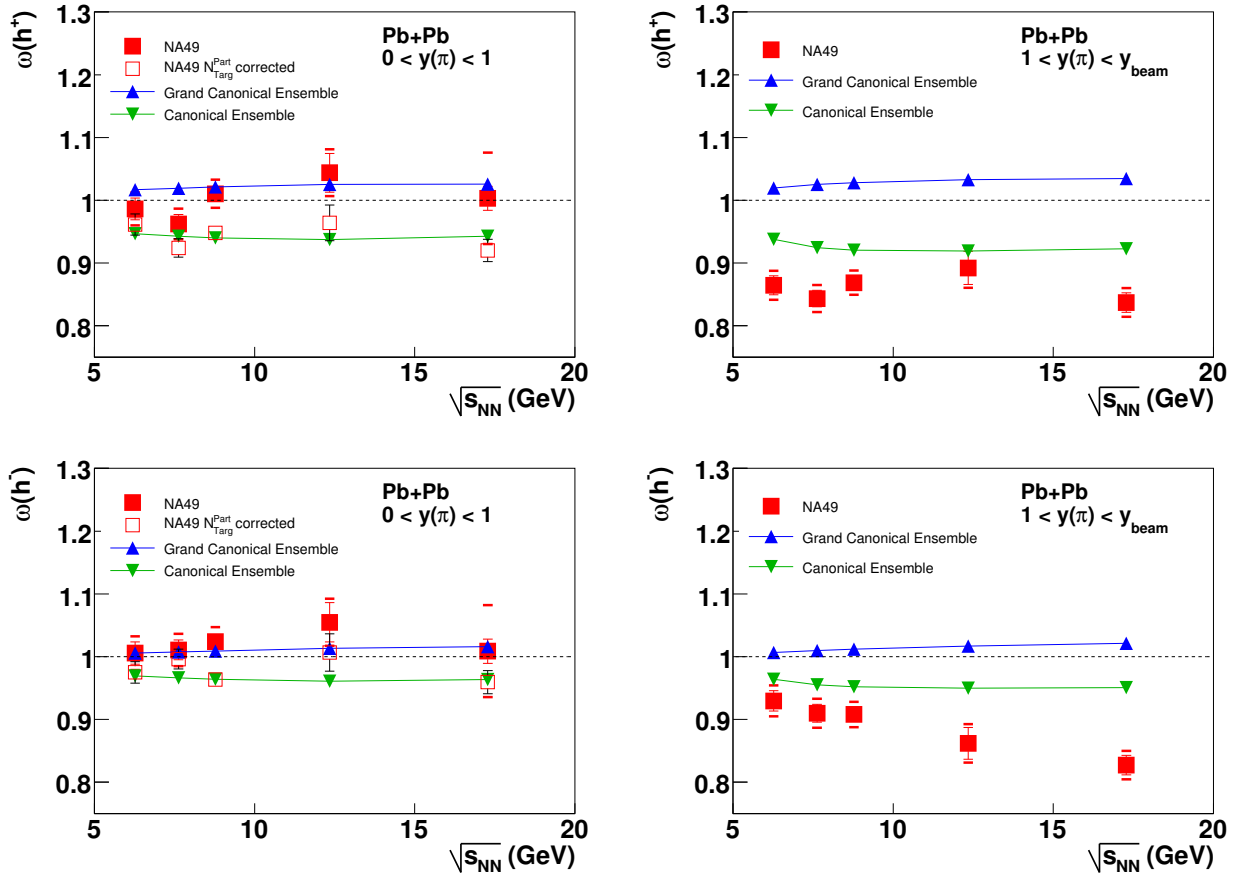


Figure 7.4: Scaled variance  $\omega$  of the multiplicity distribution of positively (top) and negatively (bottom) charged hadrons produced in central Pb+Pb collisions as a function of collision energy in  $0 < y(\pi) < 1$  (left) and  $1 < y(\pi) < y_{beam}$  (right) acceptance compared to predictions of a grand canonical and canonical ensemble [55].

UrQMD results for zero impact parameter collisions and events selected according to their veto energy (open boxes in Fig. 7.4).

In the forward acceptance the hadron-gas model both in the grand-canonical and the canonical formulation over-predict the experimental data. In the midrapidity region the data seems to be in between the grand-canonical and canonical predictions.

The shape of the measured multiplicity distribution is compared to the hadron-resonance gas model prediction for negatively charged hadrons at 158A GeV in the forward acceptance in Fig. 7.5 (left). For this comparison the multiplicity distributions for the data and the model predictions are divided by Poisson distributions with the same mean multiplicities. The hadron-resonance gas model predicts a Gaussian-like shaped multiplicity distribution in full phase space [96]. Since this model gives no prediction about the mean multiplicity, it is taken from data. In order to calculate the multiplicity distribution in the limited experimental acceptance the distribution in the full phase space is folded with a Binomial distribution accepting the same fraction  $p$  of tracks as the experimental acceptance:

$$B_n(k) = \frac{n!}{(n-k)!k!} p^k (1-p)^{n-k}, \quad (7.4)$$

where  $n$  is the multiplicity in the full phase space and  $k$  the multiplicity in the experimental acceptance. The multiplicity distribution in the experimental acceptance is given by

$$P_{acc}(k) = \sum_n P_{4\pi}(n) B_n(k). \quad (7.5)$$

Note that this procedure assumes that there are no correlations in momentum space.

The ratio for the grand-canonical ensemble has a concave shape, i.e. the multiplicity distribution is wider than a Poisson distribution. For the canonical ensemble the shape is convex, showing that the distribution is narrower. The shape for the experimental data is more convex, demonstrating that the measured multiplicity distribution is even narrower than the canonical one.

### 7.1.3 Rapidity and Transverse Momentum Dependence

Micro-canonical calculations of a pion gas including energy and momentum conservation [97] show a strong dependence of scaled variance on rapidity and transverse momentum. In order to take out the simple dependence of scaled variance on acceptance according to Eq. 2.7, the rapidity and transverse momentum bins are constructed in such a way that the mean multiplicity in each bin is the same. If Eq. 2.7 would describe the dependence of scaled variance on acceptance,  $\omega$  would be flat as a function of rapidity and transverse momentum for bins constructed in such a way. Note that the absolute scale of rapidity and transverse momentum in this toy-model calculation is not realistic, for instance no collective expansion is taken into account.

In Fig. 7.6 it can be seen that the energy conservation introduces a dependence of scaled variance on rapidity. Particles with low rapidity fluctuate more than the ones with high rapidity. When the conservation of longitudinal momentum is taken into account this effect gets even stronger. This may be explained by the fact that the large longitudinal momentum of a particle with a high rapidity has to be compensated by the particles in the other hemisphere.

In addition particles with low transverse momentum are expected to fluctuate much stronger in the micro-canonical ensemble (Fig. 7.7).

## 7 Multiplicity Fluctuations in Central Collisions: Models and Discussion

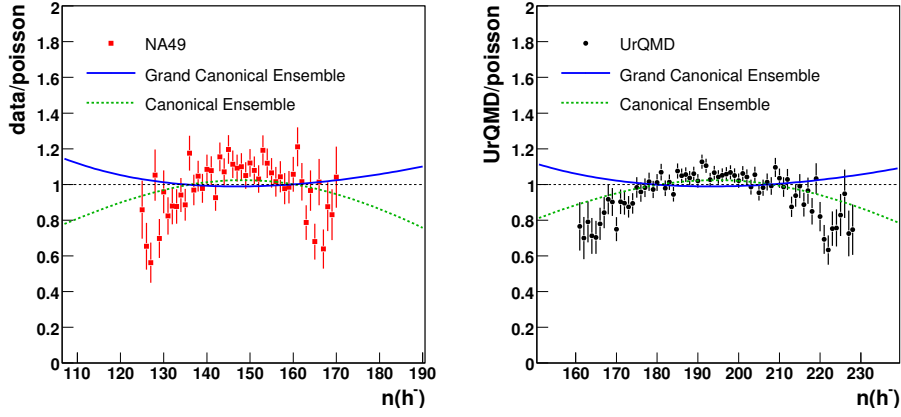


Figure 7.5: Ratio of multiplicity distribution of experimental data (left) and UrQMD simulation (right) to a Poisson distribution with the same mean value for negatively charged hadrons in Pb+Pb collisions at 158A GeV in the forward acceptance. Only points with statistical errors smaller than 20% are shown. Hadron gas model predictions in the grand-canonical and canonical ensemble with the same mean multiplicity and fraction of accepted tracks are shown by lines.

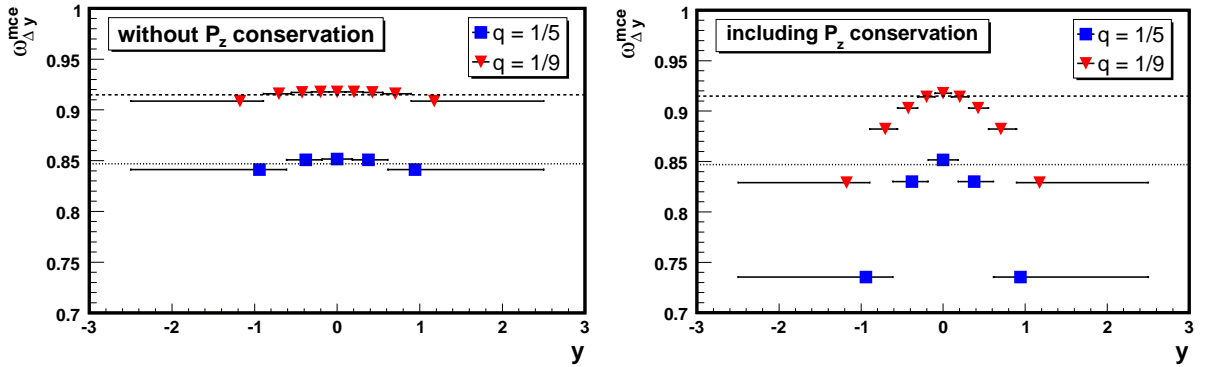


Figure 7.6: Rapidity dependence of scaled variance in a pion gas neglecting (left) and including longitudinal momentum conservation (right). Energy conservation is taken into account in both cases. The rapidity bins are constructed in such a way that the mean multiplicity in each bin is the same. The plots are taken from [97].

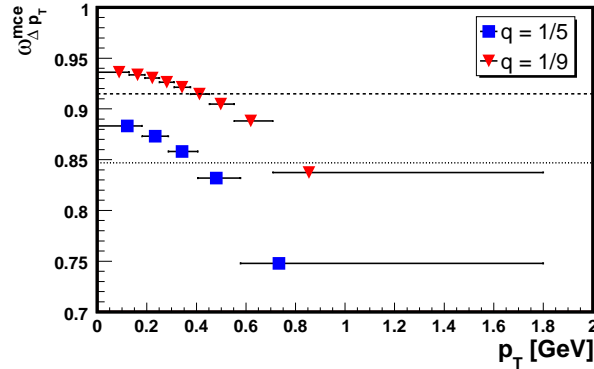


Figure 7.7: Transverse momentum dependence of scaled variance in a pion gas with energy conservation taken into account. The transverse momentum bins are constructed in such a way that the mean multiplicity in each bin is the same. The plot is taken from [97].

Putting both effects together, the multiplicity of particles with low momentum in the center of mass frame of the collision seems to fluctuate stronger than the one of particles with high momentum. This effect can be qualitatively understood by the following line of argument: It costs more energy to create high momentum particles, therefore their number is expected to fluctuate less due to energy conservation.

## 7.2 String-Hadronic Models

In this section the results for the scaled variances of the multiplicity distributions within the string-hadronic models UrQMD and HSD are shown and compared with the experimental data.

The predictions of the Ultra-relativistic Quantum Molecular Dynamics model (UrQMD v1.3) [56, 57] for the energy dependence of the scaled variance of multiplicity fluctuations were studied in detail for this thesis and the results for p+p, n+p and Pb+Pb collisions were published in [98]. Calculations for the system size dependence of  $\omega$  within the UrQMD (performed by B. Lungwitz) and HSD model (performed by V. Konchakovski) were published in [99].

The UrQMD microscopic transport approach is based on the covariant propagation of constituent quarks and di-quarks accompanied by mesonic and baryonic degrees of freedom. It simulates multiple interactions of in-going and newly produced particles, the excitation and fragmentation of color strings and the formation and decay of hadronic resonances. Towards higher energies the treatment of sub-hadronic degrees of freedom is of major importance. In the present model these degrees of freedom enter via the introduction of a formation time for hadrons produced in the fragmentation of strings [100, 101, 102]. A phase transition to a quark-gluon state is not incorporated explicitly into the model dynamics. However, a detailed analysis of the model in equilibrium, yields an effective equation of state of Hagedorn type [103, 104].

This model has been used before to study event-by-event fluctuations rather successfully [53, 105, 106, 107, 108, 109, 110, 111] and yields a reasonable description of inclusive particle

distributions. For a complete review of the model, the reader is referred to [56, 57].

The HSD [112, 113] model follows a similar strategy as UrQMD.

In sub-section 7.2.1 the energy dependence of  $\omega$  is presented for p+p, n+p and Pb+Pb collisions in the full phase space as well as in limited rapidity intervals [98]. Furthermore  $\omega$  for Pb+Pb collisions is calculated in the experimental acceptance simulating the experimental method of centrality selection and is compared to the experimental data.

The system size dependence of participant fluctuations [99] is discussed in sub-section 7.2.2. The two-dimensional dependence of  $\omega$  on energy and system size dependence is shown for different methods of centrality selection. The predictions of the UrQMD model for C+C and Si+Si collisions at 158A GeV are compared to the experimental data.

In sub-section 7.2.3 the rapidity and transverse momentum dependence of  $\omega$  are shown for Pb+Pb collisions [98] and compared to the experimental data.

### 7.2.1 Energy Dependence of $\omega$

UrQMD calculations for the energy dependence of the mean multiplicity, normalised by the number of nucleons of one projectile ( $A = 1$  for p+p, n+p,  $A = 208$  for Pb+Pb), of positively, negatively and all charged particles in p+p, n+p and Pb+Pb collisions are shown in Fig. 7.8, left. For p+p and n+p interactions all inelastic collisions (all collisions with at least 3 particles in the output channel) are selected. For Pb+Pb the impact parameter of the collisions is set to  $b = 0$ . The calculations were performed for AGS ( $E_{lab} = 6.87A$  GeV), SPS ( $E_{lab} = 20A, 30A, 40A, 80A$  and  $158A$  GeV) and RHIC ( $\sqrt{s_{NN}} = 62.4$  and  $200$  GeV) energies. In the UrQMD 1.3 model the mean multiplicity per number of projectile nucleons is significantly larger in Pb+Pb collisions in comparison to n+p interactions. The model predictions are compared to a parametrization of the experimental data on p+p interactions [63] using Eq. 2.17. Except for top RHIC energies the parametrisation of the experimental data is in agreement with the UrQMD result for p+p interactions.

The energy dependence of scaled variance in full phase space is shown in Fig. 7.8, right. An increase of scaled variance with increasing collision energy is observed for p+p, n+p and Pb+Pb collisions. For AGS and low SPS energies  $\omega(h^+)$  and  $\omega(h^-)$  are smaller than one and the multiplicity distributions are narrower than the corresponding Poisson distributions. For higher energies the scaled variance is larger than one. A similar behaviour of p+p and n+p collisions is observed. The small difference is probably caused by the additional proton in p+p collisions, which does not fluctuate. This may be the reason why the scaled variance for positively and all charged particles is a bit lower in p+p than in n+p collisions. The scaled variance in Pb+Pb collisions behaves similar as in p+p (n+p) interactions.

For positively and negatively charged hadrons the scaled variance is similar, where the values are about twice as high for all charged hadrons. This is probably partly due to resonances decaying into two oppositely charged particles. Such a resonance is detected as two charged particles, therefore the fluctuations are increased.

Fig. 7.8 shows that the energy dependence of scaled variance predicted by the UrQMD model is very different to the predictions of the statistical models (section 7.1) [55]. In the grand-canonical (GCE), canonical (CE) and micro-canonical (MCE) ensemble the scaled variance stays constant for high energies, where in the UrQMD model it strongly increases with energy. Thus, experimental data on multiplicity fluctuations, preferably at high (RHIC, LHC) energies, should be able to distinguish between statistical and string-hadronic models.

The HSD transport approach [112], following a similar strategy as the UrQMD model, yields

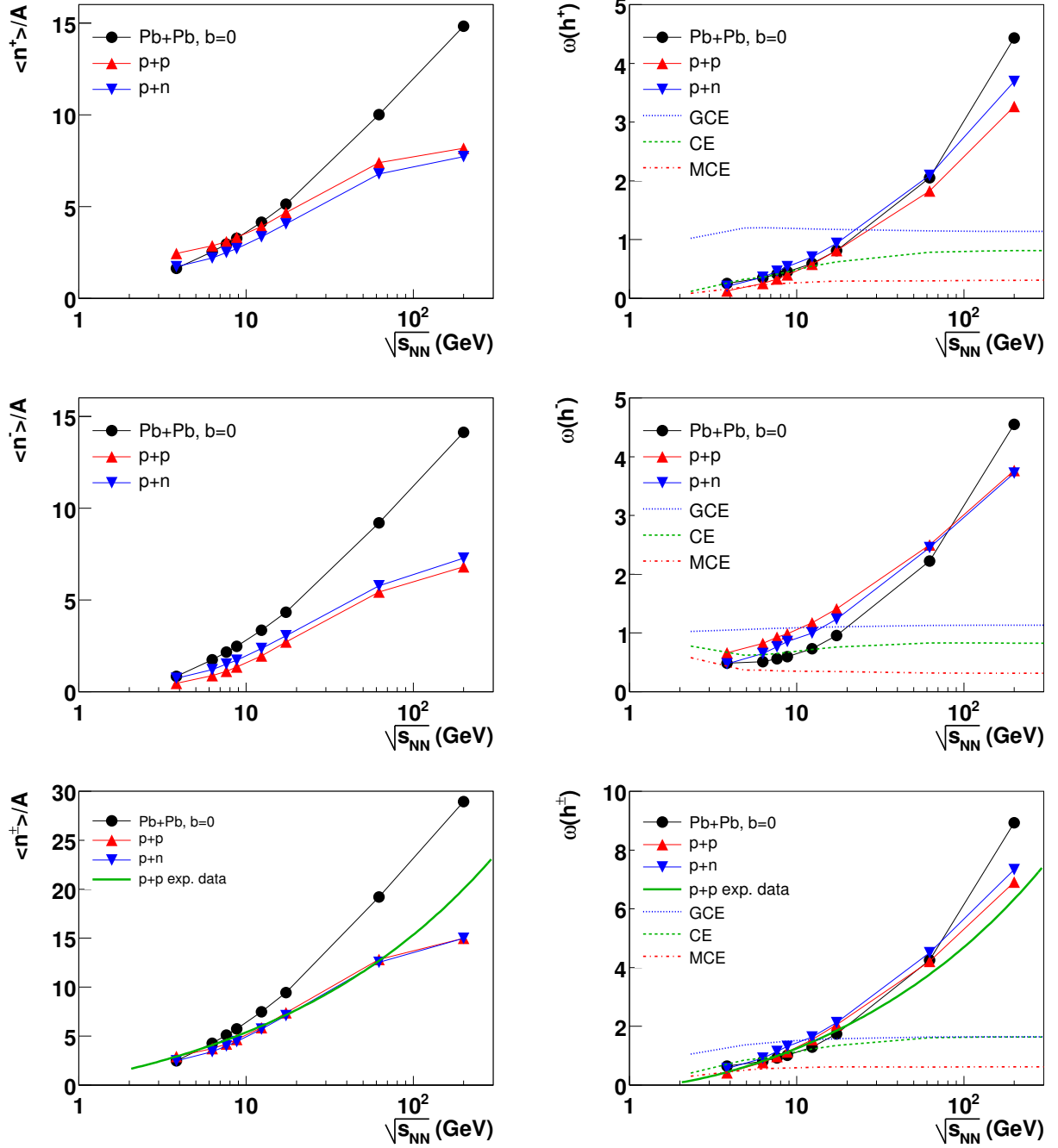


Figure 7.8: UrQMD calculations for the mean multiplicity (left) and scaled variance (right) in  $4\pi$  of inelastic p+p, n+p and central Pb+Pb collisions as a function of collision energy [98]. The scaled variance is compared to statistical model predictions (section 7.1) [55] for Pb+Pb collisions. Top: positively, middle: negatively, bottom: all charged hadrons.

7 Multiplicity Fluctuations in Central Collisions: Models and Discussion

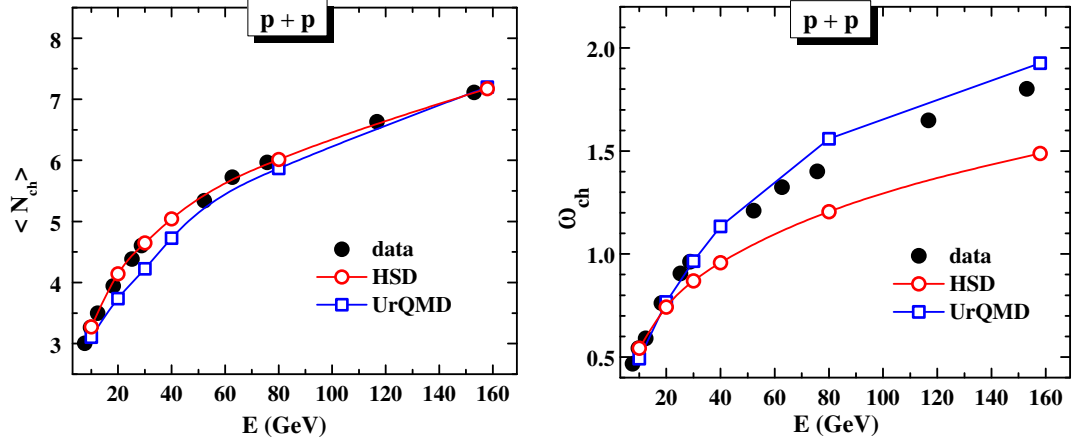


Figure 7.9: Mean multiplicity (left) and scaled variance (right) of charged hadron multiplicity in all inelastic p+p collisions [99]. The open circles and squares (connected by solid lines) show the results of HSD and UrQMD, respectively, whereas the full circles present the experimental data from Ref. [63].

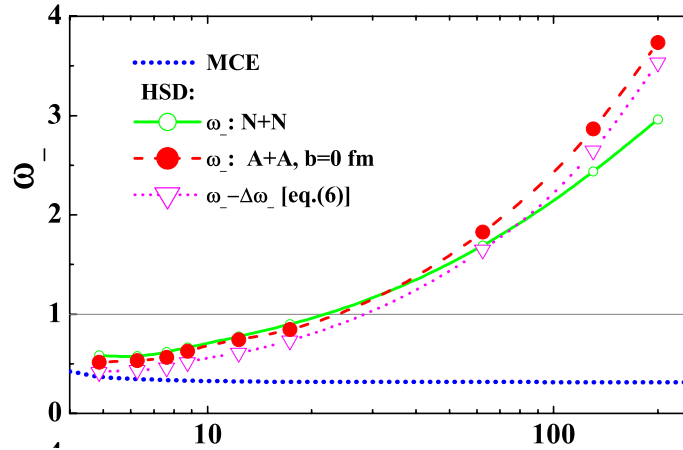


Figure 7.10: HSD predictions [113] for the energy dependence of the scaled variance in the full phase-space for nucleus-nucleus (N+N) and central (b=0) Pb+Pb collisions.



similar results for the scaled variance. The mean multiplicity and scaled variance of charged particles in all inelastic p+p interactions obtained by UrQMD, HSD and by experiment (a parametrization is taken from [63]) are compared for the SPS energy regime in Fig. 7.9. Both models describe the mean multiplicity of the data,  $\omega$  is slightly over-predicted by UrQMD and slightly under-predicted by HSD [99]. The energy dependence for central ( $b = 0$ ) Pb+Pb collisions obtained by the HSD model are presented in [113] (Fig. 7.10). The scaled variance in the full phase space increases with collision energy, both for p+p and central Pb+Pb collisions, similar to the predictions of UrQMD. In terms of multiplicity fluctuations UrQMD and HSD acts like superposition models, when the fluctuations of the number of participants in Pb+Pb collisions are added to the fluctuations obtained for p+p collisions according to Eq. 2.9, the total multiplicity fluctuations in Pb+Pb collisions are reproduced (see magenta triangles in Fig. 7.10).

### Calculations for a Limited Acceptance

For a more differential study of fluctuations and for a better comparison to the experimental data three different rapidity intervals, one at mid-rapidity  $0 < y < 1$ , one at forward rapidity  $1 < y < y_{beam}$  and a combination of both  $0 < y < y_{beam}$ , covering most of the forward hemisphere, are taken. These rapidity intervals correspond to the intervals used for the experimental data, however for the model calculations in this section full acceptance in these intervals is assumed. For n+p collisions the forward hemisphere includes the rapidity of the projectile neutron. The mean multiplicity and the scaled variance for these intervals for positively, negatively and all charged particles are shown in Figs. 7.11-7.13.

As in full phase space, in the three different rapidity intervals a similar behaviour of scaled variance of p+p, n+p and Pb+Pb collisions is observed.

The energy dependence of fluctuations in the forward hemisphere ( $0 < y < y_{beam}$ ) looks similar to the one in the full phase space, the absolute number of scaled variance is similar to the result expected when applying the acceptance extrapolation according to Eq. 2.7 (shown as stars in Figs. 7.11-7.13).

For low energies a large fraction of particles is in the mid-rapidity interval ( $0 < y < 1$ ) where a very small amount of particles is in the forward rapidity interval ( $1 < y < y_{beam}$ ). With increasing energy both the width and the number of particles in the forward rapidity interval increases strongly, where the number of particles in the forward rapidity interval increases only weakly.

At mid-rapidity ( $0 < y < 1$ ) the scaled variance is in the same order of magnitude as in the rapidity interval  $0 < y < y_{beam}$ , but the mean multiplicity is much lower. The acceptance extrapolation Eq. 2.7 strongly under-predicts fluctuations in this rapidity region. At forward rapidity ( $1 < y < y_{beam}$ ) the fluctuations are much smaller than predicted by the acceptance extrapolation formula. For lower energies the scaled variance decreases with energy, for higher energies it increases. This non-monotonous behaviour can be qualitatively understood by the interplay of an increasing fraction of particles in this rapidity interval and an increasing scaled variance in  $4\pi$ , which is smaller than 1 for lower and larger than 1 for higher energies.

### Comparison to Experimental Data

In the UrQMD model it is possible to include both the acceptance and the method of centrality selection of the NA49 experiment. This is vital for the interpretation of the experimental data

7 Multiplicity Fluctuations in Central Collisions: Models and Discussion

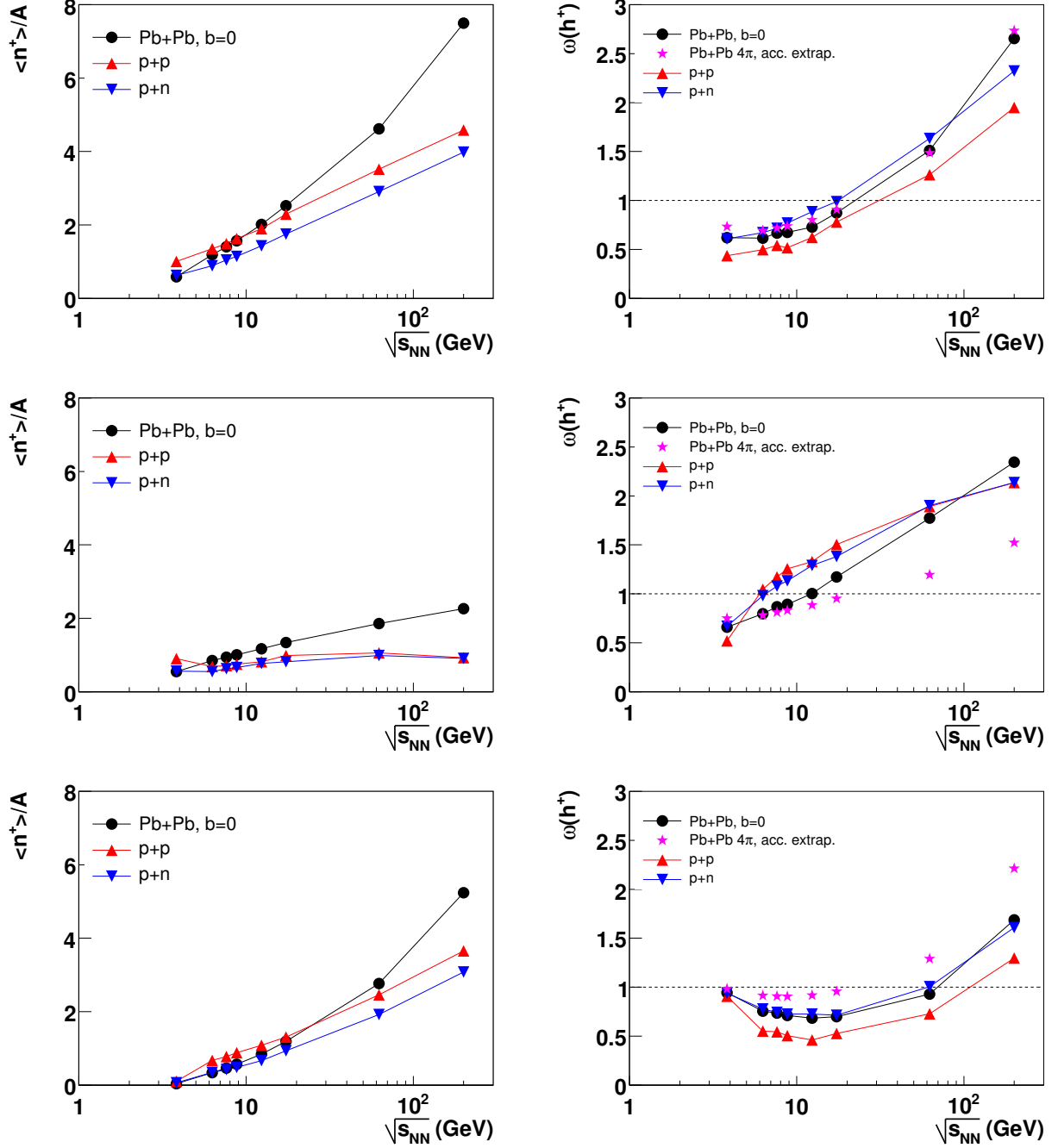


Figure 7.11: UrQMD calculations for the mean multiplicity (left) and scaled variance (right) of positively charged hadrons produced in inelastic p+p, n+p and central Pb+Pb collisions as a function of collision energy [98]. Top:  $0 < y < y_{beam}$ , middle:  $0 < y < 1$ , bottom:  $1 < y < y_{beam}$ .

## 7.2 String-Hadronic Models

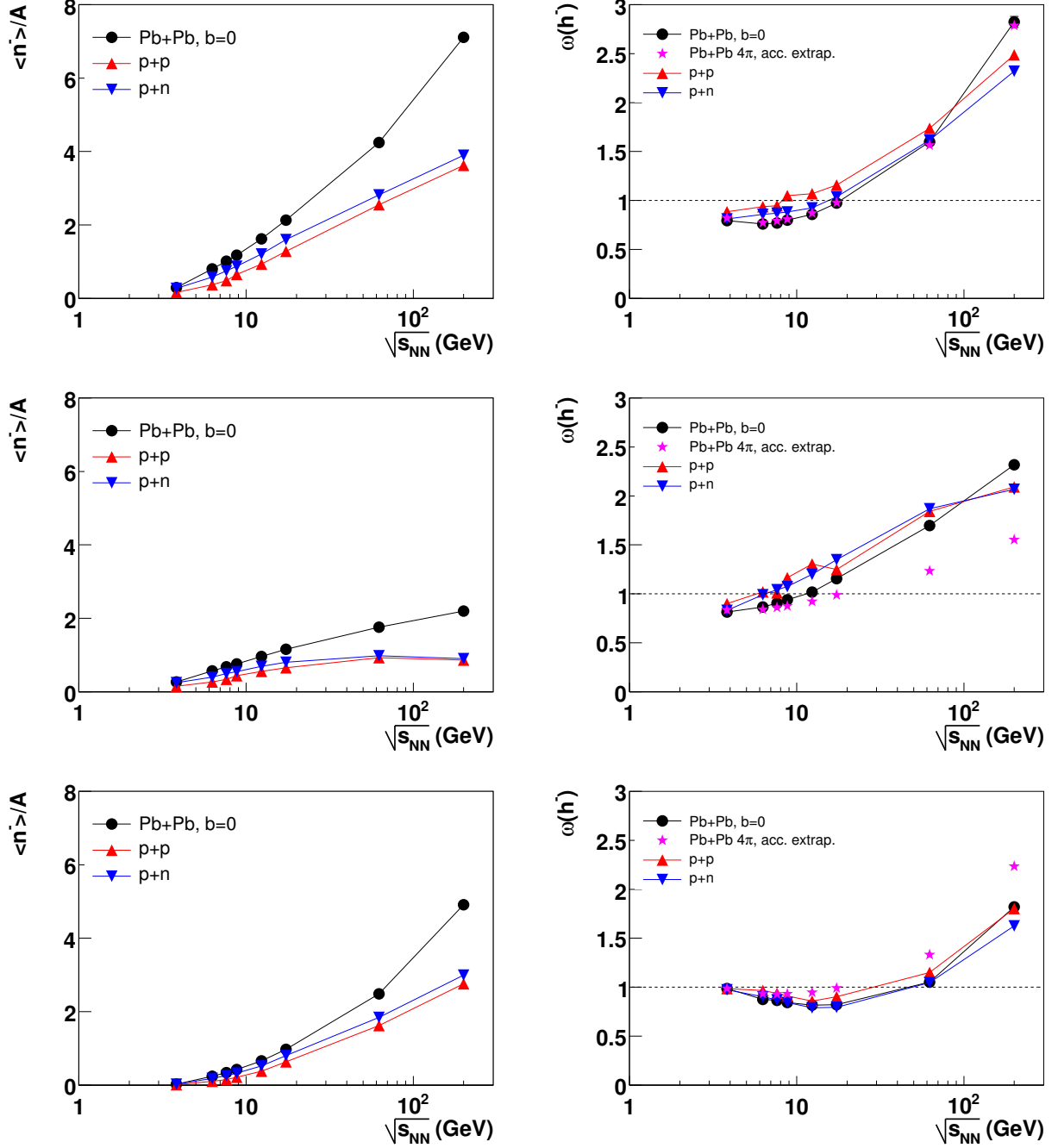


Figure 7.12: UrQMD calculations for the mean multiplicity (left) and scaled variance (right) of negatively charged hadrons produced in inelastic p+p, n+p and central Pb+Pb collisions as a function of collision energy [98]. Top:  $0 < y < y_{beam}$ , middle:  $0 < y < 1$ , bottom:  $1 < y < y_{beam}$ .

7 Multiplicity Fluctuations in Central Collisions: Models and Discussion

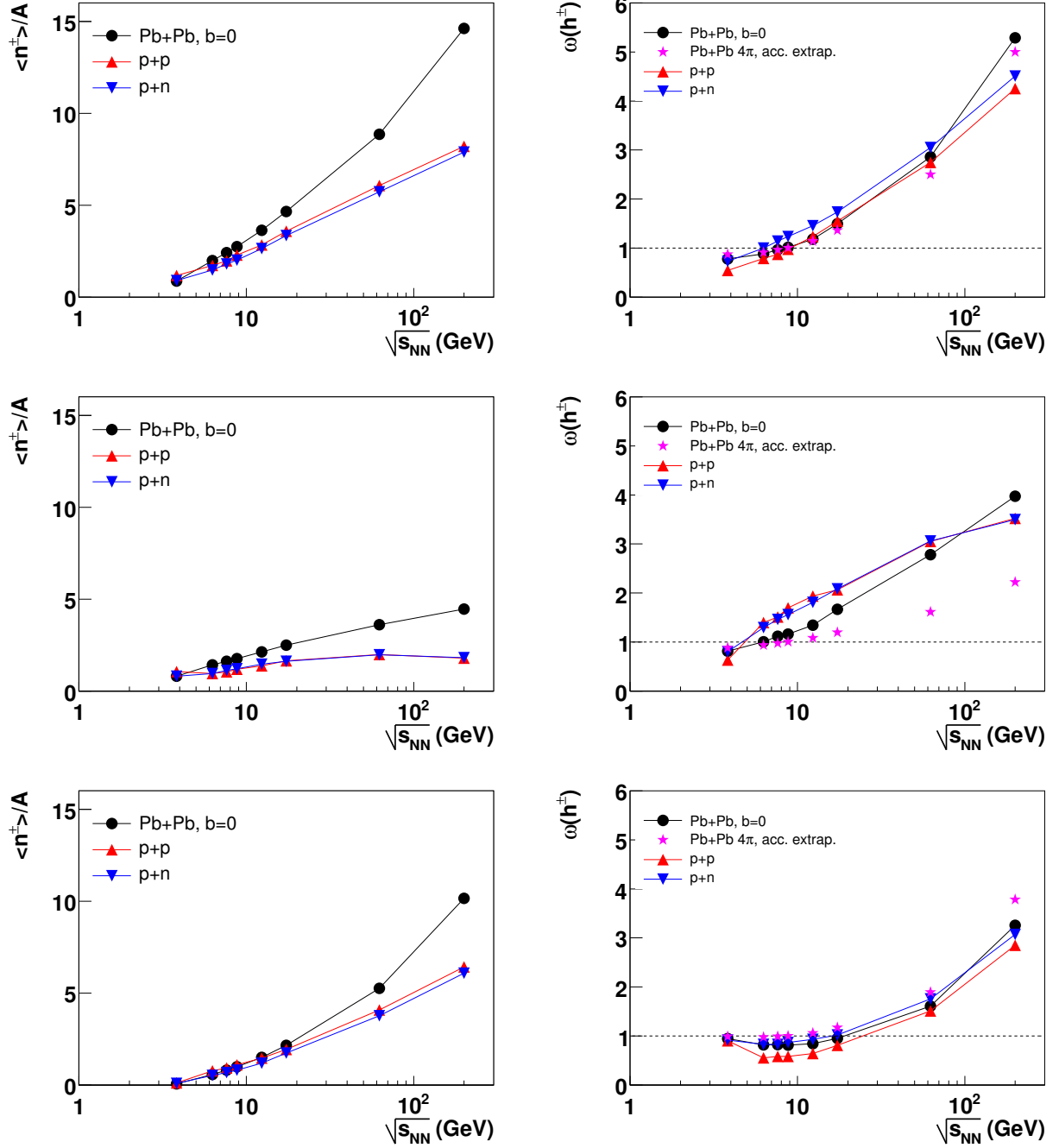


Figure 7.13: UrQMD calculations for the mean multiplicity (left) and scaled variance (right) of all charged hadrons produced in inelastic p+p, n+p and central Pb+Pb collisions as a function of collision energy [98]. Top:  $0 < y < y_{beam}$ , middle:  $0 < y < 1$ , bottom:  $1 < y < y_{beam}$ .

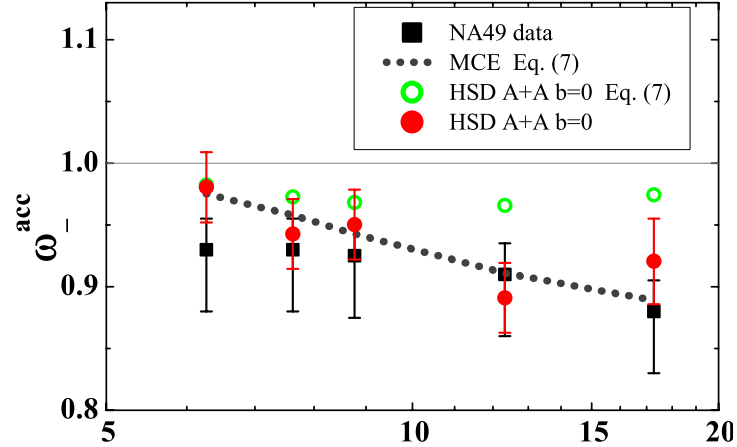


Figure 7.14: HSD predictions for the energy dependence of scaled variance in a limited region of the forward acceptance (solid points) in comparison to the preliminary NA49 data [83]. The open points show the  $4\pi$  HSD results, the broken line the predictions of the micro-canonical hadron-gas model, both extrapolated to experimental acceptance using Eq. 2.7.

because the scaled variance is predicted to depend on the acceptance in a non-trivial way. For the experimental method of centrality selection participant fluctuations might remain, which are expected to increase scaled variance. In order to compare the UrQMD model to the experimental data, both the acceptance and the centrality selection of the NA49 experiment have to be taken into account. The predictions of the model, published in [98], are shown in comparison to the experimental data in Figs. 6.2-6.4.

Two different centrality selections are used in the model: first, collisions with zero impact parameter (open circles), second the 1% most central collisions selected in the same way as done in the experimental data (section 4.2) using a simulation of the acceptance of the veto calorimeter (full dots).

The UrQMD model with collisions selected by their energy in the veto calorimeter is mostly in agreement with data for Pb+Pb collisions at all energies, acceptances and charges. UrQMD simulation of events with zero impact parameter ( $b = 0$ ) gives similar results in the forward rapidity region, whereas  $\omega$  is smaller in the midrapidity and the full experimental regions, probably due to target participant fluctuations, which are still present for events selected by their forward going energy, but not for collisions with a zero impact parameter.

The deviation of the multiplicity distribution from a Poisson distribution is similar in the model and in the data (Fig. 7.5), but the mean multiplicity is over-predicted in the UrQMD model for all rapidity intervals, charges and energies by about 20%. However, the scaled variance of the multiplicity distribution is independent of mean multiplicity for superposition models. Since it was shown that UrQMD behaves like a superposition model for  $\omega$ , it is justified to compare  $\omega$  for data and UrQMD even though the mean multiplicities are different. Within this framework one might speculate that the particle production sources in UrQMD are properly modeled but the number of sources is overestimated in central Pb+Pb collisions.

The HSD predictions are compared to the preliminary NA49 data on multiplicity fluctuations [83] and are found to agree in the forward acceptance (Fig. 7.14). An extrapolation of the scaled variance obtained by HSD in the full phase to the experimental acceptance accord-

ing to Eq. 2.7 (shown as green circles in Fig. 7.14) fails to reproduce both the theoretical and experimental results obtained for the limited phase space. Unfortunately HSD calculations for the larger acceptance of the final data are not available yet.

### 7.2.2 System Size Dependence of $\omega$

HSD and UrQMD predictions for the energy and system size dependence of multiplicity fluctuations are presented in [99]. In order to search for the critical point a two-dimensional scan in the energy and the system size of the colliding nuclei is planned by the NA61 collaboration [114, 115]. NA49 results on scaled variance are available for C+C and Si+Si collisions at 158A GeV (section 6.3).

#### Participant Fluctuations

Fluctuations in the number of participants cause additional fluctuations in multiplicity (section 2.1.2). The fluctuations in the number of participants for central collisions of small systems are studied within the HSD and UrQMD models. The number of projectile and target spectators are defined as the number of protons and neutrons in the rapidity range of 0.31 around beam and target rapidity, respectively.

Two different centrality selections are discussed. Firstly collisions with a zero impact parameter ( $b = 0$ ) are selected, secondly the 1% most central collisions according to the number of projectile spectators, similar to the experimental procedure.

The mean and the scaled variance of the number of participants obtained by HSD and UrQMD simulations for collisions with  $b = 0$  are shown in Fig. 7.15. For Pb+Pb collisions most of the incoming nuclei are participating in the collision whereas for small systems the fraction of spectators is large ( $\approx 40\%$ ), even for collisions with a zero impact parameter. The relative fluctuations of the number of participants are small for Pb+Pb collisions but increases strongly with decreasing system size. The constrain of a zero impact parameter does not fix the number of participants for collisions of small systems.

The mean and the scaled variance of the number of participants for the 1% most central collisions selected according to their number of projectile spectators are shown in Fig. 7.16. For collisions of small systems the mean number of participants are much larger and their fluctuations are much smaller for the 1% most central events than for  $b = 0$  collisions. For Pb+Pb it is the opposite, for  $b = 0$  the mean number is larger and the relative fluctuations are smaller. The selection of the 1% most central events, similar to the procedure used in the NA49 and planned to use in the NA61 experiment, is therefore preferable for small systems.

For a fixed number of projectile participants the target participants still fluctuate. The centrality dependence of target participants for nucleons of different sizes are shown in Fig. 7.17. An increase of the scaled variance of target participants  $\omega_P^{targ}$  is observed when going from central to peripheral collisions, for very peripheral collisions they decrease again. For large collision systems  $\omega_P^{targ}$  is negligible for  $N_P^{proj} = A$ , but for small colliding systems like  $C + C$   $\omega_P^{targ}$  is still significant.

#### Results for System Size Dependence

The energy and system size dependence of scaled variance obtained by the UrQMD and HSD models for collisions with  $b = 0$  is shown in Fig. 7.18. A strong dependence of  $\omega$  on system

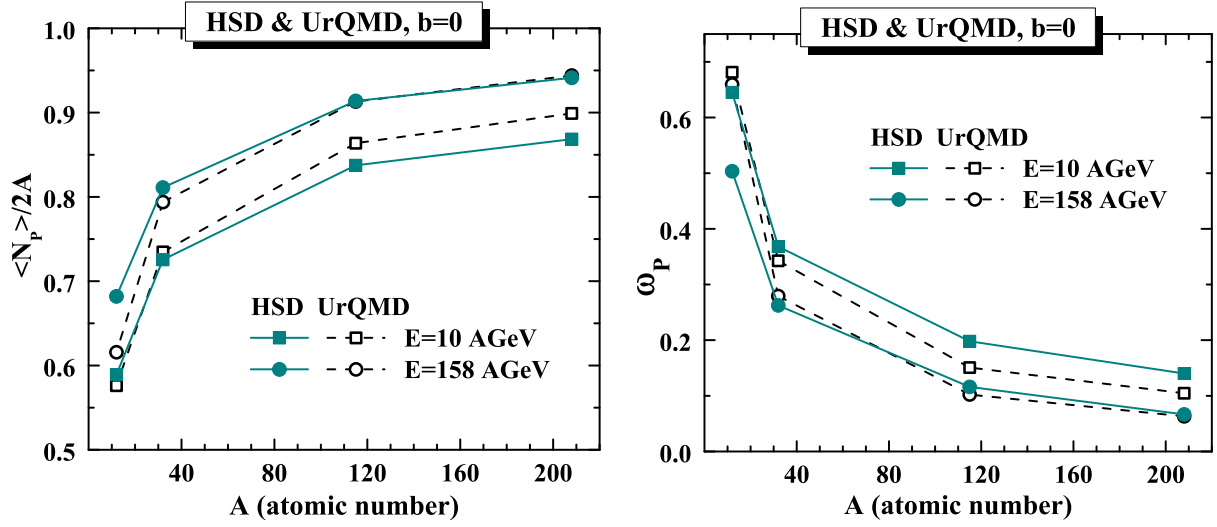


Figure 7.15: Left: Mean  $\langle N_P \rangle$ , divided by the maximum number of participants  $2A$  in events with  $b = 0$  for different nuclei at collision energies  $E_{lab}=10$  and  $158A$  GeV. Right: The scaled variance  $\omega_P$  in events with  $b = 0$  for different nuclei at collision energies  $E_{lab}=10$  and  $158A$  GeV.

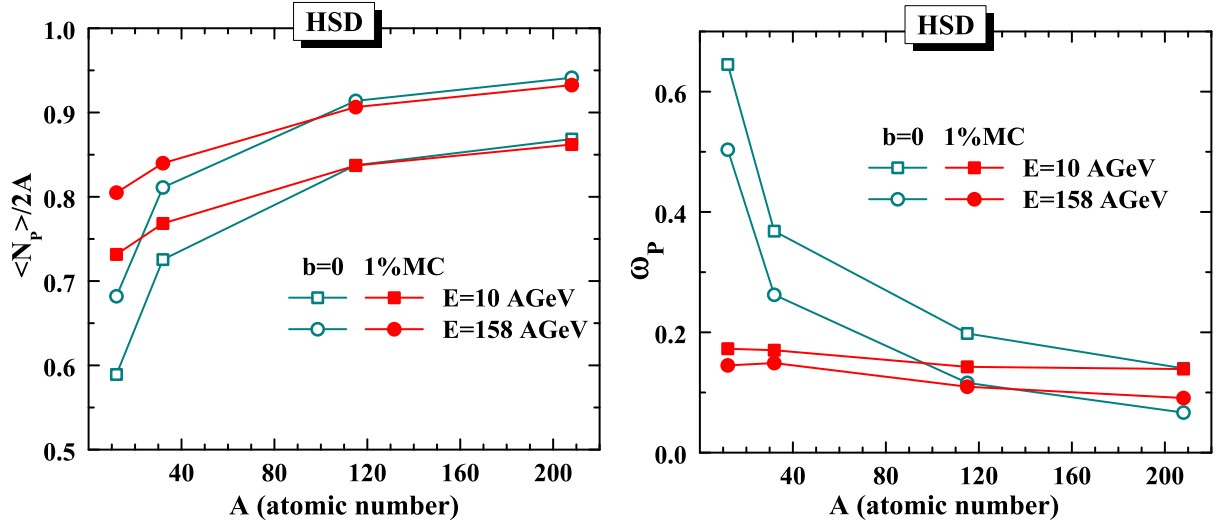


Figure 7.16: The HSD results for the ratio  $\langle N_P \rangle / 2A$  (left) and  $\omega_P$  (right) for the 1% most central collisions selected by the largest values of  $N_P^{proj}$  (full symbols) and for  $b = 0$  collisions (open symbols) for different nuclei at collision energies from  $E_{lab} = 10A$  to  $158A$  GeV [99].

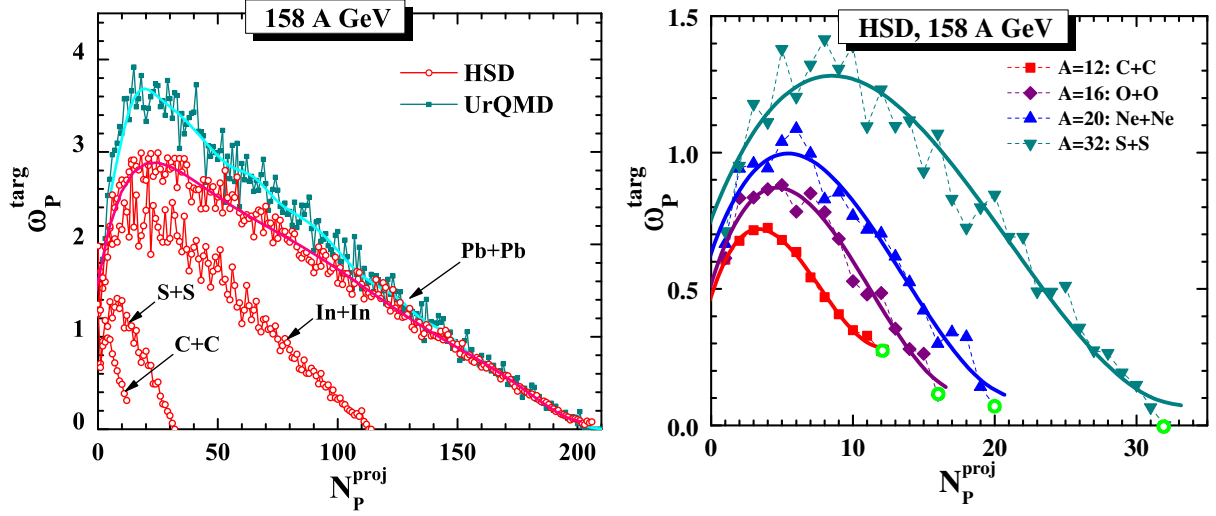


Figure 7.17: Left: The scaled variance  $\omega_P^{targ}$  for the fluctuations of the number of target participants,  $N_P^{targ}$ . The HSD simulations of  $\omega_P^{targ}$  as a function of  $N_P^{proj}$  are shown for different colliding nuclei,  $In + In$ ,  $S + S$ , and  $C + C$  at  $E_{lab}=158A$  GeV [99]. The HSD and UrQMD results for Pb+Pb collisions are taken from [53]. Right: The scaled variance  $\omega_P^{targ}$  for light nuclei,  $S + S$ ,  $Ne + Ne$ ,  $O + O$ , and  $C + C$  at  $E_{lab}=158A$  GeV as a function of  $N_P^{proj}$ .

size is found with a maximum of fluctuations for C+C collisions. It is suggested that this is caused by fluctuations in the number of participants [99].

For a different selection of central events, namely taking the 1% most central events according to their number of projectile spectators, the system size dependence of  $\omega$  is weaker (Fig. 7.19). A non-monotonous dependence of  $\omega$  on system size still remains, the maximum of fluctuations may be shifted from C+C to S+S collisions as an artifact of centrality selection.

As the 1% most central collisions are selected according to the number of projectile spectators, the number of projectile participants is more constrained than the number of target participants. For the UrQMD and HSD model fluctuations in the number of target participants mainly influence the target hemisphere ( $y < 0$ ) and vice versa ("transparency model", section 2.1.2). As seen in Fig. 7.20 the system size dependence of  $\omega$  is more pronounced in the target hemisphere ( $y < 0$ ) than in the projectile hemisphere ( $y > 0$ ).

### Comparison to Experimental Data

In order to compare the experimental data on scaled variance in small systems (C+C, Si+Si) to string-hadronic models both the acceptance of the TPCs and the centrality selection procedure has to be taken into account. A UrQMD simulation reproduces approximately the experimental data (section 6.3).

The scaled variance for collisions with a zero impact parameter, without an additional cut on the forward going energy, is predicted to be much larger for C+C and Si+Si collisions, opposite to the case for Pb+Pb collisions, where the fluctuations for  $b = 0$  are smaller.



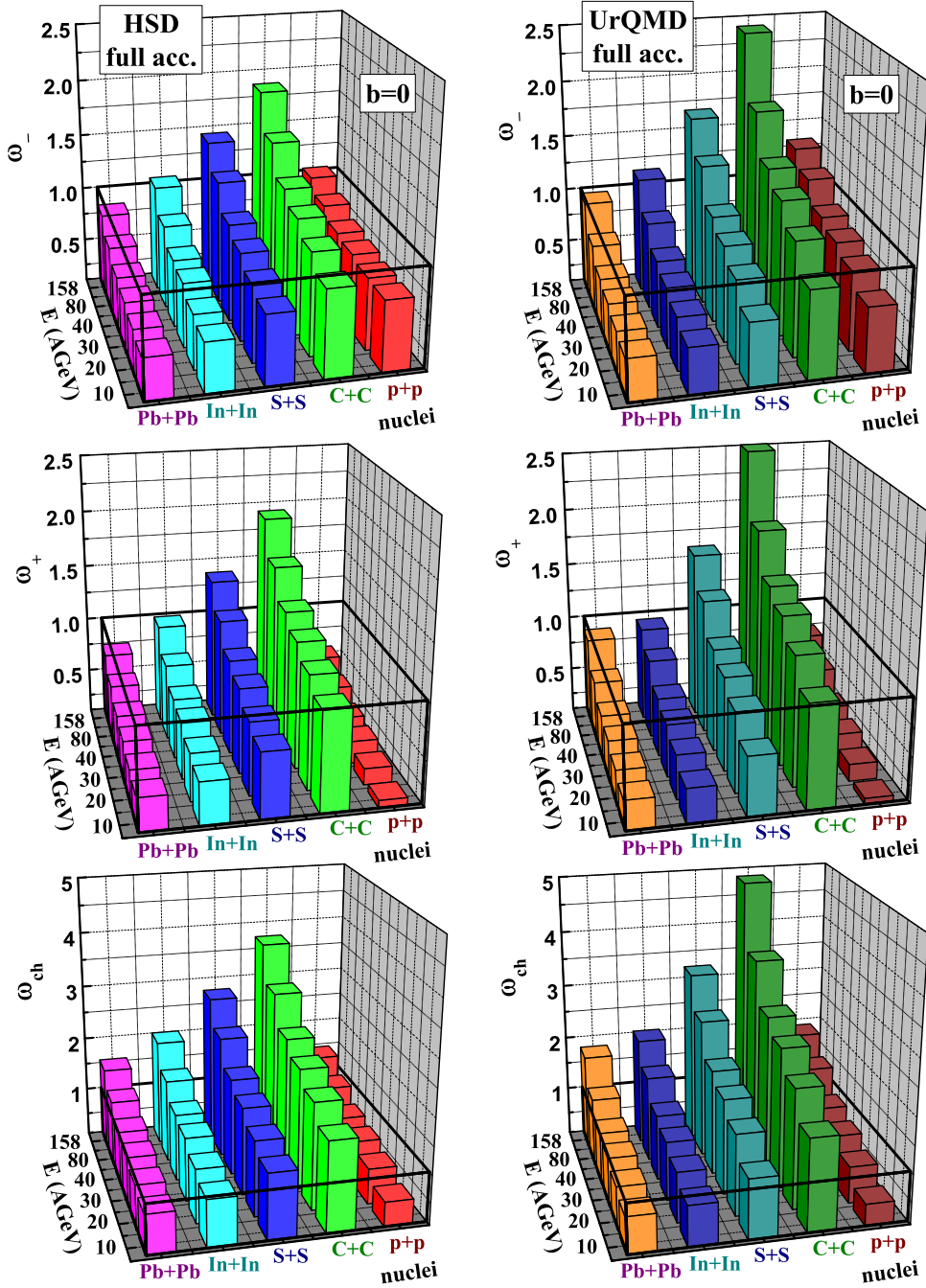


Figure 7.18: The results of HSD (left panel) and UrQMD (right panel) simulations for  $\omega(h^-)$  (top panel),  $\omega(h^+)$  (middle panel), and  $\omega(h^\pm)$  (lower panel) in  $p + p$  and central  $C + C$ ,  $S + S$ ,  $In + In$ ,  $Pb + Pb$  collisions at  $E_{\text{lab}} = 10A, 20A, 30A, 40A, 80A, 158A$  GeV in the full phase space [99]. The condition  $b = 0$  is used here as a criterion for centrality selection.

7 Multiplicity Fluctuations in Central Collisions: Models and Discussion

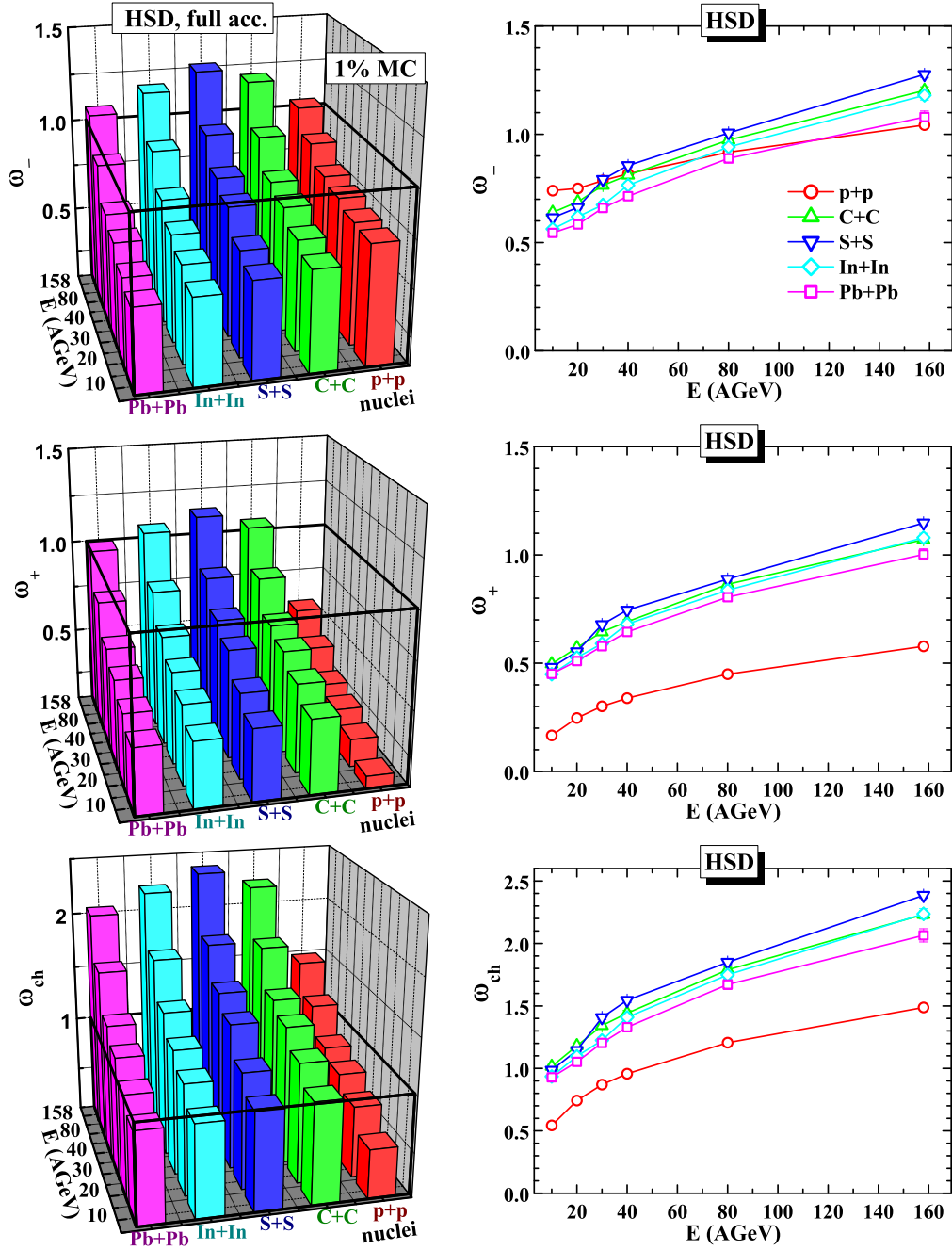


Figure 7.19: The HSD results for  $\omega(h^-)$  (upper panel),  $\omega(h^+)$  (middle panel), and  $\omega(h^\pm)$  (lower panel) in  $A + A$  and  $p + p$  collisions for the full  $4\pi$  acceptance in 3D (left) and 2D (right) projection. The 1% most central  $C + C$ ,  $S + S$ ,  $In + In$ , and  $Pb + Pb$  collisions are selected by choosing the largest values of  $N_P^{proj}$  at different collision energies  $E_{lab} = 10A, 20A, 30A, 40A, 80A, 158A$  GeV. The HSD results from inelastic  $p + p$  collisions are the same as in Fig. 7.18.

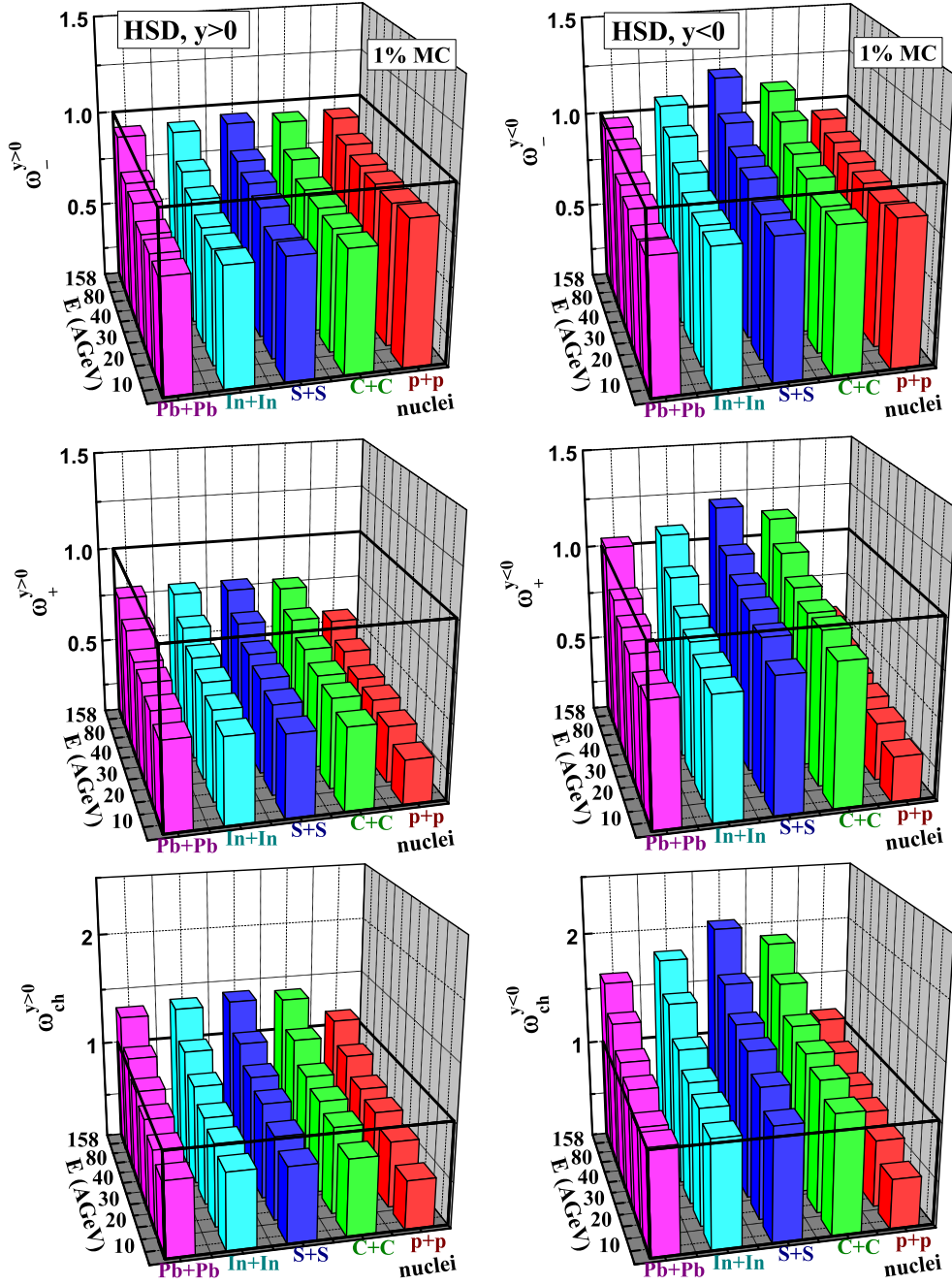


Figure 7.20: The HSD results for  $\omega(h^-)$  (upper panel),  $\omega(h^+)$  (middle panel), and  $\omega(h^\pm)$  (lower panel) in  $A + A$  and  $p + p$  collisions for  $y > 0$  (left) and  $y < 0$  (right). The 1% most central  $C + C$ ,  $S + S$ ,  $In + In$ , and  $Pb + Pb$  collisions are selected by choosing the largest values of  $N_P^{proj}$  at different collision energies  $E_{lab} = 10A, 20A, 30A, 40A, 80A, 158A$  GeV.

### 7.2.3 Rapidity and Transverse Momentum Dependence

As already showed in section 7.2.1, the scaled variance is a non-trivial function of the selected phase-space. In order to study the dependence of scaled variance on rapidity, 12 different rapidity intervals are constructed in such a way that the mean multiplicity in each interval is the same. If the scaled variance would follow the acceptance scaling Eq. 2.7, the scaled variance would be the same in each interval. In Fig. 7.21 it is shown that this is not the case. The scaled variance is much higher near mid-rapidity than in forward and backward rapidity.

This effect might be a result of energy- and momentum conservation, because it costs much more energy to create a particle with high longitudinal momentum (section 7.1). Therefore their number is expected to fluctuate much less.

The transverse momentum dependence of scaled variance is shown in Fig. 7.22 for the full longitudinal phase-space and for a mid-rapidity and a forward rapidity interval. The scaled variance decreases with increasing transverse momentum for the full acceptance and at forward rapidity. At mid-rapidity it stays approximately constant. The decrease of scaled variance is stronger for positively charged hadrons than for negatively charged ones, probably because the protons, which have smaller relative fluctuations due to the large number of protons which enter the collision, have a larger mean transverse momentum. The decrease of scaled variance for negatively charged hadrons can be attributed to energy conservation [97], like the structure in rapidity.

### Conclusion

It was shown that in full phase space the scaled variance in the string-hadronic models UrQMD and HSD increases monotonically with increasing collision energy, in contrast to the predictions of a hadron-gas model. In UrQMD and HSD  $\omega$  is similar for p+p and Pb+Pb interactions. UrQMD shows a non-trivial dependence of  $\omega$  on the selected phase-space interval, namely decreasing fluctuations for increasing  $|y|$  and  $p_T$ . When implementing the experimental acceptance and centrality selection procedure, the scaled variance of UrQMD is in agreement with the experimental data for all studied energies, collision systems and rapidity intervals.

For Pb+Pb collisions  $\omega$  for  $y > 1$  is similar when the 1% most central or  $b = 0$  collisions are selected. For  $y < 1$   $\omega$  for the 1% most central collisions is larger, probably because of target participant fluctuations. For small systems (like C+C, Si+Si)  $\omega$  for  $b = 0$  collisions is much higher than for the 1% most central collisions, selected according to the number of projectile spectators.

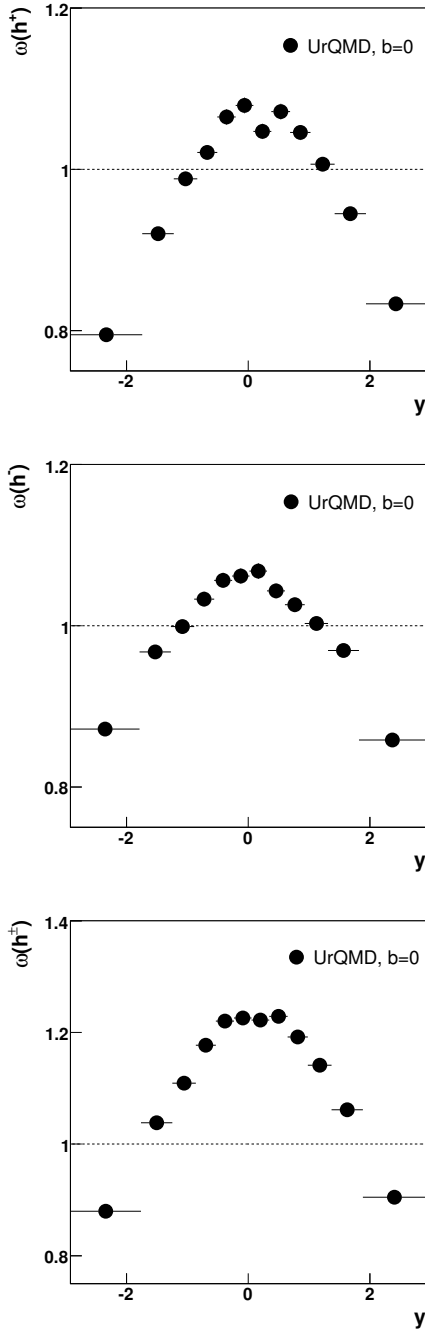


Figure 7.21: Rapidity dependence of scaled variance in UrQMD simulation performed for 158A GeV Pb+Pb collisions in full acceptance of positive (top), negative (middle) and all charged (bottom) hadrons in central Pb+Pb collisions at 158A GeV [98].

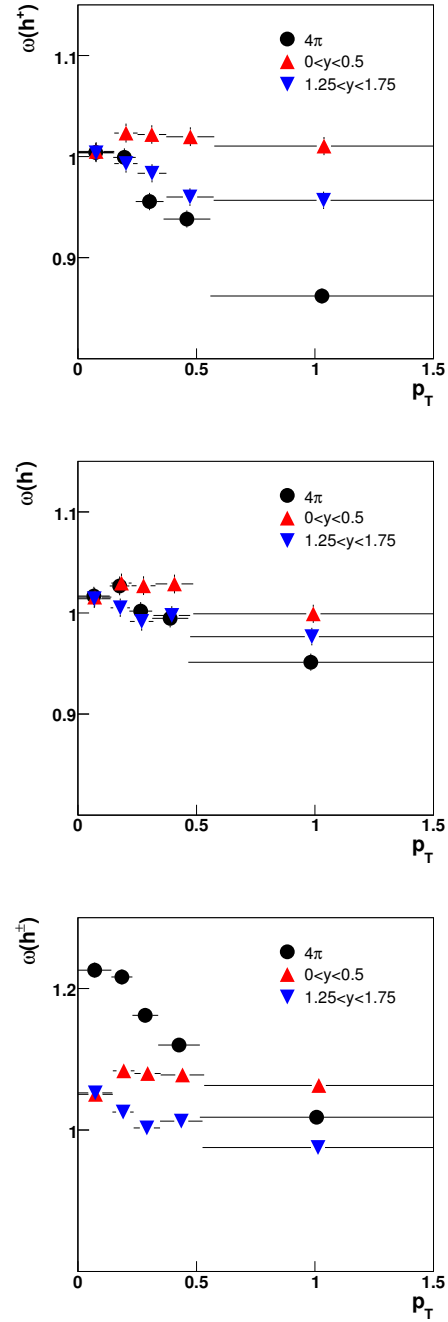


Figure 7.22: Transverse momentum dependence of multiplicity fluctuations for 158A GeV Pb+Pb collisions of positively (top), negatively (middle) and all charged hadrons (bottom) for all rapidities,  $0 < y < 0.5$  and  $1.25 < y < 1.75$  [98].

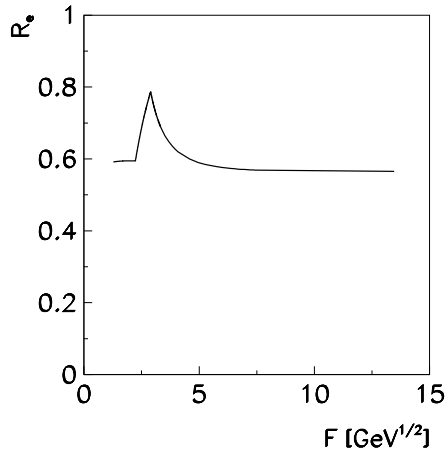


Figure 7.23:  $R_e$  as a function of collision energy, measured in the Fermi-variable  $F$  (appendix C.1.2).

### 7.3 Onset of Deconfinement

The energy dependence of various observables shows anomalies at low SPS energies which might be related to the onset of deconfinement [32, 116]. In [49] it is predicted that the onset of deconfinement should lead to additional fluctuations at medium SPS energies.

The main idea is that the inelastic energy  $E$  of a collision, the energy which is transferred from the participant nucleons to newly produced particles, fluctuates from event to event. These fluctuations in the inelastic energy lead to different fluctuations of entropy in a pure (hadron or quark) phase and in a mixed phase.

A "shark-fin" structure with a maximum near 80A GeV is predicted for the variable  $R_e$  defined as:

$$R_e = \frac{(\delta S)^2/S^2}{(\delta E)^2/E^2}, \quad (7.6)$$

where  $S$  is the entropy of the system.  $R_e$  is approximately 0.6 both in the hadron and quark gluon plasma phase, in the mixed phase it can reach values up to 0.8. In order to compare the predictions to the measured scaled variance, it is assumed that the fluctuations in entropy lead to the additional dynamical multiplicity fluctuations. In the mixed phase the fluctuations in inelastic energy are predicted to cause larger additional multiplicity fluctuations than in the pure hadronic and pure quark phase. These fluctuations should add to the background multiplicity fluctuations. The background fluctuations should have a monotonous behaviour, therefore a non-monotonous behaviour of total multiplicity fluctuations is expected at SPS energies.

The inelasticity of a heavy ion collision is measured by the parameter  $K$ , which is the ratio of the inelastic energy to the maximum inelastic energy which is allowed by momentum and baryon number conservation:

$$K = \frac{\langle E \rangle}{N_W/2 \cdot (\sqrt{s_{NN}} - 2m_N)}. \quad (7.7)$$

When the participant nucleons are fully stopped,  $K = 1$  and the inelastic energy is the largest. For the determination of the inelasticity parameter it is assumed in the model calculation that the inelastic energy is carried by the mesons produced in the collision.

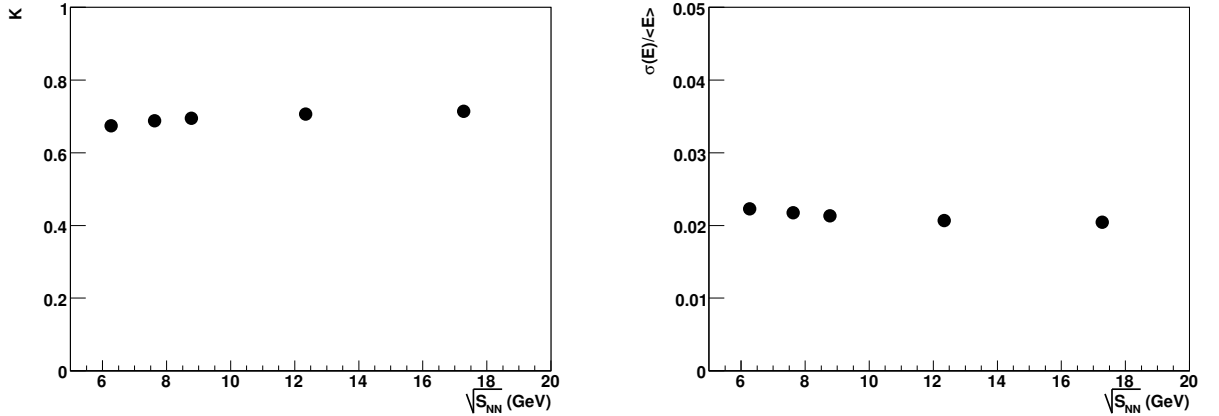


Figure 7.24: Left: UrQMD simulation of the energy dependence of the inelasticity parameter  $K$ . Right: Fluctuations in the inelastic energy as a function of energy.

The UrQMD model predicts the inelasticity parameter  $K$  to be around 0.7 at SPS energies (Fig. 7.24, left). This is in agreement with the experimental NA49 and NA35 data [117].

The fluctuations in the inelastic energy of the collision are estimated by the UrQMD model to be  $\delta E/E \approx 0.02$  for all SPS energies (Fig. 7.24, right). With these assumptions the additional multiplicity fluctuations can be estimated by [55]:

$$\omega_{dyn} \approx \frac{(\delta E)^2}{E^2} \cdot \langle n \rangle \cdot R_e. \quad (7.8)$$

For 80A GeV the mean multiplicity of negative hadrons in forward acceptance is  $\langle n^- \rangle = 93.4$ . If the system would not be in the mixed phase, the increase of scaled variance caused by fluctuations in the energy which goes into produced particles is predicted to be  $\omega_{dyn} \approx 0.02$ . For the maximum in  $R_e$  in the mixed phase  $\omega_{dyn}$  is  $\approx 0.03$ . Therefore the predicted increase of  $\omega$  due to the mixed phase is 0.01.

Unfortunately this value is smaller than the systematic error on the measurement of scaled variance, therefore the data can neither support nor disprove the existence of a mixed phase at SPS energies.

## 7.4 Critical Point

In the phase diagram of strongly interacting matter it is expected that the hadron gas and quark-gluon-plasma regions are separated by a first order phase transition line at high baryo-chemical potentials and lower temperatures. For higher temperatures and lower baryo-chemical potentials a cross-over between both phases is expected. The first order phase transition and the cross-over should be separated by a critical point (section 1.2).

If the freeze-out of the matter happens near the critical point large fluctuations, for instance in multiplicity and transverse momentum, are expected. In [50] it is estimated that the scaled variance in  $4\pi$  should increase by at least 0.1 near the critical point. These critical fluctuations are predicted to be located mainly at low transverse momenta. Unfortunately the dependence of the critical fluctuation on the phase space region used for the data analysis is presently unknown.

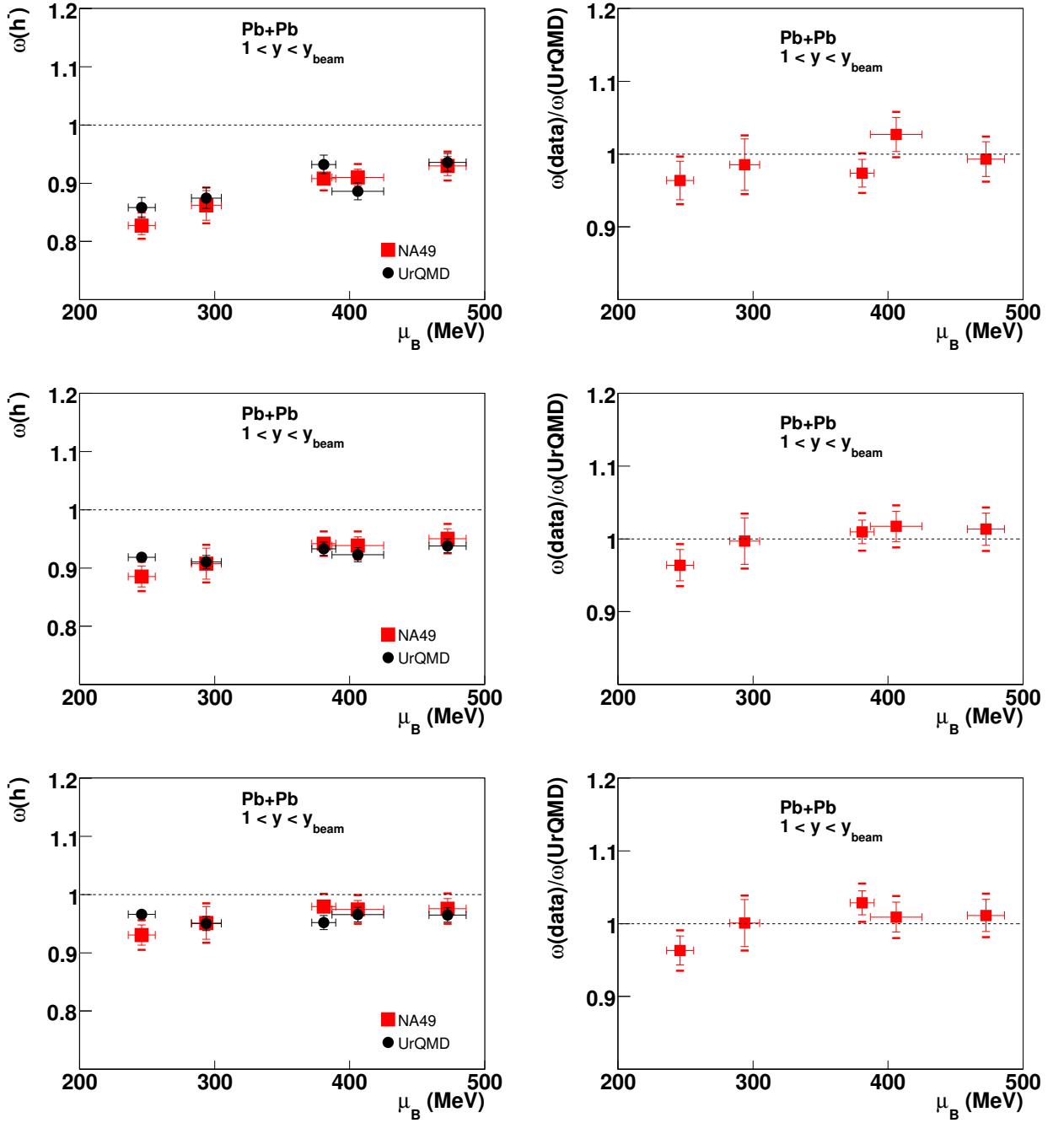


Figure 7.25: Left: Scaled variance  $\omega$  of the multiplicity distribution of negatively charged hadrons at forward rapidities produced in central Pb+Pb collisions as a function of the baryo-chemical potential  $\mu_B$  [13]. The UrQMD results are given for a centrality selection similar to the experimental data. Right: Ratio of  $\omega$  in data and UrQMD as a function of  $\mu_B$ . Top: full  $p_T$  range, middle:  $p_T < 0.5$  GeV, bottom:  $p_T < 0.3$  GeV.



The scaled variance as a function of the baryo-chemical potential is shown in Fig. 7.25, both for the experimental data and the UrQMD model, which may serve as a baseline in the search for the critical point. An excess of  $\omega$  over the UrQMD baseline of 0.1 or more can be excluded by the data. This suggests that either the chemical freeze-out of Pb+Pb collisions at the SPS energy range is not in the vicinity of the critical point or the signal of the critical point is too small in the experimental acceptance.

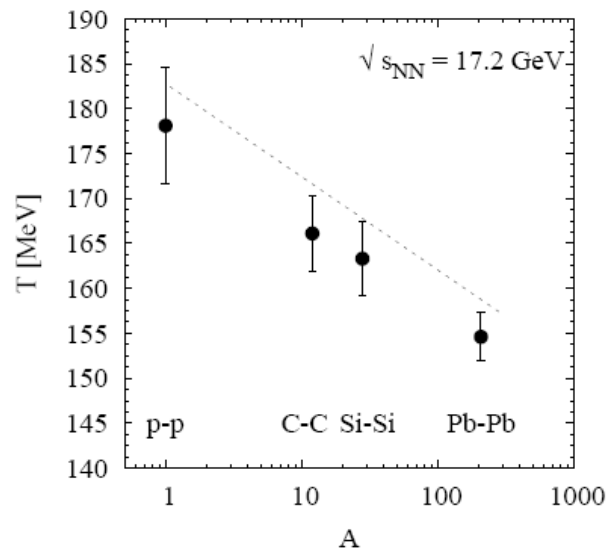


Figure 7.26: Chemical freeze-out temperature obtained by a hadron-gas model fit [13] as a function of the size of the collision system.

In order to look for the critical point not only the collision energy but also the system size of the colliding nuclei can be varied. Hadron-gas model fits to the mean multiplicities of produced particles show that the chemical freeze-out of the collision happens at larger temperatures  $T$  for smaller systems [13] (Fig. 7.26). The baryo-chemical potential  $\mu_B$  is more or less independent of the system size, but depends strongly on the collision energy. By varying both the energy and the system size of the colliding nuclei it is possible to vary the position of the chemical freeze-out point in the  $T$ - $\mu_B$ -plane.

The scaled variance of the multiplicity distributions for C+C and Si+Si collisions at 158A GeV is larger than for Pb+Pb (section 6.3). This increase can be attributed to larger participant fluctuations in smaller systems and is approximately reproduced by the UrQMD model. No indication for an additional increase of  $\omega$  due to the freeze-out in the vicinity of the critical point is observed.

In order to find the critical point the NA61 experiment [114, 115], the successor of NA49, plans to make both an energy and a system size scan by measuring p+p, C+C, S+S and In+In collisions at 10A, 20A, 30A, 40A, 80A and 158A GeV. UrQMD and HSD baseline calculations for scaled variance are shown in section 7.2.2 and in [99].

## 7.5 First Order Phase Transition

It is suggested in [118] that droplets of hadronic matter should be formed in matter when the system crosses the first order phase transition line during cool-down. These droplets are expected to produce multiplicity fluctuations 10-100 times larger than the Poisson expectation in the full phase space. No predictions of the increase of  $\omega$  for the limited experimental acceptance are available, but naively it can be expected to be in the order of 1-10 (according to Eq. 2.7).

In our acceptance an excess of multiplicity fluctuations with respect to the UrQMD baseline, which does not include an explicit phase transition, of larger than 0.1 can be excluded (see Fig. 7.25). This suggests that either the matter at these collision energies does not cross a first order phase transition line during cool-down or the droplet picture is incomplete.

In particular it has to be pointed-out that the predictions of the droplet model were derived neglecting energy and momentum conservation. The calculation within the hadron-resonance gas model using the the micro-canonical ensemble shows that resonance decays decrease the multiplicity fluctuations in contrast to the strong increase for grand-canonical and canonical ensembles. The resonances can be treated as small droplets and thus the micro-canonical results show that for any significant physics conclusions concerning the formation of droplets in nuclear collisions calculations obeying energy-momentum conservation are needed.

## 8 Additional Observables

In this chapter additional observables, which may be related to multiplicity fluctuations, are presented. As these observables are not the main subject of this thesis these results have to be considered as very preliminary. In particular no detailed study of systematic effects was done.

### 8.1 Multiplicity Correlations

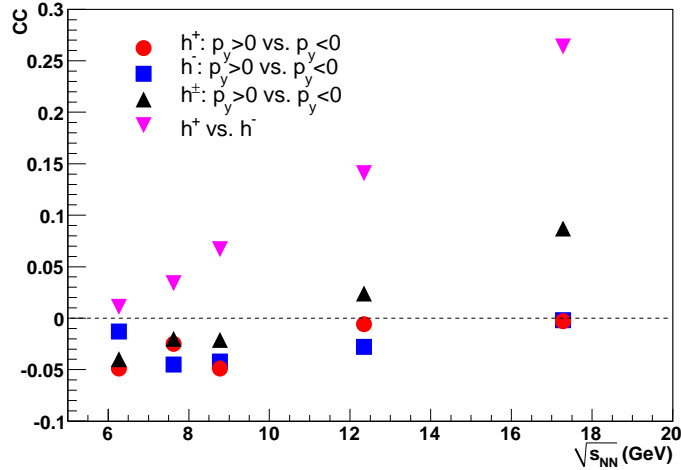


Figure 8.1: Energy dependence of the correlation coefficient for multiplicity correlations in momentum and charge.

Multiplicity correlations may provide an additional insight into the nature of multiplicity fluctuations. The covariance describes the correlation of two observables  $X$  and  $Y$ .

$$Cov(X, Y) = \sum_{x, y} P(x, y)(x - \langle x \rangle)(y - \langle y \rangle) \quad (8.1)$$

It is  $> 0$  for a positive and  $< 0$  for a negative (or anti-) correlation. Note that the definition of the covariance gives the variance for  $X = Y$ .

The correlation coefficient is defined as a normalized covariance which is  $+1$  when the two observables are totally correlated and  $-1$  when they are totally anti-correlated.

$$CC(X, Y) = \frac{Cov(X, Y)}{\sqrt{Var(X)Var(Y)}} \quad (8.2)$$

The correlations of the multiplicity of particles with a positive and a negative momentum in  $y$ -direction ( $p_Y$ ) are as well as the correlation of the multiplicity of positively and negatively

charged particles are studied. The multiplicity correlations are obtained for the 1% most central collisions in the forward acceptance described in section 4.3.2. The 2-dimensional correlation plots are shown in appendix A, the energy dependence of the correlation coefficient is shown in Fig. 8.1.

Global fluctuations in particle multiplicity, for instance caused by fluctuations in the number of participant nucleons, are expected to cause a correlation between particles of positive and negative  $p_y$ . Energy conservation is expected to lead to an anti-correlation. This is because the available total energy for particle production is fixed, more particles with negative  $p_y$  means less energy available for the production of particles with positive  $p_y$ . The momentum conservation should create a correlation between positive and negative  $p_y$ . In addition resonances decaying into two particles which are both used for the correlation analysis will lead to a positive correlation.

For positively and negatively charged particles separately the correlation coefficient is negative for all energies, the particle multiplicities in both momentum intervals are anti-correlated (Figs. A.19 and A.20). This suggests that the effect of energy conservation is larger than the effects causing a positive correlation. The effect of resonance decays is small because only a small number of resonances decay into two (or more) positively or two negatively charged daughters. For all charged particles the correlation coefficient is negative for lower energies but positive for higher ones ( $\geq 80A$  GeV) (Fig. A.21). This suggests that the influence of resonance decays increases with energy and the correlations start to be larger than the anti-correlations at intermediate SPS energies.

For the correlation of the multiplicity of positively and negatively charged particles the correlations due to global multiplicity fluctuations and resonance decays as well as the anti-correlation due to energy conservation are expected to be also present. In addition charge conservation introduces a correlation between the multiplicity of positive and negative particles. In figure A.22 it is shown that the correlation coefficient is positive for all energies, suggesting that the correlation due to charge conservation and resonance decays overbalances the anti-correlation due to energy conservation.

## 8.2 $\Delta\phi$ - $\Delta\eta$ - Correlations

Strong two-particle correlations may influence multiplicity fluctuations. The correlations in pseudo-rapidity ( $\eta$ ) and azimuthal angle ( $\phi$ ) are studied in detail for  $\sqrt{s_{NN}} = 200$  GeV by the STAR collaboration [119]. For this study the probability for two particles in one event to have a specific difference in their pseudo-rapidity and azimuthal angle  $P(\Delta\phi\Delta\eta)$  is calculated. In order to remove detector effects such as limited acceptance,  $P(\Delta\phi\Delta\eta)$  is also calculated for mixed events, where two particles from different collisions are combined and therefore no "physical" correlations are present. The correlation function is defined as

$$C(\Delta\phi\Delta\eta) = \frac{P(\Delta\phi\Delta\eta, data)}{P(\Delta\phi\Delta\eta, mixed)} - 1. \quad (8.3)$$

In this section first results of the  $\Delta\phi$ -  $\Delta\eta$ - correlations in very central (1% most central) Pb+Pb collisions of NA49 are shown. Note that these results are very preliminary and no systematic studies are done, but they may provide a starting point for a further analysis.

The correlation function is shown for pairs of positively, pairs of negatively and pairs of oppositely charged particles in Fig. 8.2 for 158A GeV. The overall magnitude of the correlations

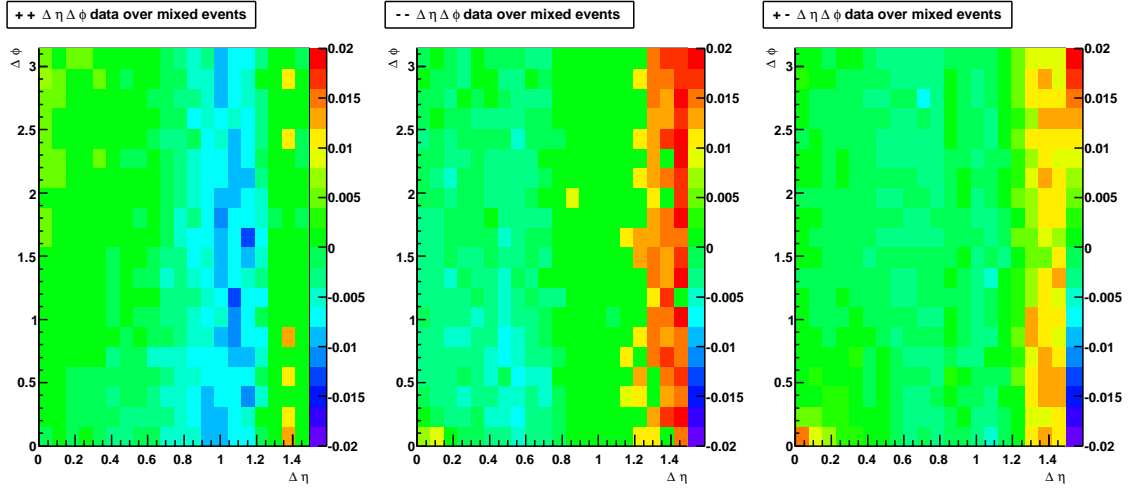


Figure 8.2: Correlations in rapidity and azimuthal angle for positive, negative and mixed charged particle pairs for the 1% most central Pb+Pb collisions at 158A GeV.

is low, the correlations are smaller than 3% for all  $\Delta\phi$ ,  $\Delta\eta$ . This is in qualitative agreement with the STAR results where the correlations are of the order of 1%.

A maximum of correlations is observed for large  $\Delta\eta$ . The origin of this effect is presently not understood, it might be related to energy- and momentum conservation or to experimental effects. For small  $\Delta\phi$  and  $\Delta\eta$  a maximum is observed for negatively and oppositely charged pairs. For negatively charged pairs it can be related to Bose-Einstein-Correlations which increases the probability for pion pairs to have the same momentum and overbalances the Coulomb repulsion due to the electrical charge. For oppositely charged particles the maximum at small momentum differences can be attributed to Coulomb attraction.

## 8 *Additional Observables*

## 9 Summary

In this work data of the NA49 experiment at CERN SPS on the energy dependence of multiplicity fluctuations in central Pb+Pb collisions at 20A, 30A, 40A, 80A and 158A GeV, as well as the system size dependence at 158A GeV, is analysed for positively, negatively and all charged hadrons. Furthermore the rapidity and transverse momentum dependence of multiplicity fluctuations are studied. The experimental results are compared to predictions of statistical hadron-gas and string-hadronic models.

It is expected that multiplicity fluctuations are sensitive to the phase transition to quark-gluon-plasma (QGP) and to the critical point of strongly interacting matter. It is predicted that both the onset of deconfinement, the lowest energy where QGP is created, and the critical point are located in the SPS energy range. Furthermore, the predictions for the multiplicity fluctuations of statistical and string-hadronic models are different, the experimental data might allow to distinguish between them.

The used measure of multiplicity fluctuations is the scaled variance  $\omega$ , defined as the ratio of the variance and the mean of the multiplicity distribution.

In the NA49 experiment the tracks of charged particles are detected in four large volume time projection chambers (TPCs). In order to remove possible detector effects a detailed study of event and track selection criteria is performed. The total selected experimental acceptance ( $0 < y(\pi) < y_{beam}$ ) is divided into a “midrapidity” ( $0 < y(\pi) < 1$ ) and a “forward rapidity” ( $1 < y(\pi) < y_{beam}$ ) region.

Fluctuations in the number of participant nucleons in the collisions are a trivial, but difficult to control, source of multiplicity fluctuations. In the NA49 experiment the number of projectile spectators is measured by a veto calorimeter so that the number of projectile participants can be fixed. Model studies show that in non-central collisions for a fixed number of projectile participants the number of target participants still fluctuates significantly. In order to avoid these fluctuations very central collisions are selected for this analysis.

Naively one would expect Poisson fluctuations in central heavy ion collisions. A suppression of fluctuations compared to a Poisson distribution is observed for positively and negatively charged hadrons at forward rapidity in Pb+Pb collisions. At midrapidity and for all charged hadrons the fluctuations are larger than the Poisson ones. The fluctuations seem to increase with decreasing system size. It is suggested that this is due to increased relative fluctuations in the number of participants. Furthermore, it was discovered that  $\omega$  increases for decreasing rapidity and transverse momentum.

A hadron-gas model [55] predicts different values of  $\omega$  for different statistical ensembles. In the grand-canonical ensemble, where all conservation laws are fulfilled only on the average, not on an event-by-event basis, the predicted fluctuations are the largest ones. In the canonical ensemble the charges, namely the electrical charge, the baryon number and the strangeness, are conserved for each event. The scaled variance in this ensemble is smaller than for the grand-canonical ensemble. In the micro-canonical ensemble not only the charges, but also the energy and the momentum are conserved in each event, the predicted  $\omega$  is the smallest one.

The grand-canonical and canonical formulations of the hadron-gas model over-predict fluc-

## 9 Summary

tuations in the forward acceptance. In contrast to the experimental data no dependence of  $\omega$  on rapidity and transverse momentum is expected. For the micro-canonical formulation, which predicts small fluctuations in the total phase space, no quantitative calculation is available yet for the limited experimental acceptance. The increase of fluctuations for low rapidities and transverse momenta can be qualitatively understood in a micro-canonical ensemble as an effect of energy and momentum conservation.

The string-hadronic model UrQMD [98] significantly over-predicts the mean multiplicities but approximately reproduces the scaled variance of the multiplicity distributions at all measured collision energies, systems and phase-space intervals. String-hadronic models predict for Pb+Pb collisions a monotonous increase of  $\omega$  with collision energy, similar to the observations for p+p interactions. This is in contrast to the predictions of the hadron-gas model, where  $\omega$  shows no energy dependence at higher energies. At SPS energies the predictions of the string-hadronic and hadron-gas models are in the same order of magnitude, but at RHIC and LHC energies the difference in  $\omega$  in the full phase space is much larger. Experimental data should be able to distinguish between them rather easily.

Narrower than Poissonian ( $\omega < 1$ ) multiplicity fluctuations measured in the forward kinematic region ( $1 < y(\pi) < y_{beam}$ ) can be related to the reduced fluctuations predicted for relativistic gases with imposed conservation laws. This general feature of relativistic gases may be preserved also for some non-equilibrium systems as modeled by the string-hadronic approaches.

A quantitative estimate shows that the predicted maximum in fluctuations due to a first order phase transition from hadron-gas to QGP [49] is smaller than the experimental errors of the present experiment and can therefore neither be confirmed nor disproved.

No sign of increased fluctuations as expected for a freeze-out near the critical point of strongly interacting matter is observed.

The future NA61 program [115] will study both the energy and system size dependence of fluctuations with increased sensitivity in a systematic search for the critical point. The main improvements in comparison to NA49 are supposed to be the higher statistics, the better centrality determination and the lower  $\delta$ -electron background. In this work a detailed study of background fluctuations in the two-dimensional energy and system-size plane within the HSD and UrQMD model using different centrality selections is performed [99]. These calculations are necessary in order to estimate background fluctuations due to variations in the number of participants for the search of the critical point.

A pilot analysis on multiplicity correlations and of long-range correlations in  $\Delta\phi$ -  $\Delta\eta$  is performed, but further work in these directions is needed.



## A Additional Plots and Tables

Scaled variance  $\omega(h^+)$  of the multiplicity distribution of positively charged hadrons:

energy	$0 < y(\pi) < y_{beam}$	$0 < y(\pi) < 1$	$1 < y(\pi) < y_{beam}$
20	$0.88 \pm 0.02 \pm 0.02$	$0.99 \pm 0.02 \pm 0.02$	$0.86 \pm 0.02 \pm 0.02$
30	$0.85 \pm 0.01 \pm 0.02$	$0.96 \pm 0.02 \pm 0.02$	$0.84 \pm 0.01 \pm 0.02$
40	$0.89 \pm 0.01 \pm 0.02$	$1.01 \pm 0.01 \pm 0.02$	$0.87 \pm 0.01 \pm 0.02$
80	$0.93 \pm 0.03 \pm 0.02$	$1.04 \pm 0.03 \pm 0.02$	$0.89 \pm 0.03 \pm 0.02$
158	$0.91 \pm 0.02 \pm 0.06$	$1.00 \pm 0.02 \pm 0.07$	$0.84 \pm 0.02 \pm 0.02$

Scaled variance  $\omega(h^-)$  of the multiplicity distribution of negatively charged hadrons:

energy	$0 < y(\pi) < y_{beam}$	$0 < y(\pi) < 1$	$1 < y(\pi) < y_{beam}$
20	$0.94 \pm 0.02 \pm 0.02$	$1.01 \pm 0.02 \pm 0.02$	$0.93 \pm 0.02 \pm 0.02$
30	$0.91 \pm 0.01 \pm 0.02$	$1.01 \pm 0.02 \pm 0.02$	$0.91 \pm 0.01 \pm 0.02$
40	$0.92 \pm 0.01 \pm 0.02$	$1.02 \pm 0.01 \pm 0.02$	$0.91 \pm 0.01 \pm 0.02$
80	$0.88 \pm 0.03 \pm 0.02$	$1.05 \pm 0.03 \pm 0.02$	$0.86 \pm 0.03 \pm 0.02$
158	$0.90 \pm 0.02 \pm 0.06$	$1.01 \pm 0.02 \pm 0.07$	$0.83 \pm 0.02 \pm 0.02$

Scaled variance  $\omega(h^\pm)$  of the multiplicity distribution of all charged hadrons:

energy	$0 < y(\pi) < y_{beam}$	$0 < y(\pi) < 1$	$1 < y(\pi) < y_{beam}$
20	$1.01 \pm 0.02 \pm 0.03$	$1.10 \pm 0.02 \pm 0.03$	$0.94 \pm 0.02 \pm 0.03$
30	$1.01 \pm 0.02 \pm 0.03$	$1.07 \pm 0.02 \pm 0.03$	$0.94 \pm 0.01 \pm 0.03$
40	$1.10 \pm 0.01 \pm 0.03$	$1.15 \pm 0.01 \pm 0.03$	$1.01 \pm 0.01 \pm 0.03$
80	$1.21 \pm 0.04 \pm 0.04$	$1.22 \pm 0.04 \pm 0.04$	$1.07 \pm 0.03 \pm 0.03$
158	$1.27 \pm 0.02 \pm 0.10$	$1.21 \pm 0.02 \pm 0.10$	$1.09 \pm 0.02 \pm 0.03$

Table A.1: Scaled variance of the multiplicity distribution of positively (top), negatively and all (bottom) charged hadrons as a function of energy.

A Additional Plots and Tables

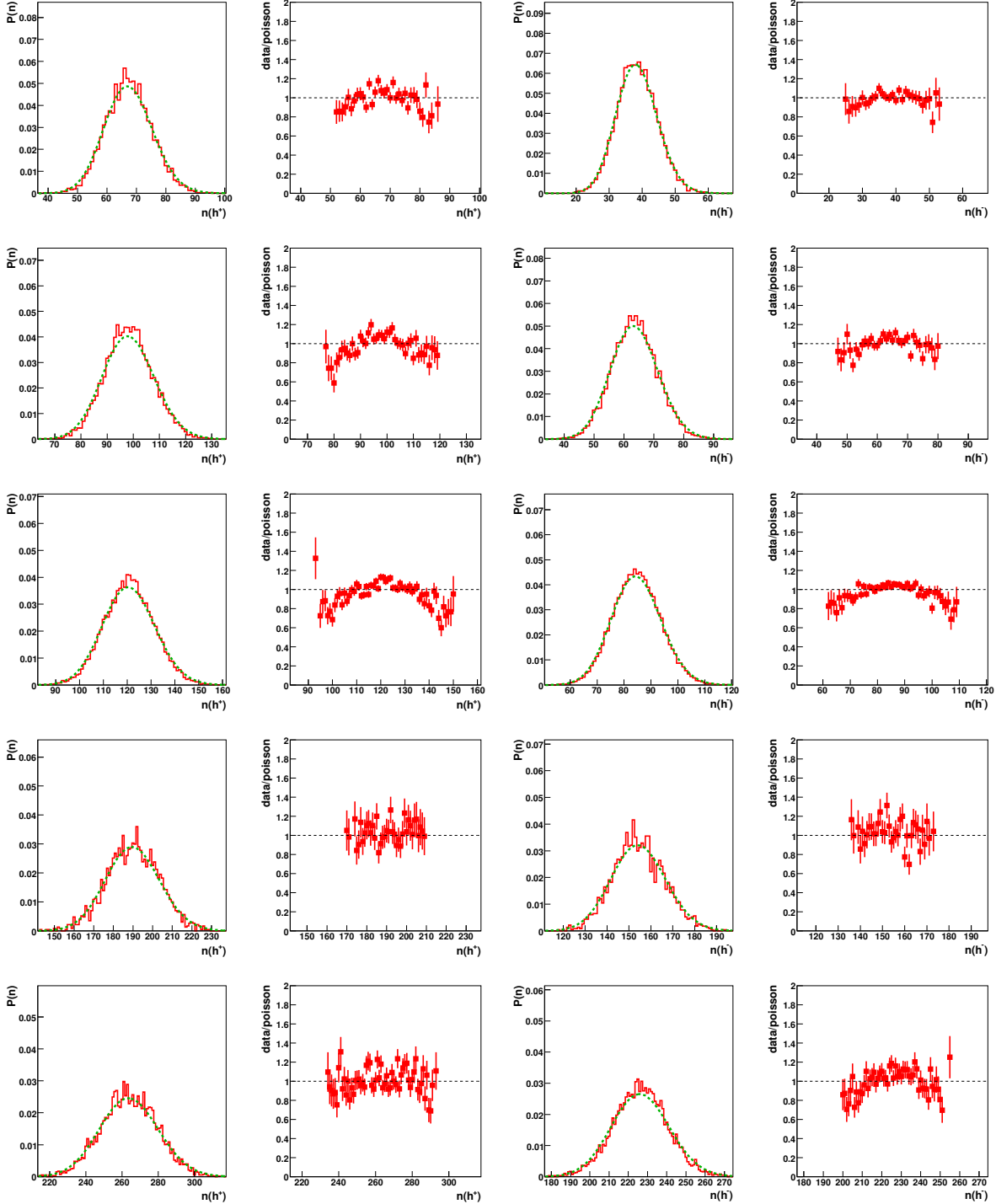


Figure A.1: Multiplicity distributions (left) and ratios to the corresponding Poisson distributions (right) of  $h^+$  in  $0 < y(\pi) < y_{beam}$  for central ( $C < 1\%$ ) Pb+Pb collisions from 20A (top) to 158A GeV (bottom).

Figure A.2: Multiplicity distributions (left) and ratios to the corresponding Poisson distributions (right) of  $h^-$  in  $0 < y(\pi) < y_{beam}$  for central ( $C < 1\%$ ) Pb+Pb collisions from 20A (top) to 158A GeV (bottom).

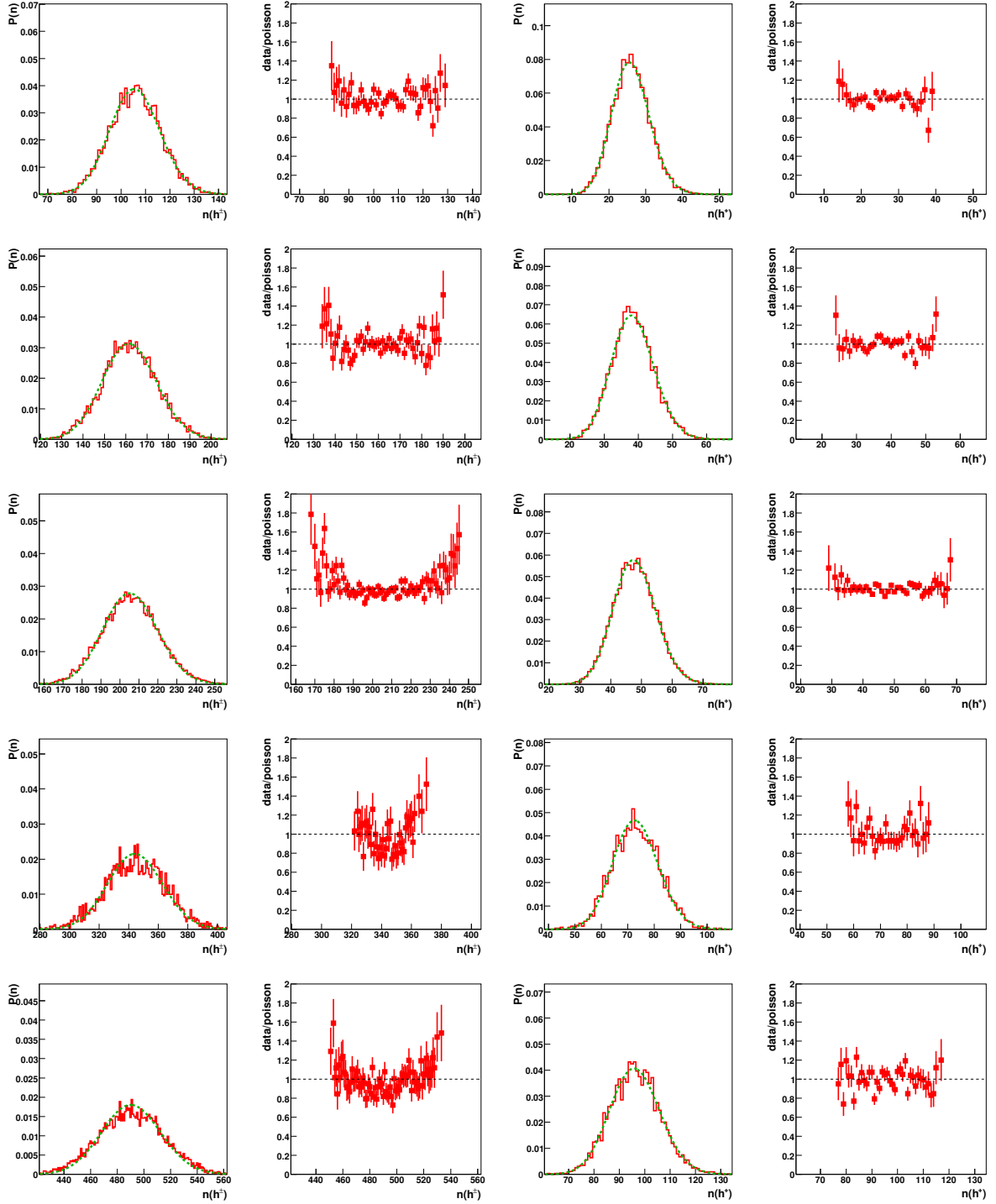


Figure A.3: Multiplicity distributions (left) and ratios to the corresponding Poisson distributions (right) of  $h^\pm$  in  $0 < y(\pi) < y_{beam}$  for central ( $C < 1\%$ ) Pb+Pb collisions from 20A (top) to 158A GeV (bottom).

Figure A.4: Multiplicity distributions (left) and ratios to the corresponding Poisson distributions (right) of  $h^+$  in  $0 < y(\pi) < 1$  for central ( $C < 1\%$ ) Pb+Pb collisions from 20A (top) to 158A GeV (bottom).

A Additional Plots and Tables

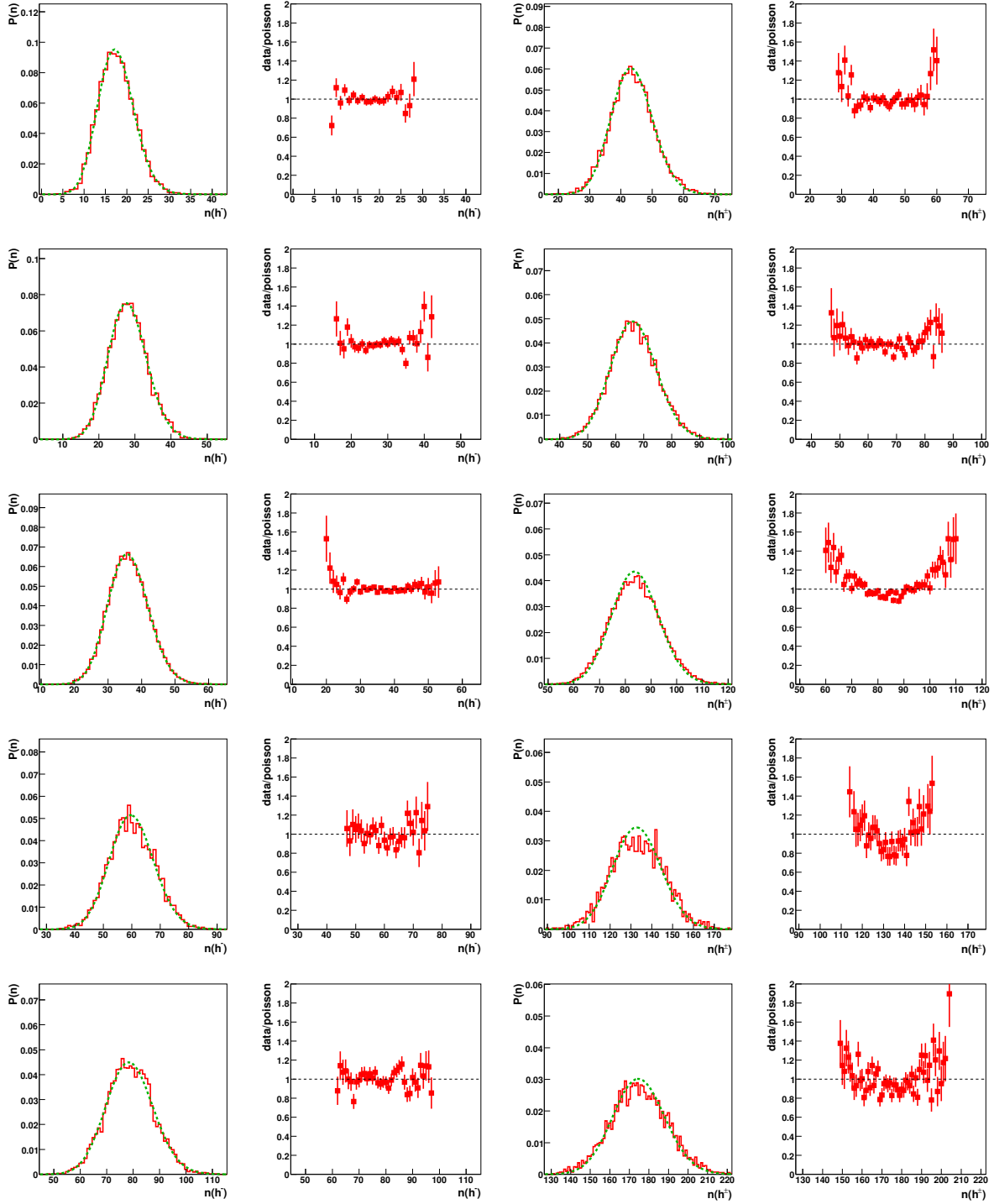


Figure A.5: Multiplicity distributions (left) and ratios to the corresponding Poisson distributions (right) of  $h^-$  in  $0 < y(\pi) < 1$  for central ( $C < 1\%$ ) Pb+Pb collisions from 20A (top) to 158A GeV (bottom).

Figure A.6: Multiplicity distributions (left) and ratios to the corresponding Poisson distributions (right) of  $h^+$  in  $0 < y(\pi) < 1$  for central ( $C < 1\%$ ) Pb+Pb collisions from 20A (top) to 158A GeV (bottom).

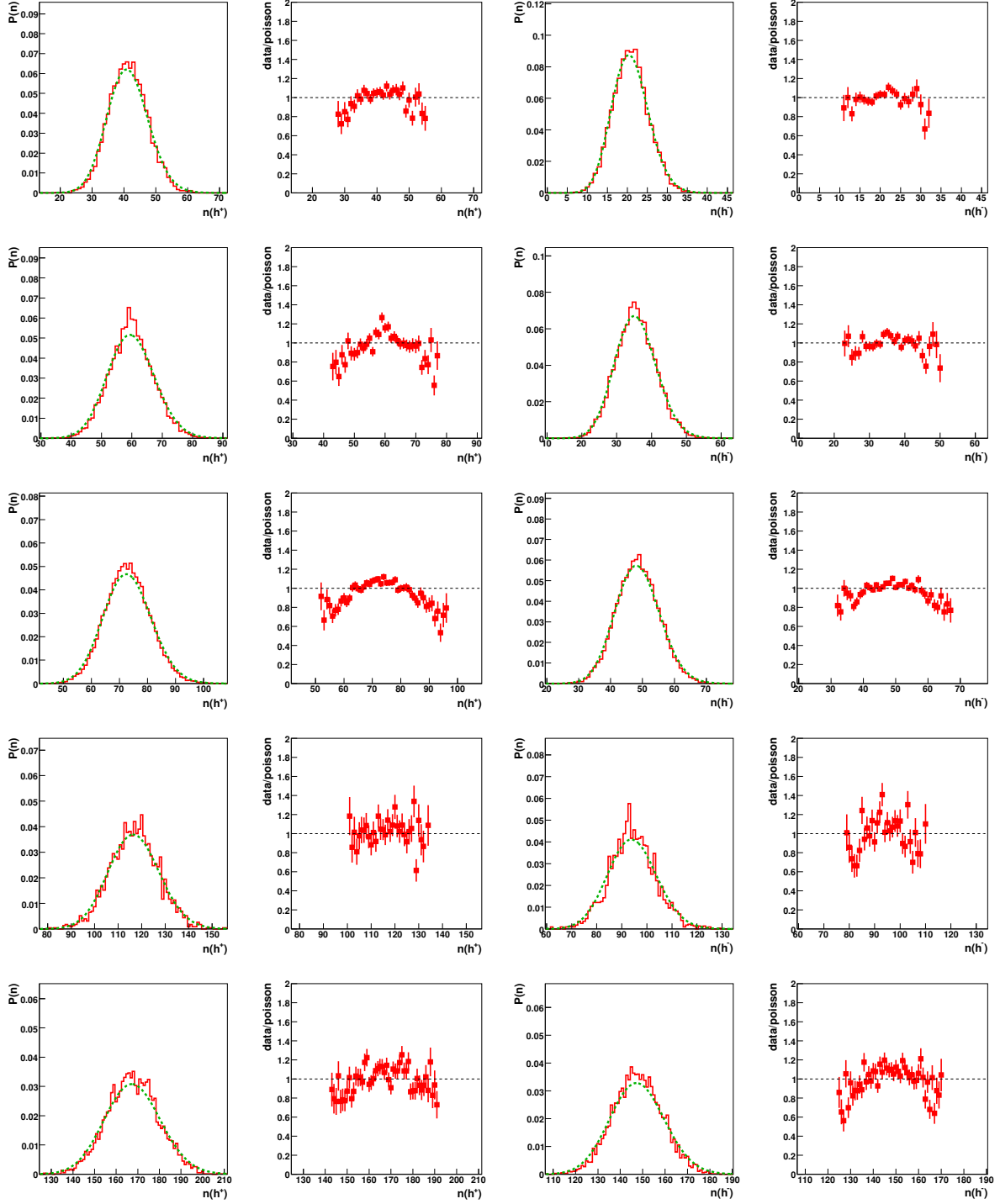


Figure A.7: Multiplicity distributions (left) and ratios to the corresponding Poisson distributions (right) of  $h^+$  in  $1 < y(\pi) < y_{beam}$  for central ( $C < 1\%$ ) Pb+Pb collisions from 20A (top) to 158A GeV (bottom).

Figure A.8: Multiplicity distributions (left) and ratios to the corresponding Poisson distributions (right) of  $h^-$  in  $1 < y(\pi) < y_{beam}$  for central ( $C < 1\%$ ) Pb+Pb collisions from 20A (top) to 158A GeV (bottom).

A Additional Plots and Tables

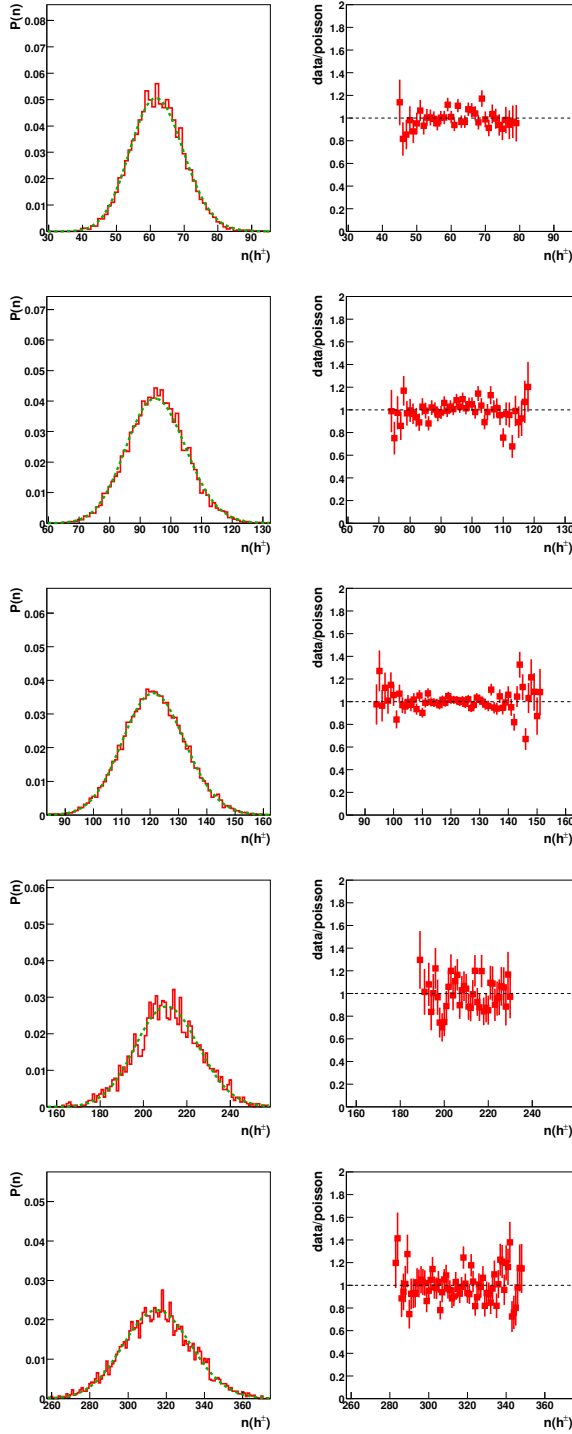


Figure A.9: Multiplicity distributions (left) and ratios to the corresponding Poisson distributions (right) of  $h^\pm$  in  $1 < y(\pi) < y_{beam}$  for central ( $C < 1\%$ ) Pb+Pb collisions from 20A (top) to 158A GeV (bottom).

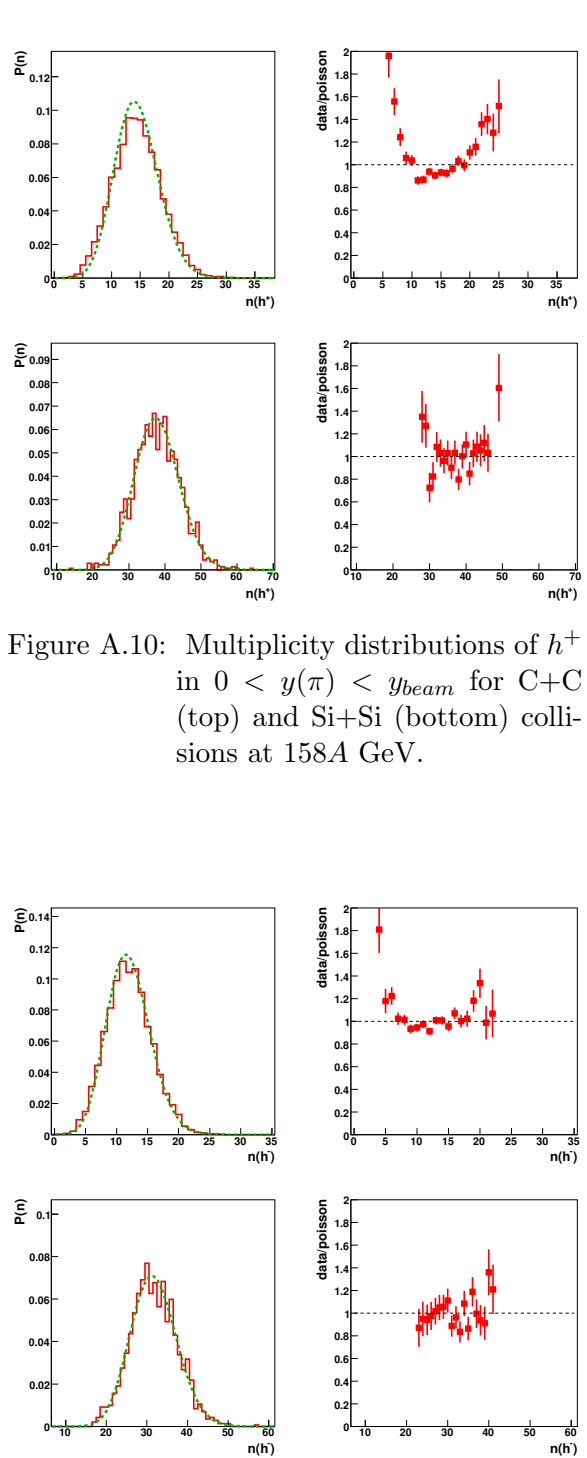


Figure A.10: Multiplicity distributions of  $h^+$  in  $0 < y(\pi) < y_{beam}$  for C+C (top) and Si+Si (bottom) collisions at 158A GeV.

Figure A.11: Multiplicity distributions of  $h^-$  in  $0 < y(\pi) < y_{beam}$  for C+C (top) and Si+Si (bottom) collisions at 158A GeV.

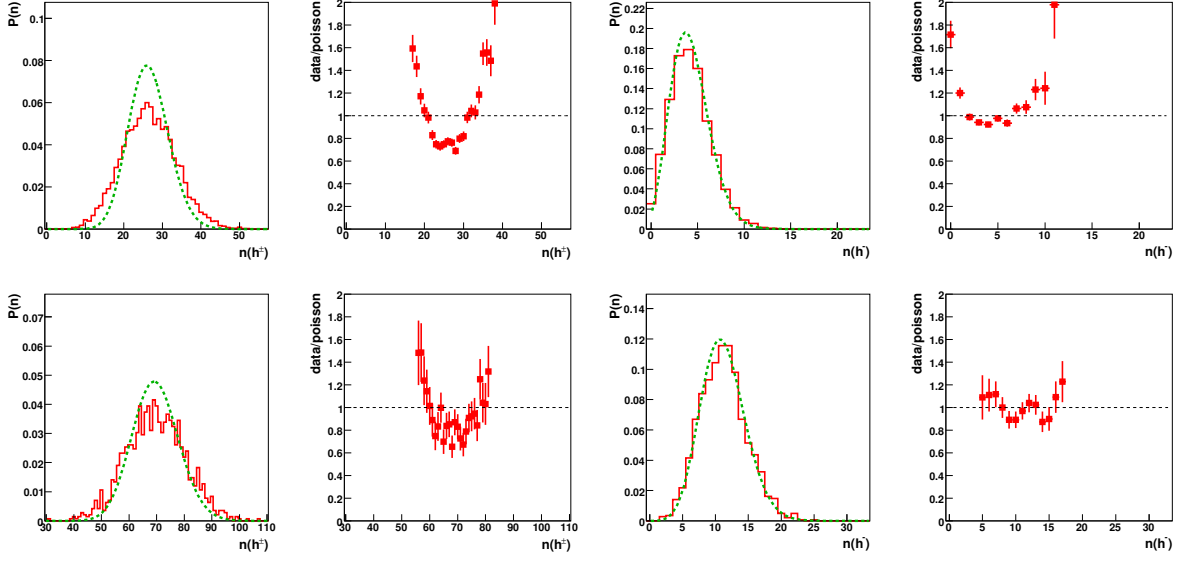


Figure A.12: Multiplicity distributions of  $h^\pm$  in  $0 < y(\pi) < y_{beam}$  for C+C (top) and Si+Si (bottom) collisions at 158A GeV.

Figure A.14: Multiplicity distributions of  $h^-$  in  $0 < y(\pi) < 1$  for C+C (top) and Si+Si (bottom) collisions at 158A GeV.

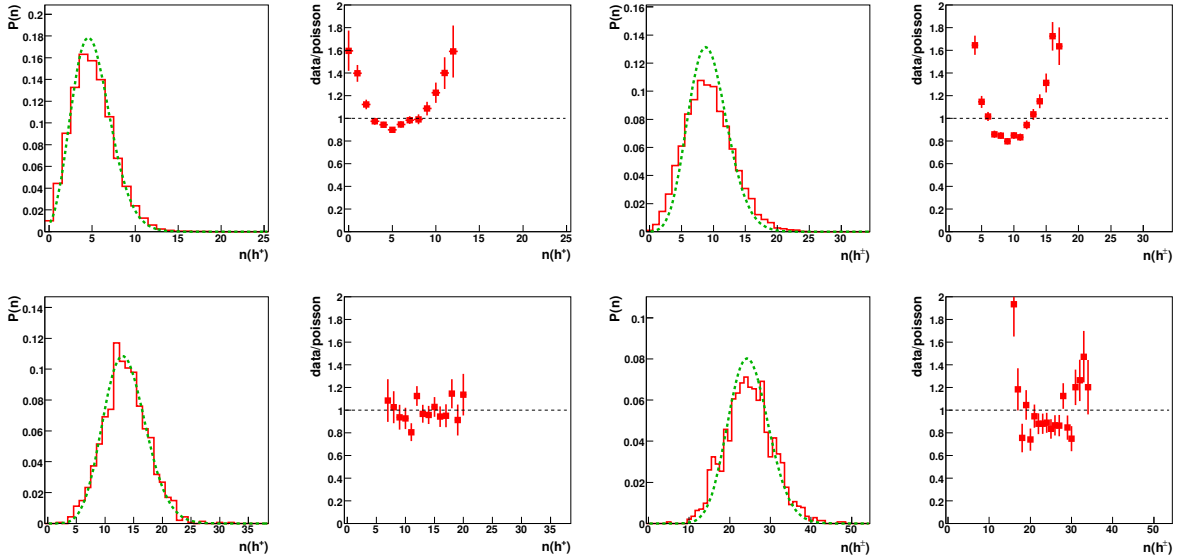


Figure A.13: Multiplicity distributions of  $h^+$  in  $0 < y(\pi) < 1$  for C+C (top) and Si+Si (bottom) collisions at 158A GeV.

Figure A.15: Multiplicity distributions of  $h^\pm$  in  $0 < y(\pi) < 1$  for C+C (top) and Si+Si (bottom) collisions at 158A GeV.

A Additional Plots and Tables

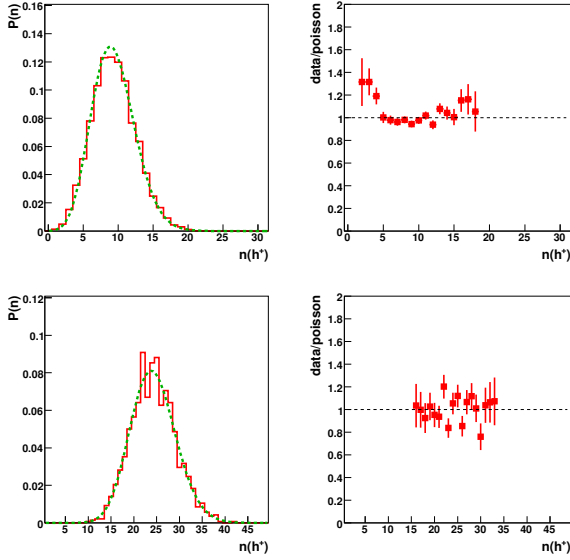


Figure A.16: Multiplicity distributions of  $h^+$  in  $1 < y(\pi) < y_{beam}$  for C+C (top) and Si+Si (bottom) collisions at 158A GeV.

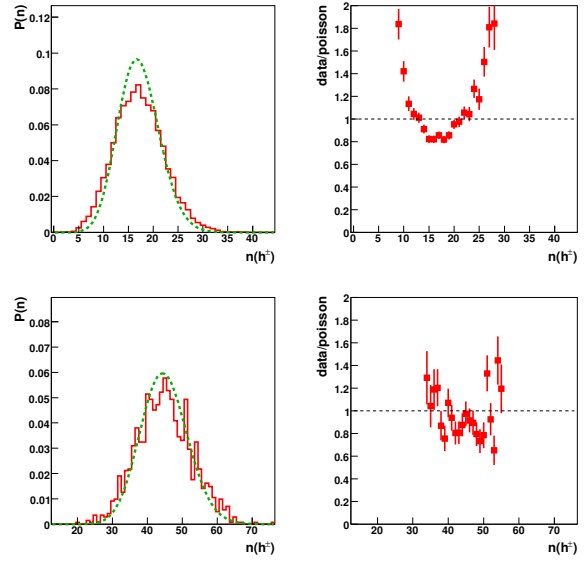


Figure A.18: Multiplicity distributions of  $h^\pm$  in  $1 < y(\pi) < y_{beam}$  for C+C (top) and Si+Si (bottom) collisions at 158A GeV.

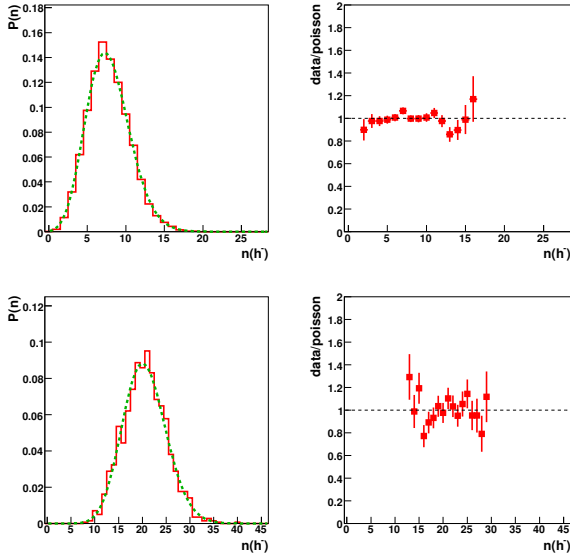


Figure A.17: Multiplicity distributions of  $h^-$  in  $1 < y(\pi) < y_{beam}$  for C+C (top) and Si+Si (bottom) collisions at 158A GeV.



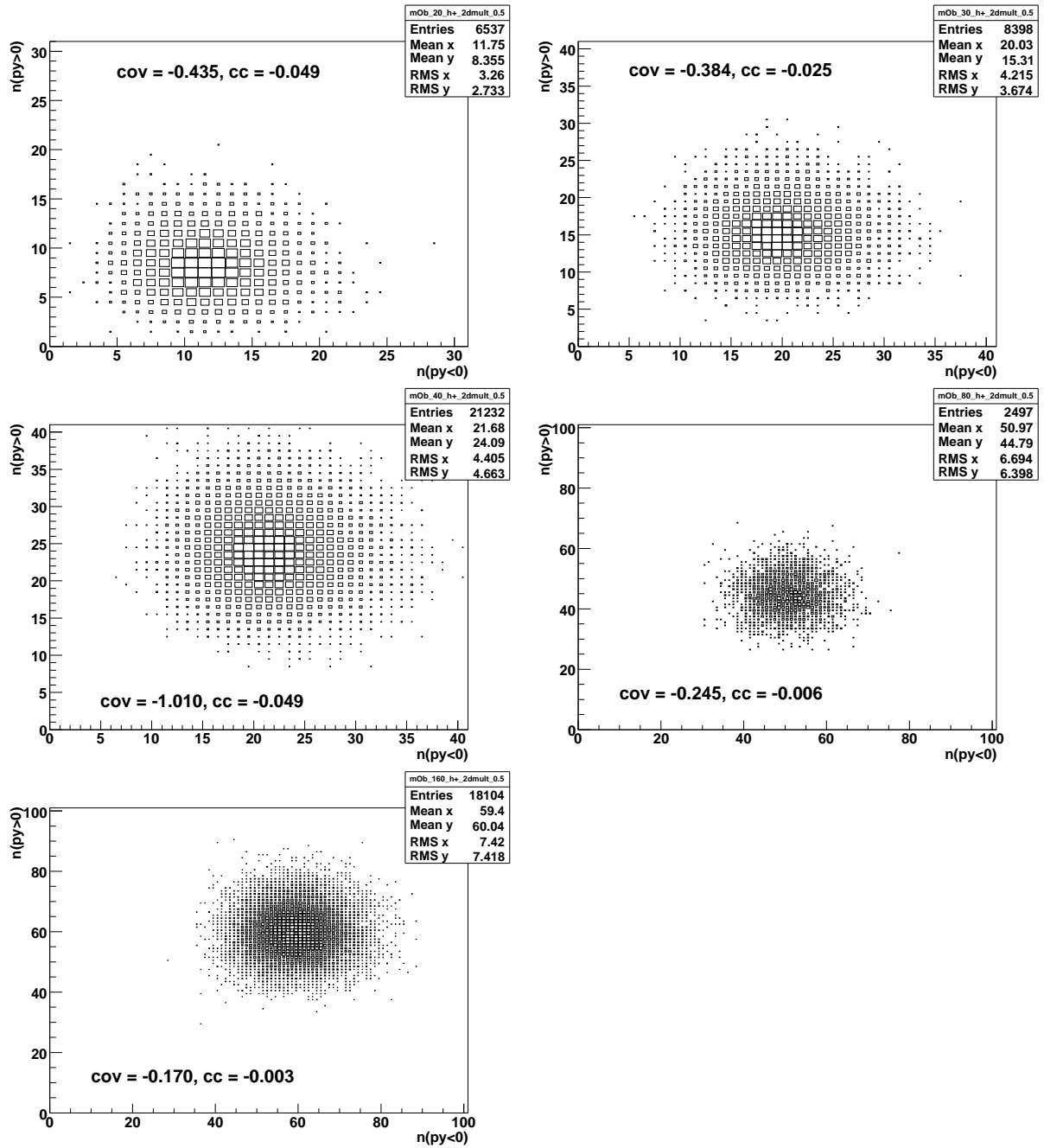


Figure A.19: Multiplicity correlations of positively charged particles with a positive and a negative momentum in y-direction. Top left: 20A GeV, bottom: 158A GeV.

A Additional Plots and Tables

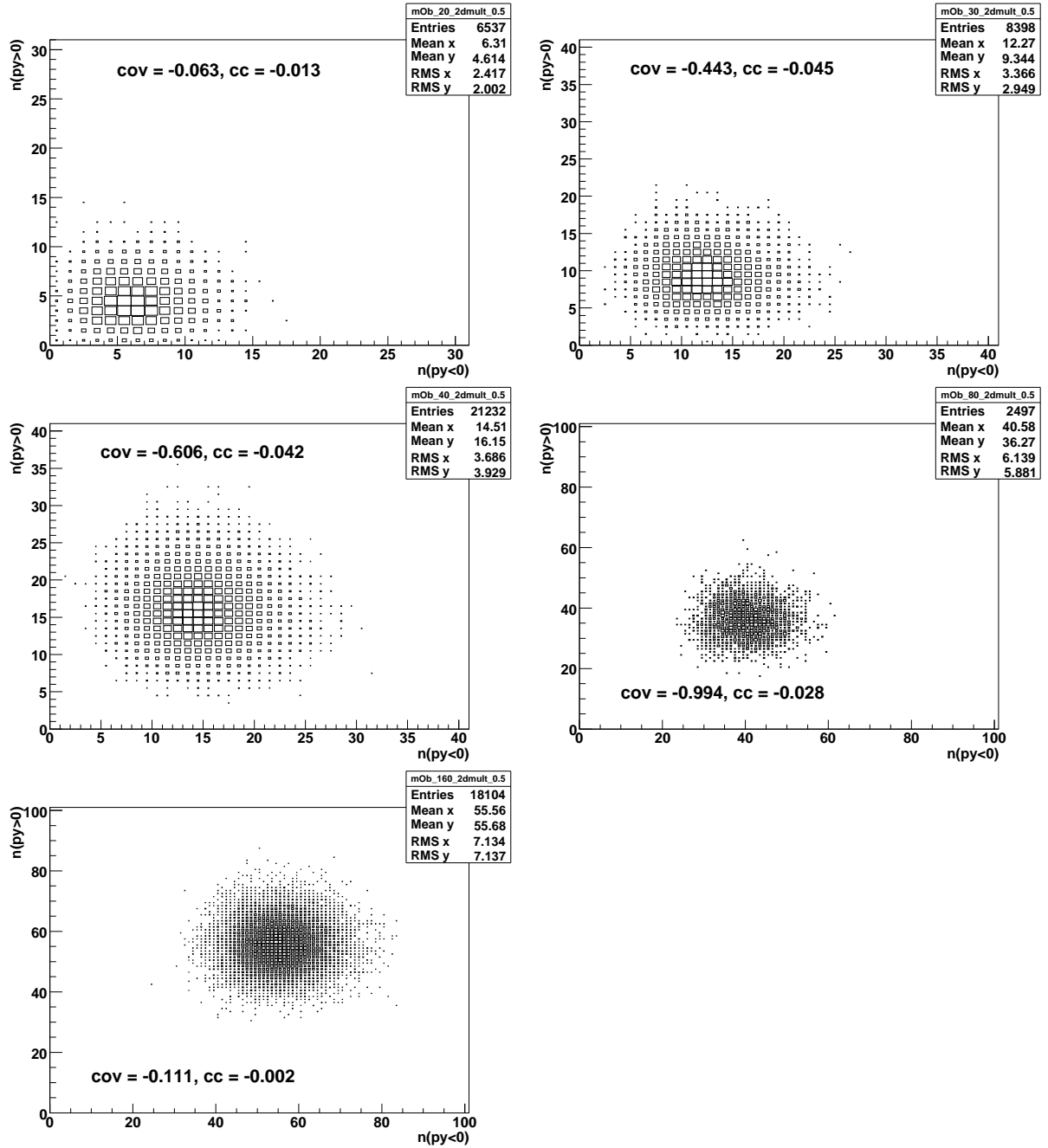


Figure A.20: Multiplicity correlations of negatively charged particles with a positive and a negative momentum in y-direction. Top left: 20A GeV, bottom: 158A GeV.

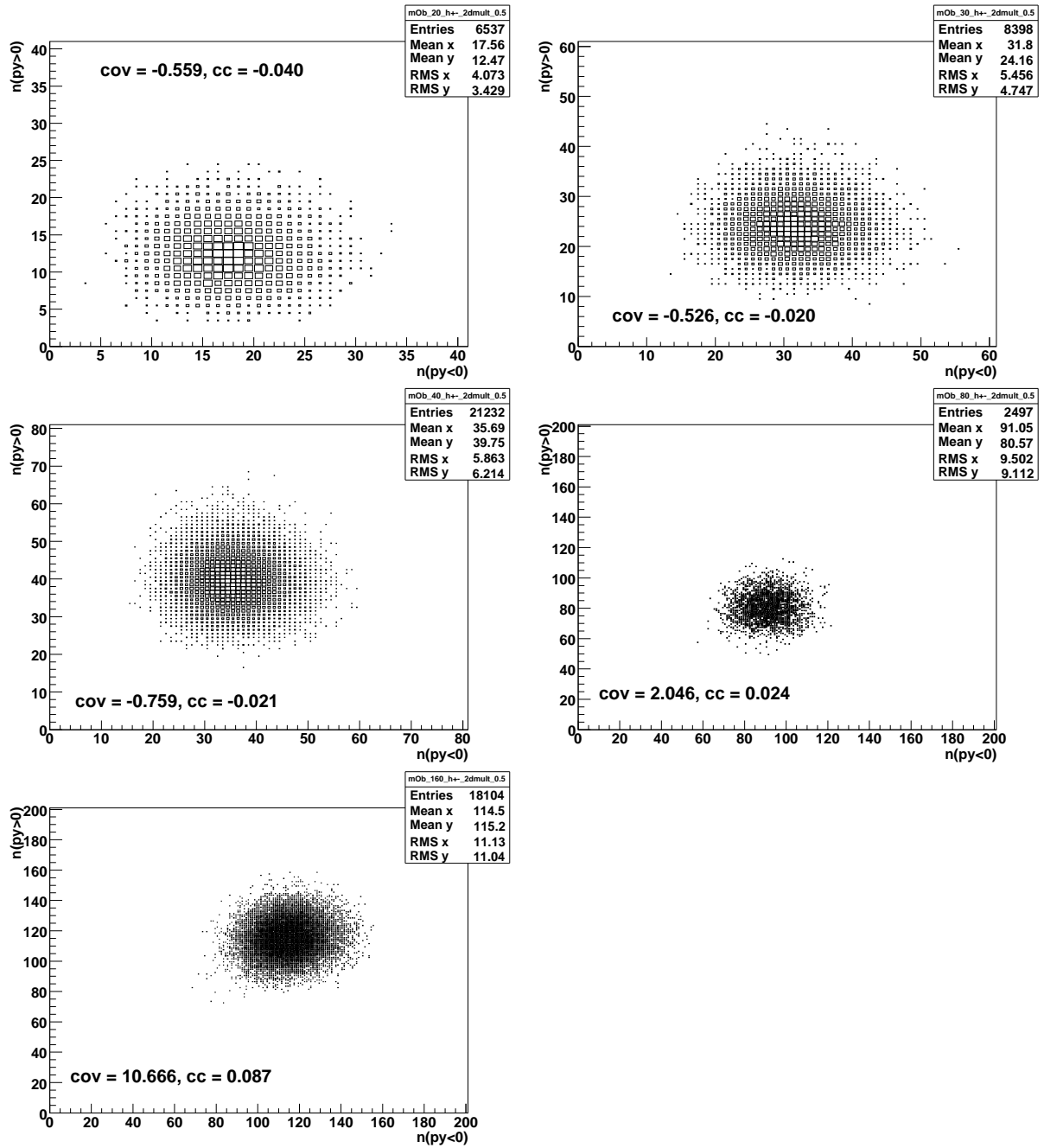


Figure A.21: Multiplicity correlations of all charged particles with a positive and a negative momentum in y-direction. Top left: 20A GeV, bottom: 158A GeV.

A Additional Plots and Tables

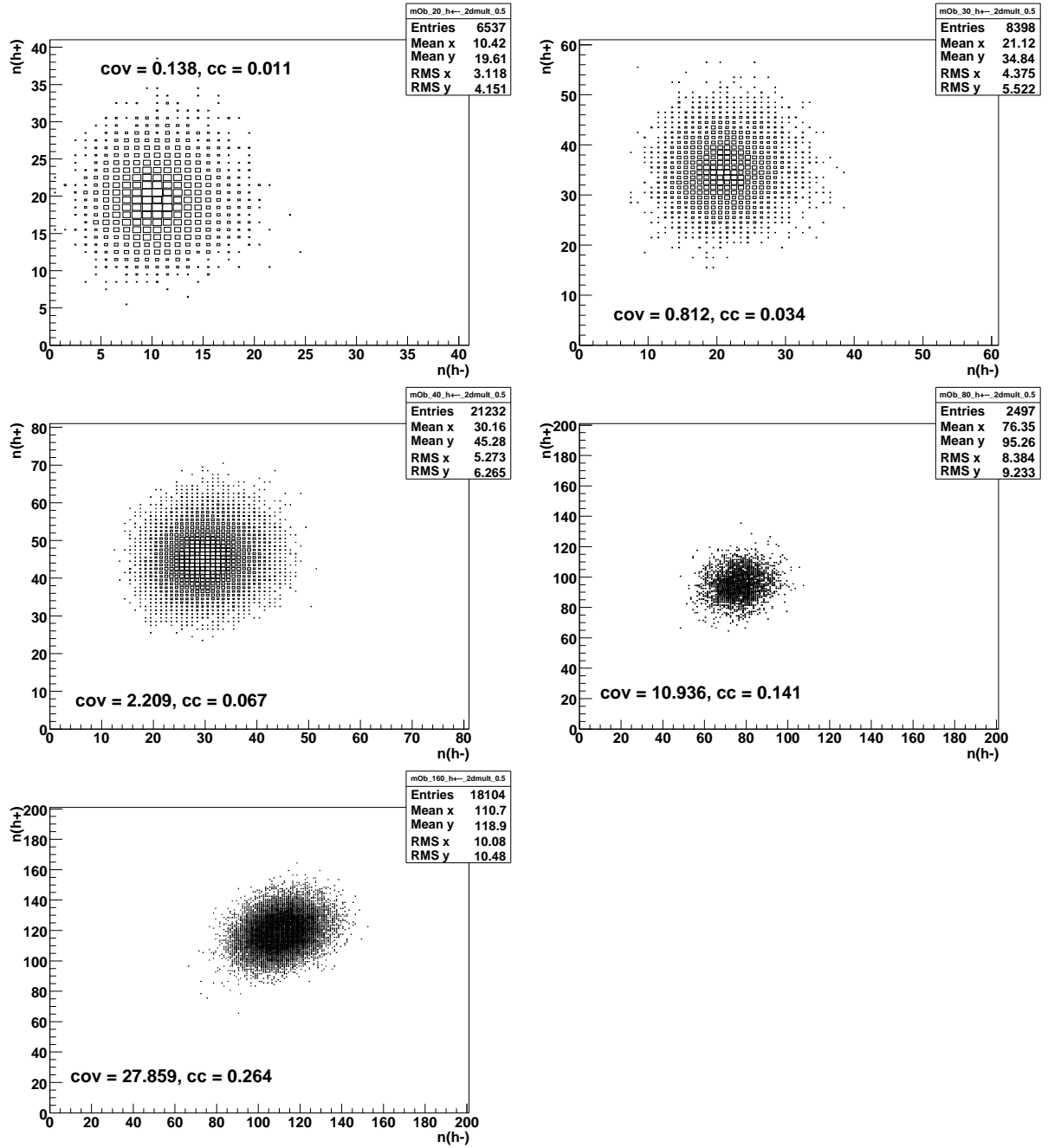


Figure A.22: Multiplicity correlations of particles with a positive and a negative charge. Top left: 20A GeV, bottom: 158A GeV.

# B Probability Distributions and Moments

## B.1 The Mean and the Variance

The mean value of a distribution  $P(n)$  is defined as:

$$\langle n \rangle = \sum_n nP(n). \quad (\text{B.1})$$

The variance is defined as follows (section 4.4.1):

$$\begin{aligned} \text{Var}(n) &= \sum_n (n - \langle n \rangle)^2 P(n) \\ &= \langle (n - \langle n \rangle)^2 \rangle = \langle n^2 \rangle - \langle n \rangle^2. \end{aligned} \quad (\text{B.2})$$

When  $N$  is the sum of  $k$  independent variables  $n_i$ , which all originate from the same distribution,

$$N = \sum_{i=1}^k n_i, \quad (\text{B.3})$$

the mean value of  $N$  is

$$\langle N \rangle = \langle k \rangle \cdot \langle n \rangle \quad (\text{B.4})$$

and the variance is

$$\text{Var}(N) = \langle k \rangle \text{Var}(n) + \langle n \rangle^2 \text{Var}(k). \quad (\text{B.5})$$

It is true for a constant  $a$  that:

$$\text{Var}(ax) = a^2 \text{Var}(x) \quad (\text{B.6})$$

and

$$\text{Var}(x + a) = \text{Var}(x). \quad (\text{B.7})$$

The variance of the sum of two random variables is

$$\begin{aligned} \text{Var}(x + y) &= \text{Var}(x) + \text{Var}(y) + 2 \langle (x - \langle x \rangle)(y - \langle y \rangle) \rangle \\ &= \text{Var}(x) + \text{Var}(y) + 2\text{Cov}(x, y). \end{aligned} \quad (\text{B.8})$$

If the random variables of  $x$  and  $y$  are statistically independent, the covariance is zero:

$$\text{Var}(x + y) = \text{Var}(x) + \text{Var}(y). \quad (\text{B.9})$$

### B.1.1 Binomial distribution

The binomial distribution is the probability distribution of the number of successes of  $n$  independent yes/no experiments, each of which yields success with probability  $p$ .

$$P_n(k) = \frac{n!}{k!(n-k)!} p^k (1-p)^{n-k} \quad (\text{B.10})$$

In order to check the normalization of the binomial distribution, the binomial expansion is used:

$$(p+q)^N = \sum_{n=0}^N \frac{N!}{n!(N-n)!} p^n q^{N-n}. \quad (\text{B.11})$$

Using this equation it can be shown that the binomial distribution is normalized to unity:

$$\sum_{k=0}^n P_n(k) = \sum_{k=0}^n \frac{n!}{k!(n-k)!} p^k (1-p)^{n-k} = (p + (1-p))^n = 1^n = 1. \quad (\text{B.12})$$

Its mean value is

$$\begin{aligned} \langle k \rangle &= \sum_{k=0}^n k P_n(k) = \sum_{k=1}^n k \frac{n!}{k!(n-k)!} p^k (1-p)^{n-k} \\ &= np \sum_{k=1}^n \frac{(n-1)!}{(k-1)!((n-1)-(k-1))!} p^{k-1} (1-p)^{(n-1)-(k-1)} \\ &= np \sum_{k=0}^{n-1} k \frac{(n-1)!}{k!((n-1)-k)!} p^k (1-p)^{(n-1)-k} \\ &= np \sum_{k=0}^{n-1} P_{n-1}(k) = np \end{aligned} \quad (\text{B.13})$$

and the variance of the binomial distribution is

$$\begin{aligned} \text{Var}(k) &= \langle k^2 \rangle - \langle k \rangle^2 \\ &= \sum_{k=0}^n k^2 \frac{n!}{k!(n-k)!} p^k (1-p)^{n-k} - (np)^2 \\ &= \sum_{k=0}^n (k(k-1) + k) \frac{n!}{k!(n-k)!} p^k (1-p)^{n-k} - (np)^2 \\ &= np \sum_{k=1}^n (k-1) \frac{(n-1)!}{(k-1)!((n-1)-(k-1))!} p^{k-1} (1-p)^{(n-1)-(k-1)} + np - n^2 p^2 \\ &= np^2 (n-1) \sum_{k=2}^n \frac{(n-2)!}{(k-2)!((n-2)-(k-2))!} p^{k-2} (1-p)^{(n-2)-(k-2)} + np - n^2 p^2 \\ &= np^2 (n-1) + np - n^2 p^2 = np(1-p). \end{aligned} \quad (\text{B.14})$$

### B.1.2 Poisson distribution

The Poisson distribution is the limit of the Binomial distribution for an infinite number of independent yes/no experiments ( $n \rightarrow \infty$ ) with a success probability going to zero ( $p \rightarrow 0$ ), where the expectation value  $\lambda$  is kept constant ( $\lambda = np = \text{const}$ ).

$$\begin{aligned}
 \lim_{n \rightarrow \infty} P_n(k) &= \lim_{n \rightarrow \infty} \frac{n!}{k!(n-k)!} \left(\frac{\lambda}{n}\right)^k \left(1 - \frac{\lambda}{n}\right)^{n-k} \\
 &= \lim_{n \rightarrow \infty} \left( \frac{(n-k)!(n-k+1) \cdots (n-2)(n-1)n}{(n-k)!n^k} \right) \left(\frac{\lambda^k}{k!}\right) \left(1 - \frac{\lambda}{n}\right)^n \left(1 - \frac{\lambda}{n}\right)^{-k} \\
 &= \lim_{n \rightarrow \infty} \underbrace{\left(\frac{n}{n}\right) \left(\frac{n-1}{n}\right) \left(\frac{n-2}{n}\right) \cdots \left(\frac{n-k+1}{n}\right)}_{=1} \left(\frac{\lambda^k}{k!}\right) \underbrace{\left(1 - \frac{\lambda}{n}\right)^n}_{=e^{-\lambda}} \underbrace{\left(1 - \frac{\lambda}{n}\right)^{-k}}_{=1} \\
 &= \frac{\lambda^k e^{-\lambda}}{k!}
 \end{aligned} \tag{B.15}$$

The distribution is normalised to unity:

$$\begin{aligned}
 \sum_k P_\lambda(k) &= \sum_{k=0}^{\infty} \frac{\lambda^k e^{-\lambda}}{k!} \\
 &= e^\lambda e^{-\lambda} = 1
 \end{aligned} \tag{B.16}$$

The mean value of the Poisson distribution is

$$\begin{aligned}
 \langle P_\lambda(k) \rangle &= \sum_{k=0}^{\infty} k \frac{\lambda^k e^{-\lambda}}{k!} \\
 &= \lambda \sum_{k=1}^{\infty} \frac{\lambda^{k-1} e^{-\lambda}}{(k-1)!} \\
 &= \lambda e^\lambda e^{-\lambda} = \lambda.
 \end{aligned} \tag{B.17}$$

The variance of a Poisson distribution is the same as the mean value:

$$\begin{aligned}
 \text{Var}(P_\lambda(k)) &= \sum_{k=0}^{\infty} k^2 \frac{\lambda^k e^{-\lambda}}{k!} - \lambda^2 \\
 &= \sum_{k=1}^{\infty} (k(k-1) + k) \frac{\lambda^k e^{-\lambda}}{k!} - \lambda^2 \\
 &= \sum_{k=2}^{\infty} k(k-1) \frac{\lambda^k e^{-\lambda}}{k!} + \lambda - \lambda^2 \\
 &= \lambda \sum_{l=1}^{\infty} l \frac{\lambda^l e^{-\lambda}}{l!} + \lambda - \lambda^2 \\
 &= \lambda^2 + \lambda - \lambda^2 = \lambda,
 \end{aligned} \tag{B.18}$$

therefore the scaled variance of a Poisson distribution is 1:

$$\omega = \frac{\text{Var}(P_\lambda(k))}{\langle P_\lambda(k) \rangle} = \frac{\lambda}{\lambda} = 1. \tag{B.19}$$

## B.2 Conditional Probabilities

$P(X|Y)$  is the probability distribution of the variable  $X$  under the condition that the variable  $Y$  has a specific value.

The probability that two variables  $X$  and  $Y$  have a specific value is:

$$P(X, Y) = P(X|Y)P(Y) = P(Y|X)P(X). \quad (\text{B.20})$$

The probability that a variable  $X$  has a specific value is:

$$P(X) = \sum_Y P(X|Y)P(Y), \quad (\text{B.21})$$

the mean value of  $X$  is

$$\langle X \rangle = \langle \langle X|Y \rangle_X \rangle_Y, \quad (\text{B.22})$$

with the variance

$$\text{Var}(X) = \langle \text{Var}_X(X|Y) \rangle_Y + \text{Var}_Y(\langle X|Y \rangle_X). \quad (\text{B.23})$$



# C Kinetic Variables

## C.1 Collision Energy

The energy of the collision can be characterized by the energy of the incoming beam particle  $E$ . In heavy ion collisions the beam energy per nucleon  $E_N$ , or the other way around, the energy as a multiple of the number of nucleons, is commonly used. The energy is usually given in  $A$  GeV. In order to compare fixed target and collider experiments, the following measures can be used.

### C.1.1 Center of Mass Energy

The center of mass energy of a collision is denoted as  $\sqrt{s}$ . In a heavy ion collision usually the center of mass energy per nucleon-pair  $\sqrt{s_{NN}}$  is used. It is defined as the absolute value of the sum of the four-momenta  $P^\mu = (E, \vec{p})$  of the two colliding nucleons.

$$s_{NN} = (P_1^\mu + P_2^\mu)^2 = (E_1 + E_2)^2 - (\vec{p}_1 + \vec{p}_2)^2 \geq (2m_N)^2 \quad (\text{C.1})$$

In a collider experiment the center of mass energy per nucleon-nucleon pair is the sum of the energy of the two incoming nucleons when the projectile and the target nuclei are identical.

$$\sqrt{s_{NN}} = E_{N,1} + E_{N,2} \quad (\text{C.2})$$

In a fixed target experiment most of the energy of the incoming beam is used for the propagation of the center of mass of the collision. With  $\vec{p}_2 = 0$  and  $E_{N,2} = m_N$  the center of mass energy in fixed target experiments is

$$s_{NN} = (E_{N,1} + m_N)^2 - p_1^2 = 2m_N^2 + 2m_N E_{N,1} \quad (\text{C.3})$$

For large beam energies the center of mass energy  $\sqrt{s_{NN}}$  increases only with the square root of the beam energy.

### C.1.2 Fermi-Variable $F$

In some models, like the statistical model of the early stage [32], the variable  $F$  is used as a measure of the collision energy. It is defined as

$$F = \frac{(\sqrt{s_{NN}} - 2m_N)^{3/4}}{(\sqrt{s_{NN}})^{1/4}} \underset{\sqrt{s_{NN}} \gg m_N}{\approx} \sqrt{\sqrt{s_{NN}}} \quad (\text{C.4})$$

Within this model the entropy of the matter increases in proportion to  $F$ .

## C.2 Kinematic Variables

In principle every particle emerging from the collision can be characterized by its four momentum  $P^\mu$ . In heavy ion physics cylindrical symmetry is assumed with the beam axis as the symmetry axis. Under this assumption, the four momentum of a particle can be translated into a longitudinal momentum (along the beam axis), a transverse momentum and the rest mass of the particle. Both the transverse momentum and the rest mass are Lorentz-invariant under transformations along the beam axis, for example from the laboratory system in a fixed target experiment to the center of mass system of the collision. This is not true for the longitudinal momentum.

### C.2.1 Transverse Momentum

The transverse momentum is the component of the particle momentum which is orthogonal to the beam axis.

Commonly used is also the so-called transverse mass defined as:

$$m_T = \sqrt{p_T^2 + m^2}, \quad (\text{C.5})$$

where  $m$  is the rest mass of the particle.

### C.2.2 Rapidity

The rapidity  $y$  is defined as follows:

$$y = \frac{1}{2} \ln \left( \frac{E + p_Z}{E - p_Z} \right) = \text{artanh} \left( \frac{p_Z}{E} \right) = \text{artanh}(\beta). \quad (\text{C.6})$$

$$E = m_T \cosh y \quad (\text{C.7})$$

$$p_Z = m_T \sinh y \quad (\text{C.8})$$

Rapidity transforms like the velocity in the non-relativistic case from one inertial system to another:

$$y' = y - y_{system}. \quad (\text{C.9})$$

In a fixed target experiment the beam rapidity can be calculated using equation C.6. The center of mass rapidity is half of this value. Therefore the rapidity of a particle can be very easily transformed into the center of mass frame.

The experimental disadvantage of the rapidity is that it depends not only on particle momentum but also on particle mass. Therefore the particle has to be identified in order to determine its rapidity. The acceptance of the detectors depends on the momentum of the particles in the laboratory frame and are therefore different in rapidity for different particle species.

In this work no particle identification was used. As most of the produced particles are pions, the rapidity was calculated under the assumption of a pion mass and is denoted as  $y(\pi)$ . This measure is a unique function of particle momentum.

### C.2.3 Pseudo-rapidity

The definition of pseudo-rapidity  $\eta$  is similar to the one of rapidity, but the total energy of the particle is replaced by its total momentum:

$$\eta = \frac{1}{2} \ln \left( \frac{|p| + p_Z}{|p| - p_Z} \right) \quad (\text{C.10})$$

$$|p| = p_T \cosh \eta \quad (\text{C.11})$$

$$p_Z = p_T \sinh \eta \quad (\text{C.12})$$

For the calculation of the pseudo-rapidity no particle identification is needed. Strictly speaking the pseudo-rapidity is not additive, but for high momentum particles ( $p \gg m$ ) this is a good approximation.

*C Kinetic Variables*

## D Analysis Programs and T49 Procedures

In this chapter the new functions of the NA49 root framework (T49) for the centrality determination are described and it is shown how they can be used. These procedures allow to apply the time dependence veto calibration (section 4.2.5) and to determine the centrality for each collision (section 4.2.1). In addition the centrality class of each event, according to the standard NA49 centrality classes (Table D.1), can be obtained.

For the determination of the centrality class, two different methods exist and are implemented into the T49 classes. The first method was developed for this thesis and has the following strategy. The veto energy of all runs in one data-set is calibrated to the first run of the corresponding data-set. For each data-set the trigger centrality is calculated (section 4.2.2). Using the calibrated veto energy and the trigger centrality the centrality of each event can be determined (section 4.2.1).

An alternative method was developed by A. Laszlo [82]. For this strategy for each energy one run is selected which has the largest trigger centrality and is therefore least biased by the trigger. For this run the veto energies corresponding to the borders of the centrality classes are determined. The veto energies of all runs at the same energy, not only the ones of the runs in the same data-set, are calibrated to this reference run.

### D.1 Software for Centrality Determination

In the following a short reference of the T49 procedures for centrality determination is given.

#### T49Run

```
void SetEvetoCal(Int_t tdc=1)
```

Initialises the veto calibration and centrality determination for every run accessed with that T49Run object. This command must be executed before the mini-DST file and the event loop. If that is done, the `InitEvetoCalibration()`- procedure is executed automatically for each new run. The time dependent veto energy calibration can be turned off by setting

bin	min. centrality	max. centrality
1	0%	5%
2	5%	12.5%
3	12.5%	23.5%
4	23.5%	33.5%
5	33.5%	43.5%
6	43.5%	$C_{trig}$

Table D.1: The standard NA49 centrality classes.

## D Analysis Programs and T49 Procedures

`tdcal` to 0. For the use of the centrality classes of A. Laszlo they have to be initialised with `SetEvetoCal(2)` for 158A GeV (the reference run is set to 1468) and `SetEvetoCal(3)` for 40A GeV (reference run 3162). Note that for `SetEvetoCal(2)` or `SetEvetoCal(3)` the procedure `event->GetCentrality()` should not be used.

```
void InitEvetoCalibration(Int_t cent=1, Int_t refrun=0)
```

Initialises the veto calibration and centrality determination for the current run. If the first parameter `cent` is 1 (default), the centrality determination is initialised. The second parameter is the reference run for the time dependent veto energy calibration procedure by A. Laszlo. Note that only a run number of the same data-set can be specified as a reference run. If the parameter `refrun` is zero (default), the first run of the data-set is used as reference run. If `refrun = -1`, no time dependent veto calibration is used. Different centrality tables are loaded for time dependent calibration on / off. This method must be executed every time a new run is accessed before any of the new EVeto or centrality methods are used.

This procedure is obsolete when `SetEvetoCal` is used.

```
Float_t GetTDEvetoCalA()
```

```
Float_t GetTDEvetoCalB()
```

Returns the time dependent calibration constants for the actual run.

```
Float_t GetTDEvetoCalRefA()
```

```
Float_t GetTDEvetoCalRefB()
```

Returns the time dependent calibration constants for the reference run.

```
Float_t GetDatasetCrosssection()
```

Returns  $C_{trig}$  for the dataset.

### T49EventRoot

```
Float_t GetTDCalEveto()
```

Returns the veto energy after applying the time dependent calibration procedure by A. Laszlo. If the time dependent calibration procedure is not initialised or switched off, the normal veto energy is returned.

```
Float_t GetCentrality(Int_t td_cal=1)
```

Returns the centrality of the event. If `td_cal = 1` (default), the time dependent calibrated veto energy is used for the calculation of the centrality, if the calibration is activated. Note that this parameter does not change the centrality table which is used. The event centrality is determined using the centrality table, which contains veto energies for centrality values in steps of 0.5%. Between these values a linear extrapolating is used. The centrality must be initialised with `run->SetEvetoCal(0)` or `(1)`.

```
Int_t GetCentralityClass(Int_t td_cal=1)
```

Returns the centrality class according to the six NA49 standard centrality classes, to which the event belongs. The centrality must be initialised with `run->SetEvetoCal(0)` or `(1)`.

```
Int_t GetCentralityClass2()
```

Returns the centrality class obtained by the procedure of A. Laszlo according to the six NA49 standard centrality classes, to which the event belongs. The centrality must be initialised with `run->SetEvetoCal(2)` (for 158A GeV ) or `(3)` (for 40A GeV ).

## D.2 Example Program for Centrality Determination

This short program illustrates how to use the T49 procedures for centrality determination.

```

{
gROOT->Reset();
gROOT->SetStyle("Plain");
gSystem->Setenv("STAGE_POOL","na49_keep");
Int_t N_Event = 100 ;
Int_t Runstart=1;
Char_t InFile[1000];
sprintf(InFile,"%s","1/4std+-40GeV-minbias-02C");
T49Run *run = new T49Run();
T49Vertex *vertex;
T49EventRoot *event;
Int_t EventCount = 0;
Int_t acev=0;
run->SetEvetoCal(1); //initialises eveto calibration for all runs with td cal
// run->SetEvetoCal(2); //initialises centrality classes of A. Laszlo for 158A GeV

// mini dst file loop
while( (EventCount < N_Event) && run->OpenNextRun(InFile,Runstart,9999) )
{
cout << "trigger centrality: " << run->GetDatasetCrosssection() << endl;
// event loop
while((EventCount < N_Event) && (event = (T49EventRoot *) run->GetNextEvent()))
{
EventCount++;
if(EventCount%100==0)
cout << "evnr : " << EventCount << endl ;
Float_t centr=event->GetCentrality();
Int_t centclass=event->GetCentralityClass();
// Int_t centclass=event->GetCentralityClass2(); //centrality classes of A. Laszlo

Float_t Eveto=event->GetEveto();
Float_t TDcalEveto=event->GetTDcalEveto();
cout << "Eveto: " << Eveto << " TD cal. Eveto: " << TDcalEveto <<
" centrality: " << centr << " centrality class: " << centclass << endl;
} //event loop
run->Close();
} //mini dst file loop
} //eof

```

*D Analysis Programs and T49 Procedures*



## Bibliography

- [1] W. M. Yao *et al.*, (**Particle Data Group** Collaboration), “Review of particle physics,” *J. Phys.* **G33** (2006) 1–1232.
- [2] K. Rajagopal and F. Wilczek, “The condensed matter physics of QCD,” [hep-ph/0011333](#).
- [3] M. A. Stephanov, “QCD phase diagram and the critical point,” *Prog. Theor. Phys. Suppl.* **153** (2004) 139–156, [hep-ph/0402115](#).
- [4] F. Karsch, “Thermodynamic properties of strongly interacting matter at non-zero baryon number density,” *J. Phys.* **G31** (2005) S633–S640, [hep-lat/0412038](#).
- [5] S. D. Katz, “Equation of state from lattice QCD,” *Nucl. Phys.* **A774** (2006) 159–168, [hep-ph/0511166](#).
- [6] Z. Fodor and S. D. Katz, “Critical point of QCD at finite T and  $\mu$ , lattice results for physical quark masses,” *JHEP* **04** (2004) 050, [hep-lat/0402006](#).
- [7] P. de Forcrand and O. Philipsen, “Towards the QCD phase diagram,” *PoS LAT2006* (2006) 130, [hep-lat/0611027](#).
- [8] “Urknall (german),” *Wikipedia*.
- [9] “Neutronensterne (german),” *Wikipedia*.
- [10] F. Weber, “Strange quark matter and compact stars,” *Prog. Part. Nucl. Phys.* **54** (2005) 193–288, [astro-ph/0407155](#).
- [11] L. D. Landau, “On the multiparticle production in high-energy collisions,” *Izv. Akad. Nauk SSSR Ser. Fiz.* **17** (1953) 51–64.
- [12] J. D. Bjorken, “Highly Relativistic Nucleus-Nucleus Collisions: The Central Rapidity Region,” *Phys. Rev.* **D27** (1983) 140–151.
- [13] F. Becattini, J. Manninen, and M. Gazdzicki, “Energy and system size dependence of chemical freeze-out in relativistic nuclear collisions,” *Phys. Rev.* **C73** (2006) 044905, [hep-ph/0511092](#).
- [14] A. Andronic, P. Braun-Munzinger, and J. Stachel, “Hadron production in central nucleus nucleus collisions at chemical freeze-out,” *Nucl. Phys.* **A772** (2006) 167–199, [nucl-th/0511071](#).
- [15] J. Letessier and J. Rafelski, “Hadron production and phase changes in relativistic heavy ion collisions,” [nucl-th/0504028](#).

## Bibliography

- [16] F. Retiere and M. A. Lisa, “Observable implications of geometrical and dynamical aspects of freeze-out in heavy ion collisions,” *Phys. Rev.* **C70** (2004) 044907, [nucl-th/0312024](#).
- [17] S. Margetis *et al.*, (**NA49** Collaboration), “Transverse energy production in Pb-208 + Pb collisions at 158-GeV per nucleon,” *Phys. Rev. Lett.* **75** (1995) 3814–3817.
- [18] J. Adams *et al.*, (**STAR** Collaboration), “Evidence from d + Au measurements for final-state suppression of high p(T) hadrons in Au + Au collisions at RHIC,” *Phys. Rev. Lett.* **91** (2003) 072304, [nucl-ex/0306024](#).
- [19] C. Alt *et al.*, (**NA49** Collaboration), “Directed and elliptic flow of charged pions and protons in Pb + Pb collisions at 40-A-GeV and 158-A-GeV,” *Phys. Rev.* **C68** (2003) 034903, [nucl-ex/0303001](#).
- [20] A. Wetzler, (**NA49** Collaboration), “Gerichteter und Elliptischer Fluss in Blei-Blei-Stoessen bei einer Strahlenergie von 40 GeV pro Nukleon,” *Diploma thesis, University Frankfurt, Germany*.
- [21] H. Stoecker, “Collective Flow signals the Quark Gluon Plasma,” *Nucl. Phys.* **A750** (2005) 121–147, [nucl-th/0406018](#).
- [22] [http://www.interactions.org/sgtw/2006/1025/star\\_grid\\_more.html](http://www.interactions.org/sgtw/2006/1025/star_grid_more.html).
- [23] H. Petersen, Q. Li, X. Zhu, and M. Bleicher, “Directed and elliptic flow in heavy ion collisions at GSI- FAIR and CERN-SPS,” *Phys. Rev.* **C74** (2006) 064908, [hep-ph/0608189](#).
- [24] C. Alt *et al.*, (**NA49** Collaboration), “Elliptic flow of Lambda hyperons in Pb + Pb collisions at 158-A-GeV,” *Phys. Rev.* **C75** (2007) 044901, [nucl-ex/0606026](#).
- [25] B. I. Abelev *et al.*, (**the STAR** Collaboration), “Mass, quark-number, and  $s(NN)^{(1/2)}$  dependence of the second and fourth flow harmonics in ultra-relativistic nucleus nucleus collisions,” *Phys. Rev.* **C75** (2007) 054906, [nucl-ex/0701010](#).
- [26] T. Matsui and H. Satz, “J/psi Suppression by Quark-Gluon Plasma Formation,” *Phys. Lett.* **B178** (1986) 416.
- [27] H. Satz, “Quarkonium binding and dissociation: The spectral analysis of the QGP,” *Nucl. Phys.* **A783** (2007) 249–260, [hep-ph/0609197](#).
- [28] B. Alessandro *et al.*, (**NA50** Collaboration), “A new measurement of J/psi suppression in Pb - Pb collisions at 158-GeV per nucleon,” *Eur. Phys. J.* **C39** (2005) 335–345, [hep-ex/0412036](#).
- [29] A. Adare *et al.*, (**PHENIX** Collaboration), “J/psi production vs centrality, transverse momentum, and rapidity in Au + Au collisions at  $s(NN)^{(1/2)} = 200$ -GeV,” *Phys. Rev. Lett.* **98** (2007) 232301, [nucl-ex/0611020](#).
- [30] M. Gazdzicki and M. I. Gorenstein, “Evidence for statistical production of J/psi mesons in nuclear collisions at the CERN SPS,” *Phys. Rev. Lett.* **83** (1999) 4009–4012, [hep-ph/9905515](#).

- [31] P. Braun-Munzinger and J. Stachel, “(Non)thermal aspects of charmonium production and a new look at J/psi suppression,” *Phys. Lett.* **B490** (2000) 196–202, [nucl-th/0007059](#).
- [32] M. Gazdzicki and M. I. Gorenstein, “On the early stage of nucleus nucleus collisions,” *Acta Phys. Polon.* **B30** (1999) 2705, [hep-ph/9803462](#).
- [33] C. Alt *et al.*, (**NA49** Collaboration), “Pion and kaon production in central Pb+Pb collisions at 20A and 30A GeV: Evidence for the onset of deconfinement,” [arXiv:0710.0118](#) [[nucl-ex](#)].
- [34] J. Rafelski and B. Muller, “Strangeness Production in the Quark - Gluon Plasma,” *Phys. Rev. Lett.* **48** (1982) 1066.
- [35] T. Alber *et al.*, (**NA35** Collaboration), “Strange particle production in nuclear collisions at 200- GeV per nucleon,” *Z. Phys.* **C64** (1994) 195–207.
- [36] P. Seyboth *et al.*, (**NA49** Collaboration), “Onset of deconfinement in Pb + Pb collisions at the CERN SPS,” *Acta Phys. Polon.* **B37** (2006) 3429–3450, [nucl-ex/0612008](#).
- [37] M. Kliemant, B. Lungwitz, and M. Gazdzicki, “Energy dependence of transverse mass spectra of kaons produced in p + p and p + anti-p interactions. A compilation,” *Phys. Rev.* **C69** (2004) 044903, [hep-ex/0308002](#).
- [38] R. Stock, “Event by event analysis of ultrarelativistic nuclear collisions: A new method to search for critical fluctuations,”. Prepared for NATO Advanced Study Workshop on Hot Hadronic Matter: Theory and Experiment, Divonne-les-Bains, France, 27 Jun - 1 Jul 1994.
- [39] C. Roland, (**NA49** Collaboration), “Event-by-event fluctuations of particle ratios in central Pb + Pb collisions at 20-A-GeV to 158-A-GeV,” *J. Phys. Conf. Ser.* **27** (2005) 174–183.
- [40] S. Das, (**STAR** Collaboration), “Fluctuations studies in STAR,” *PoS CFRNC2006* (2006) 014.
- [41] M. I. Gorenstein, M. Gazdzicki, and O. S. Zozulya, “Fluctuations of strangeness and deconfinement phase transition in nucleus nucleus collisions,” *Phys. Lett.* **B585** (2004) 237–242, [hep-ph/0309142](#).
- [42] C. Alt *et al.*, (**NA49** Collaboration), “Electric charge fluctuations in central Pb + Pb collisions at 20-AGeV, 30-AGeV, 40-AGeV, 80-AGeV and 158-AGeV,” *Phys. Rev.* **C70** (2004) 064903, [nucl-ex/0406013](#).
- [43] S. Jeon and V. Koch, “Charged particle ratio fluctuation as a signal for QGP,” *Phys. Rev. Lett.* **85** (2000) 2076–2079, [hep-ph/0003168](#).
- [44] M. Asakawa, U. W. Heinz, and B. Muller, “Fluctuation probes of quark deconfinement,” *Phys. Rev. Lett.* **85** (2000) 2072–2075, [hep-ph/0003169](#).

## Bibliography

- [45] J. Zaraneek, “Measures of charge fluctuations in nuclear collisions,” *Phys. Rev.* **C66** (2002) 024905, [hep-ph/0111228](#).
- [46] T. Anticic *et al.*, (**NA49** Collaboration), “Transverse momentum fluctuations in nuclear collisions at 158-A-GeV,” *Phys. Rev.* **C70** (2004) 034902, [hep-ex/0311009](#).
- [47] K. Grebieszko *et al.*, “Event-by-event transverse momentum fluctuations in nuclear collisions at CERN SPS,” [arXiv:0707.4608](#) [[nucl-ex](#)].
- [48] J. Adams *et al.*, (**STAR** Collaboration), “The energy dependence of p(t) angular correlations inferred from mean-p(t) fluctuation scale dependence in heavy ion collisions at the SPS and RHIC,” *J. Phys.* **G33** (2007) 451–466, [nucl-ex/0605021](#).
- [49] M. Gazdzicki, M. I. Gorenstein, and S. Mrowczynski, “Fluctuations and deconfinement phase transition in nucleus nucleus collisions,” *Phys. Lett.* **B585** (2004) 115–121, [hep-ph/0304052](#).
- [50] M. A. Stephanov, K. Rajagopal, and E. V. Shuryak, “Event-by-event fluctuations in heavy ion collisions and the QCD critical point,” *Phys. Rev.* **D60** (1999) 114028, [hep-ph/9903292](#).
- [51] V. V. Begun, M. Gazdzicki, M. I. Gorenstein, and O. S. Zozulya, “Particle Number Fluctuations in Canonical Ensemble,” *Phys. Rev.* **C70** (2004) 034901, [nucl-th/0404056](#).
- [52] A. Bialas, M. Bleszynski, and W. Czyz, “Multiplicity Distributions in Nucleus-Nucleus Collisions at High-Energies,” *Nucl. Phys.* **B111** (1976) 461.
- [53] V. P. Konchakovski *et al.*, “Particle number fluctuations in high energy nucleus nucleus collisions from microscopic transport approaches,” *Phys. Rev.* **C73** (2006) 034902, [nucl-th/0511083](#).
- [54] M. Gazdzicki and M. I. Gorenstein, “Transparency, mixing and reflection of initial flows in relativistic nuclear collisions,” *Phys. Lett.* **B640** (2006) 155–161, [hep-ph/0511058](#).
- [55] V. Begun, M. Gazdzicki, M. Gorenstein, M. Hauer, V. Konchakovski, and B. Lungwitz, “Multiplicity fluctuations in relativistic nuclear collisions: statistical model versus experimental data,” *Phys. Rev.* **C76** (2007) 024902, [nucl-th/0611075](#).
- [56] M. Bleicher *et al.*, “Relativistic hadron hadron collisions in the ultra-relativistic quantum molecular dynamics model,” *J. Phys.* **G25** (1999) 1859–1896, [hep-ph/9909407](#).
- [57] S. A. Bass *et al.*, “Microscopic models for ultrarelativistic heavy ion collisions,” *Prog. Part. Nucl. Phys.* **41** (1998) 255–369, [nucl-th/9803035](#).
- [58] P. Slattery, “Kno semi-inclusive scaling,” *eConf* **C720906V1** (1972) 238–239.
- [59] A. I. Golokhvastov, “Koba-Nielsen-Olesen scaling,” *Phys. Atom. Nucl.* **64** (2001) 84–97.

- [60] Z. Koba, H. B. Nielsen, and P. Olesen, “Scaling of multiplicity distributions in high-energy hadron collisions,” *Nucl. Phys.* **B40** (1972) 317–334.
- [61] R. Szwed and G. Wrochna, “SCALING PREDICTIONS FOR MULTIPLICITY DISTRIBUTIONS AT LEP,” *Z. Phys.* **C47** (1990) 449–456.
- [62] A. I. Golokhvastov, “A Possible Generalization of the Concept of Similarity of Multiplicity Distributions for Nonasymptotic Energies,” *Sov. J. Nucl. Phys.* **27** (1978) 430.
- [63] H. Heiselberg, “Event-by-event physics in relativistic heavy-ion collisions,” *Phys. Rept.* **351** (2001) 161–194, [nucl-th/0003046](#).
- [64] S. Afanasev *et al.*, (**NA49** Collaboration), “The NA49 large acceptance hadron detector,” *Nucl. Instrum. Meth.* **A430** (1999) 210–244.
- [65] <http://linac2.home.cern.ch/linac2/sources/source.htm>.
- [66] H. Bethe, “Theory of the passage of fast corpuscular rays through matter,” *Annalen Phys.* **5** (1930) 325–400.
- [67] T. Kolleger, “Kaonproduktion in ultrarelativistischen Blei-Blei- Sten,” *Diploma thesis, University Frankfurt, Germany* (2001).
- [68] B. Lungwitz, (**NA49** Collaboration), “Pionenproduktion in Sten leichter Kerne bei 40 und 158 GeV pro Nukleon,” *Diploma thesis, University Frankfurt, Germany*.
- [69] C. De Marzo *et al.*, “A SEGMENTED PHOTON - HADRON CALORIMETER USING A TWO COLORED WAVELENGTH SHIFTER OPTICAL READOUT SYSTEM,” *Nucl. Instrum. Meth.* **217** (1983) 405–417.
- [70] H. Appelshauser *et al.*, (**NA49** Collaboration), “Spectator nucleons in Pb + Pb collisions at 158-A-GeV,” *Eur. Phys. J.* **A2** (1998) 383–390.
- [71] M. Mitrovski *Dissertation, University Frankfurt, Germany* (2007).
- [72] R. Zybert and P. Buncic, “DSPACK: Object manager for high energy physics,”. Prepared for International Conference on Computing in High- energy Physics (CHEP 95), Rio de Janeiro, Brazil, 18-22 Sep 1995.
- [73] R. Brun, R. Hagelberg, M. Hansroul, and J. C. Lassalle, “GEANT: SIMULATION PROGRAM FOR PARTICLE PHYSICS EXPERIMENTS. USER GUIDE AND REFERENCE MANUAL,”. CERN-DD-78-2-REV.
- [74] R. Brun and F. Rademakers, “ROOT: An object oriented data analysis framework,” *Nucl. Instrum. Meth.* **A389** (1997) 81–86.
- [75] N. Buncic *et al.*, “ROOT. An interactive object-oriented framework and its application to NA49 analysis,”. Talk given at Computing in High-energy Physics (CHEP 97), Berlin, Germany, 7-11 Apr 1997.
- [76] B. Lungwitz. <https://edms.cern.ch/document/885236/1>.

## Bibliography

- [77] C. Hoehne *Dissertation, University Marburg, Germany* (2003).  
<http://archiv.ub.uni-marburg.de/diss/z2003/0627/>.
- [78] C. Alt *et al.*, (**NA49** Collaboration), “Centrality and system size dependence of multiplicity fluctuations in nuclear collisions at 158-A-GeV,” *Phys. Rev.* **C75** (2007) 064904, `nuc1-ex/0612010`.
- [79] M. Rybczynski *Dissertation, University Kielce, Poland* (2006).
- [80] A. V. Dementev and N. M. Sobolevsky, “SHIELD: Universal Monte Carlo hadron transport code: Scope and applications,”. Prepared for 3rd Workshop on Simulating Accelerator Radiation Environments (SARE3), Tsukuba, Japan, 7-9 May 1997.
- [81] M. Mitrovski *private communication*.
- [82] A. Laszlo, “Time-dependence calibration of the Veto Calorimeter,” *internal NA49 note* (2006).
- [83] B. Lungwitz *et al.*, (**NA49** Collaboration), “Energy dependence of multiplicity fluctuations in heavy ion collisions,” *PoS CFRNC2006* (2006) 024, `nuc1-ex/0610046`.
- [84] B. Lungwitz, “Multiplicity fluctuations in heavy ion collisions at CERN SPS,” *AIP Conf. Proc.* **892** (2007) 400–403, `nuc1-ex/0610047`.
- [85] S. V. Afanasiev *et al.*, (**The NA49** Collaboration), “Energy dependence of pion and kaon production in central Pb + Pb collisions,” *Phys. Rev.* **C66** (2002) 054902, `nuc1-ex/0205002`.
- [86] M. Rybczynski and Z. Wlodarczyk, “Non-monotonic behavior of multiplicity fluctuations,” *J. Phys. Conf. Ser.* **5** (2005) 238–245, `nuc1-th/0408023`.
- [87] L. Cunqueiro, E. G. Ferreira, F. del Moral, and C. Pajares, “Multiplicity fluctuations in the string clustering approach,” *Phys. Rev.* **C72** (2005) 024907, `hep-ph/0505197`.
- [88] M. M. Aggarwal *et al.*, (**WA98** Collaboration), “Event-by-event fluctuations in particle multiplicities and transverse energy produced in 158-A-GeV Pb + Pb collisions,” *Phys. Rev.* **C65** (2002) 054912, `nuc1-ex/0108029`.
- [89] K. Adcox *et al.*, (**PHENIX** Collaboration), “PHENIX detector overview,” *Nucl. Instrum. Meth.* **A499** (2003) 469–479.
- [90] J. T. Mitchell, (**PHENIX** Collaboration), “A survey of multiplicity fluctuations in PHENIX,” `nuc1-ex/0510076`.
- [91] S. S. Adler *et al.*, (**PHENIX** Collaboration), “Systematic studies of the centrality and  $s(\text{NN})^{1/2}$  dependence of  $dE(T)/d\mu$  and  $dN(\text{ch})/d\mu$  in heavy ion collisions at mid-rapidity,” *Phys. Rev.* **C71** (2005) 034908, `nuc1-ex/0409015`.
- [92] V. P. Konchakovski, M. I. Gorenstein, and E. L. Bratkovskaya, “Multiplicity fluctuations in Au+Au collisions at ultrarelativistic energies,” *Phys. Rev.* **C76** (2007) 031901.

- [93] C. Alt *et al.*, (**NA49** Collaboration), “Energy Dependence of Multiplicity Fluctuations in Heavy Ion Collisions at the CERN SPS,” [arXiv:0712.3216](#) [nucl-ex].
- [94] F. Becattini, M. Gazdzicki, A. Keranen, J. Manninen, and R. Stock, “Study of chemical equilibrium in nucleus nucleus collisions at AGS and SPS energies,” *Phys. Rev.* **C69** (2004) 024905, [hep-ph/0310049](#).
- [95] R. Stock, “Hadronization revisited: The dynamics behind hadro-chemical equilibrium,” *PoS CPOD2006* (2006) 040, [nucl-th/0703050](#).
- [96] M. Hauer, V. V. Begun, and M. I. Gorenstein, “Multiplicity Distributions in Canonical and Microcanonical Statistical Ensembles,” [arXiv:0706.3290](#) [nucl-th].
- [97] M. Hauer, “Multiplicity Fluctuations in Limited Segments of Momentum Space in Statistical Models,” [arXiv:0710.3938](#) [nucl-th].
- [98] B. Lungwitz and M. Bleicher, “Searching for the Critical Point of QCD: Theoretical Benchmark Calculations,” [arXiv:0707.1788](#) [nucl-th].
- [99] V. P. Konchakovski, B. Lungwitz, M. I. Gorenstein, and E. L. Bratkovskaya, “Multiplicity Fluctuations in Nucleus-Nucleus Collisions: Dependence on Energy and Atomic Number,” [arXiv:0712.2044](#) [nucl-th].
- [100] B. Andersson, G. Gustafson, and B. Nilsson-Almqvist, “A Model for Low  $p(t)$  Hadronic Reactions, with Generalizations to Hadron - Nucleus and Nucleus-Nucleus Collisions,” *Nucl. Phys.* **B281** (1987) 289.
- [101] B. Nilsson-Almqvist and E. Stenlund, “Interactions Between Hadrons and Nuclei: The Lund Monte Carlo, Fritiof Version 1.6,” *Comput. Phys. Commun.* **43** (1987) 387.
- [102] T. Sjostrand, “High-energy physics event generation with PYTHIA 5.7 and JETSET 7.4,” *Comput. Phys. Commun.* **82** (1994) 74–90.
- [103] M. Belkacem *et al.*, “Equation of state, spectra and composition of hot and dense infinite hadronic matter in a microscopic transport model,” *Phys. Rev.* **C58** (1998) 1727–1733, [nucl-th/9804058](#).
- [104] L. V. Bravina *et al.*, “Local equilibrium in heavy ion collisions: Microscopic model versus statistical model analysis,” *Phys. Rev.* **C60** (1999) 024904, [hep-ph/9906548](#).
- [105] M. Bleicher *et al.*, “Fluctuations and inhomogenities of energy density and isospin in Pb + Pb at the SPS,” *Nucl. Phys.* **A638** (1998) 391–394.
- [106] M. Bleicher *et al.*, “Can momentum correlations prove kinetic equilibration in heavy ion collisions at 160-A-GeV?,” *Phys. Lett.* **B435** (1998) 9–12, [hep-ph/9803345](#).
- [107] M. Bleicher, S. Jeon, and V. Koch, “Event-by-event fluctuations of the charged particle ratio from non-equilibrium transport theory,” *Phys. Rev.* **C62** (2000) 061902, [hep-ph/0006201](#).
- [108] M. Bleicher, J. Randrup, R. Snellings, and X. N. Wang, “Enhanced event-by-event fluctuations in pion multiplicity as a signal of disoriented chiral condensates at RHIC,” *Phys. Rev.* **C62** (2000) 041901, [nucl-th/0006047](#).

## Bibliography

- [109] S. Jeon, L. Shi, and M. Bleicher, “Detecting QGP with charge transfer fluctuations,” *Phys. Rev.* **C73** (2006) 014905, [nucl-th/0506025](#).
- [110] S. Haussler, H. Stoecker, and M. Bleicher, “Event-by-event analysis of baryon-strangeness correlations: Pinning down the critical temperature and volume of QGP formation,” *Phys. Rev.* **C73** (2006) 021901, [hep-ph/0507189](#).
- [111] S. Haussler, M. Abdel-Aziz, and M. Bleicher, “Forward-backward charge fluctuations at RHIC energies,” *Nucl. Phys.* **A785** (2007) 253–256, [nucl-th/0608021](#).
- [112] W. Ehehalt and W. Cassing, “Relativistic transport approach for nucleus nucleus collisions from SIS to SPS energies,” *Nucl. Phys.* **A602** (1996) 449–486.
- [113] V. P. Konchakovski, M. I. Gorenstein, and E. L. Bratkovskaya, “Multiplicity fluctuations in proton proton and nucleus nucleus collisions,” *Phys. Lett.* **B651** (2007) 114–118, [nucl-th/0703052](#).
- [114] N. Antoniou *et al.*, “Study of hadron production in collisions of protons and nuclei at the CERN SPS,”. CERN-SPSC-2006-001.
- [115] M. Gazdzicki *et al.*, (**NA49-future** Collaboration), “A new SPS programme,” *PoS CPOD2006* (2006) 016, [nucl-ex/0612007](#).
- [116] M. Gazdzicki *et al.*, (**NA49** Collaboration), “Report from NA49,” *J. Phys.* **G30** (2004) S701–S708, [nucl-ex/0403023](#).
- [117] C. Blume, (**Na49** Collaboration), “Centrality and energy dependence of proton, light fragment and hyperon production,” *J. Phys.* **G34** (2007) S951–954, [nucl-ex/0701042](#).
- [118] I. N. Mishustin, “Possible links between the liquid - gas and deconfinement - hadronization phase transitions,” *Eur. Phys. J.* **A30** (2006) 311–316, [hep-ph/0609196](#).
- [119] J. Adams *et al.*, (**Star** Collaboration), “Delta(phi) Delta(eta) correlations in central Au + Au collisions at  $s(NN)^{1/2} = 200\text{-GeV}$ ,” *Phys. Rev.* **C75** (2007) 034901, [nucl-ex/0607003](#).
- [120] C. Alt *et al.*, (**NA49** Collaboration), “System-size dependence of strangeness production in nucleus nucleus collisions at  $s(NN)^{1/2} = 17.3\text{-GeV}$ ,” *Phys. Rev. Lett.* **94** (2005) 052301, [nucl-ex/0406031](#).
- [121] B. Lungwitz, “NA49 results on hadron production: Indications of the onset of deconfinement?,” *AIP Conf. Proc.* **828** (2006) 321–326, [nucl-ex/0509041](#).
- [122] B. Lungwitz *et al.*, (**NA49** Collaboration), “Energy, Rapidity and Transverse Momentum Dependence of Multiplicity Fluctuations in Heavy Ion Collisions at CERN SPS,” [arXiv:0709.1646 \[nucl-ex\]](#).



# Publications and Presentations of the Author

## Publications

M. Kliemant, B. Lungwitz and M. Gazdzicki, “Energy dependence of transverse mass spectra of kaons produced in p + p and p + anti-p interactions. A compilation,” *Phys. Rev. C* **69** (2004) 044903 [arXiv:hep-ex/0308002]. [37]

C. Alt *et al.* [NA49 Collaboration], “System-size dependence of strangeness production in nucleus nucleus collisions at  $s(\text{NN})^{1/2} = 17.3\text{-GeV}$ ,” *Phys. Rev. Lett.* **94** (2005) 052301 [arXiv:nucl-ex/0406031]. [120]

B. Lungwitz, “NA49 results on hadron production: Indications of the onset of deconfinement?,” *AIP Conf. Proc.* **828** (2006) 321 [arXiv:nucl-ex/0509041]. [121]

B. Lungwitz *et al.* [NA49 Collaboration], “Energy dependence of multiplicity fluctuations in heavy ion collisions,” *PoS C FRNC2006* (2006) 024 [arXiv:nucl-ex/0610046]. [83]

V. V. Begun, M. Gazdzicki, M. I. Gorenstein, M. Hauer, V. P. Konchakovski and B. Lungwitz, “Multiplicity fluctuations in relativistic nuclear collisions: statistical model versus experimental data,” *Phys. Rev. C* **76** (2007) 024902 [arXiv:nucl-th/0611075]. [55]

B. Lungwitz and M. Bleicher, “Searching for the Critical Point of QCD: Theoretical Benchmark Calculations,” *Phys. Rev. C* **76** (2007) 044904 [arXiv:0707.1788 [nucl-th]]. [98]

C. Alt *et al.* [NA49 Collaboration], “Centrality and system size dependence of multiplicity fluctuations in nuclear collisions at 158-A-GeV,” *Phys. Rev. C* **75** (2007) 064904 [arXiv:nucl-ex/0612010]. [78]

N. Antoniou *et al.*, “Study of hadron production in collisions of protons and nuclei at the CERN SPS,” [114]

B. Lungwitz, “Multiplicity fluctuations in heavy ion collisions at CERN SPS,” *AIP Conf. Proc.* **892** (2007) 400 [arXiv:nucl-ex/0610047]. [84]

B. Lungwitz *et al.* [NA49 Collaboration], “Energy, Rapidity and Transverse Momentum Dependence of Multiplicity Fluctuations in Heavy Ion Collisions at CERN SPS,” arXiv:0709.1646 [nucl-ex]. [122]

## *Publications and Presentations*

V. P. Konchakovski, B. Lungwitz, M. I. Gorenstein and E. L. Bratkovskaya, “Multiplicity Fluctuations in Nucleus-Nucleus Collisions: Dependence on Energy and Atomic Number,” arXiv:0712.2044 [nucl-th]. [99]

C. Alt *et al.* [NA49 Collaboration], “Energy Dependence of Multiplicity Fluctuations in Heavy Ion Collisions at the CERN SPS,” arXiv:0712.3216 [nucl-ex]. [93]

## **Presentations**

Spring Meeting of the German Physical Society (DPG) 2004, Cologne, 8.3.- 12.3.2004  
“Energy dependence of transverse mass spectra of kaons produced in p+p and p+pbar interactions. A compilation.” [37]

Spring Meeting of the German Physical Society (DPG) 2005, Berlin, 4.3.- 9.3.2005  
“Pionenproduktion in Stößen leichter Kerne bei 40 und 158 GeV pro Nukleon”

2nd international Workshop on the Critical Point and Onset of Deconfinement, Bergen, Norway, 30.3.- 3.4. 2005  
“System size dependence of hadron production”

XXXV International Symposium on Multiparticle Dynamics 2005, Kromeriz, Tschech Republic, 9.8.- 15.8.2005  
“NA49 results on hadron production: indication of the onset of deconfinement?” [121]

Spring Meeting of the German Physical Society (DPG) 2006, Munich, 20.3.- 24.3.2006  
“Multiplizitätsfluktuationen in Schwerionenkollisionen am CERN SPS”

Correlations and Fluctuations in Relativistic Nuclear Collisions, Florence, Italy, 7.7.- 9.7.2006  
“Energy dependence of multiplicity fluctuations in NA49” [83]

Quark Confinement and the Hadron Spectrum VII, Ponta Delgada, Azores, Portugal, 2.9.- 7.9.2006  
“Multiplicity Fluctuations in Heavy Ion Collisions at CERN SPS” [84]

Spring Meeting of the German Physical Society (DPG) 2006, Gießen, 12.- 16.3.2007  
“Energy Dependence of Multiplicity Fluctuations in Heavy Ion Collisions”

Critical Point and Onset of Deconfinement, GSI, Darmstadt, 9.-13.7.2007 “Energy, rapidity and transverse momentum dependence of multiplicity fluctuations in heavy ion collisions at CERN SPS” [122]

Various talks at meetings of the NA49 and NA61 collaboration

# Danksagung

An dieser Stelle möchte ich mich bei allen Kollegen und Freunden bedanken, die mir einen erfolgreichen Abschluss dieser Arbeit und ein schönes Arbeitsklima ermöglicht haben.

Insbesondere danke ich meinem Doktorvater, Prof. Dr. Marek Gazdzicki. Er hat mich in das interessante Gebiet der Multiplizitätsfluktuationen eingeführt und mir während meiner Promotionszeit mir stets freundlich und kompetent zur Seite gestanden.

Ich möchte auch Prof. Dr. Herbert Ströbele danken, der sich stets für mich eingesetzt hat und der mir oft neue Denkanstöße gegeben hat.

Bei Prof. Reinhard Stock möchte ich mich dafür bedanken, dass er mich als Betreuer meiner Diplomarbeit in das Gebiet der Schwerionenphysik eingeführt hat und bei Gesprächen stets neue Begeisterung für unsere Physik weckt.

Vielen Dank an Prof. Dr. Peter Seyboth, den Sprecher des NA49-Experiments, für unsere Diskussionen und seine Unterstützung.

Bei Dr. Katarzyna Grebieszkow, Prof. Dr. Stanislaw Mrowczynski und Dr. Maciej Rybczynski möchte ich mich für die lebhaften Diskussionen über Fluktuationen bedanken.

Ich danke weiterhin Prof. Dr. Christoph Blume für seine Hilfe, unter anderem bei Problemen mit den T49-Klassen.

Ein großer Dank an alle derzeitigen und ehemaligen Mitglieder der NA49-Kollaboration, die die hier analysierten experimentellen Daten aufgenommen und rekonstruiert haben und mich auch sonst bei meiner Arbeit unterstützt haben. Die Meetings der Kollaboration waren stets sehr interessant und aufschlussreich.

Weiterhin danke ich der NA61-Kollaboration dafür, dass ich bei der ganzen Daten-Analyse das Experiment nicht ganz aus den Augen verloren habe.

Ein Dank gebührt auch meinen NA49-Kollegen und Ex-Kollegen in Frankfurt. Ich danke Claudia Strabel, Tim Schuster, Dr. Alexander Wetzler, Dr. Michael Mitrovski und den beiden Neulingen Hans Beck und Julian Book für die gute Zusammenarbeit. Peter Dinkelaker danke ich für seine Unterstützung, insbesondere während meiner Diplomarbeit. Bei "meiner" Diplomantin Milica Utric möchte ich mich für die gute Zusammenarbeit und ihre Geduld bedanken. Ich danke Michael Kliemant, dass er mir während des Studiums und der Promotion ein guter Freund war und für seine Versuche, mir das Mensa-Essen schmackhaft zu machen.

Ich danke Dr. Reiner Renfordt dafür, dass er mir die Hardware-Seite des NA49-Experiments näher gebracht hat. Bei Werner Ahmend möchte ich mich dafür bedanken, dass er mir stets bei Computer- und Netzwerkproblemen geholfen hat. Ulrich Köpf hat unter anderem dafür gesorgt, dass ich stets meine Reisekosten problemlos erstattet bekommen habe, auch dafür vielen Dank. Ich danke Prof. Dr. Harald Appelshäuser unter anderem dafür, dass er mir eine Kernphysik-Tutoriumsgruppe überlassen hat. Weiterhin möchte ich mich bei allen Kollegen der Hochenergiephysik-Gruppe für das gute Arbeitsklima bedanken. Hierbei möchte ich unter anderem Jutta Berschin, Simone Schuchmann, Amely Tampe, Hannelore Hinke, Dr. Matthias Hartig, Dr. Henner Büsching, Frederick Kramer, Wolfgang Sommer, Stefan Kniege, Andreas Fick, Dominik Wegerle, Konstantin Antipin, Dr. Mateusz Ploskon, Dr. Dariusz Antonczyk

## *Danksagung*

und Arnold Wiesenäcker danken. Außerdem bedanke ich mich bei Claudia Freudenberger für das Binden meiner Arbeit.

Ich bedanke mich bei Prof. Dr. Marcus Bleicher für die erfolgreiche Zusammenarbeit bei unserer Publikation der Multiplizitätsfluktuationen in UrQMD und dafür, dass er mich erst auf die Idee gebracht hat, das Paper zu schreiben.

Bei Michael Hauer möchte ich mich für die erfolgreiche Zusammenarbeit von theoretischer und experimenteller Physik in der Interpretation der Fluktuationsdaten im statistischen Modell bedanken. In diesem Zusammenhang möchte ich mich weiterhin bei Prof. Dr. Mark Gorenstein, Dr. Victor Begun und Prof. Dr. Igor Mishustin bedanken.

Bei Volodymyr Konchakovski und Dr. Elena Bratkovskaya bedanke ich mich für ihre HSD-Modellrechnungen und für die Zusammenarbeit bei unserem System-Size-Paper.

Weiterhin möchte ich mich bei der Universität Frankfurt, dem Institut für Kernphysik Frankfurt, dem europäischen Kernforschungszentrum CERN, der Gesellschaft für Schwerionenforschung GSI, dem virtuellen Institut VI-SIM der Helmholtz-Gemeinschaft und dem Bundesministerium für Bildung und Forschung (BMBF) bedanken, die diese Arbeit und das NA49-Experiment unterstützt haben.

Der größte Dank jedoch gebührt meiner Familie, insbesondere meinen Eltern Anita und Jürgen, die mir mein Studium ermöglicht haben und mich auch während meiner Promotion stets unterstützt haben. Weiterhin danke ich meiner Schwester Sandra und meiner Großmutter Hildegard.

# Lebenslauf

## Persönliche Daten:

Benjamin Lungwitz  
Wilhelmshöher Straße 70  
60389 Frankfurt  
geboren am 14.05.1981 in Frankfurt



## Schulbildung:

1987 - 1991 Grundschule Zentralfschule Frankfurt  
1991 - 2000 Gymnasium Helmholtzschule Frankfurt,  
Abschluss: Abitur (Note: 1,0)

## Studium und Promotion:

2000-2004 Studium der Physik an der Johann-Wolfgang-Goethe Universität Frankfurt  
11.04.2002 Vordiplom Physik (Note: sehr gut), Nebenfach Informatik  
2003-2004 Diplomarbeit bei Herrn Prof. Dr. Reinhard Stock am Institut für Kernphysik, Universität Frankfurt, Titel: Pionenproduktion in Stößen leichter Kerne bei 40 und 158 GeV pro Nukleon (NA49-Experiment am CERN)  
26.11.2004 Diplom in Physik (Note: sehr gut und mit Auszeichnung), Nebenfach Astrophysik  
2006 Philipp-Siedler-Preis des Physikalischen Vereins  
ab 01.12.2004 Promotion bei Herrn Prof. Dr. Marek Gazdzicki am Institut für Kernphysik, Universität Frankfurt, Titel: Energy Dependence of Multiplicity Fluctuations in Heavy Ion Collisions at the CERN SPS (NA49 und NA61-Experiment)